THE UNIVERSITY OF CHICAGO

ODD ELASTICITY, EXCITABLE INTERFACES, AND SPONTANEOUS WRINKLING OF ATOMICALLY THIN FILMS

A DISSERTATION SUBMITTED TO
THE FACULTY OF THE DIVISION OF THE PHYSICAL SCIENCES
IN CANDIDACY FOR THE DEGREE OF
DOCTOR OF PHILOSOPHY

DEPARTMENT OF PHYSICS

BY
COLIN ROSS SCHEIBNER

CHICAGO, ILLINOIS
AUGUST 2023

To my grandparents, Paul, Elaine, Evan, and Kathleen.

"It is hopeless for the occasional visitor to try to keep up with Chicago—she outgrows his prophecies faster than he can make them. She is always a novelty; for she is never the Chicago you saw when you passed through the last time."—Mark Twain, *Life on the Mississippi* (1883)

TABLE OF CONTENTS

LIST OF FIGURES vii

ACKNOWLEDGMENTS xviii

ABSTRACT xix

1 INTRODUCTION 1
1.1 Publications: 3

2 ODD ELASTICITY 5
2.1 What is elasticity? 5
2.2 Elasticity without a potential energy 6
2.2.1 Odd elasticity in two dimensions 8
2.3 Elastostatics 12
2.3.1 Poisson ratio, Young's modulus, and odd ratio 12
2.3.2 Airy stress function 14
2.3.3 Response to point force 15
2.4 Elastodynamics and wave mechanics 16
2.4.1 Continuum wave equations 16
2.4.2 Chiral earthquakes: odd elastic Rayleigh waves 19
2.5 Microscopic models and experimental systems 22
2.5.1 Pairwise interactions: odd springs 22
2.5.2 Active hinges 25
2.5.3 Odd metabeam 27
2.6 Topological defects 30
2.6.1 What is a topological defect? 30
2.6.2 Static strain and stress fields 32
2.6.3 Defect motion 36
2.7 Appendix: Nonlinear formulation of odd elasticity 44
2.7.1 The geometry of material deformation 44
2.7.2 Linear momentum conservation and the stress tensor(s) 46
2.7.3 Angular momentum conservation 47
2.7.4 Conservative and nonconservative forces 47
2.7.5 Linear elasticity 49
2.7.6 Background on topological defects in elasticity 50
2.7.7 Peach-Koehler force 52
2.7.8 Mass conservation constraint 55

3 SPIKING AT THE EDGE . . . 58
3.1 Motivation and overview . . . 58
3.1.1 The role of spatial extent . . . 63
3.1.2 A spiking phase diagram . . . 65
3.1.3 Overview of mathematical structure . . . 67
3.1.4 Spiking mode transition . . . 70
3.1.5 Trigger waves along 2D interfaces . . . 71
3.2 Spike generation in fast-slow systems without spatial extent . . . 72
3.3 Phase diagram for spiking at a Dirichlet boundary . . . 75
3.3.1 General Setting . . . 75
3.3.2 Construction of the phase diagram . . . 78
3.4 Details on population dynamics model . . . 84
3.5 Calculations for bioelectric interfaces . . . 87
3.5.1 Conductance-based biolectric model . . . 87
3.5.2 Dynamics of a single cell . . . 90
3.5.3 Phase diagram for interfacial spiking . . . 91
3.5.4 Limits: $r \to 0$, $r \to \infty$ . . . 96
3.5.5 Shape of unstable modes . . . 97
3.5.6 Example ion channels . . . 98
3.6 Calculations for oscillating chemical reactions . . . 100
3.7 Details on two-dimensional waveguides . . . 103
3.7.1 Two-dimensional media: interfacial trigger waves . . . 103
3.7.2 Design of the binary half adder . . . 104
3.8 Appendix: numerical details and mathematical background . . . 105
3.8.1 Numerics . . . 105
3.8.2 Explicitly solvable bioelectric interface model . . . 110
3.8.3 Preliminaries on the Conley index . . . 115

4 SPONTANEOUS WRINKLING OF ATOMICALLY THIN FILMS . . . 120
4.1 Atomically thin films . . . 120
4.1.1 Realizing freestanding atomically thin films on water . . . 122
4.2 Disordered strain model . . . 124
4.2.1 Continuum model . . . 124
4.2.2 Numerical discretization . . . 126
4.3 Universal scaling relations . . . 129
4.3.1 Tension induced wrinkling . . . 129
4.3.2 Implications for disordered strain field . . . 132
4.4 Indentation experiments . . . 133
4.4.1 Föppl-von Kármán theory . . . 134
4.4.2 Nondimensionalization . . . 139
4.4.3 Mechanical resolution . . . 144

REFERENCES . . . 146

LIST OF FIGURES

2.1 **Odd-elastic energy cycle. a.** The odd modulus A couples compression to an internal torque density, while rotations induce no stresses. The applied strains are represented by the black arrows, the undeformed shape by the dotted lines, and the internal stresses by the blue icons. **b.** The odd modulus K^o couples the two independent shear deformations. Unlike shear coupling in anisotropic passive solids, the induced stress is always rotated 45° counterclockwise relative to the applied strain. **c.** An odd-elastic material is subjected to a closed cycle in deformation space. First, a counterclockwise rotation is followed by a volumetric strain ϵ_V, inducing a torque density $A\epsilon_V$. Next, the object does work $A\epsilon_V\epsilon_\theta$ on its surrounding as it is rotated clockwise through an angle ϵ_θ, before being compressed to its original size. The total work done is A times the area enclosed in deformation space: $\epsilon_V\epsilon_\theta$. **d.** An analogous cycle involving only shear stress and shear strain. Adapted from Scheibner et al. [2020b]. 9

2.2 **Uniaxial compression of an odd elastic solid. a.** A uniaxial compression of a passive material generically results in symmetric deformation. If the material sides move outward, its Poisson ratio ν is positive. **b.** A uniaxial compression of an odd elastic block results in a tilt whose intensity is proportional to the odd ratio ν^o. If K^o is sufficiently large, the material also becomes auxetic ($\nu < 0$), meaning that the material contract in response to compression. Adapted from Scheibner et al. [2020b]. 13

2.3 **Odd elastodynamics. a.** A transverse wave in a passive solid is illustrated. **b.** An odd elastic wave propagates with a circular polarization. The thin red lines represent the displacement field. **c.** For an overdamped passive solid, the displacement field of the transverse mode decays towards its rest position. **d.** For an overdamped odd elastic solid with $K^o > 0$, the displacement field traces out spirals that become closed ellipses when $B = \mu = 0$. **e.** A phase diagram for wave beahvior featuring the moduli A and K^o. The red lines denote exceptional points. The dashed black line corresponds to a hexagonal lattice of bonds with transverse forces discussed in §2.5. Adapted from Scheibner et al. [2020b]. . . . 17

2.4 **Odd elasticity from pairwise interactions. a.** A pairwise interaction with a longitudinal force $F^{\parallel}(r)$ (black) and a transverse force $F^{\perp}(r)$ (red) connects two particles (gray circles). **b.** Janus particles and **c.** hematite colloids driven to spin by external magnetic fields. Adapted from Yan et al. [2015], Bililign et al. [2021]. **d**. A network of gyroscopes connected by springs is a realization of gyroscopic matter, whose elastodynamics can be mapped onto odd elasticity in the limit of fast spinning gyroscopes. Adapted from Nash et al. [2015]. **e.** Skyrmion lattices exhibit transverse interaction via a Magnus force. Adapted from Bauer and Pfleiderer [2016]. **f.** Starfish embryos and **g.** bacteria form chiral crystals with particle rotation driven by flagella and cilia, respectively. Adapted from Tan et al. [2022], Petroff et al. [2015]. **h.** Rayleigh-Bénard convection cells organized in a hexagonal pattern. When the system is put under rotation, odd elasticity can appear. Adapted from Koschmieder and Pallas [1974]. Figure adapted from Fruchart et al. [2023]. 23

2.5 **Active hinges. a.** Three rigid linkages are connected by motorized vertices. **b.** A hand pushes in on the left, and the right vertex contracts. **c.** A hand pushes in on the right, and the left vertex expands. **d-f.** Schematics summarizing the asymmetric (or odd) stiffness for $\kappa^a > 0$. Adapted from Brandenbourger et al. [2022]. 26

2.6 **Simulations of an odd wall. a.** Snapshots of a simulation of the active wall in its undeformed state (top) and after a quasistatic compression (bottom). The horizontal strains $u_{yy} = -\frac{\delta y}{y}$, the vertical strains $u_{xx} = -\frac{\delta x}{x}$ and the simple shear $u_{xy} = \frac{\delta x}{2y}$ are calculated by averaging the strains over all hexagons. The vertices within each red hexagon are coupled via active feedback κ^a. **b.** Shear strain u_{xy} (top) and normal strain u_{xx} (bottom) as a function of the normal strain u_{yy} for a range of values of the ratio between the active feedback and the hinge stiffness κ^a/κ. These curves were fitted polynomially and the slope at $u_{yy} = 0$ defines the odd ratio (Poisson's ratio). **c.** The odd ratio (top) and Poisson's ratio (bottom) as a function of κ^a/κ. A cubic fit $\nu^0 = 0.58\frac{\kappa^a}{\kappa} - 0.03\left(\frac{\kappa^a}{\kappa}\right)^3$ is used to calibrate the value of ν^o in experiments. **d.** The odd modulus K^o (top) and Young's modulus E (bottom) as a function of κ^a/κ. Adapted from Brandenbourger et al. [2022]. 27

2.7 **Impact of a passive projectile on an odd wall. a.** A passive projectile is launched at a wall of 120 motorized vertices ($\kappa^a > 0$), forming a tiling 17 robotic hexagons [denoted by the double-line hexagons in (b).] Scale bar: 10 cm. (Inset) Active vertices colored by their deformation. **b.** Experimental reconstructions of the wall. Color represents the average vertical displacement u_y of each hexagon and $L = 128$ cm. **c.** The displacement averaged over each column u_y as a function of time and horizontal coordinate x. **d.** The average shear deformation in the wall with color indicating time. Adapted from Brandenbourger et al. [2022]. . . 28

2.8 **Design and mechanics of an odd micropolar metabeam. a.** A single unit cell featuring three piezoelectric patches mounted on a beam: one that acts as a sensor, and two that act as actuators. **b.** A segment of the full metabeam. **c.** Each unit cell has an electronic loop. The voltage V_s induced by the central piezoelectric is fed into a transfer function $H(\omega) = V_a(\omega)/V_s(\omega)$ that sends opposing voltages V_a and $-V_a$ to the piezoelectric actuators. **d.** A photograph of the metabeam (horizontal) with the electronic circuits in the foreground. The mechanical forces from the attached wires are negligible: they act only as sources of energy and computation, but not of linear or angular momentum. **e.** The motion of the metabeam can be described by two independent fields, φ and h, which parameterize the angular and vertical displacements of the metabeam. Notice that under a reflection about the $\hat{z}$ axis, I have $\varphi \to -\varphi$ and $h \to h$. **f.** When the beam bends, the center piezoelectric is stretched. **g.** The antisymmetric electronic actuation then gives rise to a shearing stress proportional to the modulus P. Adapted from Chen et al. [2021]. 29

2.9 **Strain field of a dislocation pair. a-c.** The distribution of rotation (u^1), shear 1 (u^2), and shear 2 (u^3) surrounding a pair of dislocations in an odd elastic solid with $\nu = 0.8$ and $\nu^o = -0.88$. The right panels visualize the continuum theory while the left panel is the result of numerics. The inset to panel (a) renders the individual masses and bonds comprising the dislocation pair before (top) and after (bottom) relaxation. Panels **d-f.** quantitatively compare theory and numerical experiments by sampling the strain (green dots) at points between 8.0 and 9.2 lattice spacings from the center. The green line is the theoretical curve with $\nu = 0.8$ and $\nu^o = -0.88$. The shaded background accounts in the variation in distance from the center. The orange lines, provided for reference, are theoretical curves for a passive solid with $\nu = 0.8$ and $\nu^o = 0$. The dilation (u^0) is too small for numerical validation. Adapted from Braverman et al. [2021]. 32

2.10 **Core and Peach-Koehler forces. a.** A dislocation is embedded in a triangular lattice of bonds exerting clockwise transverse forces. The dislocation consists of a particle with only five neighbors (labeled 5) paired with a particle with seven neighbors (labeled 7). These are separated by a horizontal line known as the glide plane. The transverse forces from the bonds not crossing the glide plane (highlighted in red) give rise to opposing lateral forces on the rows of atoms containing the 5 and the 7. These forces motivate the dislocation to travel left and can be captured in the continuum by the Peach–Koehler force F^{PK}. **b.** The bonds that straddle the glide plane push in the opposite direction and, therefore, motivate the dislocation to move to the right. This effect, dubbed the core force F^{core}, evades a continuum description. The core force vanishes when the microscopic interactions are entirely longitudinal. Adapted from Fruchart et al. [2023]. 33

2.11 **Schematic of dislocation core. a.** A rendering of the dislocation core with certain particles highlighted by their index $(R(\alpha), C_R(\alpha))$. **b.** Bonds connecting rows 2 and 3 are plotted in the space of their relative coordinates (r_x, r_y). The inset shows the contour $\Gamma(2, 3, 1)$ which interpolates between each of the bond positions. **c.** The bonds connecting rows 0 and 1 are shown. The individual contours $\Gamma(0, 1, n)$ do not close since the rows 0 and 1 are on opposite sides of the glide plane. Instead, the bonds can be concatenated into a single continuous contour $\mathcal{C}(0, 1)$. Adapted from Braverman et al. [2021]. 39

2.12 **Dislocations self propel via active work cycles at their cores. a.** Three transverse interactions $F^{\perp}_{\mathrm{LJ}}$ (purple), $F^{\perp}_{\mathrm{Lub}}$ (teal), and $F^{\perp}_{\delta}$ (orange), with the neighbor shells highlighted by grey lines. Inset: A hexagonal lattice with first and second neighbor shells highlighted. **b.** Particles are arranged in a free floating circular cluster with a single dislocation located at the center, and the dislocation position is tracked as a function of time. Simulations are performed with clusters of radius $R = 50$ (dashed) and $R = 100$ (solid). **c**. Bonds crossing the glide plane of a dislocation are highlighted. Hue indicates the bond's position in real space (blue: left, red: right). Opacity indicates the length of the bond (nearest neighbors darkest). **d.** The highlighted bonds are plotted with their bases aligned. As the dislocation moves one unit cell to the right, the tops of the bonds traces out a contour $\mathcal{C}$ (black dashed). The gray arrows depict the interaction force field. **e.** The interaction $F^{\perp}_{\delta}$ is varied by changing the location δ of its peak (pink: smaller δ, green: larger δ). For each value of δ, the dislocation's position is tracked as a function of time. **f.** The magnitude of the Peach-Koehler force f^{PK} and the active core force f^{core} as a function of the peak position δ. The vertical lines represent the values of δ used in the simulation. The direction change of the dislocation motion coincides with the crossover between f^{core} and f^{PK}. Adapted from Braverman et al. [2021]. 40

2.13 **An illustration of the coordinate systems defined in § 2.7.1.** Adapted from Braverman et al. [2021]. 45

2.14 **Geometric properties of disclinations and dislocations.** An illustration of the dislocation angle θ and Burgers vector $\mathbf{b}$, as well as the contours used in §2.7.6. Adapted from Braverman et al. [2021]. 50

2.15 **Branch cuts for dislocation motion.** Illustration of the branch cut construction used in §2.7.7-2.7.8. Adapted from Braverman et al. [2021]. 52

2.16 **Glide constraints on dislocations.** An illustration of the kinematic constraints that restrict dislocation motion to lie along the glide plane. When a dislocation glides, the total mass (i.e. number of particles) within the selected region does not change and the motion is localized to the particles near the core. (In this realization $\mathbf{v}$ is the velocity of the particle with the most motion during the rearrangement.) However, when the dislocation climbs, significant motion extends all the way out to the boundary of the sample since a column of particles moves downward. The net change in mass of the highlighted region is $\delta M = \rho \delta \mathbf{X} \times \mathbf{b} = m$, where $\mathbf{b} = \hat{\mathbf{x}}a$ is the Burgers vector, $\delta \mathbf{X} = -\hat{\mathbf{y}}a$ is the motion of the dislocation, m is the mass of the particle, $\rho = m/a^2$ is the density, and a is the lattice spacing. Adapted from Braverman et al. [2021]. 55

3.1 **Edge spiking in electrophysiology, population dynamics, and chemistry. a.** Experiments from Ref. [Ori et al., 2023] in which an action potential propagates along a tissue interface, as revealed by a voltage sensitive red dye. Scale bar 1 mm. The left column shows a schematic vertical cross-section of the interface: the top tissue features sodium ion channels (inward arrows), while the bottom tissue features potassium ion channels (outward arrows). The vertical lines represent gap junction coupling between the cells. **b.** A fast diffusing predator (lumberjacks) and relatively immobile prey (trees) are described by an interfacial Lotka-volterra model [Eqs. (3.3-3.4)]. A kymograph generated by the model reveals spikes in the lumberjack population generated at the interface. **c.** An interface between two chemical reservoirs, neither of which are capable of oscillating, is described by Eqs. (3.10-3.11). A kymograph of the fast, mobile catalyst a reveals repeated spikes generated at the interface. Adapted from Scheibner et al. [2023]. 59

3.2 **Spikes induced by weak diffusion and large system size. a.** (inset) A predator-prey system with a desert (red) and a forest (blue) described by Eqs. (3.1-3.2). In the forest, the predators (lumberjacks, p) consume the prey (trees, n) with predation rate $1/q$. The predators cross from the forest to the desert (and subsequently perish) with hopping rate ϵ. **a-c.** Three phase portraits, for $\epsilon = 0$, $0 < \epsilon \ll 1$, and $1 \ll \epsilon$, illustrate the role of diffusion across a boundary: For $\epsilon = 0$ (a), the lumberjacks reach their carrying capacity and the trees go extinct. For $\epsilon \gg 1$ (c), the lumberjacks go extinct and the trees reach their carrying capacity. Spikes can only occur in the intermediate range $0 < \epsilon \ll 1$ (b), in which the effective death rate due to hopping is present but not overpowering. Orange curves are example trajectories. The $\dot{p} = 0$ and $\dot{n} = 0$ nullclines are denoted by black and grey lines, respectively. **d.** A phase diagram for Eqs. (3.1-3.2) summarizes the possible behaviors: if the lumberjack hopping rate ϵ is too large, the lumberjack population cannot spike. The phase boundaries are determined by the consumption nonlinearity $k(q)$ in Eqs. (3.1-3.2). **e-g.** A chain of N forests (blue lines) are coupled to a desert (red line) by a large hopping rate $\epsilon = 4$. Kymographs for systems with $N = 2$, $N = 4$, and $N = 100$ exemplify a distinctive transition: oscillation onset is driven by increasing system size, even as ϵ is held constant. (See §3.4 for simulation details.) **h.** A phase diagram for Eqs. (3.3-3.4), applicable for $N \gg 1$, reveals a crucial distinction between the spatially and non-spatially extended systems: the vertical axis in (h) features $N/\sqrt{\epsilon}$, implying that spiking occurs for a much larger range of ϵ in the spatially extended limit. The curve $X(q)$ determines the locations of the phase boundaries and is given in Eq. (3.20). Adapted from Scheibner et al. [2023]. 60

3.3 **A spiking interface is more than the sum of its parts. a.** A spiking phase diagram is shown for the bioelectric interface in Eqs. (3.5-3.6). Here, $L/\sqrt{D}$ is the ratio of the system size to the diffusion strength and r and V_* appear in $h_\infty(V) = r\,\Theta(V_* - V)$. The parameter r is the ratio of the amplifier (sodium channel) strength to the suppressor (potassium channel) strength. **b.** At small $L/\sqrt{D}$, diffusion forces the membrane potential to be approximately constant across the entire tissue, creating an effective single cell with both ion channels. For large $L/\sqrt{D}$, the coupling is weak, so the dynamics are spatially heterogeneous. **c-k.** A table comparing the $L/\sqrt{D} \to 0$ (single cell) and the $L/\sqrt{D} \to \infty$ (interfacial) limits. The left column (c, f, i) shows three examples of voltage-current curves for potassium (red) and sodium (blue) ion channels. Their reversal potentials are denoted V_{K} and V_{Na}, respectively. Adapted from Scheibner et al. [2023]. 62

3.4 **A geometric construction for interfacial spiking. a.** Starting from Eqs. (3.5-3.6), the antiderivatives of $f_{\mathrm{K}}(V)$ (solid red line) and $h_\infty(V)f_{\mathrm{Na}}(V)$ (solid blue line) are visualized as hills. The dashed blue line is the antiderivative of $rf_{\mathrm{Na}}(V)$. To construct the stationary solution with no-flux boundary conditions, consider letting a ball roll from the top of one hill to the other (orange curve). **b.** The stationary voltage solution $V_0(x)$ in space corresponds to the trajectory of a ball (in time) rolling across the potentials in (a). **c.** The ability to spike is determined by the number and stability of critical points of Φ in Eq. (3.9). To determine the critical points, release a ball from a voltage V_R and measure the "time" X it takes to reach the intersection. **d.** A plot of X vs. V_R reveals three cases. When x_* intersects X once, the interface is unable to spike. **e.** When x_* intersects X three times and V_* corresponds to an increasing branch of X, the interface is excitable. **f.** When x_* intersects 3 times and V_* corresponds to the decreasing branch, the voltage at the interface oscillates. **g.-h.** Kymographs illustrating no spiking, excitability, and oscillating at the interface. See Appendix 3.8 for simulation details. Adapted from Scheibner et al. [2023]. 66

3.5 **Nonlinear waveguides from interfacial spiking. a-b.** Two distinct non-spiking materials (light and dark grey) are patterned for form a four way junction of excitable interfaces. When two nonlinear wave trains arrive at a junction in-phase (a), they propagate through uninterrupted. When the two wave trains arrive out-of-phase, they annihilate at the junction. The color corresponds to the intensity I of the fast, diffusively coupled variable. **c-d.** A network of excitable interfaces acts as a binary half adder, which takes the sum of two 0 or 1 inputs. Here, the presence of a wave indicates the value 1 while the absence of a wave indicates the value 0. The color $I_{\max}$ is the maximum value of I over time when the network has reached steady state. See §3.7.1-3.7.2 and Appendix 3.8 for simulation details. Adapted from Scheibner et al. [2023]. 68

3.6 **Spike generation in fast-slow systems without spatial extent. a.** (top) A phase portrait of an excitable fast-slow system. The black curve corresponds to $\dot{A} = 0$, and the grey curve corresponds to $\dot{B} = 0$. The light blue arrow represents an external perturbation. The solid green curves are the fast trajectory, and the dashed orange curve is the refractory period. The solid orange circle denotes the global fixed point. The open (closed) green circle represents an unstable (stable) fixed point of the fast dynamics. (bottom) On short time scales, the potential $U(A)$ governs the dynamics. The system is excitable since $U(A)$ has multiple minima. **b.** (top) A phase portrait of a fast-slow system exhibiting oscillations. The dashed orange curve is a limit cycle. The open orange circle denotes an unstable global fixed point. The closed green circles are stable fixed points of the fast dynamics if initialized at the open orange circle. (bottom) On short time scales, the potential $U(A)$ governs the dynamics. The system is exhibits oscillations since since $U(A)$ has multiple minima and the orange circle (global fixed point) is not one of them. Adapted from Scheibner et al. [2023]. 74

3.7 **Stationary solutions and critical points. a.** The potentials $U(A)$ and $U_{\text{clip}}(A)$ are depicted by dashed and solid lines, respectively. The red points correspond to type I stationary solutions that lie along the non-clipped part of the potential. The blue point corresponds to a type II stationary solution, which lies at the point A_*. The grey circle symbolizes a ball moving this 1D potential. If released from rest at either of the red points, the ball will take a "time" ℓ to reach $A = 0$. If the ball is released from the blue point, it will take a "time" $X(A_*)$ to reach the origin. **b.** The stationary solutions are plotted in real space. Type I solutions intersect the curve $X(A)$ along the $x = \ell$ boundary and type II solutions intersect the curve $X(A)$ along the $A = A_*$ boundary. **c.** The (A_*, ℓ) parameter space is shown, with $X(A_*)$ plotted. A specific choice of parameters corresponds to a point P. Type I stationary solutions lie along the dashed red line, while type II lie along the dashed blue line. The critical points associated with the blue stationary solution are indicated with purple circles. Adapted from Scheibner et al. [2023]. 75

3.8 **Determining the stability of critical points.** The critical points of $\Phi(A; e)$ are shown for three values of e. **a.** At low e, there exists only one critical point, $\mathcal{A}$. **b.** At moderate e, there exist three critical points $\mathcal{A}$, $\mathcal{B}$, and $\mathcal{C}$. The solids arrows indicate heteroclinic orbits. **c.** At large e, only one critical point ($\mathcal{C}$) remains. Critical points $\mathcal{A}$ and $\mathcal{C}$ must be minima (i.e. unstable dimension of 0), while $\mathcal{B}$ has an unstable dimension of 1. Adapted from Scheibner et al. [2023]. 78

3.9 **Phase diagram for spiking at a Dirichlet boundary**. **a.** A phase diagram in the A_*-ℓ plane is divided into 11 distinct regions. The solid black curve is $X(A_*)$. The color code indicates the qualitative behavior. Green: no spiking; olive: bistable; blue: excitable; pink: oscillating. **b.** The qualitative behavior may be inferred from diagrams that summarize the topological features of the flow. In each diagram, the black circles represent stationary solutions, and the grey circles represent the critical points of the associated potentials. Solid circles are stable, and the open circles are unstable. The light grey lines represent heteroclinic orbits in the fast dynamics, and the black lines convey the evolution of the system on longer time scales. Adapted from Scheibner et al. [2023]. 79

3.10 **A spiking phase diagram for a single bioelectric cell. a.** A representative phase portrait for Eqs. (3.54-3.55). The fixed point (here unstable) appears at the intersection h_{eq} (black) and h_∞ (red). **b.** An annotated phase diagram showing the fixed points, limit cycles, and heteroclinic orbits in each phase. The light grey points and arrows represent features that are only present in the $\tau \to \infty$ dynamics. **c.** The h_{eq} and h_∞ curves for each phase in the phase diagram. Adapted from Scheibner et al. [2023]. 83

3.11 **Bifurcation analysis of interfacial spiking.** **a.** The Hamiltonian flow in Eqs. (3.61-3.62) for $x < 0$ is depicted. The separatrix P_{K} (solid blue line) results from an advection of $P = 0$ (dashed blue line) through a distance $\ell \to \infty$. **b.** Similarly, the Hamiltonian flow in Eqs. (3.61-3.62) for $x > 0$ is depicted. The separatrix P_{Na} (solid red line) results from an advection of $P = 0$ (dashed red line) through a distance $\ell \to -\infty$. **c.** In real space, composing the separatrices yields the stationary solution $V_0(x)$. The curve $V_0(x)$ matches the $x < 0$ and $x > 0$ solutions subject to the requirement that the right solution obtains a slope of zero at $V = V_*$. **d.** The curve $P_{\mathrm{Na}}(V, V_R)$ is shown in black. V_R is the V coordinate of the intersection with $P = 0$, and V_1 marks the intersection with P_{K}. The function $X(V_R)$ represents the x distance transversed in real space between the voltages V_R and $V_1(V_R)$. **e.** The function X is plotted as a function of V_R. The number of solutions to the equation $X(V_R) = x_*$ varies from 1 to 3 depending on x_*. **f.** One can visualize the function $X(V_R)$ by plotting a range of trial solutions with different slopes at their interface. The function $X(V_R)$ corresponds to the x value at which each curve first attains its maximum. The thick lines correspond to the critical points of Φ. **g.** If x_* intersects X once, then the system does not exhibit spikes. **h.** If x_* intersects X three times with V_* corresponding to an increasing branch, then the system exhibits excitability. **i.** If V_* lies on the decreasing branch of X, then the system exhibits oscillations. In (e-i), the circles represent critical points of the functional Φ in Eqs. (3.68). The orange circle represents $V_0(x)$, the stationary solution of Eqs. (3.5-3.6). Solid arrows represent fast heteroclinic orbits, and the dashed arrows represent slow dynamics in Eqs. (3.5-3.6). Open circles are unstable critical points, while solid circles are stable critical points of Φ. Adapted from Scheibner et al. [2023]. . . 88

3.12 **Linearized dynamics and interface confinement.** **a.** An example of three solutions to Eq. (3.68) (black lines), which constitute critical points of the functional Φ. The light gray curves represent trial solutions that do not meet the boundary conditions. **b-d.** The linearized dynamics about each critical point p is governed by a Schrödinger equation with an effective potential U_p. Each effective potential features a well near the interface. The unstable dimension, m, of each critical point corresponds to the number of negative energy states of the Hamiltonian. Because the negative energy states must be bound states, the unstable modes that drive the spiking feature a spatial profile that is localized near the interface. The sole negative energy state in (c) is highlighted in red. Adapted from Scheibner et al. [2023]. 90

3.13 **A phase portrait of an excitable chemical reaction.** A phase portrait for Eqs. (3.96-3.97) with $m_1 = 2$, $m_2 = 10^{-3}$, $\tau = 10^4$. The black curve is $b_{\text{eq}}(a)$ [Eq. (3.98)] and the grey curve is $b_\infty(a)$ [Eq. (3.95)]. The solid and filled green circles represent critical points of the fast dynamics (c.f. Fig. 3.6). The orange curve is an example trajectory starting at the star and ending at the orange solid circle and exhibiting a spike. The same parameters are used to integrate Eqs. (3.102-3.103) in Fig. 3.1c. Notably, the interface exhibits oscillation, rather than excitability, due to the presence of diffusion. Adapted from Scheibner et al. [2023]. 94
3.14 **Examples of OR, AND, NOT, XOR, and CROSS logic gates.** The black lines represent interfaces between distinct materials (purple and green). Solid lines fit an integer number of wavelengths, while dashed lines fit a half integer number of wavelengths. The black circles represent termination points. Adapted from Scheibner et al. [2023]. 95
3.15 **Decomposition of binary half adder.** A binary half adder can be decomposed into and AND gate and an XOR gates. Since the XOR gate generates an output of the system, it can be simplified to the XOR* gate. Adapted from Scheibner et al. [2023]. 99
3.16 **Piecewise linear ion channels.** Adapted from Scheibner et al. [2023]. 114

4.1 **Freestanding atomically thin MoS_2 on water. a.** Schematic describing the mechanical imaging of atomically thin membrane on water. **b.** Optical micrograph of mm-scale floating MoS_2 membrane with ≤ 2 μm gap created by laser patterning. The inset shows a membrane of same dimensions, displaced after 2 hours following patterning of 100 μm gap (the dotted line depicts the initial position). Scale bar=400μm. **c.** Time-dependent change of the gap distance between floating and anchored MoS_2. The standard deviation is shown as gray area. **d-e.** AFM height and the strain maps (inset) of (d) confined and (e) free membranes, respectively. **f-g.** The histogram of (f) height and (g) strain variation between confined and free membranes. Adapted from Yu et al. [2023]. 121
4.2 **Scaling of wrinklings via continuum elasticity. a.** Experimental measurements of MoS_2 surface topography on the water with increasing domain size D from left to right. Scale bar = 500 nm. **b.** The average wrinkle width λ wavelength and amplitude A plotted as a function of average domain size D and wrinkle length ℓ. The theoretical scaling in Eqs. (4.31-4.33) predicts a linear relationship $A\lambda \propto \ell$. **c.** Numerical relaxation of thin sheets with Gaussian distributed random strain [see Eq. (4.8)]. As the correlation length increases (left to right), the wrinkles become taller in amplitude and more eccentric. **d.** The trace of the strain tensor [Eq. (4.8)] prior to (left) and after (right) relaxation. Adapted from Yu et al. [2023]. 123

4.3 **Effective mechanical properties of wrinkled MoS_2. a.** Force-displacement curve for a sheet of MoS_2 by AFM. Red and blue line corresponds large-grain ($D = 1200nm$) and small-grain ($D = 100nm$), respectively. The dotted line shows the theoretical simulation of the floating membrane indentation with different Young's modulus given by Y_0, $Y_0/10$, and $Y_0/100$, where Y_0 is Young's modulus of pristine MoS_2, and Gray dotted line shows without the membrane. Inset shows the schematic of AFM indentation on a floating monolayer MoS_2 membrane. **b.** The surface topography of floating MoS2 with different domain sizes. i) $D = 100nm$, and ii) $D = 1200nm$. Scale bar = $5\mu m$. **c.** Theoretical strain energy profiles of a membrane for a given indentation depth h as a function of radius from the point of indenter $r = 0$ on water with different Modulus. Dotted lines show the size of the typical domains for D = 1200nm(LG), and D = 100 nm(SG). **d-e.** The force response map of $D = 100nm$ (d), and $D = 1200nm$ (e) on the area presented in (b). The force is measured at the indentation depth $\delta = 240nm$. Scale bar = $5\mu m$. Adapted from Yu et al. [2023]. 133

4.4 **Boundary conditions and indentation regimes.** The spatial profiles $h(r)$ are shown for increasing values of $\Lambda = \frac{Y}{2\gamma}\left(\frac{\delta}{R}\right)^2$. **a.** $\Lambda = 0.0$ corresponds to exposed water with no membrane. **b.** $\Lambda = 0.1$ is the maximum value probed in our experiments. **c.** $\Lambda = 10$ is a regime familiar from nanoindentation of $1\mu m$ drum-heads. The blue curve has an inflection point, indicating that the solution is unstable to an azimuthal buckling instability. The red curves correspond to a pinned boundary condition, as is the case for suspended membrane experiments. The blue curves correspond to constant stress boundary conditions, applicable for floating membranes. The grey dashed lines are asymptotic solutions that can be calculated analytically. Adapted from Yu et al. [2023]. 134

4.5 **Identification of mechanical resolution a.** The fraction f of deformation energy as a function of $\xi = r/R$ for $\Lambda \ll 1$, see Eq. (4.81). The shoulder in each curve sets a radius, the mechanical resolution, within which the majority of the deformation energy resides. **b.** The location of the shoulder can be collapsed by rescaling r by $r_{\text{res}} = \delta\sqrt{Y/2\gamma}$. Adapted from Yu et al. [2023]. 139

ACKNOWLEDGMENTS

It is my great pleasure to acknowledge the many individuals who have supported me throughout my PhD. Thank you to my advisor, Professor Vincenzo Vitelli. I am consistently inspired by your stamina and creativity. You have so many valuable lessons to teach, and—despite my best efforts—I am still quite far from learning the all! Thank you also to my thesis committee, Sidney Nagel, Dam Son, William Irvine, and mentors Thomas Witten, Jiwoong Park, and Heinrich Jaeger. Each if you have contributed to environment that is challenging, inspiring, and supportive. I owe a special thanks to my former groupmate (and now Professor) Anton Souslov, who was a crucial mentor to me when I first joined Vincenzo's group. Likewise, thank you to my long-term officemates, Tali Khain and Michel Fruchart, with whom I had the pleasure of writing papers and sharing many stimulating and formative conversations. In addition, I had the privilege of working with talented undergraduate and masters students, Lara Braverman, Michele Fossati, and Livia Guttieres, who certainly taught me more than I taught them. I would also like to thank all the members of the Vitelli group with whom I had the pleasure of interacting: Daniel Seara, Luca Scharrer, Jonathan Colen, Matthew Schmitt, Rituparno Mandal, Yael Avni, David Martin, Nitin Upadhyaya, Maciej Koch-Janusz, Siqi Ni, Ege Eren, Howard Timlin, Hamed Abbaszadeh, Claudia Yao, Shoshanna Chipman, Ming Han, Bryan VanSaders, and Rosalind Huang. Thank you to my co-authors who, in addition to those appearing above, include: Jonas Veenstra, Corentin Coulais, Martin Brandenbourger, Debu Banerjee, Yangyang Chen, Xiaopeng Li, Guoilian Huang, Adam Cohen, Hillel Ori, Suriyanarayanan Vaikuntanathan, Juan J. de Pablo, Jaehyung Yu, and Piotr Surówka. Thank you also to my roommates, Lucas Beaufore, Anora Hamann, and Siddhartha Sohoni, and my many supportive friends and peers. Lastly, I would like to thank my family: my parents John and Emer, my sisters Aileen and Katie, my grandmother Elaine Scheibner, and my many aunts, uncles, and cousins.

ABSTRACT

This thesis explores three distinct topics, each requiring a generalization of a classical continuum theory in order to capture a striking phenomenon from a coarsegrained perspective.

Chapter 2 revisits the time-honored subject of elasticity theory, which describes how solids exert stresses in response to deformation. Classical elasticity is strongly constrained by the assumption that stress is related to strain through gradients of a potential energy. This assumption is not generally valid for systems with internal sources of energy or that are governed by non-energetic effective interactions. In this chapter, I formulate a continuum theory known as *odd elasticity*, which generalizes classical elasticity to include nonconservative forces. Phenomenological consequences and experimental implications are discussed.

Chapter 3 visits the topic of reaction-diffusion equations. In homogeneous media, it is known that adversarial forces (present everywhere in space) can give rise to local bistabilities, resulting in spikes and wave propagation. In this chapter, I show how global bistability can emerge and cause spikes and wave propagation in the presence of heterogeneities, e.g. boundaries and interfaces, that segregate competing forces. These surprisingly robust interfacial excitations arise in models of chemical reactions and predator-prey dynamics, as well as in recent experiments wherein localized action potentials are created at the interface of distinct, nonspiking bioelectric tissues.

Finally, Chapter 4 studies the emergence of spontaneous wrinkles recently observed in novel confinement-free measurements of atomically thin films. I show that a classic thin sheet model with a minimal twist, disordered strain, is sufficient to recreate these wrinkles. Using continuum theory, I derive scaling predictions for the wrinkle morphology that are consistent with experimental observations and independent of atomistic details. A theoretical analysis of indentation experiments reveals that these wrinkles have dramatic implications for the effective strength and heterogeneity of unconfined atomically thin films.

CHAPTER 1

INTRODUCTION

The unifying goal of this thesis to enlarge our ability to see the world through a continuum lens. This goal is anchored in the mind set that it doesn't matter what a system (a material, living organism, or engineered structure) is made of at its microscopic scale so long as its behavior can be self-consistently described in a macroscopic way. This thesis explores three incarnations of this broad theme, each of which enhances the scope of our macroscopic vocabulary in a distinct way, and allows for novel predictions in a variety of physical systems.

The first topic discussed in detail is called *Odd Elasticity*. Here, elasticity refers to the ability of a solid medium or a pattern to resist deformation, i.e. shape change, by exerting internal forces known as stress. This time-honored subject, whose relevance extends from biomechanics to structural engineering, is typically formulated around the following assumption: the relationship between stress and shape change is governed by a potential energy. While this assumption is natural for traditional materials (like wood or metal), it needs to be revisited when the constituents of a medium are capable of metabolizing energy, such as in crystals made from self-spinning particles, collections of living organisms, or in condensed matter systems for which the simplest description of the dynamics involves non-conservative forces. This chapter formulates a version of elasticity applicable to these systems, explores their phenomenological consequences, and makes predictions for natural and synthetic media.

The following chapter is titled *Spiking at the Edge*. Spatially extended nonlinear processes, such as chemical reactions or muscular contractions, are often described macroscopically by reaction diffusion equations. In such systems, a spike is a rapid nonlinear surge in a measured variable (e.g., a chemical's concentration or a cell's membrane potential) followed by a recovery period in which no spike can occur again. These processes are crucial for a wide range of biological functions, such as pacemaking in the heart and information quantization in the brain, as well as disastrous events, like forest fires and disease outbreaks. Yet the ex-

treme nonlinearity of these systems poses a mathematical challenge, often forcing scientists to make simplifications that are not universally appropriate. For instance, almost all analytical progress has been confined to situations in which the underlying reaction-diffusion system are spatially homogeneous. This chapter will present a study spike generation in reaction-diffusion systems with strong heterogenities (e.g. interfaces and boundaries). A spiking phase diagram will show that neglecting heterogeneity is not always safe: diffusion near a boundary or interface can cause edge spiking even when the media on either side cannot spike separately nor when mixed. The tools developed will be applied to population dynamics and oscillating chemical reactions, as well as recent experimental observations of interfacial spikes in hetergeneous bioelectric tissues.

The third topic is titled *Spontaneous Wrinkling of Atomically Thin Films*. Atomically thin films are the most slender form of matter that can be made from atoms—they are typically only one to three atoms thick. Perfect monolayers can now be fabricated on the wafer scale, meaning that their thickness is only a few angstroms, while their width is several millimeters. This is no small feat of engineering, considering that a sheet of paper of the same aspect ratio would easily cover a professional football stadium. Recent experiments took an unconventional approach to study the mechanics of these atomically thin films: they were floated on water. The experiments led to an unexpected observation: the atomically thin films, when released from solid boundaries, are not flat. Instead, they form large scale, athermal wrinkles whose peak-to-peak height is an order of magnitude larger than the membrane thickness. In this chapter, I will argue that the wrinkles are independent of the presence of water and instead depend on one minimal ingredient: disordered internal strain. A continuum analysis that is agnostic to atomistic structural details shows how the wrinkle morphology scales with the typical crystalline domain size of the monolayer film. In addition, other results from these experiments, such as the effective strength and heterogeneity of the wrinkled membranes, is studied through a continuum perspective.

When the details fade away, my hope is that this thesis expands our ability and our inclination to view the world through a coarsegrained lens.

1.1 Publications:

This thesis is the culmination of the following works:

1. Fruchart*, **Scheibner***, Vitelli. Odd Viscosity and Odd Elasticity. *Annu. Rev. Condens. Matter Phys.* **14:1**, 471-510 (2023)

2. Ori, Duque Ramirez, Frank Hayward, **Scheibner**, Tian, Ortiz, Vitelli, Cohen. Observation of topological action potentials in engineered tissues. *Nat. Phys.* **19**, 290-296 (2023)

3. Khain, **Scheibner**, Fruchart, Vitelli. Stokes flows in three-dimensional fluids with odd and parity-violating viscosities. *JFM.* **934**, A23 (2022)

4. Braverman*, **Scheibner***, VanSaders*, Vitelli. Topological Defects in Solids with Odd Elasticity. *Phys. Rev. Lett.* **127**, 269001 (2021) (Editors' Suggestion)

5. Han, Fruchart, **Scheibner**, Vaikuntanathan, de Pablo, Vitelli. Fluctuating hydrodynamics of chiral active fluids. *Nat. Phys.* **17**, 1260-1269 (2021)

6. Chen*, Li*, **Scheibner***, Vitelli, Huang. Realization of active metamaterials with odd micropolar elasticity. *Nat. Commun.* **12**, 5935 (2021)

7. **Scheibner**, Irvine, Vitelli. Non-Hermitian Band Topology and Skin Modes in Active Elastic Media. *Phys. Rev. Lett.* **125**, 118001 (2020)

8. **Scheibner***, Souslov*, Banerjee, Surówka, Irvine, Vitelli. Odd Elasticity. *Nat. Phys.* **16**, 475-480 (2020)

9. Yu*, **Scheibner***, Vitelli, Witten, Park. Mechanics of atomically thin films on water. *In prep.* (2023)

10. **Scheibner**, Ori, Cohen, Vitelli. Spiking at the edge. *Under review.* (2023)

11. Fossati, **Scheibner**, Fruchart, Vitelli. Odd elasticity and topological waves in active surfaces. *Under review.* (2022)

12. Fruchart, Han, **Scheibner**, Vitelli. The odd ideal gas: Hall viscosity and thermal conductivity from non-Hermitian kinetic theory. *In revision.* (2022)

13. Brandenbourger*, **Scheibner***, Veenstra, Vitelli, Coulais. Limit cycles turn active matter into robots. *In revision.* (2022)

* denotes equal contribution.

CHAPTER 2

ODD ELASTICITY

2.1 What is elasticity?

Elasticity is the continuum description of the relationship between the way a solid medium deforms (strain) and the way it exerts internal forces (stress). For many systems, when the deformations occur on length scales much larger than the size of a typical microscopic constituent, the stress-strain relationship becomes universal in the sense that it is described by a small number of phenomenological parameters. These parameters can be constrained by examining two facets of the system under consideration: symmetries and conservation laws. For instance, should an experiment look the same if one watches it in a mirror? Is angular momentum conserved or can be drawn from a hidden reservoir? The conservation law of interest in this chapter is energy conservation. When valid, this constraint imposes that stresses are related to the strains through the gradient of an energy functional. For most conventional materials, like metal, rubber, or wood, this property naturally applies because these systems typically operate near thermodynamic equilibrium, in which stresses act to push the system down free-energy gradients. However, this constraint does not hold universally. For example, in crystals of living organisms or spinning particles, the microscopic units are constantly metabolizing energy. Moreover, in systems such as coupled gyroscopes or particles experiencing hydrodynamic interactions, the dynamically relevant notion of force is not energetically conjugate to displacements. In such systems, one can ask what the correct form of the elasticity looks like? Elasticity without the assumption of energy conservation is what I will refer to as *odd* elasticity. This chapter is based on a sequence of papers including Scheibner et al. [2020b,a], Brandenbourger et al. [2022], Fossati et al. [2022], Chen et al. [2021], Braverman et al. [2021], Fruchart et al. [2023].

2.2 Elasticity without a potential energy

To see what motivates the name *odd* elasticity, it is useful to review the typical story of elasticity itself [Landau et al., 1986]. To describe the deformation of a material, we will say that a piece of material originally at point x_i winds up at point $x_i + u_i(\mathbf{x})$, where $u_i(\mathbf{x})$ is the displacement field. Our goal is to find rules to connect a given deformation to a stress tensor σ_{ij}. For many practitioners, the canonical way of doing this is to write down an energy function (or free energy) that is compatible with basic assumptions about the deformed medium [Chaikin et al., 1995]. For instance, if one assumes that no work is done via a solid-body translation, then the energy can only depend on gradients of u_i. Assuming gradients are small and the undeformed state is stable, one can proceed in a gradient expansion and write:

$$E \approx \frac{1}{2} \int K_{ijkl} \partial_i u_j \partial_k u_l \, \mathrm{d}\mathbf{x} \tag{2.1}$$

Here K_{ijkl} is a tensor that determines how much energy a given deformation costs. The stress tensor σ_{ij} is given by:

$$\sigma_{ij} = \frac{\partial E}{\partial \partial_i u_j} = \frac{1}{2}\big(K_{ijkl} + K_{klij}\big)\partial_k u_l \tag{2.2}$$

The coefficient relating the stress and the strain is $C_{ijkl} = \frac{1}{2}\big(K_{ijkl} + K_{klij}\big)$ is known as the *stiffness* or *elastic modulus* tensor. Notice that the gradient-like structure of the stress strain relationship has endowed the elastic modulus tensor with a symmetry:

$$C_{ijkl} = C_{klij} \tag{2.3}$$

which is known as the major symmetry of the elastic modulus tensor. This result, that energy conservation imposes a major symmetry on the linear response coefficient, is known

as Betti's theorem [Truesdell, 1963]. However, if the stress-strain relationship is not derived from an energy function, then the major symmetry need not apply. Without an energy, one could either (a) proceed by direct coarse-graining of the microscopic forces or (b) start by postulating that a linear stress-strain relationship $\sigma_{ij} = C_{ijkl}\partial_k u_l$ should hold for sufficiently small deformations. In the latter case, C_{ijkl} need not be symmetric, and so one can write

$$C_{ijkl} = C^e_{ijkl} + C^o_{ijkl} \tag{2.4}$$

where $C^e_{ijkl} = C^e_{klij}$ is the symmetric part and $C^o_{ijkl} = -C^o_{klij}$ the antisymmetric part of the elastic modulus tensor. In this setting, odd elasticity refers to the antisymmetric (or *odd*) part of the elastic modulus tensor.

More generally, I will refer to odd elasticity is any nonconservative contribution to the quasi-static stress-strain relationship. Here, nonconservative is being used in the same sense as non-potential. For a point particle at position $\mathbf{r}$ in a force field $\mathbf{F}(\mathbf{r})$, the force field is called nonconservative if there exists at least one closed path Γ such that $\oint_\Gamma \mathbf{F}\cdot \mathrm{d}\mathbf{r} \neq 0$ [1]. Likewise, for odd elasticity, the statement that the stress is not the gradient of a potential can be restated as: there exists quasi-static cycles of strain such that the (canonical) work integral is nonzero. Whether the work is done on or by the elastic medium is determined by the direction in which the cycle is transversed. In linear elasticity, one can easily compute the work integral given the elastic modulus tensor:

$$W = \oint_\Gamma \sigma_{ij}\mathrm{d}u_{ij} \tag{2.5}$$

$$= \oint_\Gamma C_{ijkl}u_{kl}\mathrm{d}u_{ij} \tag{2.6}$$

$$= -\oint_\Gamma C_{ijkl}u_{ij}\mathrm{d}u_{kl} \tag{2.7}$$

1. Here it is crucial that the domain is simply connected.

Adding Eqs. (2.6-2.7) yields:

$$W = \oint_\Gamma C^o_{ijkl} u_{ij} \mathrm{d}u_{kl} = \oint C^o_{ijkl} \mathrm{d}u_{ij} \wedge \mathrm{d}u_{kl} \tag{2.8}$$

Hence, within linear elasticity, the odd elastic coefficient relates the area enclosed in strain space to the net work done by the material. The name odd elasticity is also a reference to an analogous but distinct concept is fluid mechanics known as *odd viscosity*, in which the tensor of viscous coefficients η_{ijkl} violates its major symmetry because the viscous stresses do not directly climb entropy gradients [Avron et al., 1995, Banerjee et al., 2017, de Groot and Mazur, 1954, Onsager, 1931, Hulsman et al., 1970, Soni et al., 2019, Geracie and Son, 2014, Hoyos and Son, 2012, Fruchart et al., 2023]. It should also be noted that odd elasticity, as I am using it, refers to the static stress-strain relationship, and is therefore distinct from effects such as viscoelasticity or plastic deformation, although it can be thought of as a special case of hypoelasticity [Truesdell and Toupin, 1960]. In Appendix 2.7, derivations of the above statements are done more rigorously in order to address the roles of geometric and material nonlinearity. Yet, for the majority of calculations in this thesis, the discussion above is sufficient.

2.2.1 Odd elasticity in two dimensions

To illustrate the consequences of odd elasticity, here I provide a detailed discussion of the elasticity of a two-dimensional medium [2]. In two dimensions, the stress σ_{ij} and displacement gradient $\partial_i u_j$ tensors each have 4 independent components, implying that the elastic modulus tensor has 16 independent components if no further restrictions are imposed. To visualize these components it is useful to decompose the stress and strain tensors into irreducible

2. Analogous results can be obtained in three dimensions [Scheibner et al., 2020b].

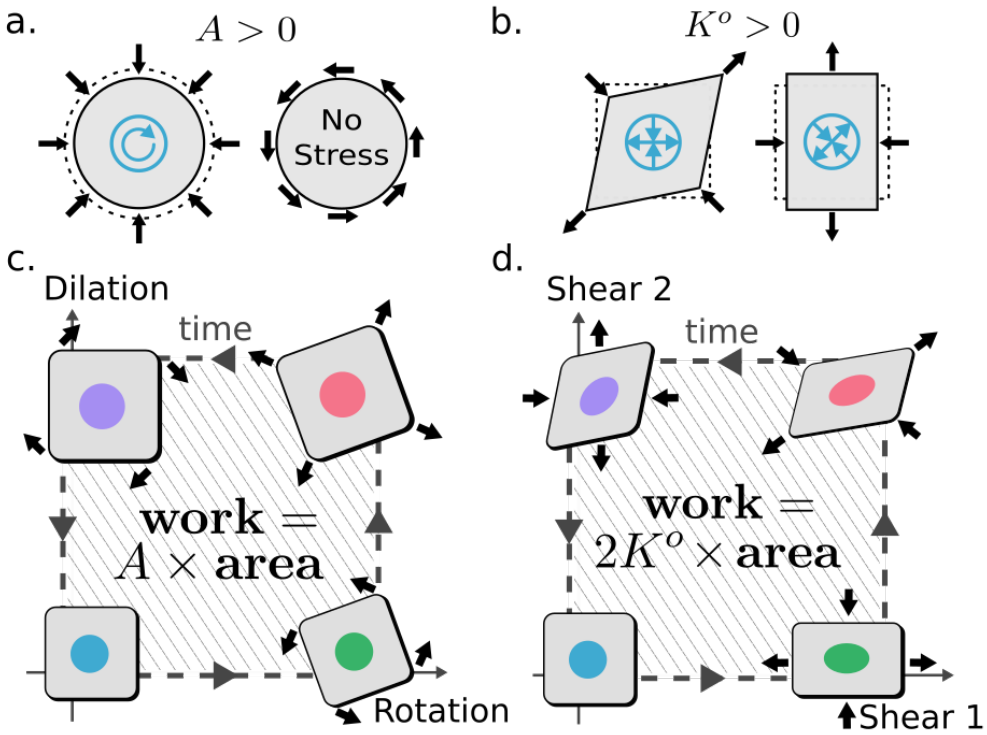

Figure 2.1: **Odd-elastic energy cycle. a.** The odd modulus A couples compression to an internal torque density, while rotations induce no stresses. The applied strains are represented by the black arrows, the undeformed shape by the dotted lines, and the internal stresses by the blue icons. **b.** The odd modulus K^o couples the two independent shear deformations. Unlike shear coupling in anisotropic passive solids, the induced stress is always rotated 45° counterclockwise relative to the applied strain. **c.** An odd-elastic material is subjected to a closed cycle in deformation space. First, a counterclockwise rotation is followed by a volumetric strain ϵ_V, inducing a torque density $A\epsilon_V$. Next, the object does work $A\epsilon_V\epsilon_\theta$ on its surrounding as it is rotated clockwise through an angle ϵ_θ, before being compressed to its original size. The total work done is A times the area enclosed in deformation space: $\epsilon_V\epsilon_\theta$. **d.** An analogous cycle involving only shear stress and shear strain. Adapted from Scheibner et al. [2020b].

representations of $SO(2)$. To do so, we introduce the two-by-two matrices:

$$\boldsymbol{\tau}^0 = \begin{pmatrix} 1 & 0 \\ 0 & 1 \end{pmatrix} \qquad \boldsymbol{\tau}^1 = \begin{pmatrix} 0 & -1 \\ 1 & 0 \end{pmatrix} \qquad \boldsymbol{\tau}^2 = \begin{pmatrix} 1 & 0 \\ 0 & -1 \end{pmatrix} \qquad \boldsymbol{\tau}^3 = \begin{pmatrix} 0 & 1 \\ 1 & 0 \end{pmatrix} \tag{2.9}$$

Using the $\boldsymbol{\tau}^\alpha$, define $u^\alpha = \tau^\alpha_{ij}\partial_i u_j$ and $\sigma^\alpha = \tau^\alpha_{ij}\sigma_{ij}$. In this basis, the elastic modulus tensor may be expressed as a four-by-four matrix $C^{\alpha\beta} = \frac{1}{2}\tau^\alpha_{ij}C_{ijmn}\tau^\beta_{mn}$. Thus, a linear constitutive

equation may be written as:

$$\begin{pmatrix} \sigma^0 \\ \sigma^1 \\ \sigma^2 \\ \sigma^3 \end{pmatrix} = \begin{pmatrix} \sigma_0^0 \\ \sigma_0^1 \\ \sigma_0^2 \\ \sigma_0^3 \end{pmatrix} + \begin{pmatrix} C^{00} & C^{01} & C^{02} & C^{03} \\ C^{10} & C^{11} & C^{12} & C^{13} \\ C^{20} & C^{21} & C^{22} & C^{23} \\ C^{30} & C^{31} & C^{32} & C^{33} \end{pmatrix} \begin{pmatrix} u^0 \\ u^1 \\ u^2 \\ u^3 \end{pmatrix}. \tag{2.10}$$

where σ_0^α corresponds to the an ambient stress that is present prior to deformation.

Notice that $C^{\alpha\beta}$ has 16 independent components when no physical restrictions are imposed. Now, let's examine the implications of common symmetries and conservation laws. If angular momentum is conserved, then the stress tensor is required to be symmetric (See Appendix 2.7). This implies that $\sigma_0^1 = C^{1\alpha} = 0$ for all α. Next, a common assumption is that solid body rotations do not contribute to the elastic stress, because solid body rotations do not involve changing the distances between constituent particles. If no stress is induced by solid-body rotations, then $C^{\alpha 1} = 0$ for all α, since the stress tensor should not couple to the antisymmetric part of the displacement gradient tensor under this assumption. Finally, one can restrict the components of $C^{\alpha\beta}$ via spatial symmetries. For example, a material is called *isotropic* if its properties are invariant under rotations of the coordinate system. Upon a passive rotation of the coordinate system through angle θ, the elastic modulus tensor transforms as

$$C'_{ijmn} = \mathcal{R}_{ik}\mathcal{R}_{jl}\mathcal{R}_{mp}\mathcal{R}_{nq}C^{klpq} \quad \text{where} \quad \mathcal{R}_{ij} = \begin{pmatrix} \cos\theta & \sin\theta \\ -\sin\theta & \cos\theta \end{pmatrix} \tag{2.11}$$

Hence $C^{\alpha\beta}$ transforms as $C'^{\alpha\beta} = R^{\alpha\gamma}R^{\beta\sigma}C^{\gamma\sigma}$, where

$$R^{\alpha\beta} = \begin{pmatrix} 1 & 0 & 0 & 0 \\ 0 & 1 & 0 & 0 \\ 0 & 0 & \cos 2\theta & \sin 2\theta \\ 0 & 0 & -\sin 2\theta & \cos 2\theta \end{pmatrix}. \tag{2.12}$$

Requiring that $C'^{\alpha\beta} = C^{\alpha\beta}$ for all θ implies that $C^{\alpha\beta}$ must take the form:

$$C^{\alpha\beta} = 2\begin{pmatrix} B & \Lambda & 0 & 0 \\ A & \Gamma & 0 & 0 \\ 0 & 0 & \mu & K^o \\ 0 & 0 & -K^o & \mu \end{pmatrix}. \tag{2.13}$$

Finally, note that $C^{\mathrm{C}}_{ijmn} = \frac{1}{2}\tau^{\alpha}_{ij}\tau^{\beta}_{mn}(C^{\mathrm{C}})^{\alpha\beta}$. Thus, in standard Cartesian coordinates, the elastic modulus tensor reads:

$$C^{\mathrm{C}}_{ijmn} = B\delta_{ij}\delta_{mn} + \mu(\delta_{im}\delta_{jn} + \delta_{jm}\delta_{in} - \delta_{ij}\delta_{mn}) - A\epsilon_{ij}\delta_{mn} \tag{2.14}$$

$$+ K^o E_{ijmn} + \Gamma\epsilon_{ij}\epsilon_{mn} - \Lambda\delta_{ij}\epsilon_{mn} \tag{2.15}$$

where

$$E_{ijmn} = \frac{1}{2}(\epsilon_{im}\delta_{jn} + \epsilon_{in}\delta_{jm} + \epsilon_{jm}\delta_{in} + \epsilon_{jn}\delta_{im}). \tag{2.16}$$

In terms of $C^{\alpha\beta}$, the energy conservation condition reads $C^{\alpha\beta} = C^{\beta\alpha}$ [3]. Hence, the isotropic odd elastic modulus tensor, Eq. (2.13) is compatible with a potential energy if and only if

3. There is a crucial subtlety here about whether σ_{ij} represents the Cauchy stress or the Piola-Kirchhoff stress tensor. If it is the Cauchy stress tensor, then the preceding statement is not entirely true in the presence of ambient stress σ^0_{ij}. See Appendix 2.7 for a discussion

$K^o = 0$ and $A = \Lambda$. Figure 2.1 Shows an example of two cyclic paths of deformation that extract energy if A or K^o is the only nonzero modulus.

2.3 Elastostatics

How does the presence of odd elasticity affect the way a solid bears a load? I will present here two example calculations which solve classic problems in the presence of odd elastic coefficients. First though, it is useful to make some general comments. The condition for a system (loaded at it its boundaries) to be in mechanical equilibrium is

$$\partial_i \sigma_{ij} = 0 \tag{2.17}$$

Notice that if stress boundary conditions are applied to the medium, then Eq. (2.17) is independent of the constitutive relations, and hence odd elasticity will not affect the stress distribution. It will, however, generically affect the shape of the medium under loading. If mixed stress and displacement boundary conditions are applied, the odd elasticity will generically affect both the stress and strain distribution.

2.3.1 Poisson ratio, Young's modulus, and odd ratio

Let us first examine the classic experiment of uniaxial compression, shown in Fig. 2.2. Consider the special case of an odd-elastic material with only B, μ, and K^o nonzero. In a uniaxial compression with free boundaries on the two sides parallel to the direction of compression, the material stress is given by $\sigma_{yy} = p$, $\sigma_{xx} = \sigma_{xy} = \sigma_{yx} = 0$, paired with the condition $u_{xy} = 0$, so that the top and bottom horizontal boundaries remain horizontal. The goal is to solve for the strain everywhere inside the material. Using the notation $\sigma^\alpha = C^{\alpha\beta} u^\beta$, one

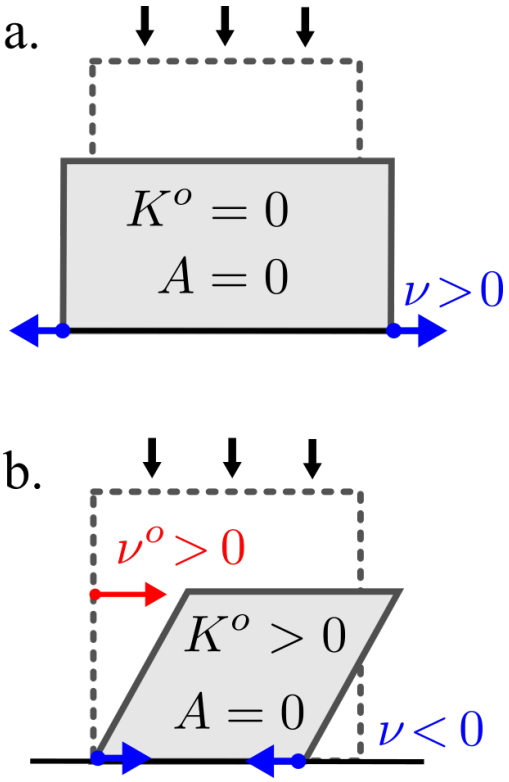

Figure 2.2: **Uniaxial compression of an odd elastic solid. a.** A uniaxial compression of a passive material generically results in symmetric deformation. If the material sides move outward, its Poisson ratio ν is positive. **b.** A uniaxial compression of an odd elastic block results in a tilt whose intensity is proportional to the odd ratio ν^o. If K^o is sufficiently large, the material also becomes auxetic ($\nu < 0$), meaning that the material contract in response to compression. Adapted from Scheibner et al. [2020b].

obtains:

$$\begin{pmatrix} p \\ 0 \\ -p \\ 0 \end{pmatrix} = 2 \begin{pmatrix} B & 0 & 0 & 0 \\ 0 & 0 & 0 & 0 \\ 0 & 0 & \mu & K^o \\ 0 & 0 & -K^o & \mu \end{pmatrix} \begin{pmatrix} u^0 \\ -u^3 \\ u^2 \\ u^3 \end{pmatrix}, \tag{2.18}$$

Noting that $u_{xx} = \frac{1}{2}(u^0 + u^2)$ and $u_{yy} = \frac{1}{2}(u^0 - u^2)$ and $u_{yx} = \frac{1}{2}(u^3 - u^1)$, one can invert Eq. (2.18) to obtain:

$$u_{xx} = \frac{p}{4}\left(\frac{(K^o)^2 + \mu^2 - B\mu}{B[(K^o)^2 + \mu^2]}\right) \tag{2.19}$$

$$u_{yy} = \frac{p}{4}\left(\frac{(K^o)^2 + \mu^2 + B\mu}{B[(K^o)^2 + \mu^2]}\right) \tag{2.20}$$

$$u_{yx} = \frac{p}{2}\left(\frac{-K^o}{(K^o)^2 + \mu^2}\right). \tag{2.21}$$

Equations (2.19-2.21) depend only on three numbers. The first number is the Poisson's ratio, which gives the ratio of horizontal contraction to vertical compression:

$$\nu = -\frac{u^s_{xx}}{u^s_{yy}} = \frac{B\mu - (K^o)^2 - \mu^2}{(K^o)^2 + \mu^2 + B\mu} \tag{2.22}$$

The second is an overall stiffness scale known as the Young's modulus

$$E = \frac{p}{u^s_{yy}} = \frac{4B[(K^o)^2 + \mu^2]}{(K^o)^2 + \mu^2 + B\mu}. \tag{2.23}$$

The final dimensionless quantity will be referred to as the *odd ratio*, and it gives the transverse deflection of the medium under uniaxial loading.

$$\nu^o = -\frac{u^s_{yx}}{u^s_{yy}} = \frac{K^o B}{(K^o)^2 + \mu^2 + B\mu} \tag{2.24}$$

Here, $u^s_{ij} \equiv \frac{1}{2}(u_{ij} + u_{ji})$ denotes the linearized strain tensor.

2.3.2 Airy stress function

A useful tool in two-dimensional elastostatics is the Airy stress function. Assuming conservation of angular momentum, the elastostatic condition Eq. (2.17) implies that the stress tensor may be expressed as $\sigma_{ij} = \epsilon_{ik}\epsilon_{jl}\partial_k\partial_l\chi$, where χ is known as the Airy stress function.

When K^o is the only nonzero odd elastic modulus, an invertible relationship exists between the symmetric stress σ_{ij} and the linearized strain $u^s_{ij} = (\partial_i u_j + \partial_j u_i)/2$:

$$u^s_{ij} = \frac{1}{E}\Big\{(1-\nu)\delta_{ij}\delta_{mn} + (1+\nu)(\delta_{im}\delta_{jn} + \delta_{in}\delta_{jm} - \delta_{ij}\delta_{mn}) - 2\nu^o E_{ijmn}\Big\}\sigma_{mn} \tag{2.25}$$

From the definition of u^s_{ij} and Eq. (2.25), notice that

$$\Delta^2\chi = \partial_i\epsilon_{ik}\partial_j\epsilon_{jl}u^s_{kl} = 0 \tag{2.26}$$

implying that the Airy stress function is biharmonic. The Airy stress function will make an appearance in the response to a point force below, and once again again when I discuss topological defects in §2.6.

2.3.3 Response to point force

Let's poke an odd elastic solid. Consider a point force of magnitude F on the boundary of a semi-infinite medium with stress free boundaries. The well known the Airy stress function for such a perturbation is given by [Landau et al., 1986]:

$$\chi = -\frac{F}{\pi} r\phi\cos\phi \tag{2.27}$$

where ϕ is the angle with respect to the direction of the applied force. The corresponding stress is: $\sigma_{rr} = -\frac{2F}{\pi r}\cos\phi$ and $\sigma_{r\phi} = \sigma_{\phi\phi} = 0$. The strain is obtained from Eq. (2.25):

$$u_{ij} = \frac{1}{E}\Big\{(1-\nu)\delta_{ij}\delta_{mn} + (1+\nu)(\delta_{im}\delta_{jn} + \delta_{in}\delta_{jm} - \delta_{ij}\delta_{mn}) - 2\nu^o E_{ijmn}\Big\}\sigma_{mn} \tag{2.28}$$

Eq. (2.28) yields the differential equations:

$$u_{rr} = \partial_r u_r = -\frac{4F}{\pi E r}\cos\phi \tag{2.29}$$

$$u_{\phi\phi} = \frac{1}{r}\partial_\phi u_\phi + \frac{u_r}{r} = \nu\frac{4F}{\pi E r}\cos\phi \tag{2.30}$$

$$2u_{r\phi} = \partial_r u_\phi - \frac{u_\phi}{r} + \frac{1}{r}\partial_\phi u_r = -\nu^o\frac{8F}{\pi E r}\cos\phi \tag{2.31}$$

whose solutions are

$$u_r = \frac{4F}{\pi E}\left[-\log r\cos\phi + \frac{\nu-1}{2}\sin\phi - \nu^o(\sin\phi + \phi\cos\phi)\right] \tag{2.32}$$

$$u_\phi = \frac{4F}{\pi E}\left[\frac{1+\nu+2\log r}{2}\sin\phi + \frac{\nu-1}{2}\phi\cos\phi + \nu^o\phi\sin\phi\right] \tag{2.33}$$

As expected, the piece that breaks mirror symmetry $\phi \to -\phi$ is proportional to the odd ratio ν^o. Noting that $u_y = -u_r\cos\phi + u_\phi\sin\phi$, the solutions in Eqs. (2.32-2.33) predicts which way an isotropic odd elastic solid will deflect if poked at its boundary. As will be discussed in Sec 2.5, Eqs. (2.32-2.33) give the correct qualitative behavior for the experiments involving the impact of a projectile on a wall of odd elastic building blocks shown in Fig. 2.7.

2.4 Elastodynamics and wave mechanics

2.4.1 Continuum wave equations

So far, our discussion of elasticity has not yet involved any equations of motion. For inertial systems, the dynamics of the displacement field can be described by

$$\rho\partial_t^2 u_i + \gamma\partial_t u_i = f_i = \partial_j\sigma_{ij} \tag{2.34}$$

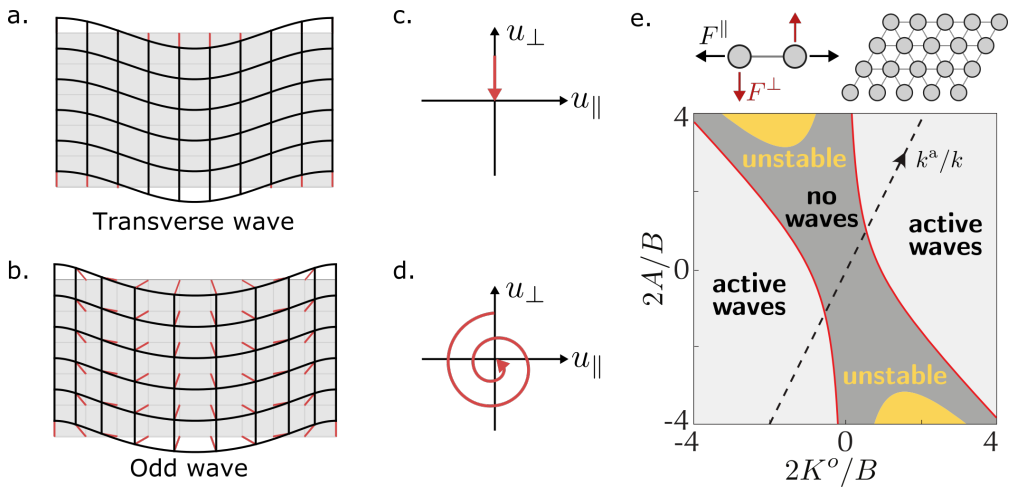

Figure 2.3: **Odd elastodynamics. a.** A transverse wave in a passive solid is illustrated. **b.** An odd elastic wave propagates with a circular polarization. The thin red lines represent the displacement field. **c.** For an overdamped passive solid, the displacement field of the transverse mode decays towards its rest position. **d.** For an overdamped odd elastic solid with $K^o > 0$, the displacement field traces out spirals that become closed ellipses when $B = \mu = 0$. **e.** A phase diagram for wave beahvior featuring the moduli A and K^o. The red lines denote exceptional points. The dashed black line corresponds to a hexagonal lattice of bonds with transverse forces discussed in §2.5. Adapted from Scheibner et al. [2020b].

where ρ is the mass density and the term $\gamma\partial_t u_i$ represents friction on a lubricated substrate. For an isotropic medium described by Eq. (2.13) the equations of motion read

$$\rho\partial_t^2\vec{u} + \gamma\partial_t\vec{u} = (B-\Gamma)\nabla(\nabla\cdot\vec{u}) + (\mu+\Gamma)\Delta\vec{u} + (K^o+\Lambda)\boldsymbol{\epsilon}\cdot\Delta\vec{u} - (A+\Lambda)\boldsymbol{\epsilon}\cdot\nabla(\nabla\cdot\vec{u}). \tag{2.35}$$

In the rest of this paragraph, I set $\Lambda = 0$ and $\Gamma = 0$[4]. Because Eq. (2.35) is linear, it supports plane wave solutions $\vec{u}(\vec{x}) = \vec{u}\,e^{i(\vec{q}\cdot\vec{x}-\omega t)}$ with wave number $\vec{q}$ and frequency ω. As a matrix equation in terms of the longitudinal $u_\parallel = \hat{\vec{q}}\cdot\vec{u}$ and transverse $u_\perp = \hat{\vec{q}}\times\vec{u}$ components,

4. Notice that in Eq. (2.35) only four independent coefficients appear, and hence the six elastic moduli are redundant from the point of view of the bulk elastodynamics equation.

Eq. (2.35) reads

$$-(\rho\omega^2 + i\gamma\omega)\begin{pmatrix} u_\parallel \\ u_\perp \end{pmatrix} = -q^2\begin{pmatrix} B+\mu & K^o \\ -K^o + A & \mu \end{pmatrix}\begin{pmatrix} u_\parallel \\ u_\perp \end{pmatrix} = D\begin{pmatrix} u_\parallel \\ u_\perp \end{pmatrix}. \tag{2.36}$$

The matrix D in Eq. (2.36), known as the dynamical matrix, relates forces to displacements. When $\gamma = 0$ and $A = K^o = 0$, one recovers the two usual types of elastic phonons: a longitudinal and a transverse mode, with dispersions $\omega = \pm q\sqrt{\frac{B+\mu}{\rho}}$ and $\omega = \pm q\sqrt{\frac{\mu}{\rho}}$, respectively. The transverse wave is illustrated in Fig. 2.3a. In contrast, in an overdamped system ($\rho = 0$ and $\gamma > 0$) passive elastodynamics ($A = K^o = 0$) becomes diffusive: $\omega = -iq^2\frac{B+\mu}{\gamma}$ and $\omega = -iq^2\frac{\mu}{\gamma}$. In our convention, a negative imaginary frequency implies that a wave is attenuated. In the case of an overdamped odd elastic solid with $A, K^o \neq 0$, one obtains

$$\omega = -iq^2\frac{B/2 + \mu \pm \sqrt{(B/2)^2 - K^o(K^o - A)}}{\gamma} \tag{2.37}$$

Notice that when $K^o(K^o - A) > (B/2)^2$, the frequency has a real part, implying oscillations even though the system is overdamped (light grey regions in Fig. 2.3e). Just as in the case of a damped harmonic oscillator, the transition between exponential relaxation and damped oscillations is marked by an exceptional point (red lines in Fig. 2.3e), where the dynamical matrix D is not diagonalizable. When the imaginary part of ω becomes positive, the solid can even become unstable (yellow regions in Fig. 2.3a). In Fig. 2.3b, an odd elastic phonon is shown for $K^o, \mu, B > 0$. Notice that the displacement field is circularly polarized, i.e. it traces out ellipses. A single point in the displacement field is shown as a function of time for an overdamped passive solid ($A = K^o = 0$, Fig. 2.3c) and an overdamped odd elastic solid ($K^o, \mu, B > 0$, Fig. 2.3d).

2.4.2 Chiral earthquakes: odd elastic Rayleigh waves

The previous calculation address elastic wave that propagated through the bulk of the solid, but the dispersion changes in the presence of a boundary. For an inertial system, the bulk equations of motion read

$$\rho\partial_t^2 u_j = \partial_i \sigma_{ij} \tag{2.38}$$

Assuming the medium occupies the $y < 0$ half plane, the boundary conditions for Eq. (2.38) read

$$\sigma_{yi}(y=0) = 0 \quad \text{and} \quad u_i(y \to -\infty) = 0 \tag{2.39}$$

where u_i is the displacement field. The stress tensor σ_{ij} is given by $\sigma_{ij} = C_{ijmn}\partial_m u_n$. It is useful to parameterize the elastic modulus tensor in terms of the Young's modulus E, Poisson's ratio ν, and odd ratio ν^o. One can then non-dimensionalize the equations of motion by defining $r \equiv k_y/k_x$ and $\tilde{k}_x = k_x\sqrt{\frac{E}{\rho\omega^2}}$, where $\mathbf{k}$ is the wave-vector. In this notation, Eq. (2.38) takes the form:

$$\begin{bmatrix} u_x \\ u_y \end{bmatrix} = \underbrace{\frac{\tilde{k}_x^2}{2(1-\nu)} \begin{bmatrix} \frac{(r^2+1)(1-\nu^2)}{(\nu+1)^2+4(\nu^o)^2} + 1 & \frac{2(r^2+1)(1-\nu)\nu^o}{(\nu+1)^2+4(\nu^o)^2} + r \\ -\frac{2(r^2+1)(1-\nu)\nu^o}{(\nu+1)^2+4(\nu^o)^2} + r & \frac{(r^2+1)(1-\nu^2)}{(\nu+1)^2+4(\nu^o)^2} + r^2 \end{bmatrix}}_{M(r,\tilde{k}_x)} \begin{bmatrix} u_x \\ u_y \end{bmatrix} \tag{2.40}$$

yielding the secular equation $0 = \det\Big[M(r,\tilde{k}_x) - 1\Big]$, which is equivalent to

$$0 = (r^2+1)^2\tilde{k}_x^4 - [2(1-\nu^2) + (\nu+1)^2 + 4(\nu^o)^2](r^2+1)\tilde{k}_x^2 + 2(1-\nu)[(\nu+1)^2 + 4(\nu^o)^2] \tag{2.41}$$

The solutions to Eq. (2.41) take the form:

$$r_1^{\pm} = \pm \sqrt{\frac{2(1-\nu^2) + (\nu+1)^2 + 4(\nu^o)^2 - \sqrt{(1+\nu)^4 - 8(1-6\nu+\nu^2)(\nu^o)^2 + 16(\nu^o)^4}}{2\tilde{k}_x^2} - 1} \tag{2.42}$$

$$r_2^{\pm} = \pm \sqrt{\frac{2(1-\nu^2) + (\nu+1)^2 + 4(\nu^o)^2 + \sqrt{(1+\nu)^4 - 8(1-6\nu+\nu^2)(\nu^o)^2 + 16(\nu^o)^4}}{2\tilde{k}_x^2} - 1} \tag{2.43}$$

Each solution comes with a normalized vector $n_i(r, \tilde{k}_x) \in \ker[M(r, \tilde{k}_x) - 1]$. Each n_i represents a candidate mode for a Rayleigh wave, and one must find a linear combinations of candidate modes that satisfy Eq. (2.39). Moreover, it is required $\mathrm{Im}(r\tilde{k}_x) < 0$ for all modes in the superposition in order to ensure that each mode decays into the bulk. The condition $\mathrm{Im}(r\tilde{k}_x) < 0$ implies that linear combinations are of the form:

$$n_i^{++}(\tilde{k}_x) \equiv a_1 n_i(r_1^+, \tilde{k}_x) + a_2 n_i(r_2^+, \tilde{k}_x) \tag{2.44}$$

$$n_i^{+-}(\tilde{k}_x) \equiv a_1 n_i(r_1^+, \tilde{k}_x) + a_2 n_i(r_2^-, \tilde{k}_x) \tag{2.45}$$

$$n_i^{-+}(\tilde{k}_x) \equiv a_1 n_i(r_1^-, \tilde{k}_x) + a_2 n_i(r_2^+, \tilde{k}_x) \tag{2.46}$$

$$n_i^{--}(\tilde{k}_x) \equiv a_1 n_i(r_1^-, \tilde{k}_x) + a_2 n_i(r_2^-, \tilde{k}_x) \tag{2.47}$$

One can express the stress at the boundary by:

$$\begin{bmatrix} \sigma_{yx} \\ \sigma_{yy} \end{bmatrix} = \begin{bmatrix} S_{x1}^{\pm\pm}(\tilde{k}_x) & S_{x2}^{\pm\pm}(\tilde{k}_x) \\ S_{y1}^{\pm\pm}(\tilde{k}_x) & S_{y2}^{\pm\pm}(\tilde{k}_x) \end{bmatrix} \begin{bmatrix} a_1 \\ a_2 \end{bmatrix} \tag{2.48}$$

where the matrix $S^{\pm\pm}(\tilde{k}_x)$ is determined by computing $\sigma_{yj} = C_{ijmn}k_i k_m n_n^{\pm\pm}$. Hence, the stress free boundary condition Eq. (2.39) can be expressed algebraically as:

$$0 = g^{\pm\pm}(\tilde{k}_x) \equiv \det\Big[S^{\pm\pm}(\tilde{k}_x)\Big] \tag{2.49}$$

For the special case that $\nu = 1$, which corresponds to an incompressible solid, the algebraic expressions may be written explicitly. One finds:

$$r_1^{\pm} = \pm\, i \tag{2.50}$$

$$r_2^{\pm} = \pm\sqrt{\frac{4 + 4(\nu^o)^2 - \tilde{k}_x^2}{\tilde{k}_x^2}} \tag{2.51}$$

Moreover, $g^{\pm\pm}$ up to an unimportant denominator reads

$$g^{++} = 0 \implies 0 = 4[1 + (\nu^o)^2] + \tilde{k}_x^4 - 2(i\nu^o + 2)\tilde{k}_x^2 - (2i\nu^o\tilde{k}_x + \tilde{k}_x^3)\sqrt{\tilde{k}_x^2 - 4[1 + (\nu^o)^2]} \tag{2.52}$$

$$g^{+-} = 0 \implies 0 = 4[1 + (\nu^o)^2] + \tilde{k}_x^4 - 2(i\nu^o + 2)\tilde{k}_x^2 + (2i\nu^o\tilde{k}_x + \tilde{k}_x^3)\sqrt{\tilde{k}_x^2 - 4[1 + (\nu^o)^2]} \tag{2.53}$$

$$g^{--} = 0 \implies 0 = 4[1 + (\nu^o)^2] + \tilde{k}_x^4 + 2(i\nu^o - 2)\tilde{k}_x^2 + (2i\nu^o\tilde{k}_x - \tilde{k}_x^3)\sqrt{\tilde{k}_x^2 - 4[1 + (\nu^o)^2]} \tag{2.54}$$

$$g^{-+} = 0 \implies 0 = 4[1 + (\nu^o)^2] + \tilde{k}_x^4 + 2(i\nu^o - 2)\tilde{k}_x^2 - (2i\nu^o\tilde{k}_x - \tilde{k}_x^3)\sqrt{\tilde{k}_x^2 - 4[1 + (\nu^o)^2]} \tag{2.55}$$

Notice that $g^{++} = 0$ and $g^{+-} = 0$ are both equivalent to the condition

$$\tilde{k}_x^6 - (6 - 4i\nu^o)\tilde{k}_x^4 + 4(1 - i\nu^o)(2 - i\nu^o)\tilde{k}_x^2 - 4(1 - i\nu^o)^2 = 0 \tag{2.56}$$

while $g^{--} = 0$ and g^{-+} are both equivalent to the condition

$$\tilde{k}_x^6 - (6 + 4i\nu^o)\tilde{k}_x^4 + 4(1 + i\nu^o)(2 + i\nu^o)\tilde{k}_x^2 - 4(1 + i\nu^o)^2 = 0 \tag{2.57}$$

The condition $\mathrm{Im}(r\tilde{k}_x) < 0$ then implies that that the roots of Eq. (2.56) should be taken for right traveling waves ($\mathrm{Re}(\tilde{k}_x) > 0$) and the roots of Eq. (2.57) should be taken for left traveling waves ($\mathrm{Re}(\tilde{k}_y) < 0$). The quantity $q_x = -\mathrm{Im}(k_x)$ describes the in which direction the Rayleigh wave is exponentially localized. Inspection of Eqs (2.56-2.57) imply that the dispersion is chiral: the waves are unidirectionaly amplified in a direction determined by the odd ratio ν^o. In the impact experiments discussed in §2.5, one half of the wall vibrations noticeably more than the other half after the impacter departs. The sign of q_x correctly gives which half of the wall exhibits more wiggling in experiment.

2.5 Microscopic models and experimental systems

In this section, I present experimental systems and minimal microscopic models that give rise to odd elasticity.

2.5.1 Pairwise interactions: odd springs

The simplest microscopic model of an elastic solid is a collection of masses connected by springs. More generally, one can model a solid as a collection of point particles with interaction forces that depend on their relative position [Scheibner et al., 2020b,a, Braverman et al., 2021, Bililign et al., 2021]. Consider a collection of N particles with positions $\mathbf{x}^\alpha(t)$ and denote the total force on each particle is given by $\mathbf{F}^\alpha(\mathbf{x}^1, \ldots, \mathbf{x}^N)$ (here, α labels the particle). This force is said to be potential if $F_i^\alpha = -\partial V/\partial x_i^\alpha$ for some potential function $V(\mathbf{x}^1, \ldots, \mathbf{x}^N)$. Odd elasticity describes the contribution to the microscopic interactions that are not compatible with a potential, but are still compatible with Newton's

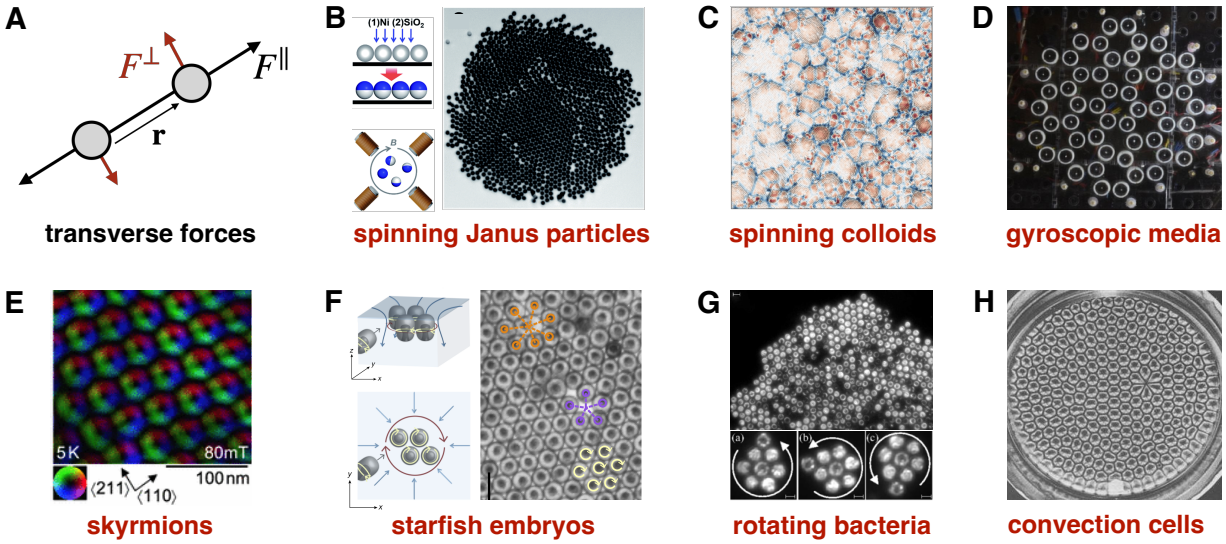

Figure 2.4: **Odd elasticity from pairwise interactions. a.** A pairwise interaction with a longitudinal force $F^\parallel(r)$ (black) and a transverse force $F^\perp(r)$ (red) connects two particles (gray circles). **b.** Janus particles and **c.** hematite colloids driven to spin by external magnetic fields. Adapted from Yan et al. [2015], Bililign et al. [2021]. **d**. A network of gyroscopes connected by springs is a realization of gyroscopic matter, whose elastodynamics can be mapped onto odd elasticity in the limit of fast spinning gyroscopes. Adapted from Nash et al. [2015]. **e.** Skyrmion lattices exhibit transverse interaction via a Magnus force. Adapted from Bauer and Pfleiderer [2016]. **f.** Starfish embryos and **g.** bacteria form chiral crystals with particle rotation driven by flagella and cilia, respectively. Adapted from Tan et al. [2022], Petroff et al. [2015]. **h.** Rayleigh-Bénard convection cells organized in a hexagonal pattern. When the system is put under rotation, odd elasticity can appear. Adapted from Koschmieder and Pallas [1974]. Figure adapted from Fruchart et al. [2023].

third law. Formally, Newton's third law means that the forces $\mathbf{F}^\alpha$ can be decomposed as $\mathbf{F}^\alpha(\mathbf{x}^1,\dots,\mathbf{x}^N) = \sum_\beta \mathbf{F}^{\alpha\beta}(\mathbf{x}^1,\dots,\mathbf{x}^N)$ with $\mathbf{F}^{\alpha\beta} = -\mathbf{F}^{\beta\alpha}$.

For concreteness, let us focus on two-dimensional systems with pairwise forces that are covariant under rotation. In this case, the force law takes the form $\mathbf{F}^{\alpha\beta}(\mathbf{x}^1,\dots,\mathbf{x}^N) = \mathbf{F}(\mathbf{x}^\alpha - \mathbf{x}^\beta)$ where

$$\mathbf{F}(\mathbf{r}) = F^\parallel(r)\,\hat{\mathbf{r}} - F^\perp(r)\,\hat{\boldsymbol{\phi}} \tag{2.58}$$

in which $\hat{\mathbf{r}} = \mathbf{r}/r$, $r = \|\mathbf{r}\|$, and $\hat{\boldsymbol{\phi}} = -\boldsymbol{\epsilon}\cdot\hat{\mathbf{r}}$. As illustrated in Fig. 2.4a, $F^\parallel(r)$ is a radial

force and $F^{\perp}(r)$ is a transverse force. The force law is said to be *transverse* or *noncentral* when $F^{\perp} \neq 0$. Notice that such an interaction is compatible with a potential if and only if $\nabla \times \mathbf{F} = \frac{1}{r}\partial_r(rF^{\perp}) = 0$. Except for the special case of $F^{\perp} \propto 1/r$ (relevant to vortices [Sonin, 1987, Gifford and Baym, 2008, Nguyen et al., 2020, Moroz et al., 2018, Fetter, 2009, Blatter et al., 1994, Tkachenko, 1969, 1966b,a]), the force is nonpotential if $F^{\perp} \neq 0$.

Particles interacting via Eq. (2.58) tend to form hexagonal lattices. With a denoting the preferred lattice spacing, Eq. (2.58) may be linearized as

$$F^{\parallel}(r) \approx F^{\parallel}(a) - k(r-a) \qquad\qquad F^{\perp}(r) \approx F^{\perp}(a) - k^{a}(r-a). \tag{2.59}$$

The linearized interactions in Eq. (2.59) can be thought of as (odd) Hookean springs with spring constant k and a transverse spring constant k^a. When $\mathbf{F}(r)$ falls off sufficiently rapidly, a useful approximation is to keep only the interactions between nearest neighbors. In this approximation, the ambient pressure $p^{(\mathrm{pre})}$ and ambient torque $\tau^{(\mathrm{pre})}$ in a triangular lattice are

$$p^{(\mathrm{pre})} = \sqrt{3}\,\frac{F^{\parallel}(a)}{a} \qquad\qquad \tau^{(\mathrm{pre})} = -\sqrt{3}\,\frac{F^{\perp}(a)}{a} \tag{2.60}$$

and the isotropic 2D elastic moduli are

$$B = \frac{\sqrt{3}}{2}\left(k + \frac{F^{\parallel}(a)}{a}\right) \qquad\qquad \mu = \frac{\sqrt{3}}{4}\left(k - \frac{3F^{\parallel}(a)}{a}\right) \tag{2.61}$$

$$A = -\frac{\sqrt{3}}{2}\left(k^{a} + \frac{F^{\perp}(a)}{a}\right) \qquad\qquad K^{o} = \frac{\sqrt{3}}{4}\left(k^{a} - \frac{3F^{\perp}(a)}{a}\right) \tag{2.62}$$

One can see explicitly from Eq. (2.62) that the transverse force gives rise to odd elastic moduli. See Born and Huang [1954], Goldhirsch [2010], Irving and Kirkwood [1950], Lutsko [1989], Scheibner et al. [2020b], Fruchart and Vitelli [2020], Poncet and Bartolo [2022], Braverman et al. [2021] for more details on coarse-graining procedures.

Transverse, pairwise interactions can serve a minimal model for variety of experimentally relevant interactions. A noteworthy example includes solids made of collections of spinning particles that push transversely on each other via a fluid-mediated interactions or steric friction. For instance, when magnetic colloidal particles are spun by an external magnetic field, hydrodynamic interactions give rise to transverse forces [Bililign et al., 2021, Yan et al., 2015]. In a related category are spinning living organisms such as bacterial and starfish embryos [Tan et al., 2022, Petroff et al., 2015]. Another important class are systems that have a rotated mobility matrix: their velocity is rotated with respect to the applied force. Examples in this category include vortex-like objects such as Skyrmions [Benzoni et al., 2021, Huang et al., 2020, Ochoa et al., 2017, Mühlbauer et al., 2009, Yu et al., 2010, Brearton et al., 2021] as well as gyroscopes [Wang et al., 2015, Zhao et al., 2020, Carta et al., 2014, Hassanpour, 2014, Carta et al., 2017, Nash et al., 2015, Mitchell et al., 2018b,c,a, Brun et al., 2012] in their fast spinning limit.

2.5.2 Active hinges

In an inertial system, the transverse force in Eq. (2.58) inherently requires a torque to be provided to each bond. The building blocks must therefore have an internal or external reservoir of angular momentum. However, such a reservoir is not necessary for odd elasticity in systems with non-pairwise interactions. For example, the linkage shown in Fig. 2.5 has two angular degrees of freedom θ_1, θ_2, each determined by the location of three vertices. When an angle deforms, it experiences a torsional force τ_i proportional to the change in angle $\delta\theta_i$, for example given by

$$\begin{pmatrix} \tau_1 \\ \tau_2 \end{pmatrix} = \begin{pmatrix} -\kappa & \kappa^a \\ -\kappa^a & -\kappa \end{pmatrix} \begin{pmatrix} \delta\theta_1 \\ \delta\theta_2 \end{pmatrix}. \tag{2.63}$$

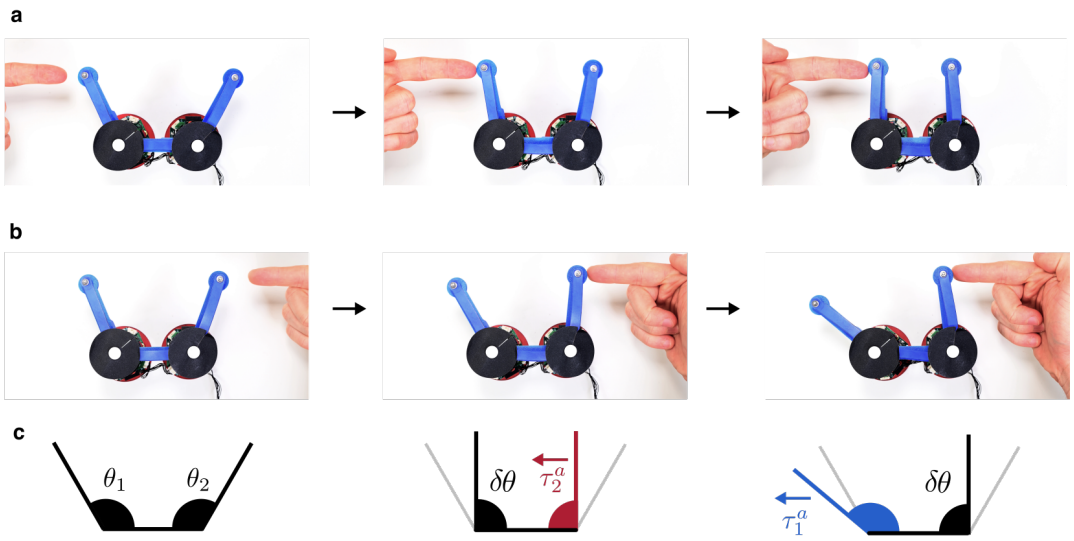

Figure 2.5: **Active hinges. a.** Three rigid linkages are connected by motorized vertices. **b.** A hand pushes in on the left, and the right vertex contracts. **c.** A hand pushes in on the right, and the left vertex expands. **d-f.** Schematics summarizing the asymmetric (or odd) stiffness for $\kappa^a > 0$. Adapted from Brandenbourger et al. [2022].

Here κ is the standard bond bending stiffness provided, for example, by the elastic band subtending the joint. The coefficient κ^a is an antisymmetric coupling that would not appear in passive systems. Both the usual bond bending stiffness and the odd bending stiffness describe non-pairwise interactions because the angle at each vertex (and hence the force) is determined by the locations of three vertices. For this system, the power done by the torsional forces is $\dot{W} = \tau_i \dot{\theta}_i$, so the work done along a closed cycle vanishes if and only if $\kappa^a = 0$. Hence the torque-angle relationship is nonconservative when $\kappa^a \neq 0$. Consequently, a lattice made of such units generically exhibits odd elasticity in the continuum limit. Since the microscopic building block has no unbalanced torques, $A = 0$ and $\tau^{(\mathrm{pre})} = 0$ in the continuum description. In Fig. 2.5, the building block is realized using motors and electronic feedback, and in Fig. 2.7 these units are assembled into a planar geometry. A simulation in Fig. 2.6 shows measurements of the Young's modulus and odd ratio as a function of the microscopic parameter κ^a. In experiments, the linear continuum description gives correct

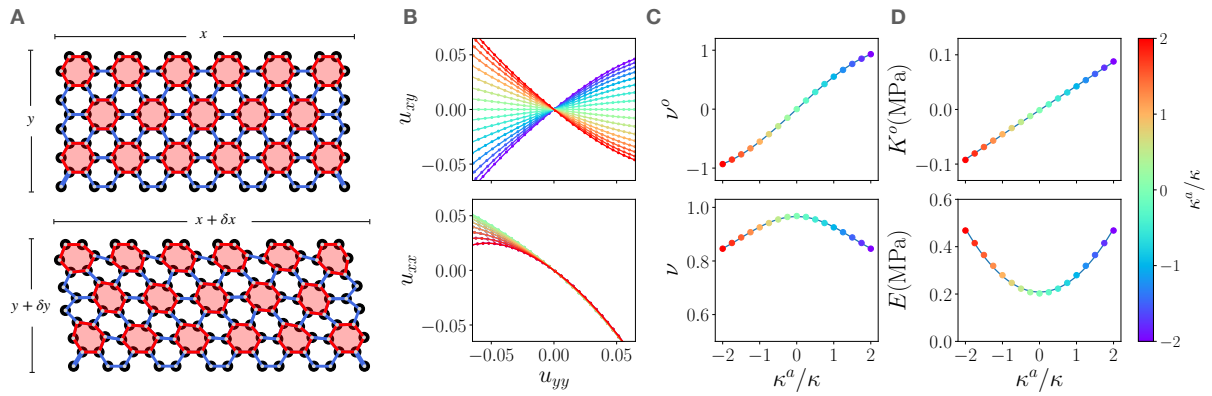

Figure 2.6: **Simulations of an odd wall. a.** Snapshots of a simulation of the active wall in its undeformed state (top) and after a quasistatic compression (bottom). The horizontal strains $u_{yy} = -\frac{\delta y}{y}$, the vertical strains $u_{xx} = -\frac{\delta x}{x}$ and the simple shear $u_{xy} = \frac{\delta x}{2y}$ are calculated by averaging the strains over all hexagons. The vertices within each red hexagon are coupled via active feedback κ^a. **b.** Shear strain u_{xy} (top) and normal strain u_{xx} (bottom) as a function of the normal strain u_{yy} for a range of values of the ratio between the active feedback and the hinge stiffness κ^a/κ. These curves were fitted polynomially and the slope at $u_{yy} = 0$ defines the odd ratio (Poisson's ratio). **c.** The odd ratio (top) and Poisson's ratio (bottom) as a function of κ^a/κ. A cubic fit $\nu^0 = 0.58\frac{\kappa^a}{\kappa} - 0.03\left(\frac{\kappa^a}{\kappa}\right)^3$ is used to calibrate the value of ν^o in experiments. **d.** The odd modulus K^o (top) and Young's modulus E (bottom) as a function of κ^a/κ. Adapted from Brandenbourger et al. [2022].

qualitative insights into experiments in which the wall is subject to impact by a projectile (see § 2.1). In particular, the point force solution correctly predicts the sign of the rotation of the projectile, and the spectrum for the Rayleigh waves correctly predicts which side of the wall will vibrate more after the impact.

2.5.3 Odd metabeam

So far, the discussion odd elasticity has focused on Cauchy elasticity, but stress can also couple to other geometric degrees of freedom. For example, Fig. 2.8a-c shows a quasi-1D metamaterial in which each unit cell consists of three piezoelectric patches mounted on a steel beam [Chen et al., 2021]. The beam has two modes of deformation, bending (Fig. 2.8f, left) and shearing (Fig. 2.8g, right). These modes of deformation in turn induce a shear

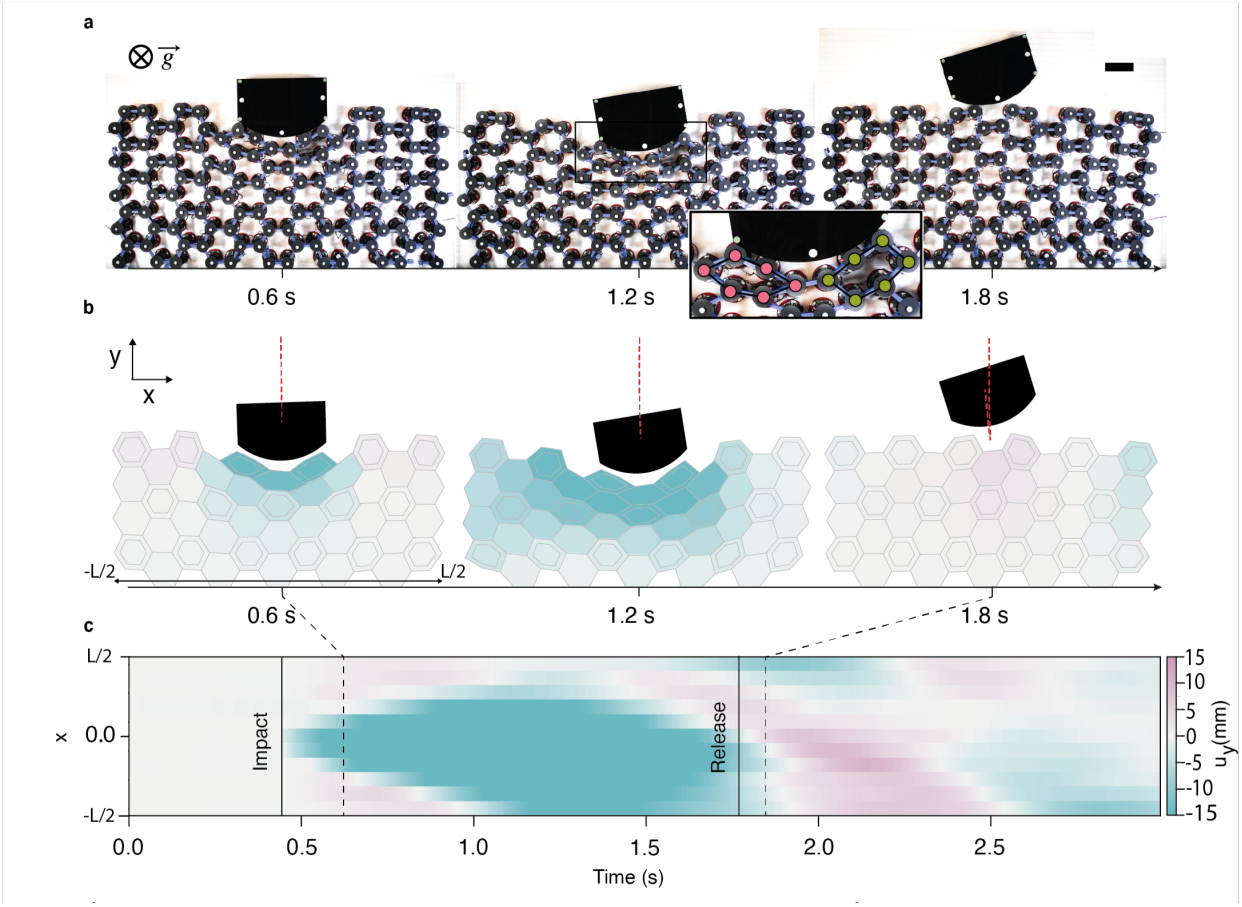

Figure 2.7: **Impact of a passive projectile on an odd wall. a.** A passive projectile is launched at a wall of 120 motorized vertices ($\kappa^a > 0$), forming a tiling 17 robotic hexagons [denoted by the double-line hexagons in (b).] Scale bar: 10 cm. (Inset) Active vertices colored by their deformation. **b.** Experimental reconstructions of the wall. Color represents the average vertical displacement u_y of each hexagon and $L = 128$ cm. **c.** The displacement averaged over each column u_y as a function of time and horizontal coordinate x. **d.** The average shear deformation in the wall with color indicating time. Adapted from Brandenbourger et al. [2022].

stress σ and a bending moment M. The constitutive relation between the two takes the form

$$\begin{pmatrix} \sigma \\ M \end{pmatrix} = \underbrace{\begin{pmatrix} \mu & P \\ 0 & B \end{pmatrix}}_{C} \begin{pmatrix} s \\ b \end{pmatrix} \tag{2.64}$$

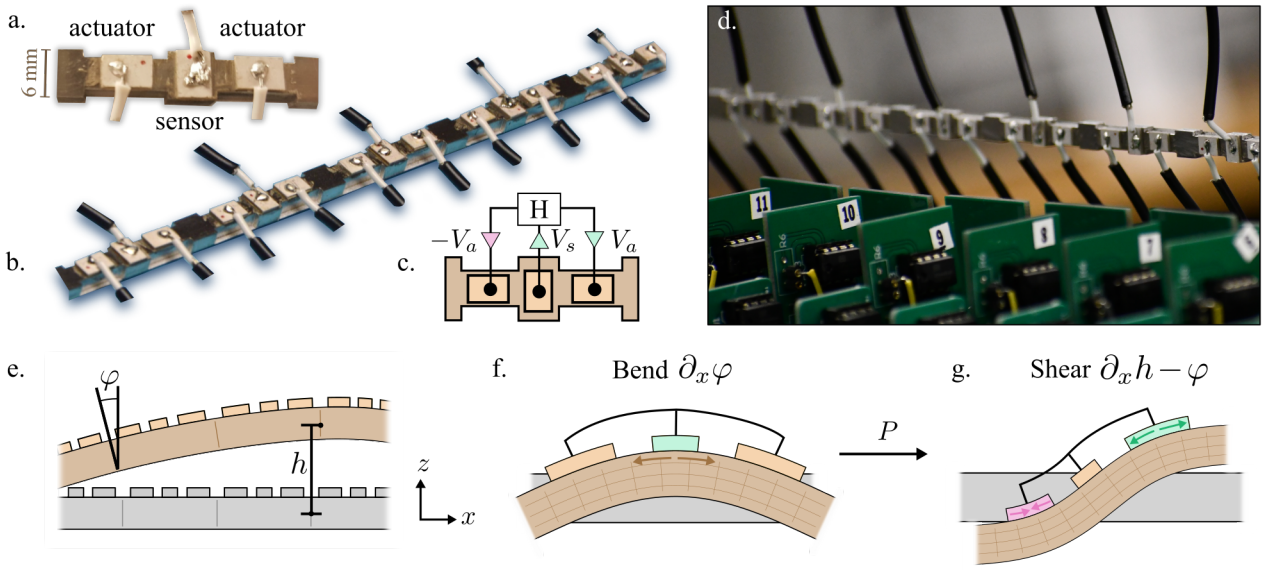

Figure 2.8: **Design and mechanics of an odd micropolar metabeam. a.** A single unit cell featuring three piezoelectric patches mounted on a beam: one that acts as a sensor, and two that act as actuators. **b.** A segment of the full metabeam. **c.** Each unit cell has an electronic loop. The voltage V_s induced by the central piezoelectric is fed into a transfer function $H(\omega) = V_a(\omega)/V_s(\omega)$ that sends opposing voltages V_a and $-V_a$ to the piezoelectric actuators. **d.** A photograph of the metabeam (horizontal) with the electronic circuits in the foreground. The mechanical forces from the attached wires are negligible: they act only as sources of energy and computation, but not of linear or angular momentum. **e.** The motion of the metabeam can be described by two independent fields, φ and h, which parameterize the angular and vertical displacements of the metabeam. Notice that under a reflection about the $\hat{z}$ axis, I have $\varphi \to -\varphi$ and $h \to h$. **f.** When the beam bends, the center piezoelectric is stretched. **g.** The antisymmetric electronic actuation then gives rise to a shearing stress proportional to the modulus P. Adapted from Chen et al. [2021].

The matrix C plays the role of the elasticity tensor, and μ and B are, respectively, the shear and bending moduli that one would expect from Timoshenko-Ehrenfest beam theory [Timoshenko, 1940]. An electronic feedback between the piezoelectric patches induces an additional modulus P. Since the energy differential is $\delta W = \sigma \delta s + M \delta b$, the asymmetric part of C corresponds to a violation of Maxwell-Betti reciprocity and therefore requires a source of energy. The parity-violating and nonconservative modulus P also induces unidirectional wave amplification [Chen et al., 2021].

2.6 Topological defects

2.6.1 What is a topological defect?

The introductory discussion in §2.1 assumed that the deformation of a solid is described by a continuous displacement field $u_i(\mathbf{x})$, but the stress only depends on the displacement gradient $\partial_i u_j$, or, quite often, on the strain $u^s_{ij} = (\partial_i u_j + \partial_j u_i)/2$. The question then becomes: given a strain field, can one always back out a continuous displacement field that is compatible with it? The answer is no. The strain tensor is invariant under the Euclidean group, which is generated by translations and rotations. Therefore, geometries can arise in which the strain tensor $u_{ij}(\mathbf{x})$ is continuous along a closed path Γ, but when integrated along the path Γ, the displacement field will not return to its original value: it will be off by a translation and/or a rotation. Such occurrences are known as topological defects. In the context of two-dimensional crystals, these are known as dislocations and disclinations, respectively. For a curve Γ, dislocations are defined by:

$$b_j = \oint_\Gamma \partial_i u_j \mathrm{d}r_j \tag{2.65}$$

where $\mathbf{b}$ is known as the Burger's vector, which indicates the extra translation that arises when the displacement gradient is integrated. Disclinations are defined by an angular mismatch

$$\theta = \frac{1}{2} \oint \partial_k \partial_i \epsilon_{ij} u_j \mathrm{d}r_k \tag{2.66}$$

Notably, if the displacement gradient $\partial_i u_j$ is continuous everywhere inside the contour Γ, then Stokes' theorem says $\mathbf{b} = 0$ and $\theta = 0$. However, if there is a local discontinuity, say a point defect, then $\mathbf{b}$ and θ are nonzero and that point is a quasiparticle known as a topological defect. The value of $\mathbf{b}$ or θ is invariant under continuous perturbations of Γ

so long as Γ does not cross a topological defect (and hence the name topological). In an amorphous or continuous medium, $\mathbf{b}$ and θ can in principle obtain any value. However, if the microscopic structure of the medium is crystalline, then the underlying symmetry group is not the full Euclidean group, but rather just those rotations and translations that are compatible with the crystal structure. This means that $\mathbf{b}$ and θ become quantized. In particular, for a hexagonal crystal, one has $\mathbf{b} = n_1\mathbf{a}_1 + n_2\mathbf{a}_2$ and $\theta = s\pi/3$, where s, n_1 and n_2 are integers and $\mathbf{a}_1$ and $\mathbf{a}_2$ are lattice vectors. It should be noted that Eqs. (2.65-2.66) are approximate expressions valid the far field limit. They are given a nonlinear, geometric treatment in Appendix 2.7.

Topological defects are crucial features in the study of solids. Their motion mediates large scale rearrangements such as plastic deformation, and they play a crucial role in melting of a crystalline solid into a hexatic in two dimensions [Nelson and Halperin, 1979]. Topological defects can also exist in phases with other types of order, such as hexatic or nematic symmetry, in which case activity is known to give rise to defect motility [Shankar et al., 2022, Duclos et al., 2020, Rouzaire and Levis, 2021, Kole et al., 2021, Maitra et al., 2020, Kumar et al., 2014, VanSaders and Glotzer, 2021, Poncet and Bartolo, 2022]. The following sections will study the role of transverse forces (which give rise to odd elasticity in the continuum limit) on the behavior of topological defects. It has been shown in recent experimental works that defects play a vibrant role in solids with transverse interactions, often nucleating instabilities at boundaries and creating churning phases in which polycrystalline grains constantly massage against each other [Bililign et al., 2021, Yan et al., 2015]. In the following subsections, I will present two types of calculations. The first involves computing stress and strain around static defects. These calculations are based on continuum odd elasticity and show signatures that can in principle be used to detect odd elasticity [Tan et al., 2022]. Second, I will discuss the motion of defects, a topic that involves going beyond continuum calculations. Throughout, the analytical calculations are compared with numerical experiments.

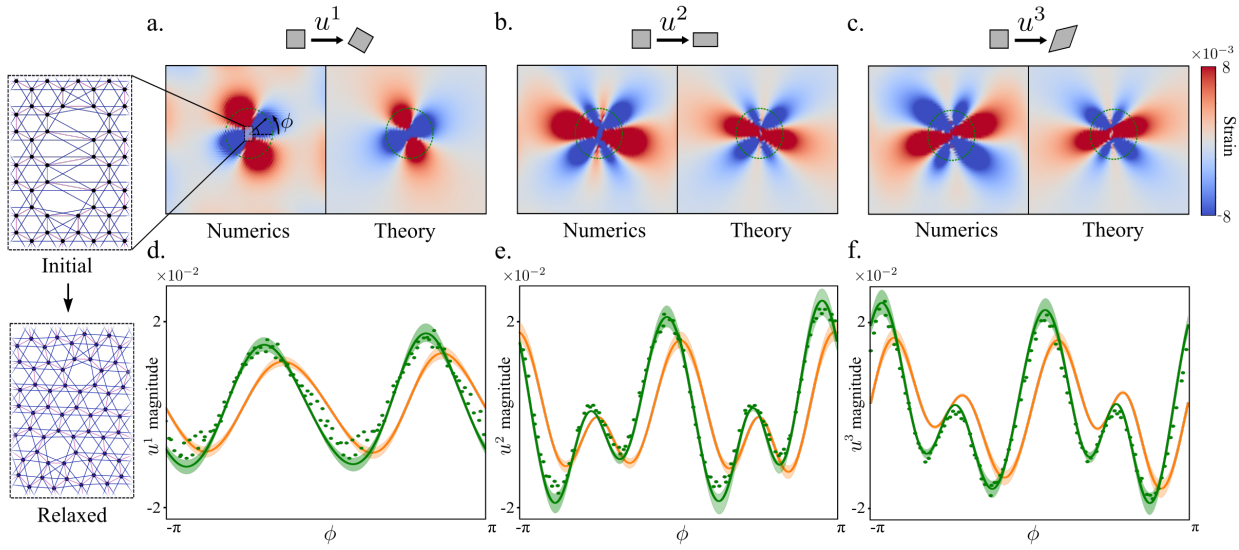

Figure 2.9: **Strain field of a dislocation pair. a-c.** The distribution of rotation (u^1), shear 1 (u^2), and shear 2 (u^3) surrounding a pair of dislocations in an odd elastic solid with $\nu = 0.8$ and $\nu^o = -0.88$. The right panels visualize the continuum theory while the left panel is the result of numerics. The inset to panel (a) renders the individual masses and bonds comprising the dislocation pair before (top) and after (bottom) relaxation. Panels **d-f.** quantitatively compare theory and numerical experiments by sampling the strain (green dots) at points between 8.0 and 9.2 lattice spacings from the center. The green line is the theoretical curve with $\nu = 0.8$ and $\nu^o = -0.88$. The shaded background accounts in the variation in distance from the center. The orange lines, provided for reference, are theoretical curves for a passive solid with $\nu = 0.8$ and $\nu^o = 0$. The dilation (u^0) is too small for numerical validation. Adapted from Braverman et al. [2021].

2.6.2 Static strain and stress fields

For a single isolated disclination or dislocation, how does odd elasticity modify the static distribution of stress and strain? For a disclination, Eq. (2.66) implies that the displacement field has an essential singularity that can be parameterized as

$$u_i(\mathbf{r}) = -\frac{s}{6}\phi\epsilon_{ik}r_k + v_i(\mathbf{r}), \tag{2.67}$$

where ϕ is the polar angle and $v_i(\mathbf{r})$ is a single-valued function. The force balance condition, $\partial_i\sigma_{ij}(\mathbf{r}) = 0$, with the constitutive relation $\sigma_{ij}(\mathbf{r}) = C_{ijkl}\partial_k u_l(\mathbf{r})$ together yield the following

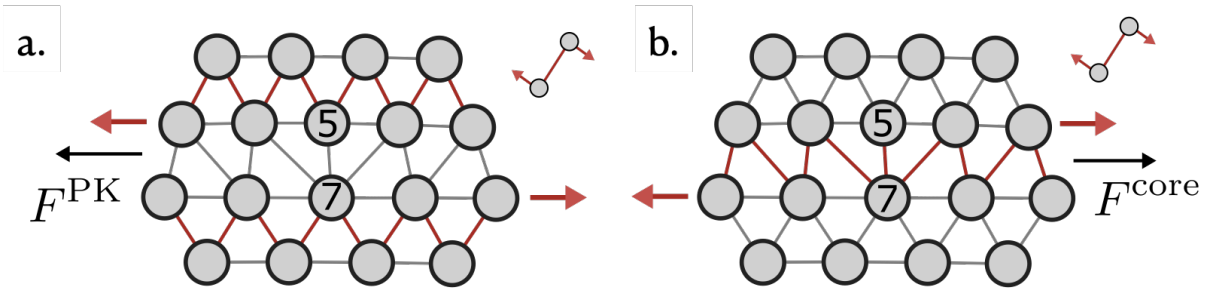

Figure 2.10: **Core and Peach-Koehler forces. a.** A dislocation is embedded in a triangular lattice of bonds exerting clockwise transverse forces. The dislocation consists of a particle with only five neighbors (labeled 5) paired with a particle with seven neighbors (labeled 7). These are separated by a horizontal line known as the glide plane. The transverse forces from the bonds not crossing the glide plane (highlighted in red) give rise to opposing lateral forces on the rows of atoms containing the 5 and the 7. These forces motivate the dislocation to travel left and can be captured in the continuum by the Peach–Koehler force F^{PK}. **b.** The bonds that straddle the glide plane push in the opposite direction and, therefore, motivate the dislocation to move to the right. This effect, dubbed the core force F^{core}, evades a continuum description. The core force vanishes when the microscopic interactions are entirely longitudinal. Adapted from Fruchart et al. [2023].

differential equation for $v_i(\mathbf{r})$:

$$\Delta(\partial_i v_i) = \frac{s}{3}\left(\frac{1-\nu}{2}\right)\delta(\mathbf{r}) \tag{2.68}$$

$$\Delta(\partial_i \epsilon_{ij} v_j) = -\frac{s}{3}\nu^o \delta(\mathbf{r}) \tag{2.69}$$

where ν and ν^o are, respectively, the Poisson's and odd ratios given by:

$$\nu \equiv \frac{\mu(B-\mu) + K^o(A-K^o)}{\mu(B+\mu) + K^o(A+K^o)} \tag{2.70}$$

$$\nu^o \equiv \frac{BK^o - A\mu}{\mu(B+\mu) + K^o(A+K^o)} \tag{2.71}$$

For boundary conditions, it is required that $\hat{r}_i\sigma_{ij} = \hat{r}_i\sigma^0_{ij}$ along a circle of radius R. This yields the solution

$$u_i(\mathbf{r}) = \frac{s}{6}\left\{-\phi\epsilon_{ij}x_j + \frac{(1-\nu)}{2}r_i\log(r/R_1) + \nu^o\epsilon_{ij}r_j\log(r/R_2)\right\} \tag{2.72}$$

Here, $R_1 = R_2 = R/\sqrt{e}$ are constants introduced to ensure the stress boundary conditions are satisfied. From $\sigma_{ij} = C_{ijmn}\partial_m u_n$, the stresses are given by:

$$\sigma_{ij}(\mathbf{r}) = (1-\nu)\frac{s}{12}\left\{B\left[2\log(r/R_1)\delta_{ij} - \left(\frac{2r_ir_j}{r^2} - \delta_{ij}\right)\right] - A\left[2\log(r/R_2)\epsilon_{ij} + \frac{r_i\epsilon_{jl}r_l + r_j\epsilon_{il}r_l}{r^2}\right]\right\} + \sigma^0_{ij} \tag{2.73}$$

A similar approach can be applied to the displacement and strain field surrounding a dislocation. The definition of the Burger's vector [Eq. (2.65)] implies that the solution for u_i is of the form:

$$u_i(\mathbf{r}) = \frac{b_i}{2\pi}\phi + v_i(\mathbf{r}) \tag{2.74}$$

where once again $v_i(\mathbf{r})$ is a single-valued function. The requirement that $\partial_i\sigma_{ij}(\mathbf{r}) = 0$ for $\mathbf{r} \neq 0$ yields the following differential equation for $v_i(\mathbf{r})$:

$$\Delta(\partial_i v_i) = \nu b_i\epsilon_{ij}\partial_j\delta(\mathbf{r}) \tag{2.75}$$

$$\Delta(\partial_i\epsilon_{ij}v_j) = (-b_i + 2\nu^o\epsilon_{ij}b_j)\partial_i\delta(\mathbf{r}) \tag{2.76}$$

As a boundary condition, it is required that $\sigma_{ij} \to \sigma^0_{ij}$ as $r \to \infty$. One obtains the following

solution for the displacement field:

$$u_i(\mathbf{r}) = \frac{1}{2\pi}\Bigg\{ b_i\phi + \epsilon_{ik}b_k\frac{(1-\nu)}{2}\log(r) + \frac{(1+\nu)}{2}\frac{\epsilon_{im}r_m b_n r_n}{r^2} - \nu^o\left[b_i\log(r) - \frac{\epsilon_{im}r_m r_n \epsilon_{nk}b_k}{r^2}\right]\Bigg\} \tag{2.77}$$

and the stress is given by:

$$\sigma_{ij}(\mathbf{r}) = \frac{(1-\nu)}{2\pi r^2}\Bigg\{ B\left[r_m\epsilon_{mn}b_n\delta_{ij} - b_k r_k\left(\frac{r_i\epsilon_{jm}r_m + r_j\epsilon_{im}r_m}{r^2}\right)\right] - A\left[r_m\epsilon_{mn}b_n\epsilon_{ij} - b_k r_k\left(\frac{2r_i r_j}{r^2} - \delta_{ij}\right)\right]\Bigg\} + \sigma^0_{ij} \tag{2.78}$$

For both the disclination and the dislocation, the ratio of the torque density to the pressure is given by $\tau(\mathbf{r})/p(\mathbf{r}) = A/B$ and the shear stress is rotated by an angle $\delta\chi(\mathbf{r}) = -\arctan(A/B)/2$. Moreover, the local dilation is unmodified by A and K^o (except through the value of ν) and the shear strain is locally rotated by $\delta\alpha(\mathbf{r}) = -\arctan[2\nu^o/(1+\nu)]/2$.

When K^o is the only nonzero odd elastic modulus, the expressions in Eqs. (2.78,2.72) may be obtained more simply using the Airy stress function. Differential versions of Eq. (2.65) and Eq. (2.66) read

$$\epsilon_{ij}\partial_i\partial_j u_k = \sum_\alpha b_k^\alpha \delta(\mathbf{r} - \mathbf{r}^\alpha) \tag{2.79}$$

$$\epsilon_{ij}\partial_i\partial_j\epsilon_{lk}\partial_l u_k = \frac{2\pi}{3}\sum_\alpha s^\alpha\delta(\mathbf{r} - \mathbf{r}^\alpha) \tag{2.80}$$

where b_i^α and s^α are the charges associated with a defect at point $\mathbf{r}^\alpha$. By evaluating $\partial_k\epsilon_{ki}\partial_l\epsilon_{lk}u^s_{ij}$, one obtains an expression identical in form to that of standard isotropic 2D elasticity:

$$\Delta^2\chi = Es(\mathbf{r}) \tag{2.81}$$

where

$$s(\mathbf{r}) = \sum_{\alpha} \left[\frac{\pi}{3} s^{\alpha} + b_i^{\alpha} \epsilon_{ij} \partial_j \right] \delta(\mathbf{r} - \mathbf{r}^{\alpha}) \tag{2.82}$$

is the defect density. For a single disclination at the origin, one obtains $\Delta^2 \chi = E\pi s \delta(\mathbf{r})/3$, which yields a stress:

$$\sigma_{ij} = \frac{sE}{12} \left[\frac{\epsilon_{il}\epsilon_{jk} r_l r_k}{r^2} + \log(r) \right] \tag{2.83}$$

which agrees with Eq. (2.73) upon setting $A = 0$ and using $E = 2B(1 - \nu)$. Similarly, for a single dislocation, solving $\Delta^2 \chi = E b_i \partial_i \delta(\mathbf{x})$ yields

$$\sigma_{ij} = \frac{E}{4\pi r^2} \left[r_m \epsilon_{mn} b_n \delta_{ij} - b_k r_k \left(\frac{r_i \epsilon_{jm} r_m + r_j \epsilon_{im} r_m}{r^2} \right) \right], \tag{2.84}$$

in agreement with Eq. (2.78) with $A \to 0$.

In Fig. 2.9, a numerical validation of the strain field surrounding the defects is performed. A honeycomb lattice is formed by using nearest and next-nearest neighbor odd springs. A dipole of dislocations is formed and the lattice is relaxed with fixed bond topology. The strain is numerically measured and compared to analytical expressions.

2.6.3 Defect motion

Motion of topological defects, in particular dislocations, can lead to large scale plastic deformation of a crystalline structure. In a passive medium, dislocations are stationary until an external stress is applied (typically at the boundary of the medium). Elastic stresses then propagate this energy inward causing small scale rearrangements that constitute defect motion. In systems with transverse forces, the dislocations need not be stationary even in the absence of externally imposed stresses. The simplest question to ask is: which way and

when does a dislocation move?

The first constraint comes from a microscopic consideration: dislocations are are fractons, meaning that they only want to move in certain directions. This direction is their glide plane, which is the plane defined by their Burger's vector. To move a dislocation perpendicular to its glide plane would require pushing an entire row of atoms, and ejecting one atom out of the solid. This would require breaking and reforming many bonds, so it is dynamically very hard to accomplish. Motion along the glide plane, by contrast, involves just one set of neighbor reassignments at a time, and so it is much easier to coordinate. In the language of fractons, the restricted mobility (though originating from microscopic considerations) can be incorporated macroscopically on the continuum field theory by imposing an additional conservation law. In the case of dislocations, this conservation law is a mass conservation (see Appendix 2.7).

But then the question remains: which way along the glide plane do the dislocations move, and when? In a system with transverse forces, there are two distinct competing effects. Figure 2.10 shows an example of a dislocation in which the Burgers vector is pointing to the right, and the glide plane is the plane separating the 5- and 7-fold coordinated particles. All the bonds are exerting clockwise a transverse forces. In panel (a), all the bonds that do not straddle the glide plane are highlighted in red. They want to push the row of atoms on top of the glide plane to the left, and the row below the glide plane to the right. (This would mean that the defect itself goes to the left). This effect can be rationalized by the tendency of the bulk media to rotate, and so it can be captured in the continuum by an effective force known as the Peach-Koehler force. In panel (b), all the bonds crossing the glide plane are highlighted. These bonds want to push the dislocation to the right. This force is labeled F^{core} since it is dominated by bonds near the core of the defect. So which of the two forces, F^{PK} or F^{core} will dominate? As will be discussed below, either can dominate and the winner depends on the details of the interactions.

The core force is normally not considered in the study of topological defects because in a conservative medium, it is zero. This will be shown mathematically below, but the fact can also be seen qualitatively: all the bonds participating in the core force are internal to the medium with none extending to the upper and lower boundaries at which an external force is applied. Hence, in a conservative medium, that force can do no work since the initial and final configurations of defect motion are related by translational symmetry. However, for nonconservative media, I will show that this force is actually crucial.

Before diving into the derivation, it is worth emphasizing that motion of an effective force on a topological defect is nonsensical in a medium with nonconservative microscopic forces. The total work done over any trajectory is given by:

$$W = \sum_{\alpha} \int_0^{t_f} \mathbf{F}^{\alpha} \cdot \mathrm{d}\mathbf{r}^{\alpha} \tag{2.85}$$

where $\mathbf{F}^{\alpha}$ is the net force on the particle α, which has position $\mathbf{r}^{\alpha}$. In a conservative system, the net work done only depends on the final and initial configurations, and not the trajectory in-between. Therefore, in the case of topological defects, one can specify the initial and final configurations by the location $\mathbf{X}$ of the topological defect, and define the force $\mathbf{f}$ on that defect via the relation $W = \mathbf{f} \cdot \delta\mathbf{X}$. However, in a nonconservative medium, the work done is trajectory dependent, so simply specifying $\delta\mathbf{X}$ does not determine W, and so the force $\mathbf{f}$ is completely arbitrary. This does not mean that the following calculations are nonsense, though. Instead, what one is actually interested in is simply solving the equations of motion $\dot{\mathbf{r}}^{\alpha} = \mathbf{F}^{\alpha}$. Along trajectories that satisfy this equation of motion, it is easily seen that $\dot{W} \geq 0$. Hence, if the system has a small number of plausible and qualitatively distinct motions (say the defect goes right or left), one can impose a set of guesses for the trajectory and compute $\dot{W}$ for those guesses. Only the guess trajectories with $\dot{W} \geq 0$ are actually physical candidates. Actually computing $\dot{W}$ will require mathematical machinery that that can be thought of as an effective force (once the guess trajectory is specified).

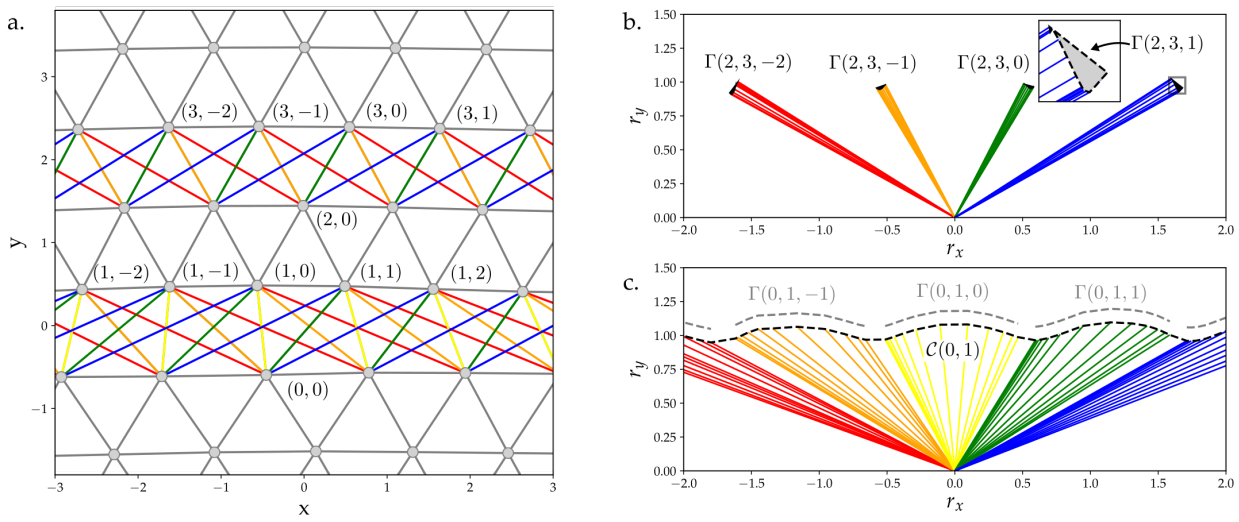

Figure 2.11: **Schematic of dislocation core. a.** A rendering of the dislocation core with certain particles highlighted by their index $(R(\alpha), C_R(\alpha))$. **b.** Bonds connecting rows 2 and 3 are plotted in the space of their relative coordinates (r_x, r_y). The inset shows the contour $\Gamma(2, 3, 1)$ which interpolates between each of the bond positions. **c.** The bonds connecting rows 0 and 1 are shown. The individual contours $\Gamma(0, 1, n)$ do not close since the rows 0 and 1 are on opposite sides of the glide plane. Instead, the bonds can be concatenated into a single continuous contour $\mathcal{C}(0, 1)$. Adapted from Braverman et al. [2021].

I now derive the active contribution to the dislocation force that arises from bond reassignment at the core. I begin by considering an infinite lattice with a single isolated dislocation. The quantity I wish to compute is the total work done by all the interactions if the dislocations glides one lattice spacing. If the interactions are described by a potential energy that depends only on relative coordinates and is symmetric under exchange of particles, then no work is done since the final configuration is a translation of the previous arrangement (up to a relabeling of particles). However, the work is generally nonzero if the interactions are nonconservative, and the total work depends on the microscopic path that interpolates between the two configurations. Explicitly, the total work done by the interactions is given by:

$$W_{\text{glide}} = \int_{t_i}^{t_f} \mathrm{d}t \sum_{\alpha} \sum_{\alpha' > \alpha} \mathbf{F}^{\alpha\alpha'} \cdot \frac{\mathrm{d}\mathbf{r}^{\alpha\alpha'}}{\mathrm{d}t} \tag{2.86}$$

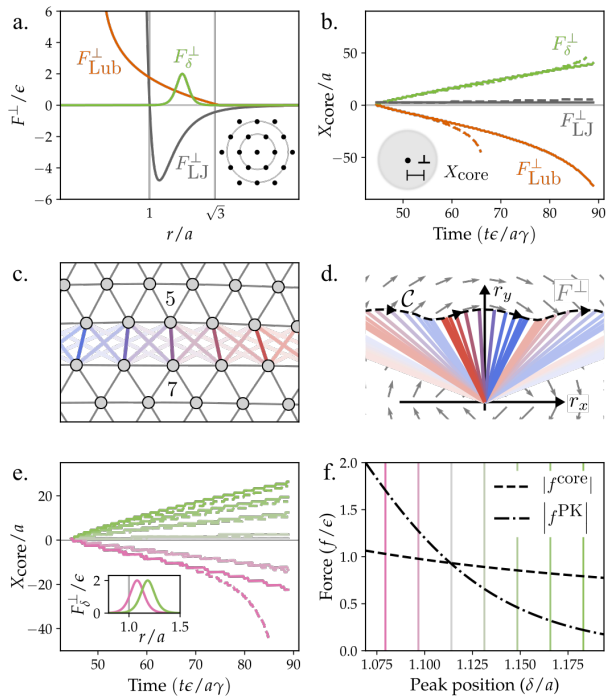

Figure 2.12: **Dislocations self propel via active work cycles at their cores. a.** Three transverse interactions $F^{\perp}_{\mathrm{LJ}}$ (purple), $F^{\perp}_{\mathrm{Lub}}$ (teal), and $F^{\perp}_{\delta}$ (orange), with the neighbor shells highlighted by grey lines. Inset: A hexagonal lattice with first and second neighbor shells highlighted. **b.** Particles are arranged in a free floating circular cluster with a single dislocation located at the center, and the dislocation position is tracked as a function of time. Simulations are performed with clusters of radius $R = 50$ (dashed) and $R = 100$ (solid). **c**. Bonds crossing the glide plane of a dislocation are highlighted. Hue indicates the bond's position in real space (blue: left, red: right). Opacity indicates the length of the bond (nearest neighbors darkest). **d.** The highlighted bonds are plotted with their bases aligned. As the dislocation moves one unit cell to the right, the tops of the bonds traces out a contour $\mathcal{C}$ (black dashed). The gray arrows depict the interaction force field. **e.** The interaction $F^{\perp}_{\delta}$ is varied by changing the location δ of its peak (pink: smaller δ, green: larger δ). For each value of δ, the dislocation's position is tracked as a function of time. **f.** The magnitude of the Peach-Koehler force f^{PK} and the active core force f^{core} as a function of the peak position δ. The vertical lines represent the values of δ used in the simulation. The direction change of the dislocation motion coincides with the crossover between f^{core} and f^{PK}. Adapted from Braverman et al. [2021].

Here, $\mathbf{r}^{\alpha\alpha'}$ is the relative coordinate pointing from particle α to particle α' and $\mathbf{F}^{\alpha\alpha'}$ is the force from particle α on α'. To arrange the sum, I use a labeling system shown in Fig. 2.11a. I first label each horizontal (i.e. parallel to the glide plane) row of atoms by an integer. In Fig. 2.11a, I choose $R = 0$ to be the row containing the 7-fold and $R = 1$ to be the row

containing the five fold. Let $R(\alpha)$ denote the row containing particle α.

Within each row R, I label the each particle by an integer $C_R(\alpha)$ that increases from left to right. Then each particle α can be uniquely identified by the ordered pair $(R(\alpha), C_R(\alpha))$. I may then write the work in the following form:

$$W_{\text{glide}} = \int_{t_i}^{t_f} \mathrm{d}t \sum_{R\in\mathbb{Z}} \sum_{R'\geq R} \sum_{n\in S_{R',R}} \sum_{m\in\mathbb{Z}} \mathbf{F}\cdot\frac{\mathrm{d}\mathbf{r}^{(R,m),(R',m+n)}}{\mathrm{d}t} \tag{2.87}$$

where $S_{R',R} = \mathbb{Z}\setminus\{0\}$ if $R' = R$ and $S_{R',R} = \mathbb{Z}$ otherwise. Usage of $S_{R,R'}$ simply precludes self-interaction among the particles. I have suppressed indices on $\mathbf{F}$ for simplicity of notation.

Upon translation of the dislocation by one unit cell, one has

$$\mathbf{r}^{(R,m),(R',m')}(t_f) = \mathbf{r}^{(R,m-1),(R',m'-1)}(t_i) \tag{2.88}$$

Hence, one may concatenate the trajectory of individual bonds into the following continuous contours:

$$\Gamma(R,R',n) \equiv \bigcup_{m\in\mathbb{Z}} \left\{\mathbf{r}^{(R,m),(R',m+n)}(t) : t\in[t_i,t_f]\right\}. \tag{2.89}$$

Notice that

$$\sum_{m\in\mathbb{Z}} \int_{t_i}^{t_f} \mathbf{F}\cdot\frac{\mathrm{d}\mathbf{r}^{(R,m),(R',m+n)}}{\mathrm{d}t}\mathrm{d}t = \int_{\Gamma(R,R',n)} \mathbf{F}\cdot\mathrm{d}\mathbf{r}. \tag{2.90}$$

Hence, the expression for the work becomes:

$$W_{\text{glide}} = \sum_{R\in\mathbb{Z}} \sum_{R'>R} \sum_{n\in S_{R',R}} \int_{\Gamma(R,R',n)} \mathbf{F}\cdot\mathrm{d}\mathbf{r}. \tag{2.91}$$

To further simplify the sum, I introduce the following two sets

$$\mathcal{B} \equiv \{(R, R') : R' > R \text{ and either } R \geq 1 \text{ or } 0 \geq R'\} \tag{2.92}$$

$$\mathcal{G} \equiv \{(R, R') : R' \geq 1 \text{ and } 0 \geq R\} \tag{2.93}$$

Here, $\mathcal{B}$ is the set of of all pairs of rows that do not straddle the glide plane and $\mathcal{G}$ is the set of all pairs of rows that do straddle the glide plane. For $(R, R') \in \mathcal{B}$, one has

$$\mathbf{r}^{(R,m),(R',m+n)} = \mathbf{r}^{(R,-m),(R',-m+n)} \text{ as } m \to \infty. \tag{2.94}$$

Equation (2.94) is a consequence of the lattice being undeformed far away from the dislocation. From Eq. (2.94), I deduce that $\Gamma(R, R', n)$ is a closed contour for $(R, R') \in \mathcal{B}$.

However, for $(R, R') \in \mathcal{G}$, one has

$$\mathbf{r}^{(R,m),(R',m+n)} = \mathbf{r}^{(R,-m),(R',-m+n-1)} \text{ as } m \to \infty. \tag{2.95}$$

Equation (2.95) follows from the definition of a dislocation: there is a mismatch in the number of particles in the rows above and below the glide plane. Notice that Eq. (2.95) implies $\Gamma(R, R', n)$ is *not* a closed contour for $(R, R') \in \mathcal{G}$. However, Eq. (2.95) implies that I may form a single infinite continuous contour $\mathcal{C}(R', R)$ by concatenating the individual pieces

$$\mathcal{C}(R, R') \equiv \bigcup_{n \in \mathbb{Z}} \Gamma(R, R', n) \tag{2.96}$$

Whenever the interactions decay faster than $1/r$, I will be able to close the contour $\mathcal{C}(R, R')$

in the upper half plane. Hence, the expression for the work becomes:

$$W_{\text{glide}} = \sum_{(R,R')\in\mathcal{B}} \sum_{n\in S_{R',R}} \oint_{\Gamma(R,R',n)} \mathbf{F}\cdot \mathrm{d}\mathbf{r} + \sum_{(R,R')\in\mathcal{G}} \oint_{\mathcal{C}(R,R')} \mathbf{F}\cdot \mathrm{d}\mathbf{r} \tag{2.97}$$

$$= \sum_{(R,R')\in\mathcal{B}} \sum_{n\in S_{R',R}} \int_{V_n(R,R')} \nabla\times\mathbf{F}\,\mathrm{d}^2 r + \sum_{(R,R')\in\mathcal{G}} \int_{V(R,R')} \nabla\times\mathbf{F}\,\mathrm{d}^2 r \tag{2.98}$$

where $V_n(R,R')$ and $V(R,R')$ are the signed areas enclosed by $\Gamma(R,R',n)$ and $\mathcal{C}(R,R')$

From the point of view of the bonds in set $\mathcal{B}$, the solid is actually two disjoint sets separated by a cut along the glide plane. One could estimate various contributions from $\mathcal{B}$ by taking the dot product of the average motion with the boundary stresses on the cut surface. This approach is the essence of the Peach-Koehler force computed in the continuum. The contributions from $\mathcal{G}$, however, involves bond reassignment through the core. This piece is disregarded in the Peach-Koehler calculation when a branch cut discontinuity is introduced into the derivation. Assuming short ranged interaction, the dominant contribution from the $\mathcal{G}$ terms comes from $\mathcal{C}(0,1)$, i.e. the bonds that directly span the glide plane. In this approximation, one has:

$$W_{\text{glide}} \approx \oint_{\mathcal{C}(0,1)} \mathbf{F}\cdot \mathrm{d}\mathbf{r} \tag{2.99}$$

If the force from the bonds fall off faster than $1/r$, then the contour $\mathcal{C}(0,1)$ can be compactified to enclose an area $\mathcal{A}$. In this case, Eq. (2.99) may be rewritten as:

$$W_{\text{glide}} \approx \int_{\mathcal{A}} \nabla\times\mathbf{F}\mathrm{d}^2 r \tag{2.100}$$

This form emphasizes that if the interparticle force $\mathbf{F}$ is conservative, i.e. $\nabla\times\mathbf{F}=0$, then the glide force is zero, as is the case in traditional solid mechanics.

Furthermore, notice that the above derivation does not actually tell us what W_{glide},

but merely provides an alternative expression for it in terms of $\mathcal{C}(0,1)$, which is not *a priori* known. However, this re-writing is useful because it sets up effective approximation schemes. The simplest approximation is to assume that all the atoms move along straight lines parallel to the glide plane, in which case $\mathcal{C}$ is given by the horizontal line $r_y = \frac{\sqrt{3}}{2}a$ traversed from right to left. In this approximation, the work becomes:

$$W_{\text{glide}} \approx \int_{-\infty}^{\infty} F_x^{\perp} \mathrm{d}r_x \Big|_{r_y=\frac{\sqrt{3}}{2}a} \tag{2.101}$$

One can use this approximation to make predictions. In Fig. 2.12, a raft of particles is prepared with a single dislocation in the middle. Depending on which force is used (orange or green in panel a), the defect moves left or right. In panels e-f, the location of the maximum for the green force $F_{\delta}^{\perp}$ is moved in and out. The Peach-Koehler force and the core force according to Eq. (2.101) are computed. The reversal in dislocation motion coincides with the reversal of dislocation motion.

2.7 Appendix: Nonlinear formulation of odd elasticity

2.7.1 The geometry of material deformation

This appendix introduces the geometric definition necessary to define stress, strain, elasticity, and odd elasticity in a way that extends beyond linear response. The discussion will focus on a d-dimensional material embedded in d-dimensional Euclidean space $\mathbb{E}^d$. Each point in the material is labeled by a coordinate $q = (q^1, q^2, \ldots, q^d)$. Each point q is assigned a reference position $\mathbf{r}(q)$, which defines the "undeformed" state, and a point $\mathbf{R}(q,t)$ that corresponds to location of point q at time t. The change is rest and deformed position defines the displacement $\mathbf{u}(q,t) = \mathbf{R}(q,t) - \mathbf{r}(q)$. The velocity of a material element is $\mathbf{v}(q,t) = \partial_t \mathbf{R}(q,t)$. See Figure 2.13 for an illustration.

In order to think about changes in shape, one needs to be able to take derivatives of the

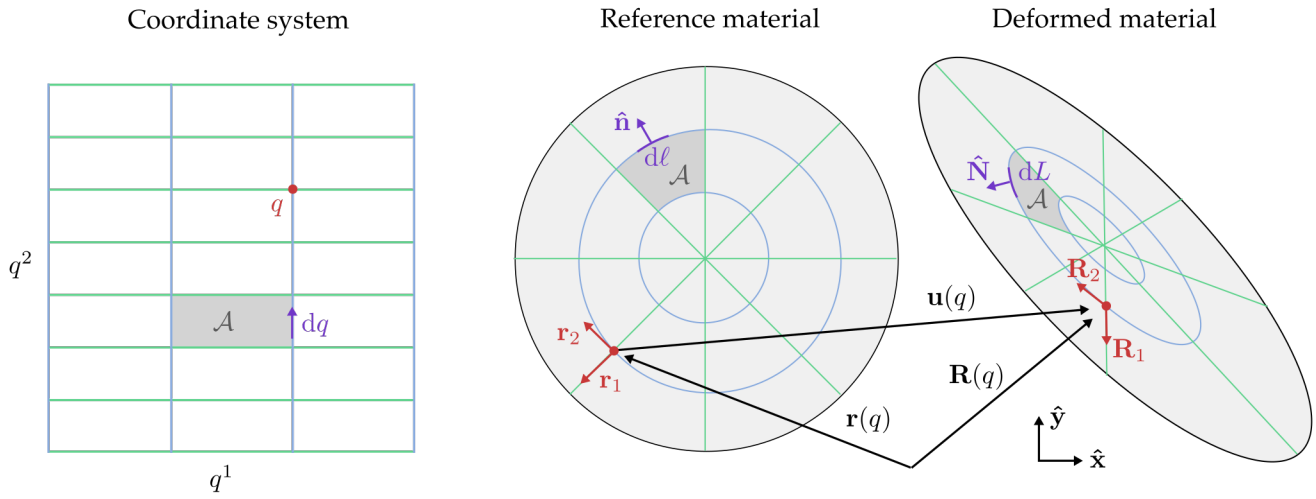

Figure 2.13: **An illustration of the coordinate systems defined in § 2.7.1.** Adapted from Braverman et al. [2021].

displacement field. To do so, two sets of basis vectors are utilized: $\mathbf{R}_i = \frac{\partial \mathbf{R}}{\partial q^i}$ and $\mathbf{r}_i = \frac{\partial \mathbf{r}}{\partial q^i}$. The basis vectors come paired with duals $\mathbf{R}^i$ and $\mathbf{r}^i$ defined such that $\mathbf{R}^i \cdot \mathbf{R}_j = \delta^i_j$ and $\mathbf{r}^i \cdot \mathbf{r}_j = \delta^i_j$, where δ^i_j is the Kronecker-δ. Given an arbitrary tensor field $\mathbf{T}(q)$, I will use the following two types of derivatives

$$\operatorname{Grad} \mathbf{T} = \mathbf{R}^i \otimes \frac{\partial \mathbf{T}}{\partial q^i} \qquad \operatorname{grad} \mathbf{T} = \mathbf{r}^i \otimes \frac{\partial \mathbf{T}}{\partial q^i} \tag{2.102}$$

$$\operatorname{Div} \mathbf{T} = \mathbf{R}^i \cdot \frac{\partial \mathbf{T}}{\partial q^i} \qquad \operatorname{div} \mathbf{T} = \mathbf{r}^i \cdot \frac{\partial \mathbf{T}}{\partial q^i} \tag{2.103}$$

where repeated indices are summed over, $(\mathbf{a} \otimes \mathbf{b})_{\alpha\beta} = a_\alpha b_\beta$ is the direct product, and $(\mathbf{a} \cdot \mathbf{b}) = a_\alpha b_\alpha$ is the inner product, and α, β label the components of an orthonormal basis on $\mathbb{E}^d$. The change in shape is captured by the deformation tensor: $\mathbf{J}(q,t) = \operatorname{grad} \mathbf{R}(q,t) = \mathbf{r}^i \otimes \mathbf{R}_i$ and I will write $J = \det \mathbf{J}$. Notice that $\mathbf{J}(q,t) = \mathbf{I} + \operatorname{grad} \mathbf{u}$, where $\mathbf{I}$ is the identity tensor. For use later, let the induced metrics be denoted $g_{ij} = \mathbf{r}_i \cdot \mathbf{r}_j$ and $G_{ij} = \mathbf{R}_i \cdot \mathbf{R}_j$.

2.7.2 Linear momentum conservation and the stress tensor(s)

Let $\mathbf{P}(q,t)$ be the density of momentum (or any other conserved vector quantity, if you like) in real space. In order to write down a continuity equation for $\mathbf{P}$, one needs the notion of a momentum current. In continuum mechanics, this is referred to as *stress*. For concreteness, imagine (in two dimensions) drawing an infinitesimal line on the material specified by the differential $\mathrm{d}q$. In the undeformed material, this line element corresponds to the vector $d\boldsymbol{\ell} = \mathrm{d}q^i \mathbf{r}_i$, and in the deformed material, this line element corresponds to the vector $\mathrm{d}\mathbf{L} = \mathrm{d}q^i \mathbf{R}_i$. Any type of stress tensor will tell you how much momentum crosses the line $\mathrm{d}q$ in a time δt. The *Cauchy* stress tensor $\boldsymbol{\sigma}$ provides this answer in a coordinate system relevant for the deformed material $-\delta\mathbf{P} = \delta t|\mathrm{d}\mathbf{L}|\hat{\mathbf{N}}\cdot\boldsymbol{\sigma}$. The *Piola-Kirchoff* stress $\mathbf{S}$ states this in a basis that is relevant for the undeformed material $-\delta\mathbf{P} = \delta t|\mathrm{d}\boldsymbol{\ell}|\hat{\mathbf{n}}\cdot\mathbf{S}$. Here $\hat{\mathbf{N}}$ and $\hat{\mathbf{n}}$ are the normal vectors corresponding to $\mathbf{L}$ and $\boldsymbol{\ell}$, respectively. The continuity equation for momentum $\mathbf{P}$, then takes the form

$$\partial_t \mathbf{P} = \mathrm{Div}\,\boldsymbol{\sigma} \quad \text{or equivalently} \quad J\partial_t \mathbf{P} = \mathrm{div}\,\mathbf{S} \tag{2.104}$$

in the proceeding definition. The two stress tensors are related by the so-called Piola-transformation $\mathbf{S} = J\mathbf{J}^{-T}\cdot\boldsymbol{\sigma}$. For a domain $\mathcal{A}$, the integral form of the continuity condition is:

$$\frac{\mathrm{d}}{\mathrm{d}t}\int_{\mathcal{A}} \mathbf{P}\,\mathrm{d}^d R = \int_{\partial\mathcal{A}} \hat{\mathbf{N}}\cdot\boldsymbol{\sigma}\,\mathrm{d}^{d-1}R = \int_{\partial\mathcal{A}} \hat{\mathbf{n}}\cdot\mathbf{S}\,\mathrm{d}^{d-1}r \tag{2.105}$$

Where $\mathrm{d}^d R = \sqrt{G_{ij}\mathbf{R}^i\otimes\mathbf{R}^j}\mathrm{d}^d q$ and $\mathrm{d}^d r = \sqrt{g_{ij}\mathbf{r}^i\otimes\mathbf{r}^j}\mathrm{d}^d q$.

2.7.3 Angular momentum conservation

Closely related to linear momentum conservation is angular momentum conservation. Here, I will take the momentum density to be $\mathbf{P} = \frac{1}{J}\mathbf{v}$ and the angular momentum density about the origin to be $\mathbf{L} = \mathbf{R} \times \mathbf{P}$, were I am working in two dimensions for simplicity. Then the rate of change of the angular momentum density in a region $\mathcal{A}$ is

$$\frac{\mathrm{d}}{\mathrm{d}t}\int_{\mathcal{A}} \mathbf{R} \times \mathbf{p}\mathrm{d}^2R = \int_{\mathcal{A}} \mathbf{R} \times \mathrm{Div}\,\boldsymbol{\sigma}\mathrm{d}^2R \tag{2.106}$$

$$= -\oint_{\partial\mathcal{A}} \hat{\mathbf{N}} \cdot \boldsymbol{\sigma} \times \mathbf{R}\mathrm{d}R - \int_{\mathcal{A}} \boldsymbol{\epsilon} : \boldsymbol{\sigma}\mathrm{d}^2R \tag{2.107}$$

Notice that the first term in Eq. (2.107) is the torque exerted at the boundary of the region $\mathcal{A}$. Angular momentum is said to be conserved in the continuum theory if the rate of angular momentum change within $\mathcal{A}$ is equal to the torque applied at the boundary $\partial\mathcal{A}$. Hence angular momentum conservation implies that the Cauchy stress is symmetric: $\boldsymbol{\sigma} = \boldsymbol{\sigma}^T$. (Notice, however, that Piola-Kirchoff stress need not be symmetric even when angular momentum is conserved.) Physical systems can effectively violate angular momentum conservation if they have internal spinning parts that are not tracked in the total momentum flow; when these internal spinning parts speed up or slow down, they exert torques on the macroscopic center of mass motion of the particles which is presumably tracked during coarse-graining.

2.7.4 Conservative and nonconservative forces

We are now in a position to start discussing elasticity. By elasticity, here, refers to the contribution to the stress that is only a function of the instantaneous deformation $\mathbf{J}$. In a mechanical context, one is often interested in the work by the elastic stresses on a piece of material in $\mathcal{A}$. If the material is deformed quasistatically (such that the elastic forces are

always balanced with the external forces), the work per unit time done by the material is

$$\frac{\mathrm{d}W}{\mathrm{d}t} = -\int_{\mathcal{A}} \mathbf{F}\cdot\mathbf{v}\,\mathrm{d}^d R = \int_{\mathcal{A}} \boldsymbol{\sigma} : \mathrm{Grad}\,\mathbf{v}\,\mathrm{d}^d R - \oint_{\partial\mathcal{A}} \hat{\mathbf{N}}\cdot\boldsymbol{\sigma}\cdot\mathbf{v}\,\mathrm{d}^{d-1}R \tag{2.108}$$

or equivalently

$$\frac{\mathrm{d}W}{\mathrm{d}t} = -\int_{\mathcal{A}} \mathbf{f}\cdot\mathbf{v}J\,\mathrm{d}^d r = \int_{\mathcal{A}} \mathbf{S} : \mathrm{grad}\,\mathbf{v}\,\mathrm{d}^d r - \oint_{\partial\mathcal{A}} \hat{\mathbf{n}}\cdot\mathbf{S}\cdot\mathbf{v}\,\mathrm{d}^{d-1}r \tag{2.109}$$

where $\mathbf{F} = \frac{1}{J}\mathbf{f}$.

The typical assumption applied to elasticity theory is the following: if a material initially at rest is quasistatically deformed and then brought back to its original configuration, the net work done by the material on its surroundings is zero. This assumption is natural if conservative forces are responsible for the elasticity: any energy put out from the medium must have been put in from the outside at some earlier point.

By noting that $\mathrm{grad}\,\mathbf{v} = \frac{\mathrm{d}\mathbf{J}}{\mathrm{d}t}$ and choosing a deformation such that the boundary remains undeformed, one finds that the energy conservation condition is equivalent to

$$\oint \mathbf{S} : \frac{\mathrm{d}\mathbf{J}}{\mathrm{d}t}\mathrm{d}t = 0 \tag{2.110}$$

for all closed loops of deformation. Equation (2.110) then implies that

$$U(\mathbf{J}) = \int_{\mathbb{I}}^{\mathbf{J}} \mathbf{S}(\mathbf{J}') : \mathrm{d}\mathbf{J}' \tag{2.111}$$

is a well defined function. In other words, energy conservation is equivalent to the constraint that the Piola-Kirchoff stress can be expressed as the gradient of a scalar function of the deformation gradient:

$$\mathbf{S} = \frac{\partial U}{\partial \mathbf{J}} \tag{2.112}$$

However, this constraint need not apply if the system has an internal energy source or is externally driven. This is a definition of *odd elasticity* that is stated in the continuum and applies beyond the small strain approximation.

2.7.5 Linear elasticity

This section examines the nuances that arise when taking the linear limit of odd elasticity. Linear elasticity assumes that the displacement gradient tensor $\operatorname{grad}\mathbf{u}$ is assumed to be very small, say of order ε. In this limit, the stress tensors may be described by a linear approximation:

$$\boldsymbol{\sigma} = \boldsymbol{\sigma}^0 + \mathbf{C}^{\mathrm{C}} : \operatorname{grad}\mathbf{u} + \mathcal{O}\left(\varepsilon^2\right) \tag{2.113}$$

$$\mathbf{S} = \mathbf{S}^0 + \mathbf{C}^{\mathrm{PK}} : \operatorname{grad}\mathbf{u} + \mathcal{O}\left(\varepsilon^2\right) \tag{2.114}$$

Here, $\boldsymbol{\sigma}^0$ and $\mathbf{S}^0$ are stresses present prior to deformation (pre-stresses), and $\mathbf{C}^{\mathrm{C}} = C^{\mathrm{C}}_{ijkl}\mathbf{r}^i \otimes \mathbf{r}^j \otimes \mathbf{r}^k \otimes \mathbf{r}^l$ and $\mathbf{C}^{\mathrm{PK}} = C^{\mathrm{PK}}_{ijkl}\mathbf{r}^i \otimes \mathbf{r}^j \otimes \mathbf{r}^k \otimes \mathbf{r}^l$ are known as elastic modulus tensors. The elastic modulus tensor is compatible with a potential energy if and only if:

$$C^{\mathrm{PK}}_{ijkl} = C^{\mathrm{PK}}_{klij} \tag{2.115}$$

which is the *major symmetry* of the elastic modulus tensor. The presence of this major symmetry is also referred to as Maxwell-Betti reciprocity.

Notice that Eq. (2.115) is stated in terms of the tensor relating strain to the Piola-Kirchhoff stress. Often, one is interested in the Cauchy stress, since this stress is defined without respect to a reference coordinate system. One can convert between the two types of

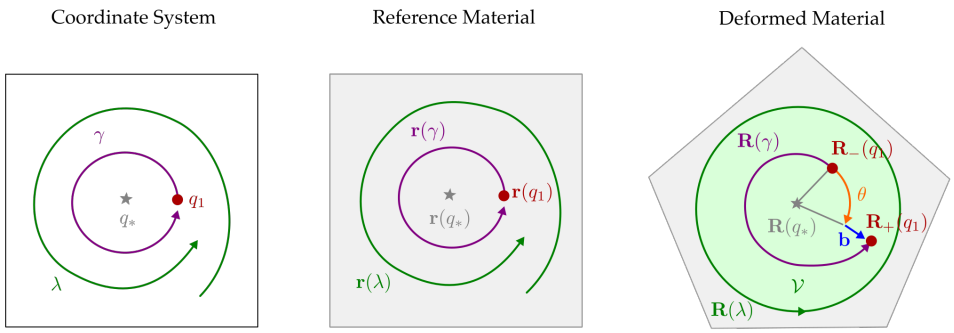

Figure 2.14: **Geometric properties of disclinations and dislocations.** An illustration of the dislocation angle θ and Burgers vector $\mathbf{b}$, as well as the contours used in §2.7.6. Adapted from Braverman et al. [2021].

elastic modulus tensors according to the formula:

$$C^{\mathrm{PK}}_{ijkl} = C^{\mathrm{C}}_{ijkl} + \sigma^0_{ij} g_{kl} - \sigma^0_{kj} g_{li} + \mathcal{O}\left(\epsilon^2\right) \tag{2.116}$$

In terms of the matrix notation used in §2.1, Maxwell-Betti reciprocity corresponds to $(C^{\mathrm{PK}})^{\alpha\beta} = (C^{\mathrm{PK}})^{\beta\alpha}$ where $(C^{\mathrm{PK}})^{\alpha\beta} = \frac{1}{2}\tau^\alpha_{ij}(C^{\mathrm{PK}})^{ijmn}\tau^\beta_{mn}$ and is related to $(C^{\mathrm{PK}})^{\alpha\beta}$ via

$$(C^{\mathrm{PK}})^{\alpha\beta} = (C^{\mathrm{C}})^{\alpha\beta} + \begin{pmatrix} \sigma^0_0 & -\sigma^1_0 & -\sigma^2_0 & -\sigma^3_0 \\ \sigma^1_0 & \sigma^0_0 & \sigma^3_0 & -\sigma^2_0 \\ \sigma^2_0 & -\sigma^3_0 & -\sigma^0_0 & -\sigma^1_0 \\ \sigma^3_0 & \sigma^2_0 & \sigma^1_0 & -\sigma^0_0 \end{pmatrix} \tag{2.117}$$

With our conventions, $\sigma^0_0 = -2p_0$ and $\sigma^1_0 = -2\tau_0$ where τ_0 and p_0 are the ambient torque and pressure. Notice that even an ambient constant torque is sufficient to give rise to odd elasticity, i.e. an antisymmetric contribution to $\mathbf{C}^{\mathrm{PK}}$.

2.7.6 Background on topological defects in elasticity

I now provide a geometric definition of the topological defects. The motivation is that the stress field $\boldsymbol{\sigma}$ only depends on the displacement gradient $\mathbf{J}$, or in even more restrictive cases,

on G_{ij}. Therefore, elasticity theory should only require that $\mathbf{J}$ (or G_{ij}) be continuous, not that the embedding $\mathbf{R}(q)$ be continuous. In that spirit, I will require the metric induced by the deformation, $G_{ij}(q)$, to be continuous and single valued everywhere except at a single point q_* representing the location of the topological defect. Given the value of $\mathbf{J}$ at a point q_1, the value of $\mathbf{J}$ at point q_2 is given by:

$$\mathbf{J}(q_2) = \exp\left(\int_\gamma \mathbf{r}_i \cdot \mathbf{\Pi}(q) \mathrm{d}q^i\right) \cdot \mathbf{J}(q_1), \tag{2.118}$$

where γ is the path through coordinate space connecting q_1 and q_2, the exponential is path ordered, and

$$\mathbf{\Pi} = \left(\mathbf{R}^n \cdot \frac{\partial \mathbf{R}_m}{\partial q^k} - \mathbf{r}_m \cdot \frac{\partial \mathbf{r}^n}{\partial q^k}\right) \mathbf{r}^k \mathbf{r}^m \mathbf{r}_n \tag{2.119}$$

see, e.g., Zubov [2008] for a derivation. (One can show that $\mathbf{\Pi}$ can be determined entirely in terms the metric $G_{ij}(q)$.) Since the deformed solid is embedded in the flat Cartesian plane, one imposes the compatibility constraint that $G_{ij}(q)$ have zero Riemann curvature. Subject to this compatibility condition, one can show that [Zubov, 2008]

$$\exp\left(\int_\gamma \mathbf{r}_i \cdot \mathbf{\Pi}(q) \mathrm{d}q^i\right) = \mathbf{1} \tag{2.120}$$

whenever γ is a closed loop that does not contain the defect q_*. If γ encloses the defect, then the integral takes the form:

$$\exp\left(\int_\gamma \mathbf{r}_i \cdot \mathbf{\Pi}(q) \mathrm{d}q^i\right) = e^{-\theta \boldsymbol{\epsilon}} \tag{2.121}$$

The right-hand side of Eq. (2.121) is a rotation matrix through angle θ representing the charge of a disinclination. The value of θ is independent of the precise path taken. Suppose $q_1 = q_2$ and let $\mathbf{J}_\pm$ represent $\mathbf{J}(q_1)$ as approached from the q_1 $(-)$ or q_2 $(+)$ side of γ.

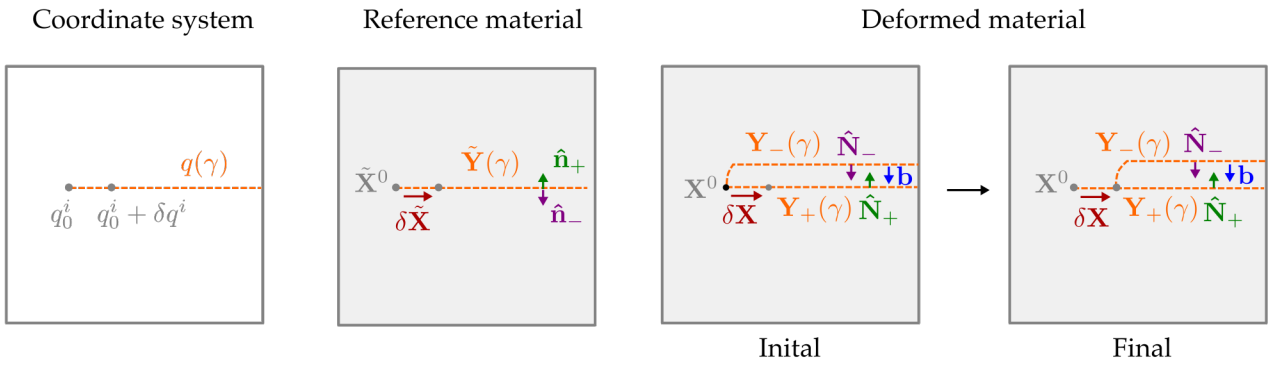

Figure 2.15: **Branch cuts for dislocation motion.** Illustration of the branch cut construction used in §2.7.7-2.7.8. Adapted from Braverman et al. [2021].

Then one has $\mathbf{J}_+ = e^{-\theta\boldsymbol{\epsilon}}\mathbf{J}_-$. Since $\mathbf{J}_\pm = \operatorname{grad}\mathbf{R}_\pm$, one has $\mathbf{R}_+ = e^{-i\theta\boldsymbol{\epsilon}} \cdot \mathbf{R}_- + \mathbf{b}$, where $\mathbf{b}$ is a constant translation known as the Burgers vector. See Fig. 2.14 for an illustration. The angle θ defines the charge of a disinclination and the vector $\mathbf{b}$ defines the charge of a dislocation. For small strains, the dislocations and disclinations the topological charges may be expressed in terms of the displacement field as given in Eqs. (2.66-2.65).

2.7.7 Peach-Koehler force

Here I provide a derivation of the Peach-Koehler formula in two dimensions. Suppose that an isolated dislocation with Burgers vector $\mathbf{b}$ is subjected to a smooth external Piola-Kirchhoff stress $\mathbf{S}^{(\mathrm{pre})}$ satisfying the equations for static equilibrium $\operatorname{div}\mathbf{S}^{(\mathrm{pre})} = 0$. One seeks to compute the work δW associated with moving the dislocation infinitesimally from the point q_0^i to the point $q_0^i + \delta q^i$ in coordinate space, see Fig. 2.15. In the reference material, the dislocation starts at position $\tilde{\mathbf{X}^0} = \mathbf{r}(q_0)$ and moves by an amount $\delta\tilde{\mathbf{X}} = \mathbf{r}_i\delta q^i$. I define a contour in coordinate space $q^i(\gamma)$ such that $\tilde{\mathbf{Y}}(\gamma) = \mathbf{r}[q(\gamma)] = \tilde{\mathbf{X}}^0 + \gamma\delta\tilde{\mathbf{X}}$. Before the dislocation moves, the displacement field $\mathbf{u}$ has a discontinuity $\mathbf{b}$ across the entire branch cut $\gamma \in [0, \infty)$. After the dislocation moves, the displacement field is continuous across the contour for $\gamma \in [0, 1)$, but retains the discontinuity for $\gamma \in [1, \infty)$. Let $\delta\mathbf{u}$ be the change in

the displacement field. The work done by the external stress $\mathbf{S}^{(\mathrm{pre})}$ is

$$\delta W = -\int_{\mathcal{A}} \mathbf{S}^{(\mathrm{pre})} : \operatorname{grad} \delta\mathbf{u} \, \mathrm{d}^2 r \tag{2.122}$$

$$= -\int_{\mathcal{A}} \operatorname{div}(\mathbf{S}^{(\mathrm{pre})} \cdot \delta\mathbf{u}) \mathrm{d}^2 r \tag{2.123}$$

$$= -\int_{\partial A} \hat{\mathbf{n}} \cdot \mathbf{S} \cdot \delta\mathbf{u} \, \mathrm{d}\ell \tag{2.124}$$

Between Eq. (2.122) and Eq. (2.123), I used the fact that $\operatorname{div} \mathbf{S}^{(\mathrm{pre})} = 0$ and then Stokes' theorem was applied. Here $\mathcal{A}$ is taken to be all of space, and $\partial\mathcal{A}$ crucially consists of two oppositely oriented surfaces lying along the branch cut $\mathbf{Y}$. As shown in Fig. 2.15, I will denote the normal vector and displacement field on either side of the branch cut by $\hat{\mathbf{n}}_\pm$ and $\mathbf{u}_\pm$, respectively. Thus I have:

$$\delta W = \int_{\gamma>0} [\hat{\mathbf{n}}_+ \cdot \mathbf{S}^{(\mathrm{pre})} \cdot \delta\mathbf{u}_+ + \hat{\mathbf{n}}_- \cdot \mathbf{S}^{(\mathrm{pre})} \cdot \delta\mathbf{u}_-] \, \mathrm{d}\ell \tag{2.125}$$

$$= \int_{\gamma>0} \hat{\mathbf{n}}_+ \cdot \mathbf{S}^{(\mathrm{pre})} \cdot [\mathbf{b}\theta(\gamma - 1) - \mathbf{b}] \, \mathrm{d}\ell \tag{2.126}$$

$$= -\int_{\gamma\in(0,1]} \hat{\mathbf{n}}_+ \cdot \mathbf{S}^{(\mathrm{pre})} \cdot \mathbf{b} \, \mathrm{d}\ell \tag{2.127}$$

Where $\theta(x)$ is the Heaviside function passing from 0 to 1 at $x = 0$. I have used the facts that $\hat{\mathbf{n}}_+ = -\hat{\mathbf{n}}_-$ and that $\mathbf{u}_+ - \mathbf{u}_- = \mathbf{b}$ when the displacement field is discontinuous. Finally assuming that $\mathbf{S}^{(\mathrm{pre})}$ is continuous near the dislocation, one may approximate the infinitesimal integral as $\int_{\gamma\in(0,1]} \mathrm{d}\ell \approx \delta\tilde{X}$. Moreover, by construction $\hat{\mathbf{n}} = \boldsymbol{\epsilon} \cdot \delta\tilde{\mathbf{X}}/\delta\tilde{X}$. Therefore,

$$\delta W \approx \delta\tilde{\mathbf{X}} \cdot \boldsymbol{\epsilon} \cdot \mathbf{S}^{(\mathrm{pre})} \cdot \mathbf{b} \tag{2.128}$$

Hence, one may express the work as $\delta W = \delta\tilde{\mathbf{X}} \cdot \tilde{\mathbf{f}}^{\mathrm{PK}}$, where $\tilde{\mathbf{f}}^{\mathrm{PK}}$ is the Peach-Koehler force on the dislocation with respect to the undeformed material. It is given by:

$$\tilde{\mathbf{f}}^{\mathrm{PK}} = \boldsymbol{\epsilon} \cdot \mathbf{S}^{(\mathrm{pre})} \cdot \mathbf{b} \tag{2.129}$$

Note that $\delta\tilde{\mathbf{X}}$ is the motion of the dislocation in the reference material. The motion of the dislocation in the deformed material is given by $\delta\mathbf{X} = \mathbf{R}_i \delta q^i = \mathbf{J}^T \cdot \delta\tilde{\mathbf{X}}$. Therefore, one has:

$$\delta W = \delta\mathbf{X} \cdot \mathbf{J}^{-1} \cdot \boldsymbol{\epsilon} \cdot \mathbf{S}^{(\mathrm{pre})} \cdot \mathbf{b} = \delta\mathbf{X} \cdot \boldsymbol{\epsilon} \cdot \boldsymbol{\sigma}^{(\mathrm{pre})} \cdot \mathbf{b} \tag{2.130}$$

where I have used the identities $-\boldsymbol{\epsilon} \cdot \mathbf{J}^{-1} \cdot \boldsymbol{\epsilon} = \frac{1}{J}\mathbf{J}^T$ and $\boldsymbol{\sigma} = \frac{1}{J}\mathbf{J}^T \cdot \mathbf{S}$. Thus I identify

$$\mathbf{f}^{\mathrm{PK}} = \boldsymbol{\epsilon} \cdot \boldsymbol{\sigma}^{(\mathrm{pre})} \cdot \mathbf{b} \tag{2.131}$$

as the Peach-Koehler force with respect to the motion $\delta\mathbf{X}$ in the deformed material. Notice first that the Peach-Koehler force is agnostic to the elasticity of the solid and relies only on the expression for the virtual work and the definition of a dislocation. Secondly, the Peach-Koehler force is conservative in the sense that its curl vanishes:

$$\operatorname{curl} \tilde{\mathbf{f}}^{\mathrm{PK}} = -\operatorname{div} \mathbf{S}^{(\mathrm{pre})} \cdot \mathbf{b} = 0 \tag{2.132}$$

$$\operatorname{Curl} \mathbf{f}^{\mathrm{PK}} = -\operatorname{Div} \boldsymbol{\sigma}^{(\mathrm{pre})} \cdot \mathbf{b} = 0 \tag{2.133}$$

where I have used the assumption that $\operatorname{div} \mathbf{S}^{(\mathrm{pre})} = 0$, the fact that $\operatorname{div} \mathbf{S} = 0$ implies $\operatorname{Div} \boldsymbol{\sigma} = 0$, and the definition $\operatorname{Curl} \boldsymbol{\Phi} = \operatorname{Div} \boldsymbol{\epsilon} \cdot \boldsymbol{\Phi}$ and $\operatorname{curl} \boldsymbol{\Phi} = \operatorname{div} \boldsymbol{\epsilon} \cdot \boldsymbol{\Phi}$.

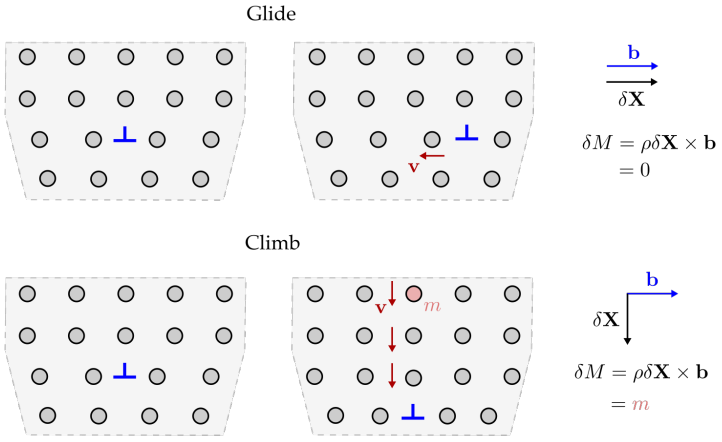

Figure 2.16: **Glide constraints on dislocations.** An illustration of the kinematic constraints that restrict dislocation motion to lie along the glide plane. When a dislocation glides, the total mass (i.e. number of particles) within the selected region does not change and the motion is localized to the particles near the core. (In this realization $\mathbf{v}$ is the velocity of the particle with the most motion during the rearrangement.) However, when the dislocation climbs, significant motion extends all the way out to the boundary of the sample since a column of particles moves downward. The net change in mass of the highlighted region is $\delta M = \rho \delta \mathbf{X} \times \mathbf{b} = m$, where $\mathbf{b} = \hat{\mathbf{x}} a$ is the Burgers vector, $\delta \mathbf{X} = -\hat{\mathbf{y}} a$ is the motion of the dislocation, m is the mass of the particle, $\rho = m/a^2$ is the density, and a is the lattice spacing. Adapted from Braverman et al. [2021].

2.7.8 Mass conservation constraint

Dislocations are fractons: they are constrained to move along their glide planes. This constraint arises from microscopic considerations regarding how a large number of discrete particles would have to slide past each other in order for the dislocation to move transverse to its glide plane. Nonetheless, the constraint can be enforced entirely in the continuum field theory by imposing a mass conservation condition. In analogy to §2.7.7 consider a dislocation that moves from $\delta\tilde{\mathbf{X}}$ to $\tilde{\mathbf{X}} + \delta\tilde{\mathbf{X}}$ in the reference material. The change in mass associated with a fixed region in real space reads:

$$\delta M = \int_{\partial \mathcal{A}} \rho \, \hat{\mathbf{N}} \cdot \delta \mathbf{u} \, \mathrm{d}L \tag{2.134}$$

where ρ is the density in physical space, and $\mathcal{A}$ is the patch of material coinciding with the region of real space prior to the motion of the dislocation. I will take $\partial\mathcal{A}$ to have two contributions, a physical boundary $\mathcal{D}$ and well as the boundary along the branch cut $q^i(\gamma)$ as introduced in §2.7.7. Thus one may write:

$$\delta M = \int_{\mathcal{D}} \rho\, \hat{\mathbf{N}} \cdot \delta\mathbf{u}\, \mathrm{d}L + \int_{\gamma>0} \rho\, [\hat{\mathbf{N}}_+ \cdot \delta\mathbf{u}_+ + \hat{\mathbf{N}}_- \cdot \delta\mathbf{u}_-]\, \mathrm{d}L \tag{2.135}$$

$$= \int_{\mathcal{D}} \rho\, \hat{\mathbf{N}} \cdot \delta\mathbf{u}\, \mathrm{d}L + \int_{\gamma>0} \rho_0\, [\hat{\mathbf{n}}_+ \cdot \mathbf{J}^{-T} \cdot \delta\mathbf{u}_+ + \hat{\mathbf{n}}_- \cdot \mathbf{J}^{-T} \cdot \delta\mathbf{u}_-]\, \mathrm{d}\ell \tag{2.136}$$

$$= \int_{\mathcal{D}} \rho\, \hat{\mathbf{N}} \cdot \delta\mathbf{u}\, \mathrm{d}L + \rho_0\, \delta\tilde{\mathbf{X}} \cdot \boldsymbol{\epsilon} \cdot \mathbf{J}^{-T} \cdot \mathbf{b} \tag{2.137}$$

In Eq. (2.136) $\rho_0 = J\rho$ is the density in the reference material, and I have used the fact that $\hat{\mathbf{N}}\, \mathrm{d}L = J\mathbf{J}^{-1} \cdot \hat{\mathbf{n}}\, \mathrm{d}\ell$. To arrive at Eq. (2.137), I have used the branch cut argument from §2.7.7 along with the fact that $\mathbf{J}$ is continuous across the branch cut for a dislocation. The first term Eq. (2.137) captures the change in material due to the macroscopic flow through the boundary. Now I make a crucial kinematical assumption: this macroscopic mass flow must be the entire mass flow. This statement implies that when the dislocation moves, the microscopic particle velocities are only discontinuous at the core, and not along an arbitrary contour located a macroscopic distance away from the core. In practice, it is typically safe to assume that the dominant mode of dislocation motion does not require microscopic rearrangements to be coordinated over arbitrarily large macroscopic distances. See Fig. 2.16 for an illustration. This assumption implies

$$\delta\tilde{\mathbf{X}} \cdot \boldsymbol{\epsilon} \cdot \mathbf{J}^{-T} \cdot \mathbf{b} = 0 \tag{2.138}$$

Recalling that the dislocation motion in real space is given by $\delta\mathbf{X} = \mathbf{J}^T \cdot \delta\tilde{\mathbf{X}}$, the constraint may be written as:

$$\delta\mathbf{X} \cdot \boldsymbol{\epsilon} \cdot \mathbf{b} = 0. \tag{2.139}$$

Notice that $\mathbf{J}^T \cdot \mathbf{b}$ points along the glide plane in material space. Hence Eq. (2.138) and Eq. (2.1382) are equivalent statements that the dislocation moves parallel to the glide plane.

CHAPTER 3

SPIKING AT THE EDGE

3.1 Motivation and overview

A spike is a large nonlinear excursion in a dynamical system followed by a time of latency known as the refractory period. Protecting the ability to spike is crucial for a wide range of biological functions, from cardiac pacemaking [Winfree, 1994a, Bers, 2002, ten Tusscher et al., 2004a, Cheng et al., 1993, Stern, 1992, Witkowski et al., 1998] to neural information processing [Rieke et al., 1997], while in other contexts, such as forest fires [Drossel and Schwabl, 1992] and disease outbreaks [Anderson and May, 1979, Murray et al., 1986, Anderson et al., 1981, Rohani et al., 1999], spiking must be avoided. In a spatially extended medium, the ability to spike gives rise to distinctive spatiotemporal patterns [Kondo and Miura, 2010, Bourret et al., 1969, Loose et al., 2008, Tompkins et al., 2014, Rotermund et al., 1990, Steinbock et al., 1995a, Vinson et al., 1997, Fuseya et al., 2021, Tan et al., 2020, Winfree, 1994b] appearing in processes ranging from morphogenesis [Turing, 1952, Nakamasu et al., 2009, Kondo and Asai, 1995, Newman and Frisch, 1979, Mitchell et al., 2022, Wigbers et al., 2021, Di Talia and Vergassola, 2022, Vergassola et al., 2018, Lechleiter et al., 1991, Michaux et al., 2018, Chang and Ferrell Jr, 2013] to spiral waves observed in electrograms of the heart [Davidenko et al., 1992, Gray et al., 1998, Fenton et al., 2002]. While analytical studies have revealed important features of excitable media whose properties are spatially homogeneous [Halatek and Frey, 2018, Cross and Hohenberg, 1993, Kim et al., 2001, Brauns et al., 2020, Alonso et al., 2003], less is understood about abrupt heterogeneities such as sample edges or interfaces [McNamara et al., 2020, Eckstein et al., 2020, Vidal-Henriquez et al., 2017, Ni and Wei, 1995, Bub et al., 2002a, Mainen and Sejnowski, 1996, Wigbers et al., 2020, Brauns et al., 2021, Bub et al., 2002b, Agladze et al., 1994, Staddon et al., 2022, Luther et al., 2011]. In this chapter, adapted from Scheibner et al. [2023], I address the

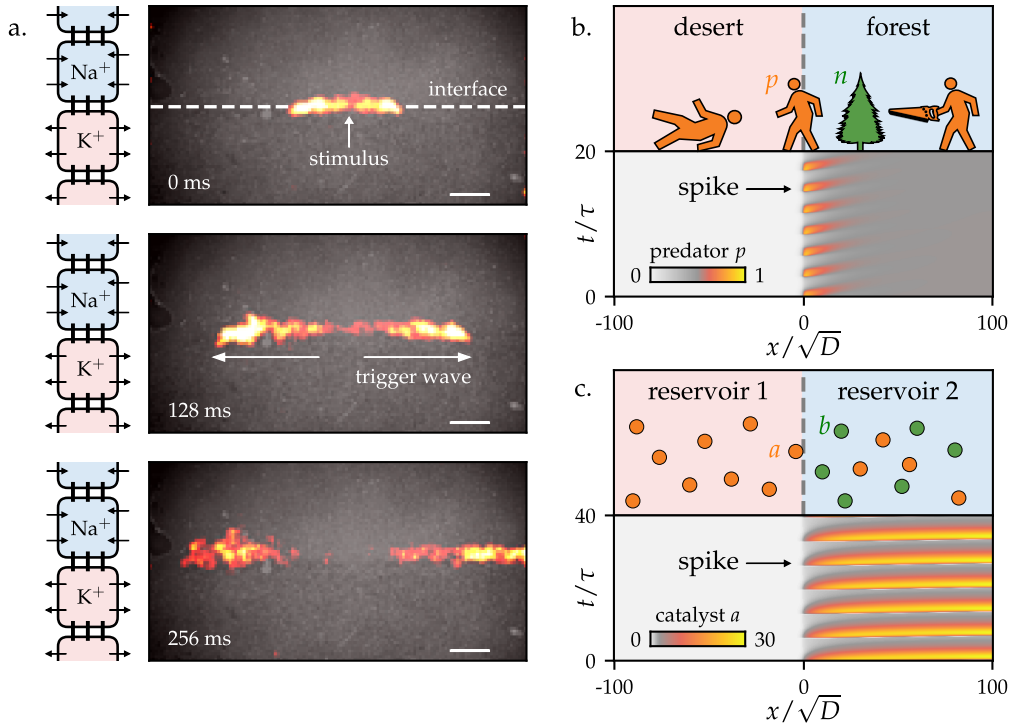

Figure 3.1: **Edge spiking in electrophysiology, population dynamics, and chemistry. a.** Experiments from Ref. [Ori et al., 2023] in which an action potential propagates along a tissue interface, as revealed by a voltage sensitive red dye. Scale bar 1 mm. The left column shows a schematic vertical cross-section of the interface: the top tissue features sodium ion channels (inward arrows), while the bottom tissue features potassium ion channels (outward arrows). The vertical lines represent gap junction coupling between the cells. **b.** A fast diffusing predator (lumberjacks) and relatively immobile prey (trees) are described by an interfacial Lotka-volterra model [Eqs. (3.3-3.4)]. A kymograph generated by the model reveals spikes in the lumberjack population generated at the interface. **c.** An interface between two chemical reservoirs, neither of which are capable of oscillating, is described by Eqs. (3.10-3.11). A kymograph of the fast, mobile catalyst a reveals repeated spikes generated at the interface. Adapted from Scheibner et al. [2023].

role of spatial segregation of nonlinear processes. As is often the case with wave mechanics, edges and interfaces can have properties that differ qualitatively from those of the bulk medium [Murugan and Vaikuntanathan, 2017, Kane and Lubensky, 2014, Hasan and Kane, 2010, Shankar et al., 2022, ge Chen et al., 2014, Mao and Lubensky, 2018, Huber, 2016].

For instance, Fig. 3.1a shows a recent experiment in which human embryonic kidney (HEK293) cells were genetically modified to express either sodium ($Na_V1.5$) or potassium ($K_{ir}2.1$) channels [Ori et al., 2023]. Usually, a cell containing both potassium and sodium

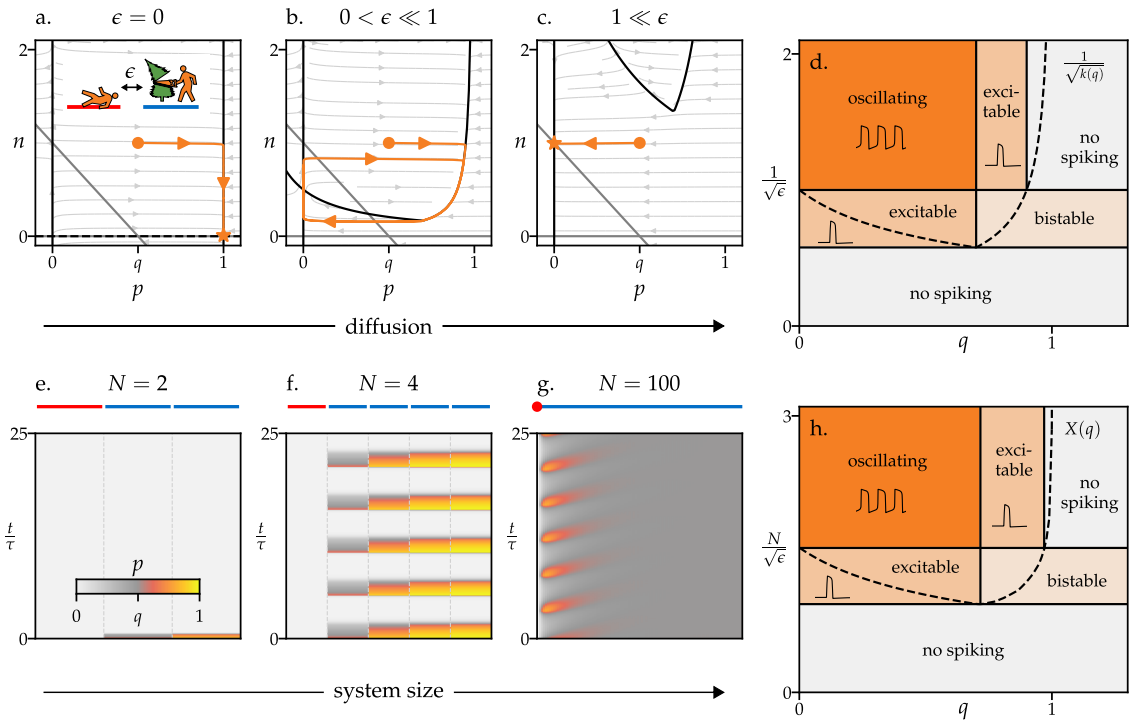

Figure 3.2: **Spikes induced by weak diffusion and large system size. a.** (inset) A predator-prey system with a desert (red) and a forest (blue) described by Eqs. (3.1-3.2). In the forest, the predators (lumberjacks, p) consume the prey (trees, n) with predation rate $1/q$. The predators cross from the forest to the desert (and subsequently perish) with hopping rate ϵ. **a-c.** Three phase portraits, for $\epsilon = 0$, $0 < \epsilon \ll 1$, and $1 \ll \epsilon$, illustrate the role of diffusion across a boundary: For $\epsilon = 0$ (a), the lumberjacks reach their carrying capacity and the trees go extinct. For $\epsilon \gg 1$ (c), the lumberjacks go extinct and the trees reach their carrying capacity. Spikes can only occur in the intermediate range $0 < \epsilon \ll 1$ (b), in which the effective death rate due to hopping is present but not overpowering. Orange curves are example trajectories. The $\dot{p} = 0$ and $\dot{n} = 0$ nullclines are denoted by black and grey lines, respectively. **d.** A phase diagram for Eqs. (3.1-3.2) summarizes the possible behaviors: if the lumberjack hopping rate ϵ is too large, the lumberjack population cannot spike. The phase boundaries are determined by the consumption nonlinearity $k(q)$ in Eqs. (3.1-3.2). **e-g.** A chain of N forests (blue lines) are coupled to a desert (red line) by a large hopping rate $\epsilon = 4$. Kymographs for systems with $N = 2$, $N = 4$, and $N = 100$ exemplify a distinctive transition: oscillation onset is driven by increasing system size, even as ϵ is held constant. (See §3.4 for simulation details.) **h.** A phase diagram for Eqs. (3.3-3.4), applicable for $N \gg 1$, reveals a crucial distinction between the spatially and non-spatially extended systems: the vertical axis in (h) features $N/\sqrt{\epsilon}$, implying that spiking occurs for a much larger range of ϵ in the spatially extended limit. The curve $X(q)$ determines the locations of the phase boundaries and is given in Eq. (3.20). Adapted from Scheibner et al. [2023].

channels spikes via the following mechanism, which is representative of excitable systems: The potassium channels favor a low membrane potential while the sodium channels favor a high membrane potential. Given a suitably large voltage stimulation, the membrane potential (a fast variable) spikes upward towards the value set by the sodium channels. The sodium channels then gradually shut due to open-state inactivation (a slow variable), causing the membrane potential to fall towards the value set by the potassium channels. The sodium channels then take some time to recover their strength (the refractory period). Because the competition between the two channels is essential, neither sodium nor potassium channels alone are sufficient for an individual cell to spike. Furthermore, even when both channels coexist in a single cell, spikes only occur when they have the appropriate ratio of open-state conductances (i.e. channel strengths).

Something visually striking happens when two distinct and non-excitable tissues (composed of the two cell types) are placed in contact and weakly coupled by gap junctions, which allow voltage diffusion. When stimulated at the interface, a voltage spike (i.e. an action potential) emerges and robustly propagates along the interface, see Fig. 3.1a. Crucially, these interfacial spikes persist for a much wider range of open-state conductances than for a single cell [Ori et al., 2023]. This observation suggests that spikes generated at an interface may have a distinct, and possibly more robust, dynamical origin than those in a homogenized system. Here, I reveal the underlying dynamical mechanism behind this phenomenon and demonstrate that it is not limited to electrophysiology. For instance, I provide examples from population dynamics (Fig. 3.1b) in which a fast, mobile predator (lumberjacks) consume a slow, sedentary prey (trees) while diffusing across an environmental (forest-desert) boundary; and from chemical reaction networks in which a fast catalyst diffuses between two chemically distinct reservoirs (Fig. 3.1c). In all these examples, the interfacial spiking does not result from merely superimposing the two halves. In fact, coupling the two halves too strongly can destroy spiking.

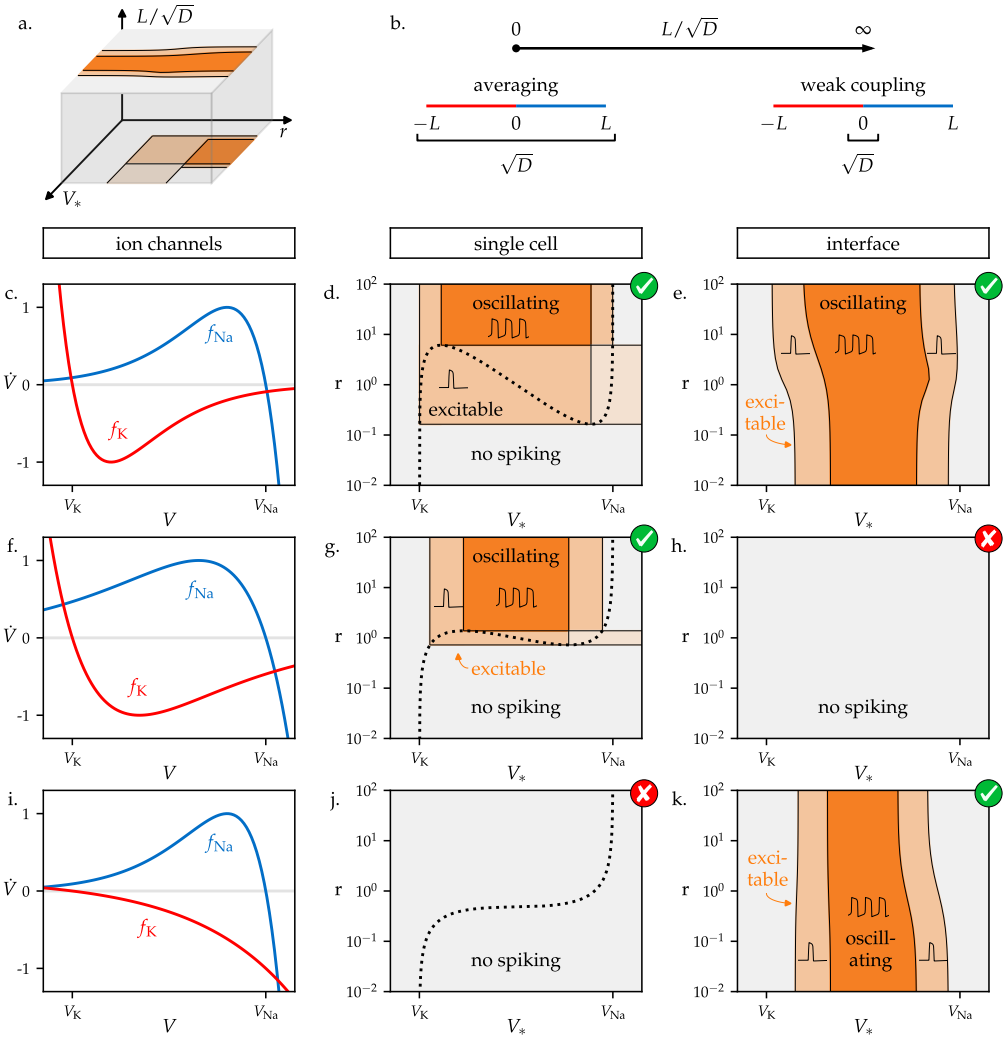

Figure 3.3: **A spiking interface is more than the sum of its parts.** **a.** A spiking phase diagram is shown for the bioelectric interface in Eqs. (3.5-3.6). Here, $L/\sqrt{D}$ is the ratio of the system size to the diffusion strength and r and V_* appear in $h_\infty(V) = r\,\Theta(V_* - V)$. The parameter r is the ratio of the amplifier (sodium channel) strength to the suppressor (potassium channel) strength. **b.** At small $L/\sqrt{D}$, diffusion forces the membrane potential to be approximately constant across the entire tissue, creating an effective single cell with both ion channels. For large $L/\sqrt{D}$, the coupling is weak, so the dynamics are spatially heterogeneous. **c-k.** A table comparing the $L/\sqrt{D} \to 0$ (single cell) and the $L/\sqrt{D} \to \infty$ (interfacial) limits. The left column (c, f, i) shows three examples of voltage-current curves for potassium (red) and sodium (blue) ion channels. Their reversal potentials are denoted V_K and V_{Na}, respectively. Adapted from Scheibner et al. [2023].

3.1.1 The role of spatial extent

The basic notion of an edge spike involves two distinct processes: transport across two domains and transport within the domains themselves. To illustrate the former, consider a two-compartment model of predator-prey dynamics shown in Fig. 3.2a (inset). The model features a population p of lumberjacks (the predators) that consumes a population n of trees (the prey). The rightmost compartment, the forest (blue bar), acts as a lumberjack amplifier in which tree consumption elevates the lumberjack population. By contrast, the desert (red bar), is an infinitely strong suppressor in which any lumberjack that enters dies instantly. Lumberjacks from the forest wander into the adjacent desert with a hopping rate ϵ. The populations evolve according to the following Lotka-Volterra equation:

$$\dot{p} = -\epsilon\, p + n\, p\, r(p) \tag{3.1}$$

$$\dot{n} = \frac{n}{\tau}\left(1 - n - \frac{p}{q}\right) \tag{3.2}$$

where $1/q$ is the predation rate, $\tau \gg 1$ is a long time scale implying that the tree population changes slowly, and $r(p)$ is a nonlinearity that encodes a lumberjack carrying capacity. A normalization has been chosen so that all variables in Eq. (3.1-3.2) are dimensionless and the carrying capacities of the lumberjacks and trees are set to 1, see §3.4. Here, the lumberjack population plays the same role as the cell-membrane potential in the electrophysiology experiment (a fast, diffusing variable), the tree population corresponds to the gating variable of the sodium channels (an immobile, slow variable), while the desert and the forest correspond to cells with potassium and sodium channels, respectively.

In this model, the ability to spike depends sensitively on the hopping rate ϵ. If $\epsilon = 0$ (a), the two halves are decoupled and the lumberjack population cannot spike: the lumberjacks will quickly return to their carrying capacity regardless of the perturbation. However, when ϵ is small but nonzero (b), the dynamics change dramatically: The lumberjacks can now spike

because the motion into the desert depletes the lumberjack population when trees are sparse and tree consumption overpowers diffusion when trees are abundant. Crucially, though, when ϵ becomes too large (c), the desert and forest become well mixed, and the lumberjack population cannot spike because the suppressor (desert) is infinitely strong. In the two-compartment model described by Eq. (3.3-3.4), the hopping rate ϵ can be reinterpreted as an effective suppression strength: even though the desert itself is infinitely strong, the finite entrance rate attenuates its effect. The phase diagram in Fig. 3.2d illustrates a basic mechanism: an amplifier and a suppressor need to be suitably well balanced for spikes to occur—attenuating a strong suppressor through weak diffusion across an interface helps achieve this balance.

Yet, this simplified model lacks a basic feature: the forest itself can be spatially extended. In Fig. 3.2e-g the desert is now connected to a chain of N compartments comprising the forest, each of which is coupled to its neighbors by a hopping rate ϵ. The size of the forest dramatically influences the dynamics. When $N = 2$ and $\epsilon = 4$, the lumberjacks rapidly go extinct in all compartments (e). Yet, when $N = 4$, the lumberjack population not only begins to survive, but undergoes large oscillations (f). A window into the relationship between N and ϵ can be obtained in the large N limit (g,h). In this limit, the dynamics can be described by a continuum reaction-diffusion equation

$$\dot{p} = D\nabla^2 p + n\, p\, r(p) \tag{3.3}$$

$$\dot{n} = \frac{n}{\tau}\left(1 - n - \frac{p}{q}\right) \tag{3.4}$$

where $L = Nd$ is the system size and d is the lattice spacing [1]. The parameter $D = \epsilon\, d^2$ denotes the diffusion coefficient times the characteristic time scale used to nondimensionalize

1. Notice that Eqs. (3.3-3.4) do not contain advective transport, which has also been shown to give rise oscillations near Dirichlet boundaries, for example in models of and experiments on *Dictyostelium discoideum* [Eckstein et al., 2020, Vidal-Henriquez et al., 2017].

ϵ (see §3.4). The lumberjack population obeys the following boundary conditions: $\partial_x p = 0$ at $x = L$ and, because of the infinitely strong desert, $p = 0$ at $x = 0$. The basic effect of spatial extent can be obtained by dimensional analysis: Only $\sqrt{D}$ and L have units of length, so any change in qualitative behavior must depend on the dimensionless ratio $L/\sqrt{D} = N/\sqrt{\epsilon}$. Therefore, in the continuum, increasing N is equivalent to decreasing ϵ. This collapse is physically consequential because the diffusion D is an intrinsic property of the material while L is an extrinsic property, so the two can often be tuned independently. Notably, by increasing L a system can support spiking over a wider range of D [2].

3.1.2 A spiking phase diagram

The dynamics is even richer when the suppressor (e.g. the desert) is no longer infinitely strong. In this case, the Dirichlet boundary becomes an interface, and spikes can arise both in the limit $L/\sqrt{D} \to 0$ and $L/\sqrt{D} \to \infty$. To illustrate this behavior, I consider a one-dimensional (1D) model for the electrophysiology experiment of [Ori et al., 2023] which takes the form of an interfacial Fitzhugh-Nagumo equation [FitzHugh, 1961]:

$$\dot{V} = D\nabla^2 V + \begin{cases} f_{\mathrm{K}}(V) & x \in [-L, 0] \\ h\, f_{\mathrm{Na}}(V) & x \in (0, L] \end{cases} \tag{3.5}$$

$$\dot{h} = \frac{h_\infty(V) - h}{\tau} \tag{3.6}$$

Here, x is the coordinate transverse to the interface (see Fig. 3.1a), V is the voltage, and $f_{\mathrm{K}}(V)$ and $f_{\mathrm{Na}}(V)$ capture the effect of the potassium and sodium channels, respectively. The sodium channels are modulated by a gating variable h that slowly approaches the

2. For simplicity, in this example I am using the same hopping rate ϵ within the forest as between the forest and desert. This distinction becomes irrelevant in the continuum limit (large ϵ and large N), because this subextensive heterogeneity is absorbed into the Dirichlet boundary condition at an edge or into the continuity requirements across an interface.

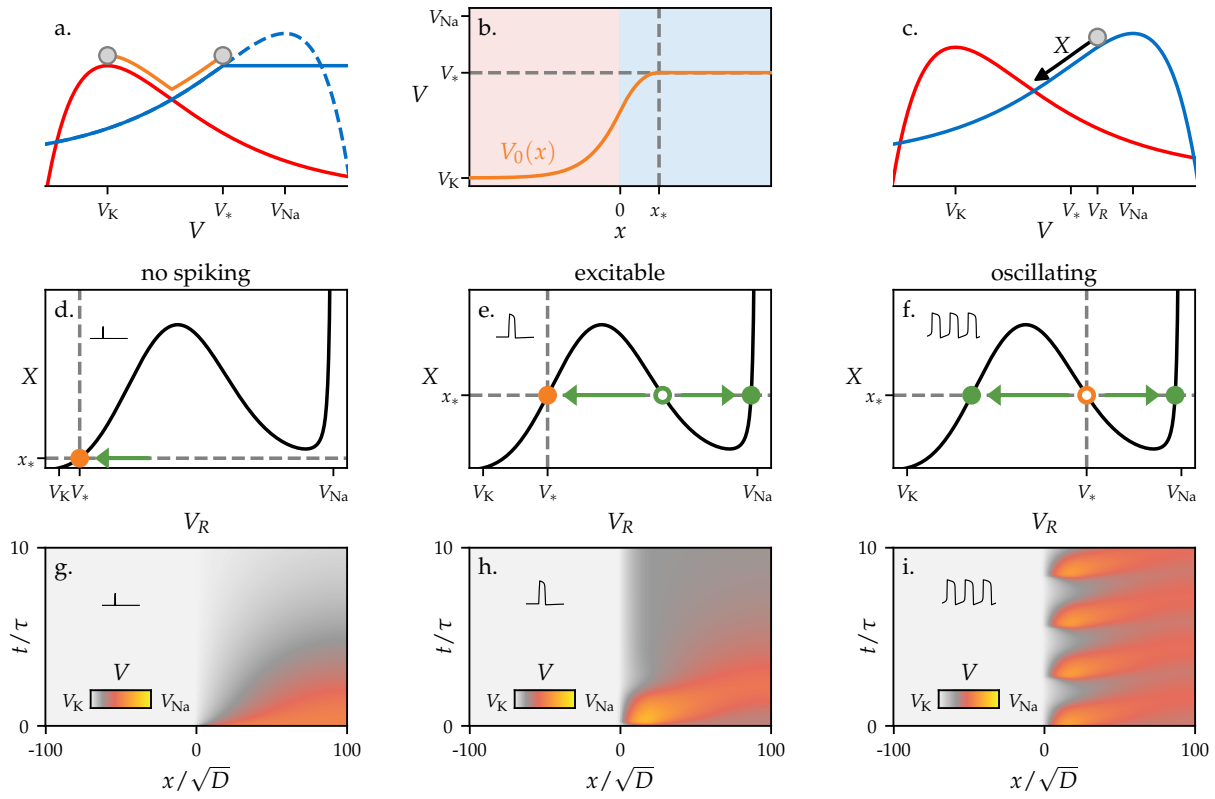

Figure 3.4: **A geometric construction for interfacial spiking. a.** Starting from Eqs. (3.5-3.6), the antiderivatives of $f_{\mathrm{K}}(V)$ (solid red line) and $h_\infty(V)f_{\mathrm{Na}}(V)$ (solid blue line) are visualized as hills. The dashed blue line is the antiderivative of $rf_{\mathrm{Na}}(V)$. To construct the stationary solution with no-flux boundary conditions, consider letting a ball roll from the top of one hill to the other (orange curve). **b.** The stationary voltage solution $V_0(x)$ in space corresponds to the trajectory of a ball (in time) rolling across the potentials in (a). **c.** The ability to spike is determined by the number and stability of critical points of Φ in Eq. (3.9). To determine the critical points, release a ball from a voltage V_R and measure the "time" X it takes to reach the intersection. **d.** A plot of X vs. V_R reveals three cases. When x_* intersects X once, the interface is unable to spike. **e.** When x_* intersects X three times and V_* corresponds to an increasing branch of X, the interface is excitable. **f.** When x_* intersects 3 times and V_* corresponds to the decreasing branch, the voltage at the interface oscillates. **g.-h.** Kymographs illustrating no spiking, excitability, and oscillating at the interface. See Appendix 3.8 for simulation details. Adapted from Scheibner et al. [2023].

function $h_\infty(V)$ on a long time scale τ. The term $D\nabla^2 V$ arises from direct cell-to-cell current flow via gap junctions. Like the predator prey system, a normalization is chosen such that the quantities $\sqrt{D}$ and x have units of length, while all others are dimensionless (see §3.5). The system is modeled by no-flux boundary conditions at both ends, $\partial_x V\big|_{\pm L} = 0$, while the

voltage V and its first derivative $\partial_x V$ are required to be continuous across the interface.

The gating switch $h_\infty(V)$ is reasonably well approximated by a step function $h_\infty(V) = r\,\Theta(V_* - V)$, where Θ is a Heaviside step function and V_* is a crossover voltage that turns off the sodium channels [ten Tusscher et al., 2004a]. The parameter r is the ratio of the open-state conductances of the sodium to the potassium ion channels. Therefore, r can be interpreted as the relative strength of the amplifier (sodium) and suppressor (potassium). When $r \ll 1$, the potassium ion channels are so strong that the interface effective becomes a Dirichlet boundary of the type considered in the predator-prey system. When $r \gg 1$, both sides of the interface are dynamic.

In Fig. 3.3a-b, I sketch a three dimensional phase diagram spanned by the parameters $L/\sqrt{D}$, V_*, and r. When $L/\sqrt{D} \to 0$, diffusion forces the voltage to be approximately constant across the entire system, so one can think of the system as an effective single cell with both ion channels. By contrast, when $L/\sqrt{D} \to \infty$, the coupling is weak and the spatial heterogeneity plays a crucial role. To illustrate the independence of these two limits, in Fig. 3.3c-k I consider three different realizations of f_{Na} and f_{K} [Xu et al., 2020, Payandeh et al., 2011]. For each realization, I show two cross-sections of the phase diagram: one for $L/\sqrt{D} \to 0$ and one for $L/\sqrt{D} \to \infty$. Fig. 3.3d-f shows an example of ion channels for which the effective single cell ($L/\sqrt{D} \to 0$) exhibits spikes but the weakly coupled interface ($L/\sqrt{D} \to \infty$) does not. Moreover, Fig. 3.3g-i shows an example in which the interface exhibits spikes for all values of r, yet no ratio of the amplifier and suppressor give rise to spiking in a single cell.

3.1.3 Overview of mathematical structure

In both the interfacial and boundary systems, the presence of spikes is associated with topologically robust features of the underlying dynamical system governed by their respective

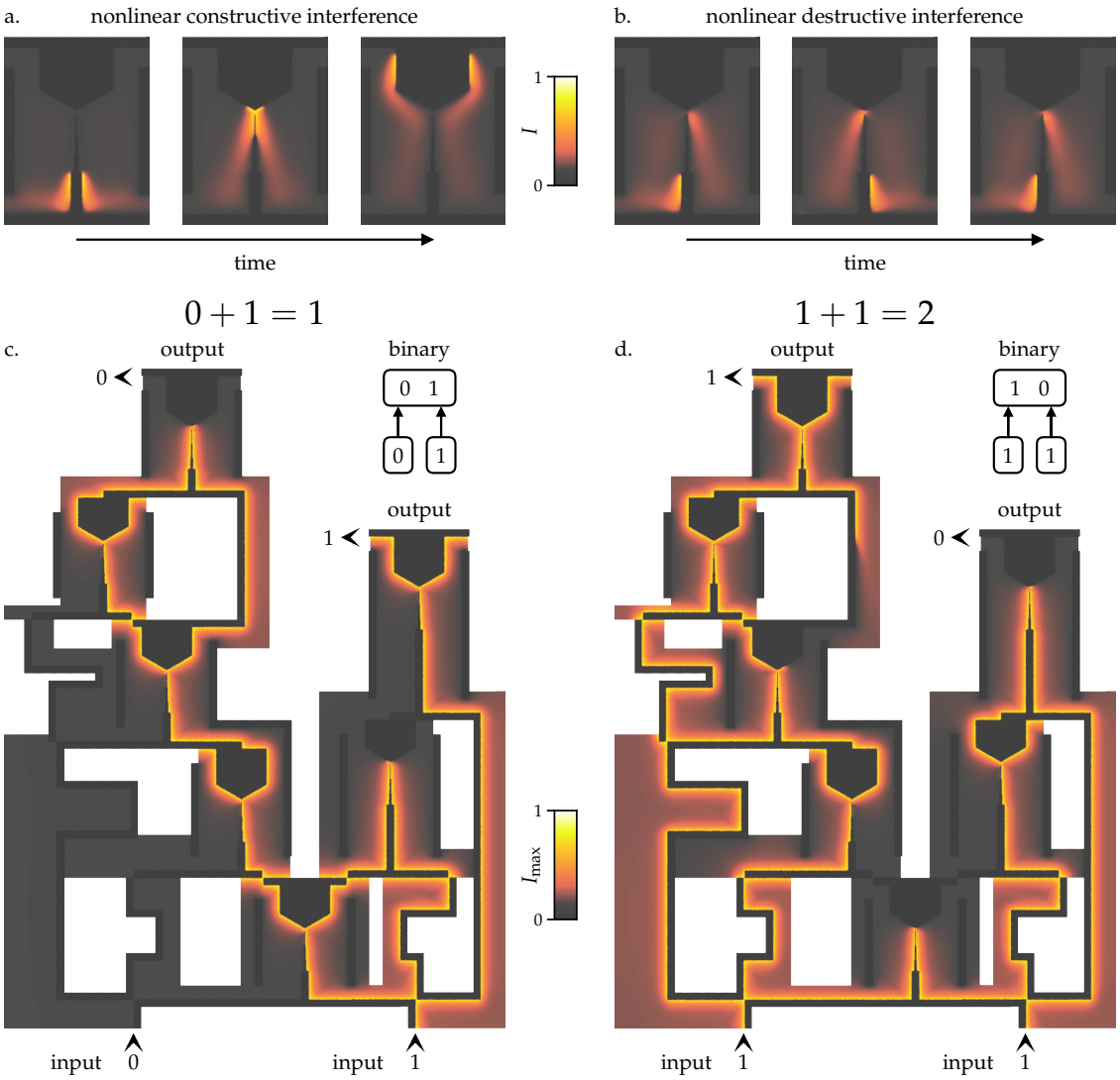

Figure 3.5: **Nonlinear waveguides from interfacial spiking.** **a-b.** Two distinct non-spiking materials (light and dark grey) are patterned for form a four way junction of excitable interfaces. When two nonlinear wave trains arrive at a junction in-phase (a), they propagate through uninterrupted. When the two wave trains arrive out-of-phase, they annihilate at the junction. The color corresponds to the intensity I of the fast, diffusively coupled variable. **c-d.** A network of excitable interfaces acts as a binary half adder, which takes the sum of two 0 or 1 inputs. Here, the presence of a wave indicates the value 1 while the absence of a wave indicates the value 0. The color $I_{\max}$ is the maximum value of I over time when the network has reached steady state. See §3.7.1-3.7.2 and Appendix 3.8 for simulation details. Adapted from Scheibner et al. [2023].

reaction-diffusion equations. Both Eqs. (3.3-3.4) and Eqs. (3.5-3.6) take the form

$$\dot{A} = D\nabla^2 A + f(A, B, x) \tag{3.7}$$

$$\dot{B} = \frac{1}{\tau} g(A, B) \tag{3.8}$$

where $A(x,t)$ is a fast field and $B(x,t)$ is a slow field. I will call $[A_0(x), B_0(x)]$ a stationary solution of Eqs. (3.7-3.8) if they satisfy $\dot{A} = \dot{B} = 0$. Each stationary solution comes paired with a functional Φ:

$$\Phi[A] = \int D(\partial_x A)^2 - U(A,x)\,\mathrm{d}x \tag{3.9}$$

where $U(A,x) = \int_0^A f(A', B_0(x), x)\,\mathrm{d}A'$. The meaning of Φ is as follows. If the system is prepared at the stationary solution and the variable A is perturbed, then on short time scales $\dot{A} \approx -\delta\Phi/\delta A$.

The number of stationary solutions and the critical points of their associated functionals encode the ability of a system to spike. For instance, suppose Eqs. (3.7-3.8) permit only one stationary solution, $[A_0(x), B_0(x)]$, and the associated functional Φ only has one minimum [namely $A_0(x)$]. Then the system will not exhibit spikes because any perturbation to $A(x)$ quickly relaxes to $A_0(x)$. However, if Φ permits a second minimum $A_1(x)$ in addition to $A_0(x)$, then the system is excitable: suitable perturbations to A will push the system into the basin of attraction of $A_1(x)$, and only on longer times ($t \propto \tau$), will the system return to $A_0(x)$. Oscillations (i.e. repeated spikes) occur when $A_0(x)$ itself is a saddle, rather than a minimum, of Φ. The number of critical points and their unstable dimensions are topologically robust quantities: these integers are unchanged under sufficiently small, generic perturbations to Eqs. (3.7-3.8).

For certain models, such as the electrophysiology equations (3.5-3.6) in the experimentally relevant limit of $h_\infty(V) = r\Theta(V_* - V)$, the stationary solutions and associated critical points are captured by a relatively simple geometric construction. The stationary solution for the membrane potential $V_0(x)$ is constructed as follows: first draw potentials for $f_{\mathrm{K}}(V)$ (red) and $h_\infty(V) f_{\mathrm{Na}}(V)$ (blue) and align their maxima as shown in Fig. 3.4a. Treating these as hills, let a ball roll from the top of one hill to the other. The trajectory of the ball in time corresponds to the voltage profile $V_0(x)$ in space (Fig. 3.4b). As I show in §3.5, the existence of spiking

at the interface is determined by an auxiliary function $X(V)$ defined in Fig. 3.4c: Place the ball at an arbitrary voltage V_R and let it roll down the blue hill. The function $X(V_R)$ is the amount of time it takes for the ball to reach the intersection. Each solution to the equation $X(V_*) = X(V)$ constitutes a critical point of $\Phi(V)$. Whenever $X(V_*) = X(V)$ has multiple solutions, the system exhibits spikes. As shown in Fig. 3.4d-f, the precise form of the spikes (excitable vs oscillatory) depends on whether the solution $V_0(x)$ is stable (excitable) or unstable (oscillatory). Using homological techniques from Conley index theory [Conley and Smoller, 1983, Mischaikow and Mrozek, 2002], I show in §3.3 that the decreasing branch of $X(V)$ must always be unstable, while the increasing branches are stable. The function $X(V)$ can be thought of as the high dimensional counterpart of the dashed lines, h_{eq}, in Figs. 3.3d,g,j that determine the phase diagrams for a single cell. An analogous function $X(q)$ demarcates the phase boundaries for the predator-prey diagram shown in Fig. 3.2h, see §3.3.

3.1.4 Spiking mode transition

So far, I have considered bulk media that alone cannot spike, but exhibit excitability or oscillations when a boundary or interface is introduced. Now I show that boundaries or interfaces can cause conversions between different modes of spiking. As illustrated in Fig. 3.1c, consider two chemical reservoirs separated by a semi-permeable membrane. The reaction in the right chamber ($x > 0$) contains two catalysts with concentrations $a(x,t)$ and $b(x,t)$ that evolve according to the Oregonator model of the celebrated Belousov-Zhabotinsky reaction [Tyson, 1976]. I assume that the catalyst a is free to diffuse across the interface, while the catalyst b is relatively immobile. In the left reservoir, the catalyst a is rapidly converted into a product that exits the reaction. Starting from a minimal chemical reaction network and applying the

law of mass action (see §3.6), I derive the following dynamical equations:

$$\dot{a} = D\nabla^2 a + \begin{cases} -a & x < 0 \\ 2m_1 b - a\left[b_\infty(a) + m_2\right] & x > 0 \end{cases} \tag{3.10}$$

$$\dot{b} = \frac{b_\infty(a) - b}{\tau} \tag{3.11}$$

where m_1 and m_2 are parameters set by internal rate constants, and $b_\infty(a)$ is a monotonically decaying function given in Eq. (3.95). For sufficiently large m_1 and small m_2, neither of the reservoirs alone can oscillate. The kymograph in Fig. 3.1c shows that allowing catalyst a to diffuse between the two reservoirs creates spontaneous oscillations at the interface. However, unlike the previous examples (predator-prey and electrophysiology), the chamber on the right alone is excitable (though not oscillatory) even without the interface (see Fig. 3.13). The presence of excitability for $x > 0$ changes a qualitative feature of the oscillations: the interfacial spikes are no longer spatially localized. Instead of dying off at large x (as in Fig. 3.1b), the spikes generated at the interface propagate at constant amplitude to the far away boundary (see Fig. 3.1c). Oscillations at chemical interfaces have been reported previously, but they often rely on a distinct mechanism in which chemicals mix at the interface to reach locally suitable conditions for oscillations [Budroni et al., 2016, Dúzs et al., 2019]. Interfacial spiking, for example using gels or other tailored chemistry [Semenov et al., 2016, Yoshida, 2010, Rabai et al., 1989, Testa et al., 2021], may serve as a promising alternative technique for spatial control of chemical reactions because the two reservoirs can remain distinct indefinitely.

3.1.5 Trigger waves along 2D interfaces

In two dimensions, an interface is a 1D line. If the interface is excitable, then the 1D line can host nonlinear waves called trigger waves, as illustrated by the bioelectric experiments

in Fig. 3.1a. The conditions for propagation as well as the unique wave speed of these trigger waves are discussed in §3.7.1. Geometric primitives, such as curves, corners, and junctions, can then be used to control the nonlinear wave propagation. For instance, Fig. 3.5a-b shows a four-way junction formed by patterning two different materials (light and dark grey). In panel (a), two trigger waves approach the junction from below. Since the trigger waves are in phase they interfere constructively and pass through the junction. However, when the pulses are sent periodically with a phase lag (b), no pulse passes through due to overlap in their refractory periods. Since the trigger waves are nonlinear, constructive interference results in outgoing waves that have the same amplitude as the incoming waves (rather than twice the amplitude). This modification to the superposition principle can form the basis of more complex devices, such as those capable of computation [Adamatzky et al., 2005, Holley et al., 2011, Tóth and Showalter, 1995, Steinbock et al., 1995b]. As an illustration, Figure 3.5c-d shows a two-dimensional (2D) surface patterned by two materials obeying equations of the form of Eqs. (3.5-3.6). The network of excitable interfaces forms an effective circuit that computes the sum of two binary numbers (see §3.7.2 for additional minimal logic gates, such as AND, OR, and NOT gates). Since only diffusion is required at the boundary, interfacial excitability is potentially useful as a form of wave control that does not require electronics, additional materials, or the fabrication precision necessary to explicitly construct a narrow channel or wire.

3.2 Spike generation in fast-slow systems without spatial extent

Here I review examples of spike generation in fast-slow systems without spatial extent. Consider equations of the form

$$\dot{A} = f(A, B) \tag{3.12}$$

$$\dot{B} = \frac{1}{\tau} g(A, B) \tag{3.13}$$

and assume that $\tau \gg 1$, which implies that A is a fast variable and B is a slow variable. Figure 3.6a (top) shows two curves known as nullclines, which are defined by $\dot{A} = 0$ (black) and $\dot{B} = 0$ (grey). The intersection of the nullclines (solid orange circle), denoted (A_0, B_0), is a fixed point of Eqs. (3.12-3.13). If an external stimulus (light blue arrow) pushes A across a threshold value (open green circle), A will evolve along the solid green line towards a high value (solid green circle) while B remains approximately constant. Over a longer period of time, known as the refractory period, A and B will move along the dashed orange line back towards their rest position (solid orange circle). This is an example of an excitable system, in which the fast variable A needs to be stimulated above a critical threshold in order to undergo a spike. Figure 3.6a (bottom) shows an equivalent description of the spike: when initially perturbed, A will evolve according to $\dot{A} = -\partial_A U$, where $\partial_A U(A) = -f(A, B_0)$. From this perspective, the system is excitable because U has a minimum (solid green circle) other than the one at A_0 (solid orange circle).

Figure 3.6b shows a similar example where the fixed point (A_0, B_0) is unstable. Since the global fixed point is unstable, this system contains a limit cycle denoted by the dashed orange line. Such a system exhibits repeated spikes even in absence of external stimulation, which I refer to as oscillation or pacemaking. In the following sections, I use an analogous fast-slow decomposition in a high-dimensional setting to identify spiking in reaction-diffusion equations, where the potential U is replaced by a functional Φ of the spatially extended fields.

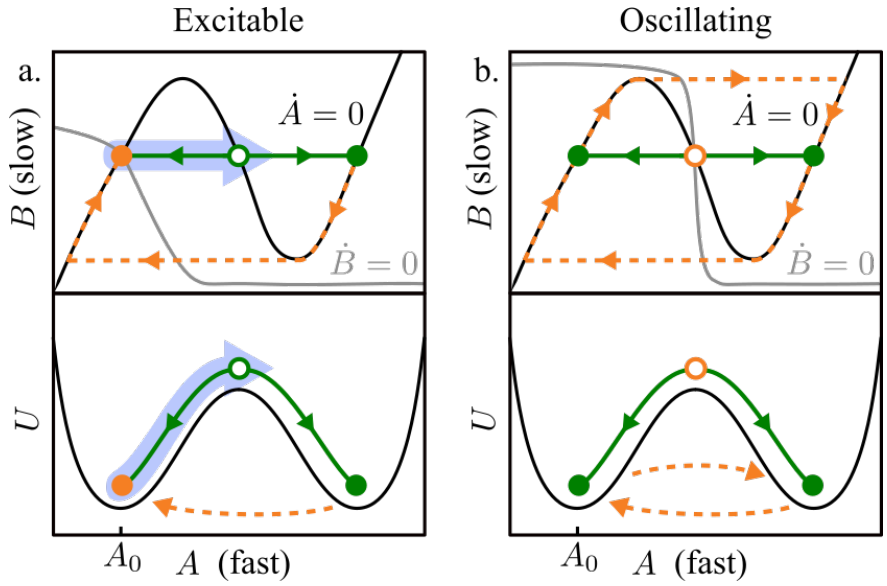

Figure 3.6: **Spike generation in fast-slow systems without spatial extent. a.** (top) A phase portrait of an excitable fast-slow system. The black curve corresponds to $\dot{A} = 0$, and the grey curve corresponds to $\dot{B} = 0$. The light blue arrow represents an external perturbation. The solid green curves are the fast trajectory, and the dashed orange curve is the refractory period. The solid orange circle denotes the global fixed point. The open (closed) green circle represents an unstable (stable) fixed point of the fast dynamics. (bottom) On short time scales, the potential $U(A)$ governs the dynamics. The system is excitable since $U(A)$ has multiple minima. **b.** (top) A phase portrait of a fast-slow system exhibiting oscillations. The dashed orange curve is a limit cycle. The open orange circle denotes an unstable global fixed point. The closed green circles are stable fixed points of the fast dynamics if initialized at the open orange circle. (bottom) On short time scales, the potential $U(A)$ governs the dynamics. The system is exhibits oscillations since since $U(A)$ has multiple minima and the orange circle (global fixed point) is not one of them. Adapted from Scheibner et al. [2023].

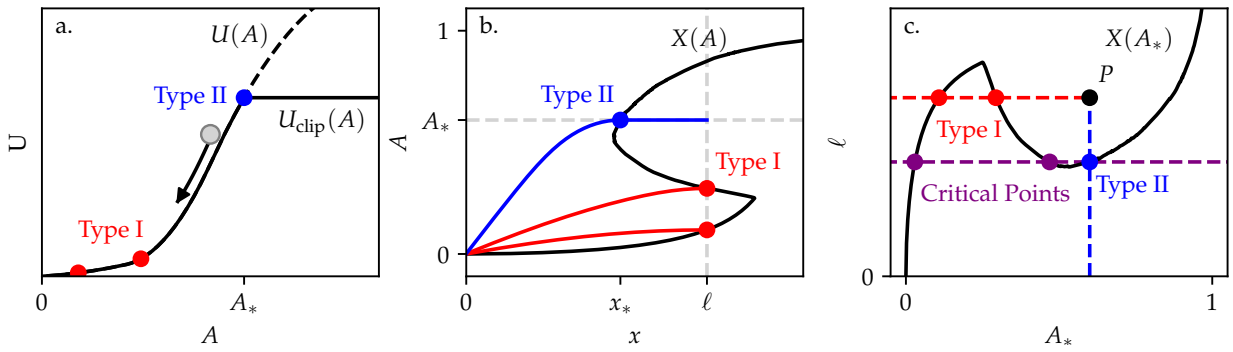

Figure 3.7: **Stationary solutions and critical points. a.** The potentials $U(A)$ and $U_{\text{clip}}(A)$ are depicted by dashed and solid lines, respectively. The red points correspond to type I stationary solutions that lie along the non-clipped part of the potential. The blue point corresponds to a type II stationary solution, which lies at the point A_*. The grey circle symbolizes a ball moving this 1D potential. If released from rest at either of the red points, the ball will take a "time" ℓ to reach $A = 0$. If the ball is released from the blue point, it will take a "time" $X(A_*)$ to reach the origin. **b.** The stationary solutions are plotted in real space. Type I solutions intersect the curve $X(A)$ along the $x = \ell$ boundary and type II solutions intersect the curve $X(A)$ along the $A = A_*$ boundary. **c.** The (A_*, ℓ) parameter space is shown, with $X(A_*)$ plotted. A specific choice of parameters corresponds to a point P. Type I stationary solutions lie along the dashed red line, while type II lie along the dashed blue line. The critical points associated with the blue stationary solution are indicated with purple circles. Adapted from Scheibner et al. [2023].

3.3 Phase diagram for spiking at a Dirichlet boundary

3.3.1 General Setting

Here I derive the phase diagram featured in Fig. 3.2h. The equations considered take the form:

$$\dot{A} = \nabla^2 A + B\tilde{f}(A) \tag{3.14}$$

$$\dot{B} = \frac{1}{\tau} g(A, B) \tag{3.15}$$

Notice that Eqs. (3.14-3.15) are a specialization of Eqs. (3.7-3.8) with $f(A, B, x) = B\tilde{f}(A)$. I will assume that $\tilde{f}(A) > 0$ for $A \in [0, 1)$ and that $\tilde{f}$ crosses zero at $A = 1$. Moreover, I will assume that there is a function $0 \leq B_\infty(A) \leq 1$ such that $g(A, B) < 0$ whenever

$B_\infty(A) < B < 1$ and $g(A, B) > 0$ whenever $0 < B < B_\infty(A)$. I will require the boundary conditions $A(0) = 0$ and $\partial_x A\big|_\ell = 0$. Here $\ell = L/\sqrt{D}$ is the nondimensionalized system size. I will assume that the maximum value of $\tilde{f}$ and g are of order 1 and that $\tau \gg 1$, implying that B is a slow variable. As I will illustrate with examples in subsequent sections, this form is general enough to capture a wide range of dynamical systems through suitable variable changes.

The calculations below comprise the following steps: I first find the fixed points of Eqs. (3.14-3.15), which I refer to as stationary solutions. Setting $\dot{B} = 0$ in Eq. (3.15) yields $B = B_\infty(A)$, and then setting $\dot{A} = 0$ in Eq. (3.14) yields the following ordinary differential equation for A:

$$\nabla^2 A = -B_\infty(A)\frac{\mathrm{d}U}{\mathrm{d}A} \tag{3.16}$$

where U is an antiderivative of $\tilde{f}$. Suppose the system is initialized to a stationary solution, given by $A_0(x)$ and $B_0(x) = B_\infty(A_0(x))$, and suppose the fast field A is subject to a perturbation $A(x, t = 0) = A_0(x) + \delta A(x)$, where δA is not necessarily small. On short time scales, $B(x, t)$ will be frozen to $B_0(x)$ and A will evolve according to

$$\dot{A} = \nabla^2 A + B_0(x)\tilde{f}(A) = -\frac{\delta \Phi}{\delta A} \tag{3.17}$$

where

$$\Phi = \int_0^\ell [(\nabla A)^2 - B_0(x)U(A)]\mathrm{d}A. \tag{3.18}$$

Solutions to Eq. (3.17) with $\dot{A} = 0$ are critical points of Φ. Notice that $A_0(x)$ is always one of the critical points. I will make inferences about the qualitative behavior of Eqs. (3.14-3.15) using the structure of the stationary solutions, critical points, and orbits connecting them.

Examples of such inferences are as follows:

- Suppose that Eqs. (3.14-3.15) only permit one stationary solution, and this stationary solution is linearly stable. If the associated Φ has no additional critical points beyond $A_0(x)$, then the system cannot exhibit spikes because $A(x,t)$ will quickly return to $A_0(x)$ after any perturbation.

- Suppose that Eqs. (3.14-3.15) only permit one stationary solution, and this stationary solution is linearly stable. If Φ has stable critical points other than $A_0(x)$, then the system is excitable. Namely, if the initial trigger $\delta A(x)$ pushes the system into the basin of attraction of a second stable critical point, then $A(x,t)$ will be attracted to the second critical point on a fast time scale ($t \ll \tau$) and remain there for a long time ($t \propto \tau$) until the slow variable $B(x,t)$ begins to evolve. This constitutes a spike.

- Suppose that Eqs. (3.14-3.15) only permit one stationary solution, and this stationary solution is linearly unstable. Assuming chaotic behavior does not occur, the system will (generically) contain a limit cycle. The presence of this limit cycle corresponds to oscillatory activity.

- Equations (3.14-3.15) may have multiple stable stationary solutions. In this case, I refer to the dynamics as multistable.

In the next section, I specialize the form of $B_\infty(A)$ to allow for an analytical calculation of the stationary solutions and critical points, and thereby an analytical construction of a spiking phase diagram.

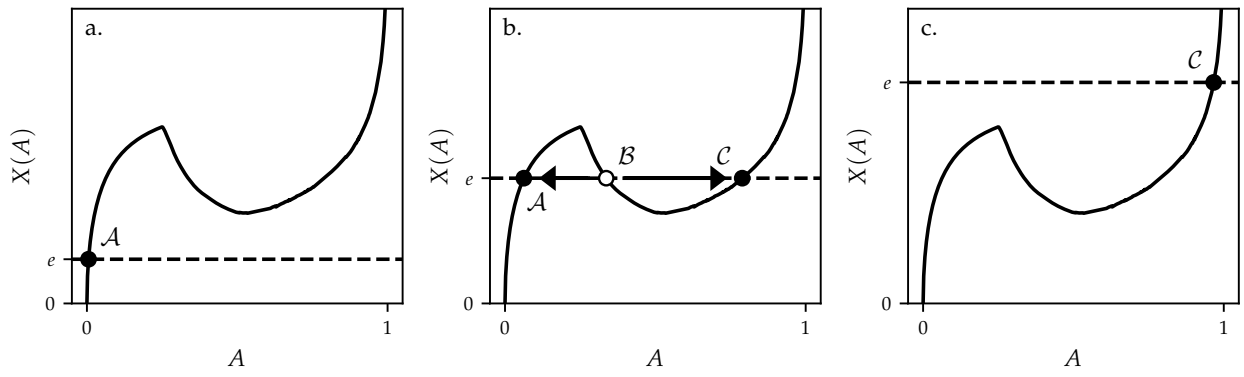

Figure 3.8: **Determining the stability of critical points.** The critical points of $\Phi(A; e)$ are shown for three values of e. **a.** At low e, there exists only one critical point, $\mathcal{A}$. **b.** At moderate e, there exist three critical points $\mathcal{A}$, $\mathcal{B}$, and $\mathcal{C}$. The solids arrows indicate heteroclinic orbits. **c.** At large e, only one critical point ($\mathcal{C}$) remains. Critical points $\mathcal{A}$ and $\mathcal{C}$ must be minima (i.e. unstable dimension of 0), while $\mathcal{B}$ has an unstable dimension of 1. Adapted from Scheibner et al. [2023].

3.3.2 Construction of the phase diagram

In this section, I specialize the form of $B_\infty(A)$ to $B_\infty(A) = \Theta(A_* - A)$, where Θ is the Heaviside step function. Then Eq. (3.16) becomes

$$\nabla^2 A = -\Theta(A_* - A)\frac{\mathrm{d}U}{\mathrm{d}A} = \frac{\mathrm{d}U_{\mathrm{clip}}}{\mathrm{d}A} \tag{3.19}$$

where $\frac{\mathrm{d}U_{\mathrm{clip}}}{\mathrm{d}A} = \Theta(A_* - A)\tilde{f}(A)$ defines a potential that has been clipped by the step function, see the solid black line in Fig. 3.7a. To construct solutions, notice that Eq. (3.19) is equivalent to the equation of motion for a ball moving in a 1D potential, where x corresponds to "time" and A corresponds to "position". The boundary condition $\partial_x A\big|_\ell = 0$ is the requirement that the ball is at rest at "time" ℓ. Likewise, the boundary condition $A(0) = 0$ is the requirement that the ball reaches "position" 0 at "time" 0. As shown in Fig. 3.7a, solutions to Eq. (3.19) can be constructed as follows: release the ball from rest at point A, allow it to move through the potential, and measure the amount of "time" it takes to reach point $A = 0$. If that "time" is equal to ℓ, then one will have constructed a valid solution to Eq. (3.19).

Fig. 3.7a demonstrates that there are two possible types of solutions. For type I (red),

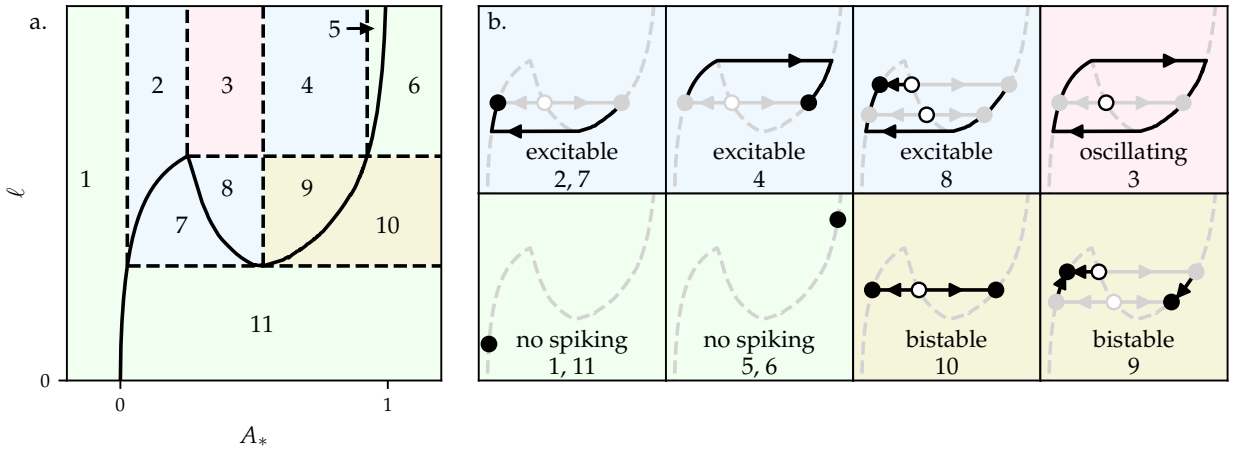

Figure 3.9: **Phase diagram for spiking at a Dirichlet boundary**. **a.** A phase diagram in the A_*-ℓ plane is divided into 11 distinct regions. The solid black curve is $X(A_*)$. The color code indicates the qualitative behavior. Green: no spiking; olive: bistable; blue: excitable; pink: oscillating. **b.** The qualitative behavior may be inferred from diagrams that summarize the topological features of the flow. In each diagram, the black circles represent stationary solutions, and the grey circles represent the critical points of the associated potentials. Solid circles are stable, and the open circles are unstable. The light grey lines represent heteroclinic orbits in the fast dynamics, and the black lines convey the evolution of the system on longer time scales. Adapted from Scheibner et al. [2023].

the ball is released along the non-clipped part of the potential ($A < A_*$). For type II, the ball is released at $A = A_*$: If the amount of "time" T it takes the ball to reach $A = 0$ is less than ℓ, then a valid solution can be constructed by letting the ball sit at rest on the flat part of the potential for a "time" $\ell - T$ before releasing it. In Fig. 3.7b, the two types of solutions are shown in real space.

To help count the number of solutions to Eq. (3.19), I introduce a function $X(A)$ that corresponds to the amount of "time" the ball takes to reach "position" 0 if released from "position" A. This is given by:

$$X(A) = \frac{1}{\sqrt{2}} \int_0^A \frac{1}{\sqrt{U(A) - U(a')}} \mathrm{d}a' \tag{3.20}$$

Fig. 3.7b-c show an example of $X(A)$ featuring one local maximum and one local minimum. Depending on the choice of $\tilde{f}(A)$, the function $X(A)$ can have many local maxima and

minima. Nevertheless, the assumptions that $\tilde{f}(1) = 0$ and $\tilde{f}(A) > 0$ for $A < 1$ imply that $X(A) > 0$, $X(0) = 0$ and $X(1) = \infty$. In terms of $X(A)$, type I and type II solutions correspond to the following:

Type I: If $a < A_*$ and $X(a) = \ell$, then there is a solution with $A(\ell) = a$. In this case, the stationary solution $A(x)$ is given by the inverse of:

$$x(A) = \frac{1}{\sqrt{2}} \int_0^A \frac{1}{\sqrt{U(a) - U(a')}} \mathrm{d}a' \tag{3.21}$$

Type II: Let $x_* = X(A_*)$. If $x_* < \ell$, then there is a solution with $A(\ell) = A_*$. In this case, the stationary solution $A(x)$ can be defined in a piecewise manner: $A(x) = A_*$ for $x \in [x_*, \ell]$; For $x < x_*$, $A(x)$ is the inverse of:

$$x(A) = \frac{1}{\sqrt{2}} \int_0^A \frac{1}{\sqrt{U(A_*) - U(a')}} \mathrm{d}a' \tag{3.22}$$

Now I can think of A_* and ℓ as being parameters of our dynamical system defined by Eqs. (3.14-3.15). Working in the A_*-ℓ plane, all the stationary solutions can be found by the graphical construction illustrated in Fig. 3.7c:

1. Represent a choice of parameters (A_*, ℓ) as a point P in the plane.
2. Draw the curve $X(A_*)$.
3. Draw a horizontal line extending to the left from P. The intersections between the horizontal line and $X(A_*)$ correspond to stationary solutions of type I.
4. Draw a vertical line extending downward from P. Intersections between the vertical line and $X(A_*)$ represent stationary solutions of type II.

This construction yields all the solutions to Eq. (3.19). Next, I derive the stability of the stationary solutions and their consequences for spiking. To do so, I will specialize to the

situation in which $X(A)$ is "N"-shaped, i.e. it has exactly one local maximum and one local minimum. I will use the following result: consider the functional

$$\Phi(A;e) = \int_0^e [(\nabla A)^2 - U(A)]\,\mathrm{d}x \tag{3.23}$$

which is minimized with respect to A subject to the boundary conditions $A(0) = 0$ and $\partial_x A\big|_e = 0$. Using a similar derivation to that above, one sees that the critical points of Φ correspond to the intersections between $X(a)$ and the horizontal line at e. As illustrated in Fig. 3.8a, for sufficiently small e, there is only one critical point (denoted $\mathcal{A}$) and therefore this critical point must be a minimum of Φ. As e increases (Fig. 3.8b), a bifurcation produces two new critical points, $\mathcal{B}$ and $\mathcal{C}$. As e increases further, $\mathcal{B}$ and $\mathcal{A}$ annihilate (Fig. 3.8c). Since $\mathcal{C}$ is now the lone remaining critical point, it must also be a minimum of Φ. Conley index theory states that two critical points that emerge or annihilate must have unstable dimensions that differ by 1 [Conley and Smoller, 1983]. Since the minima $\mathcal{A}$ and $\mathcal{C}$ have an unstable dimension of 0, the unstable dimension of $\mathcal{B}$ is 1. Moreover, the dynamical system $\dot{A} = -\frac{\delta\Phi}{\delta A}$ must have heteroclinic orbits from $\mathcal{B}$ to $\mathcal{A}$ and $\mathcal{B}$ to $\mathcal{C}$. (See Appendix 3.8 for a brief introduction to Conley index theory and a derivation of these facts.)

I now apply these facts to deduce the stability of the stationary solutions. For stationary solutions $A_0(x)$ of type I, $B_\infty(A_0(x)) = 1$. Therefore, the fast dynamics for a type I stationary solution are governed by the equation:

$$\dot{A} = \nabla^2 A + \frac{\mathrm{d}U}{\mathrm{d}A} = -\frac{\delta\Phi_{\mathrm{I}}}{\delta A}. \tag{3.24}$$

For stationary solutions $A_0(x)$ of type II, $B_\infty(A_0(x)) = \Theta(x - x_*)$, where $x_* = X(A_*)$. Hence, the fast dynamics are governed by the equation:

$$\dot{A} = \nabla^2 A + \Theta(x - x_*)\frac{\mathrm{d}U}{\mathrm{d}A} = -\frac{\delta\Phi_{\mathrm{II}}}{\delta A}. \tag{3.25}$$

Notice that the critical points of $\Phi_{\mathrm{I}}(A)$ and $\Phi_{\mathrm{II}}(A)$ can be put in correspondence with $\Phi(A;\ell)$ and $\Phi(A;x_*)$, respectively. Therefore, one can use the following graphical construction, illustrated in Fig. 3.7c, to find the critical points associated with each stationary solution:

1. Identify the point corresponding to the stationary solution of interest. (In Fig. 3.7c, the blue stationary solution is of interest.)

2. Draw a horizontal line in both directions out from the point. (Dashed purple line in Fig. 3.7c.)

3. The intersections between the horizontal line and $X(A_*)$ correspond to critical points. (The blue and purple points in Fig. 3.7c.)

4. The stability of each critical point is determined by which branch of $X(A_*)$ it lies on: those on an increasing branch are stable while those on a decreasing branch have an unstable dimension of 1.

Notice that all stationary solutions are also critical points of their associated potential. Occasionally, critical points of one stationary solution are also stationary solutions unto themselves.

These considerations allow us to construct the phase diagram shown in Fig. 3.9a. The parameter space has been divided into 11 regions based on the number of type I and type II stationary solutions, and the nature of their associated critical points. For each region, one can construct a corresponding diagram shown in Fig. 3.9b. In each diagram, the black circles denote stationary solutions while grey circles denote critical points that are not stationary solutions. Solid circles indicate stable stationary solutions/critical points, while open circles indicate unstable stationary solutions/critical points. The solid grey lines indicate heteroclinic orbits in the fast dynamics, while the solid black curves depict the evolution of the system over longer time scales.

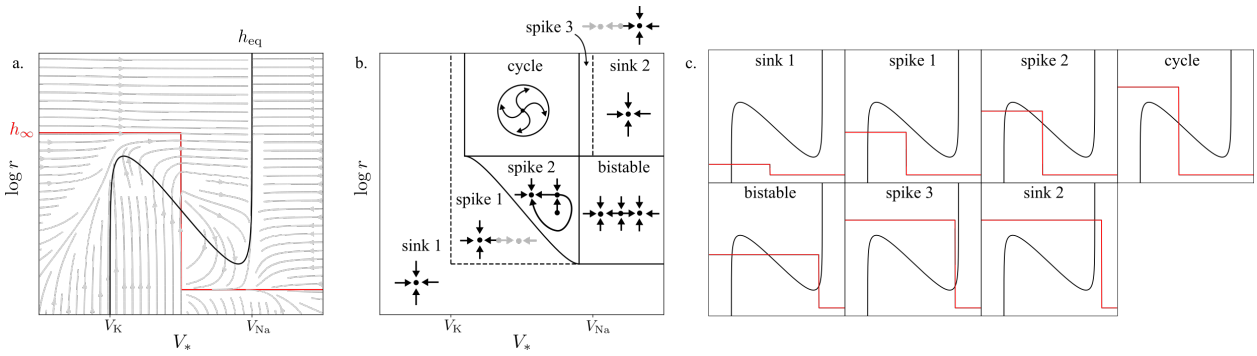

Figure 3.10: **A spiking phase diagram for a single bioelectric cell. a.** A representative phase portrait for Eqs. (3.54-3.55). The fixed point (here unstable) appears at the intersection h_{eq} (black) and h_∞ (red). **b.** An annotated phase diagram showing the fixed points, limit cycles, and heteroclinic orbits in each phase. The light grey points and arrows represent features that are only present in the $\tau \to \infty$ dynamics. **c.** The h_{eq} and h_∞ curves for each phase in the phase diagram. Adapted from Scheibner et al. [2023].

Using these diagrams, one can then classify distinct qualitative behaviors. Regions 1, 5, 6, and 11 are classified as no-spiking because they feature only one stationary solution, and the functional associated with that stationary solution has only one critical point. Regions 2, 4, 7, and 8 are classified as excitable because they have exactly one stable stationary solution, and the potential associated with this stationary solution has multiple stable critical points. Region 3 is classified as oscillating because it features only one stationary solution, and this stationary solution is unstable, and hence the system exhibits a limit cycle. Regions 9 and 10 are classified as bistable because they feature two stable stationary solutions.

Notice that this phase diagram differs slightly from the one shown in Fig. 3.2h, because $\tilde{f}$ in the lumberjack-tree setting has an additional zero at $A = 0$. It will be explained in the following section how the phase diagram in Fig. 3.9a is mapped onto the one for population dynamics in Fig. 3.2h.

3.4 Details on population dynamics model

In dimensionful units, the Lotka-Volterra model I consider takes the form [Murray, 2013]:

$$\dot{P} = -\,a\,P + b\,N\,(P+g)\,R_p(P) \tag{3.26}$$

$$\dot{N} = c\,N\,R_n(N) - d\,P\,N \tag{3.27}$$

where P is the population of the predator, N is the population of the prey, and $a, b, c, d, g > 0$. Here, a is the dimensionful hopping rate at which the lumberjacks (predator) travel into the desert and perish; b sets the benefit to the lumberjacks of consuming a tree; c is the growth rate of the trees; and d sets the intensity of the predation. The parameter g is a regularization parameter that prevents the lumberjacks from going extinct. I will eventually be interested in the limit $g \to 0$. The function $R_n(N)$ is a nonlinearity that sets the carrying capacity K_n for the prey in absence of predators. I require that $R_n(0) = 1$ and that R_n only crosses zero at K_n. Likewise, $R_p(P)$ obeys $R_p(0) = 1$ and only crosses zero at K_p, the carrying capacity of the predators.

I nondimensionalize Eqs. (3.26-3.27) by introducing a time scale $t_0 = 1/bK_n$ and defining

$$p = \frac{P}{K_p} \qquad n = \frac{N}{K_n} \tag{3.28}$$

$$\gamma = \frac{g}{K_p} \qquad \epsilon = at_0 \tag{3.29}$$

$$r(p) = R_p(pK_p) \qquad r_n(n) = R_n(nK_n) \tag{3.30}$$

$$\tau = \frac{1}{t_0 c} \qquad \tilde{t} = t/t_0 \tag{3.31}$$

$$q = \frac{1}{dK_p t_0} \tag{3.32}$$

yielding the equations:

$$\dot{p} = -\epsilon\, p + n\,(p+\gamma)\, r(p) \tag{3.33}$$

$$\dot{n} = \frac{n}{\tau}\left[r_n(n) - \frac{p}{q}\right] \tag{3.34}$$

in which all quantities are dimensionless. For the phase portraits in Fig. 3.2a-c, I use the following piecewise linear functions for $r_n(n)$ and $r(p)$:

$$r_n(n) = 1 - n \tag{3.35}$$

$$r(p) = \Theta(p_* - p)\left(\frac{p(n_* - 1)}{p_*} + 1\right) + \Theta(p - p_*)\frac{n_*(p-1)}{p_* - 1} \tag{3.36}$$

where $p_* = 0.7$ and $n_* = 3$. I use $\epsilon = 0$, 0.5, and 4.0 for panels a, b, and c respectively. For all panels I use $\tau = 50$ and $q = 0.5$.

Next, I detail the passage to the continuum shown in Fig. 3.2e-g. Consider a compartment model with local populations p_i and n_i, where $-N \le i \le N$. Here, a positive index i corresponds to the forest, and a non-positive i corresponds to the desert. The dynamics are governed by

$$\dot{p}_i = \epsilon(p_{i+1} - p_{i-1} - 2p_i) \tag{3.37}$$

$$+ \begin{cases} -\alpha p_i & -N \le i \le 0 \\ n_i(p_i + \gamma) r(p_i) & 1 \le i \le N \end{cases} \tag{3.38}$$

$$\dot{n}_i = \frac{n_i}{\tau}\left[r_n(n_i) - \frac{p_i}{q}\right] \tag{3.39}$$

with boundary conditions $p_{-N-1} \equiv p_{-N}$ and $p_{N+1} \equiv p_N$. As in Eq. (3.3), the parameter ϵ in Eq. (3.38) sets the hopping rate between sites. However, in Eq. (3.38) I allow the

desert to have an intrinsic strength α that is no longer necessarily infinite. One recovers Eqs. (3.3-3.4) by taking $N = 1$ and $\alpha \to \infty$, in which case $p_{-1} = p_0 = 0$ may be eliminated. Likewise, Fig. 3.2e, f, and g correspond to taking $\alpha \to \infty$ with $N = 2$, $N = 4$, and $N = 100$ respectively. See Appendix 3.8 for simulation details.

The continuum limit applies when $N, \epsilon \gg 1$ and the discrete index i is replaced by a continuous variable $x = id$, where d is the lattice spacing. If $\alpha \to \infty$, then $p(x < 0) = 0$, so the continuum equations take the form

$$\dot{p} = \nabla^2 p + n(p + \gamma) r(p) \tag{3.40}$$

$$\dot{n} = \frac{n}{\tau}\left[r_n(n) - \frac{p}{q} \right] \tag{3.41}$$

paired with the Dirichlet boundary $p(0) = 0$ and the no-flux boundary $\partial_x p\big|_\ell = 0$. Here, I have nondimensionalized the x-coordinate according to $x \to x/\sqrt{D}$ and $\ell = L/\sqrt{D}$. However, if α is finite, then one obtains an interfacial equation of the form:

$$\dot{p} = \nabla^2 p + \begin{cases} -\alpha p & x \in [-\ell, 0] \\ n(p + \gamma) r(p) & x \in [0, \ell] \end{cases} \tag{3.42}$$

$$\dot{n} = \frac{n}{\tau}\left[r_n(n) - \frac{p}{q} \right] \tag{3.43}$$

with no-flux boundaries at $x = \pm\ell$. I use Eq. (3.43) with $\alpha = 1$ to produce the kymograph in Fig. 3.1b. See the Appendix 3.8 for simulation details.

To compute the phase diagram in Fig. 3.2h, notice that Eqs. (3.40-3.41) take the same form as Eqs. (3.14-3.15). Here, p is the fast variable, n is the slow variable, and the function $\tilde{f}$ is given by $\tilde{f}(p) = (p+\gamma)r(p)$. The function n_∞ (which plays the role of B_∞) is determined

by the functional form of r_n. For instance, consider the piecewise linear function

$$r_n(n) = \begin{cases} 1 - mn & n \in [0, \frac{1-q}{m}] \\ q & n \in [\frac{1-q}{m}, 1 - \frac{q}{m}] \\ m(1-n) & n \in [1 - \frac{q}{m}, 1] \end{cases} \tag{3.44}$$

If $m = 1$, then $r_n(n) = 1 - n$ and $n_\infty(p) = \max\{0, 1 - p/q\}$. If $m \to \infty$, then $n_\infty(p) = \Theta(q-p)$, where q plays the role of A_* in §3.3. The phase diagrams in Fig. 3.2d and Fig. 3.2h are analytically computed for $m \to \infty$. In the limit that $\gamma \to 0$, the location of the local maximum of $X(q)$ approaches $q = 0$ and so the general phase diagram in Fig. 3.9a converges the one Fig. 3.2h.

3.5 Calculations for bioelectric interfaces

3.5.1 Conductance-based biolectric model

The bioelectric dynamics I consider are described by conductance-based (i.e. Hodgkin-Huxley type) models. Our equations focus on the role of the sodium ion channels, potassium ion channels, and gap-junction coupling between cells. If the ion channels are homogeneously distributed throughout the tissue, the dynamics are governed by

$$C\dot{V} = G\nabla^2 V + g_{\mathrm{K}}\, f_{\mathrm{K}}(V) + h g_{\mathrm{Na}}\, f_{\mathrm{Na}}(V) \tag{3.45}$$

$$\dot{h} = \frac{h_\infty(V) - h}{\tau} \tag{3.46}$$

Here, $V(x,t)$ is the local membrane potential of the tissue, C is the capacitance of the cell membrane, $g_{\mathrm{K}}\, f_{\mathrm{K}}(V)$ and $h\, g_{\mathrm{Na}}\, f_{\mathrm{Na}}(V)$ are the currents through the potassium and sodium channels, respectively. The constants g_{K} and g_{Na} are known as open-state conductances, and they set the relative strengths of the potassium and sodium channels. The functions

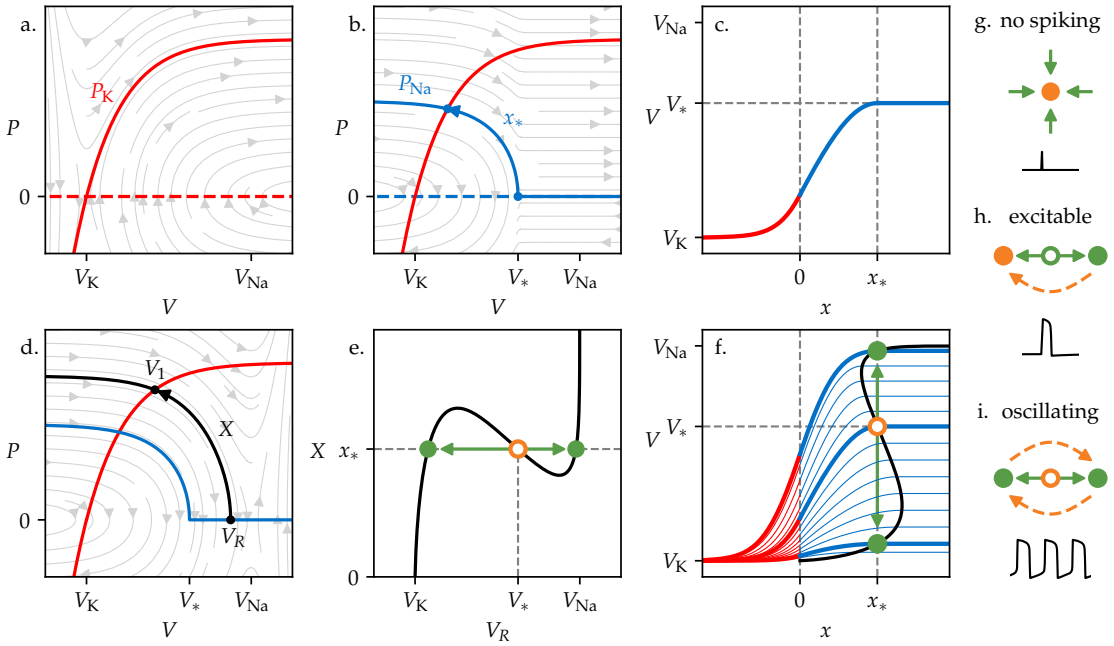

Figure 3.11: **Bifurcation analysis of interfacial spiking.** **a.** The Hamiltonian flow in Eqs. (3.61-3.62) for $x < 0$ is depicted. The separatrix $P_{\rm K}$ (solid blue line) results from an advection of $P = 0$ (dashed blue line) through a distance $\ell \to \infty$. **b.** Similarly, the Hamiltonian flow in Eqs. (3.61-3.62) for $x > 0$ is depicted. The separatrix $P_{\rm Na}$ (solid red line) results from an advection of $P = 0$ (dashed red line) through a distance $\ell \to -\infty$. **c.** In real space, composing the separatrices yields the stationary solution $V_0(x)$. The curve $V_0(x)$ matches the $x < 0$ and $x > 0$ solutions subject to the requirement that the right solution obtains a slope of zero at $V = V_*$. **d.** The curve $P_{\rm Na}(V, V_R)$ is shown in black. V_R is the V coordinate of the intersection with $P = 0$, and V_1 marks the intersection with $P_{\rm K}$. The function $X(V_R)$ represents the x distance transversed in real space between the voltages V_R and $V_1(V_R)$. **e.** The function X is plotted as a function of V_R. The number of solutions to the equation $X(V_R) = x_*$ varies from 1 to 3 depending on x_*. **f.** One can visualize the function $X(V_R)$ by plotting a range of trial solutions with different slopes at their interface. The function $X(V_R)$ corresponds to the x value at which each curve first attains its maximum. The thick lines correspond to the critical points of Φ. **g.** If x_* intersects X once, then the system does not exhibit spikes. **h.** If x_* intersects X three times with V_* corresponding to an increasing branch, then the system exhibits excitability. **i.** If V_* lies on the decreasing branch of X, then the system exhibits oscillations. In (e-i), the circles represent critical points of the functional Φ in Eqs. (3.68). The orange circle represents $V_0(x)$, the stationary solution of Eqs. (3.5-3.6). Solid arrows represent fast heteroclinic orbits, and the dashed arrows represent slow dynamics in Eqs. (3.5-3.6). Open circles are unstable critical points, while solid circles are stable critical points of Φ. Adapted from Scheibner et al. [2023].

$f_{\rm K}$ and f_{Na} are nonlinearites that control the shape of the voltage-current relationship. The variable h is a gating variable that assumes values between 0 and 1, and τ is a time constant

for its evolution towards a steady state value $h_\infty(V)$. Finally, voltage diffusion, modulated by the parameter G, arises due to gap-junction coupling.

To nondimensionalize the equations, let V_{ref} be a characteristic reference voltage, set $r = \frac{g_{\text{Na}}}{g_{\text{K}}}$ to be the relative strength of the sodium and potassium channels, and let $t_0 = \frac{V_{\text{ref}}C}{g_{\text{K}}}$ denote a characteristic time of the voltage dynamics. Next, let $D = GV_{\text{ref}}/g_{\text{K}}$ be the diffusion coefficient G/C times the characteristic time scale t_0. Note that $\sqrt{D}$ has dimensions of length. I nondimensionalize the equations according to

$$\tilde{h} = h\, r \tag{3.47}$$

$$\tilde{t} = t/t_0 \tag{3.48}$$

$$\tilde{\tau} = \tau/t_0 \tag{3.49}$$

$$\tilde{V} = V/V_{\text{ref}} \tag{3.50}$$

$$\tilde{x} = x/\sqrt{D} \tag{3.51}$$

$$\tilde{f}_{\text{K}}(\tilde{V}) = f_{\text{K}}(\tilde{V}V_{\text{ref}}) \tag{3.52}$$

$$\tilde{f}_{\text{Na}}(\tilde{V}) = f_{\text{Na}}(\tilde{V}V_{\text{ref}}) \tag{3.53}$$

In §3.1, I use dimensionless variables except for x, and hence D is also retained in Eqs. (3.5-3.6). In what follows, I will work in dimensionless quantities and omit the tildes.

As shown in Fig. 3.3c,f,i, I will require that $f_{\text{K}}(V)$ and $f_{\text{Na}}(V)$ each have exactly one zero crossing, at V_{K} and V_{Na} respectively, and that they are decreasing at this zero. Also, motivated by experimentally calibrated conductance models [ten Tusscher et al., 2004a], I take the asymptotic value of the gating variable to be a step function: $h_\infty(V) = r\,\Theta(V_* - V)$, where V_* is the crossover of the step.

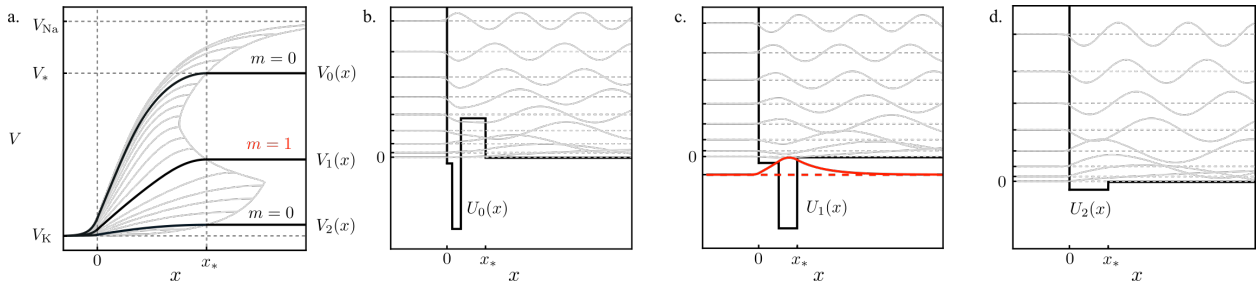

Figure 3.12: **Linearized dynamics and interface confinement. a.** An example of three solutions to Eq. (3.68) (black lines), which constitute critical points of the functional Φ. The light gray curves represent trial solutions that do not meet the boundary conditions. **b-d.** The linearized dynamics about each critical point p is governed by a Schrödinger equation with an effective potential U_p. Each effective potential features a well near the interface. The unstable dimension, m, of each critical point corresponds to the number of negative energy states of the Hamiltonian. Because the negative energy states must be bound states, the unstable modes that drive the spiking feature a spatial profile that is localized near the interface. The sole negative energy state in (c) is highlighted in red. Adapted from Scheibner et al. [2023].

3.5.2 Dynamics of a single cell

Before considering a spatially extended system, I consider a the dynamics of a single cell with both sodium and potassium channels, described by the ordinary differential equation

$$\dot{V} = f_{\mathrm{K}}(V) + h\, f_{\mathrm{Na}}(V) \tag{3.54}$$

$$\dot{h} = \frac{h_\infty(V) - h}{\tau} \tag{3.55}$$

The dynamics of a single cell can be understood in terms of the V and h nullclines. For example, in Fig. 3.10, the the solid red line indicates h_∞, which is the h-nullcline. The solid black line indicates the V-nullcline, given by

$$h_{\mathrm{eq}}(V) = -\frac{f_{\mathrm{K}}(V)}{f_{\mathrm{Na}}(V)} \tag{3.56}$$

As shown in Fig. 3.10 and Fig. 3.3d,g, the V_*-r phase diagram for single cell exhibits spiking if h_{eq} is an "N" shaped curve. However, if h_{eq} is monotonically increasing (e.g., Fig. 3.3j),

then the V_*-r phase diagram for a single cell does not exhibit spiking.

3.5.3 Phase diagram for interfacial spiking

Here I derive the phase diagram for the bioelectric interface shown in Fig. 3.3. I will consider a 1D domain, $x \in [-\ell, \ell]$, with an interface at $x = 0$. Of particular interest are in the following two limits: $\ell \to 0$, which will recover the single-cell phase diagrams in Fig. 3.3d,g,j; and $\ell \to \infty$, which will yield the interfacial phase diagrams in Fig. 3.3e,h,k. The governing equations are:

$$\dot{V} = \nabla^2 V + \begin{cases} f_{\mathrm{K}}(V) & x \in [-\ell, 0] \\ h\, f_{\mathrm{Na}}(V) & x \in (0, \ell] \end{cases} \tag{3.57}$$

$$\dot{h} = \frac{h_\infty(V) - h}{\tau} \tag{3.58}$$

I will require that V and $\partial_x V$ be continuous and that $\partial_x V\big|_{\pm\ell} = 0$. For brevity, I will write:

$$f(V, h, x) = f_{\mathrm{K}}(V)\Theta(-x) + h f_{\mathrm{Na}}(V)\Theta(x) \tag{3.59}$$

Following the general approach from §3.3, I first solve for the fixed points of Eqs. (3.57-3.58), which I refer to as stationary solutions. Setting the left-hand side of Eqs. (3.57-3.58) to zero amounts to solving the equation:

$$0 = \nabla^2 V + f(V, h_\infty(V), x) \tag{3.60}$$

which can be cast as a Hamiltonian system

$$\partial_x V = P \tag{3.61}$$

$$\partial_x P = -f(V, h_\infty(V), x) \tag{3.62}$$

with boundary conditions $P\big|_{\pm\ell} = 0$. As shown in Fig. 3.11, Eqs. (3.61-3.62) may be solved graphically. First, construct the curve $P_{\mathrm{K}}(V;\ell)$ by taking the line $P = 0$ and advecting it forward a distance ℓ according to the $x < 0$ flow, as shown in Fig. 3.11a. Second, construct the curve $P_{\mathrm{Na}}(V;-\ell)$ by advecting the line $P = 0$ backwards a distance ℓ according to the $x > 0$ flow, as shown in Fig. 3.11b. The intersections $P_{\mathrm{K}}(V;\ell) = P_{\mathrm{Na}}(V;-\ell)$ correspond to stationary solutions. I will focus on two limits:

First, I consider $\ell \to 0$. In this limit, I expect to recover the dynamics of a single cell, since V is effectively forced to be constant across the domain $[-\ell, \ell]$. Indeed, for small ℓ, one obtains

$$P_{\mathrm{K}}(V;\ell) = -\ell f_{\mathrm{K}}(V) + \mathcal{O}\Big(\ell^2\Big) \tag{3.63}$$

$$P_{\mathrm{Na}}(V;-\ell) = \ell h_\infty(V) f_{\mathrm{Na}}(V) + \mathcal{O}\Big(\ell^2\Big) \tag{3.64}$$

Equating $P_{\mathrm{K}}(V;\ell) = P_{\mathrm{Na}}(V;-\ell)$ yields

$$h_{\mathrm{eq}}(V) = h_\infty(V) \tag{3.65}$$

which is the fixed point equation for a single cell described by Eqs. (3.54-3.55).

Second, I consider $\ell \to \infty$. In this limit, $P_{\mathrm{K}}(V;\ell)$ and $P_{\mathrm{Na}}(V;-\ell)$ approach the separatrices of the Hamiltonian flow, as shown in Fig. 3.11a-b. These separatrices are given explicitly

by:

$$P_{\mathrm{K}}(V) = \sqrt{-2\int_{V_{\mathrm{K}}}^{V} f_{\mathrm{K}}(V')\mathrm{d}V'} \tag{3.66}$$

$$P_{\mathrm{Na}}(V) = \sqrt{2\int_{V}^{V_{\mathrm{Na}}} h_\infty(V')f_{\mathrm{Na}}(V')\mathrm{d}V'} \tag{3.67}$$

Since f_{K} and f_{Na} only have one zero crossing each, the separatrices are monotonic and they will only intersect once. Hence, in the limit $\ell \to \infty$, the stationary solution $V_0(x)$ is unique. Until this point, I have only required that $h_\infty(V)$ be non-negative on the interval $[V_{\mathrm{K}}, V_{\mathrm{Na}}]$. For $h_\infty(V) = r\,\Theta(V_* - V)$, the solution $V_0(x)$ is the curve that matches between the left- and right-hand side while reaching $\partial_x V = 0$ at the voltage V_*, as shown in Fig. 3.11c. I will let x_* denote the solution to the equation $V_0(x) = V_*$. Note that the intersection construction in Fig. 3.11a-b is equivalent to the hill picture provided in Fig. 3.4a in which V is the position of the ball and P is its momentum.

Having found the stationary solution $V_0(x)$, I examine the fast dynamics with h frozen to $h_\infty(V_0(x))$. The fast dynamics are governed by:

$$\dot{V} = \nabla^2 V + F(V, x) = -\frac{\delta\Phi}{\delta V} \tag{3.68}$$

where $F(V, x) = f(V, h_\infty(V_0(x)), x)$. As in §3.3, I seek to find the critical points of Φ, i.e. solve Eq. (3.68) with $\dot{V} = 0$. This amounts to solving the system:

$$\partial_x V = P \tag{3.69}$$

$$\partial_x P = -F(V, x) \tag{3.70}$$

with boundary conditions $P(\pm\ell) = 0$.

In the limit $\ell \to \infty$ I construct the solutions to Eqs. (3.69-3.70) as follows:

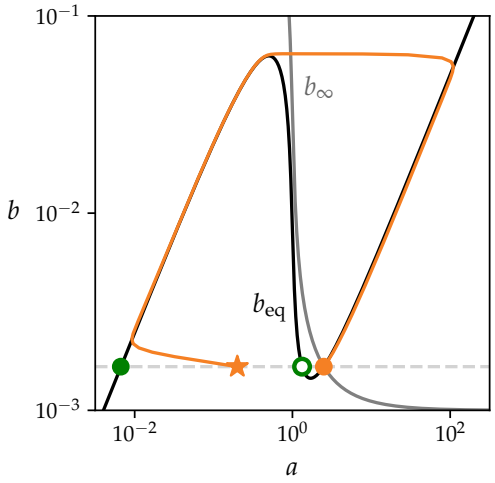

Figure 3.13: **A phase portrait of an excitable chemical reaction.** A phase portrait for Eqs. (3.96-3.97) with $m_1 = 2$, $m_2 = 10^{-3}$, $\tau = 10^4$. The black curve is $b_{\rm eq}(a)$ [Eq. (3.98)] and the grey curve is $b_\infty(a)$ [Eq. (3.95)]. The solid and filled green circles represent critical points of the fast dynamics (c.f. Fig. 3.6). The orange curve is an example trajectory starting at the star and ending at the orange solid circle and exhibiting a spike. The same parameters are used to integrate Eqs. (3.102-3.103) in Fig. 3.1c. Notably, the interface exhibits oscillation, rather than excitability, due to the presence of diffusion. Adapted from Scheibner et al. [2023].

1. First define

$$P_{\rm Na}(V, V_R) = \sqrt{2r \int_V^{V_R} f_{\rm Na}(V')\mathrm{d}V'} \tag{3.71}$$

2. Second, define $V_1(V_R)$ to be the point of intersection between the left separatrix and the right solution curves, i.e. $P_{\rm K}(V_1) = P_{\rm Na}(V_1, V_R)$, as shown in Fig. 3.11d.

3. Thirdly, compute

$$X(V_R) = \int_{V_1(V_R)}^{V_R} \frac{1}{P_{\rm Na}(V, V_R)}\mathrm{d}V \tag{3.72}$$

which is the distance in real space between the locations where the voltage crosses V_1 and V_R.

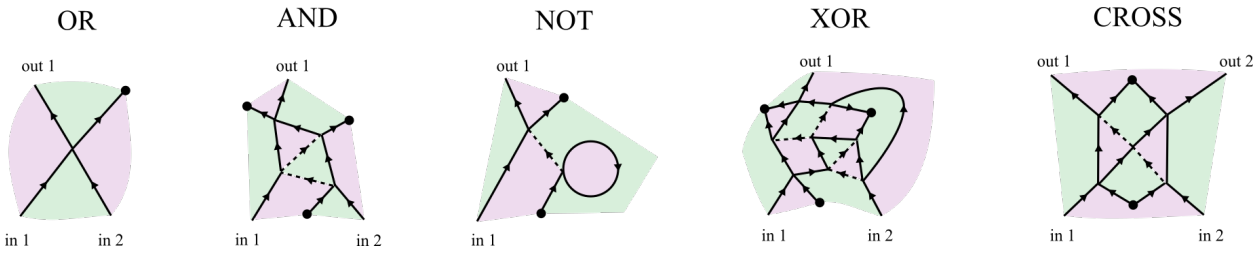

Figure 3.14: **Examples of OR, AND, NOT, XOR, and CROSS logic gates.** The black lines represent interfaces between distinct materials (purple and green). Solid lines fit an integer number of wavelengths, while dashed lines fit a half integer number of wavelengths. The black circles represent termination points. Adapted from Scheibner et al. [2023].

4. Finally, as illustrated in Fig. 3.11e, critical points [i.e. solutions of Eq. (3.69-3.70)] correspond to solutions of the equation $X(V_R) = x_*$.

As illustrated in Fig. 3.11f, the construction of $X(V)$ can be visualized in real space: for a range of trial solutions with different slopes at the interface, the points at which each curve first achieves $\partial_x V = 0$ forms the graph $(X(V), V)$. Critical points of Φ are the curves for which $X(V) = x_*$. In Appendix 3.8, I analyze a special case in which f_{K} and f_{Na} are piecewise linear, allowing $X(V)$ and $V_0(x)$ to be computed analytically in terms of trigonometric functions.

I note that the precise shape of $X(V)$ depends on the functions f_{K} and f_{Na} and the parameter r. Nevertheless, the hypotheses $f_{\mathrm{K}}(V) < 0$ and $f_{\mathrm{Na}}(V) > 0$ for $V \in (V_{\mathrm{K}}, V_{\mathrm{Na}})$ imply that $X(V_{\mathrm{K}}) = 0$ and $X(V_{\mathrm{Na}}) = \infty$. If I specialize to the situation in which $X(V)$ is "N" shaped, I can use the same stability arguments as in §3.3 to obtain the spiking phase diagrams shown in Fig. 3.3e,h,k: If $X(V_*)$ has degeneracy 1, then the system cannot spike (see Fig. 3.11g). If $X(V_*)$ has degeneracy 3, then the system can spike. If V_* lies on an increasing branch of X, then $V_0(x)$ is stable and the system is excitable (see Fig. 3.11h). If V_* lies on the decreasing branch of X, then $V_0(x)$ is unstable and the system exhibits a oscillations (see Fig. 3.11i).

3.5.4 Limits: $r \to 0$, $r \to \infty$

If the potassium channels are much stronger than the sodium channels, then one expects that the interface will behave as a Dirichlet boundary with $V(0) = V_{\mathrm{K}}$. This can be shown mathematically by taking the limit $r \to 0$. From the definition of $V_1(V_R)$, namely $P_{\mathrm{K}}(V_1) = P_{\mathrm{Na}}(V_1, V_R)$, I obtain the relationship

$$\int_{V_{\mathrm{K}}}^{V_1} f_{\mathrm{K}}(V)\mathrm{d}V + r\int_{V_1}^{V_R} f_{\mathrm{Na}}(V)\mathrm{d}V = 0 \tag{3.73}$$

From Eq. (3.73) one sees that $V_1 \to V_K$ as $r \to 0$. In this limit, the expression for $X(V_R)$ [Eq. (3.73)] becomes:

$$X_{\mathrm{low}}(V_R) = \frac{1}{\sqrt{2r}}\int_{V_{\mathrm{K}}}^{V_R} \frac{1}{\sqrt{U_{\mathrm{Na}}(V) - U_{\mathrm{Na}}(V_R)}}\mathrm{d}V \tag{3.74}$$

where U_{Na} is an antiderivative of f_{Na}. Notice that Eq. (3.74) has the same functional form as Eq. (3.20). Crucially, r only appears as a multiplicative prefactor of $X(V_R)$, implying that the phase boundaries become independent of r as $r \to 0$. Furthermore, the form of $X(V)$ and hence the phase diagram at low r only depends on the functional form f_{Na} and on the zero crossing V_{K}, but not on the detailed functional form of f_{K}.

Similarly, in the limit that $r \to \infty$, I may write $V_1 = V_R - \delta(r)$ where $\delta(r) \ll 1$. From Eq. (3.73), one concludes

$$\delta = \frac{U_{\mathrm{K}}(V_R) - U_{\mathrm{K}}(V_{\mathrm{K}})}{r f_{\mathrm{Na}}(V_R)} + \mathcal{O}\Big(1/r^2\Big) \tag{3.75}$$

where U_{K} is an antiderivative of f_{K}. Then the expression for $X(V_R)$ [Eq. (3.73)] becomes

$$X_{\mathrm{high}}(V_R) = \sqrt{\frac{2\delta}{f_{\mathrm{Na}}(V_R)}} \tag{3.76}$$

$$= \frac{\sqrt{2}}{r} \frac{\sqrt{U_{\mathrm{K}}(V_{\mathrm{K}}) - U_{\mathrm{K}}(V_R)}}{f_{\mathrm{Na}}(V_R)} \tag{3.77}$$

Once again, r appears a multiplicative prefactor, implying that the phase boundaries become vertical in the V_*-r plane. Notice that Eq. (3.77) depends on the functional form of both f_{Na} and f_{K}, implying that $X_{\mathrm{high}}(V_R)$ and $X_{\mathrm{low}}(V_R)$ can be tailored independently of each other.

3.5.5 Shape of unstable modes

Here I discuss why the spatial profile of the edge spike is often localized near the interface or boundary (see Fig. 3.1a-b for example). As illustrated in Fig. 3.11f, the critical points of Φ (i.e. the curves intersecting green circles) are monotonically increasing. However, when τ is finite, the voltage profile $V(x,t)$ approaches the critical points, but does not completely reach them because the voltage takes a non-negligible amount of time to diffuse out to the boundaries (especially for large systems). Instead, the spatial extent of the spike is better approximated by the shape of the unstable mode associated with the unstable critical point. Given a critical point p, with spatial profile $V_p(x)$, the linearized dynamics obey:

$$\partial_t \delta V = -\,\mathrm{H}\,\delta V \tag{3.78}$$

where $\delta V(x) = V(x) - V_p(x)$ and

$$\mathrm{H}(x) = -\nabla^2 + U(x) \tag{3.79}$$

with $U(x) = -\left.\frac{\partial F}{\partial V}\right|_{V_p(x)}$. Notice that Eq. (3.78) is a 1D Schrödinger equation with potential $U(x)$. As an illustration, Fig. 3.12a show the voltage profile for a biolectric interface for which Φ has three critical points, $V_0(x)$, $V_1(x)$, and $V_2(x)$. Figure 3.12b-d shows the effective potential for each of these three critical points. (In this example, f_{K} and f_{Na} are chosen to be piecewise linear, and hence each $U_p(x)$ is a square well). Negative eigenvalues of H correspond to unstable modes. Since I require $\partial_x V\big|_{\pm\infty} = 0$ and $f_{\mathrm{K}}(V)$ and $f_{\mathrm{Na}}(V)$ are both decreasing at their zero crossings, it follows that $U(x \to \pm\infty)$ approaches non-negative constants $C_1 = -h_\infty(V_{\mathrm{Na}})\partial_V f_V$ and $C_2 = -\partial_V f_K$. Therefore negative energy states, and hence the unstable modes, correspond to bound states of $U(x)$. Naturally, these bound states are confined to the well formed by $U(x)$, which coincides with the region in which $V_p(x)$ interpolates between its two asymptotic values. Examples of the linear spectrum for each critical point are shown Fig. 3.12b-d. In accordance with the stability of each critical point, only panel c has a negative energy state, which is highlighted in red.

3.5.6 Example ion channels

Here I provide the expression for the ion channels used in Fig. 3.3. For panels (c-e), I use:

$$f_{\mathrm{K}}(V) = \frac{(V_{\mathrm{K}} - V)e^{-2.5(V-V_{\mathrm{K}})}}{N_1} \tag{3.80}$$

$$f_{\mathrm{Na}}(V) = \frac{(V_{\mathrm{Na}} - V)e^{-2.5(V-V_{\mathrm{Na}})}}{N_2} \tag{3.81}$$

For panels (f-h), I use:

$$f_{\mathrm{K}}(V) = \frac{-e^{-(V-V_{\mathrm{K}})} + e^{-2(V-V_{\mathrm{K}})}}{N_3} \tag{3.82}$$

$$f_{\mathrm{Na}}(V) = \frac{e^{(V-V_{\mathrm{Na}})} - e^{2(V-V_{\mathrm{Na}})}}{N_4} \tag{3.83}$$

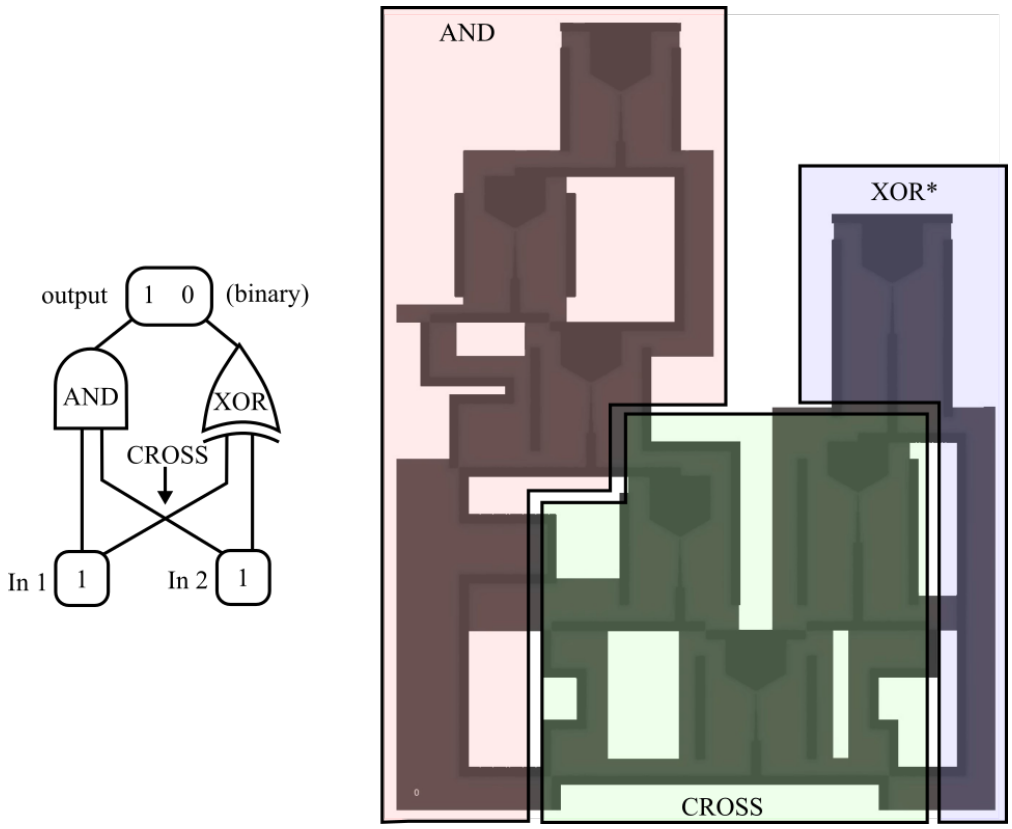

Figure 3.15: **Decomposition of binary half adder.** A binary half adder can be decomposed into and AND gate and an XOR gates. Since the XOR gate generates an output of the system, it can be simplified to the XOR* gate. Adapted from Scheibner et al. [2023].

For panels (i-k), I use:

$$f_{\mathrm{K}}(V) = \frac{0.3(1 - e^{(V - V_{\mathrm{K}})})}{N_5} \tag{3.84}$$

$$f_{\mathrm{Na}}(V) = \frac{e^{2.5V}(V_{\mathrm{Na}} - V)}{N_6} \tag{3.85}$$

with $V_{\mathrm{K}} = -1$ and $V_{\mathrm{Na}} = 1$. The normalization constants $N_1, \ldots, N_6$ are chosen such that the local minimum or maximum of each ion channel is normalized to -1 and 1, respectively.

3.6 Calculations for oscillating chemical reactions

The chemical dynamics I study involve two chemical reservoirs undergoing distinct chemical reactions. In the rightmost chamber, I consider a prototypical chemical reaction network known as the Oregonator [Field et al., 1972]. The Oregonator can be summarized by 5 elementary reactions

$$\mathrm{R} + \mathrm{A} \xrightarrow{k_1} \mathrm{C} + \mathrm{P} \tag{R1}$$

$$\mathrm{C} + \mathrm{A} \xrightarrow{k_2} 2\,\mathrm{P} \tag{R2}$$

$$\mathrm{R} + \mathrm{C} \xrightarrow{k_3} 2\,\mathrm{C} + 2\,\mathrm{B} \tag{R3}$$

$$2\,\mathrm{C} \xrightarrow{k_4} \mathrm{R} + \mathrm{P} \tag{R4}$$

$$\mathrm{B} \xrightarrow{k_5} m_1\,\mathrm{A} \tag{R5}$$

with rate constants k_i. Here R is a reactant, P is the product, A, B, and C are catalysts, and m_1 is a stoichiometric coefficient. The Oregonator was originally proposed as a minimal model for the Belousov-Zhabotinsky reaction [Tyson, 1976]. In this context, the variables can be roughly interpreted as: R = $BrO_3{}^-$, P = HOBr, A= Br^-, B=Ce^{4+}, and C= $HBrO_2$, and suitable rate constants can be determined from experiments. See Ref. [Tyson, 1976] for a detailed introduction.

In the right chamber, I assume that the reactant R is abundant, so its concentration can be treated as constant. Moreover, the product P is assumed to exit the reaction and not affect the subsequent dynamics. Hence, I need only consider the kinetic equations for the

intermediates A, B, and C:

$$\dot{A} = -k_1 R\, A - k_2 C\, A + m_1 k_5 B \tag{3.86}$$

$$\dot{B} = 2k_3 R\, C - k_5 B \tag{3.87}$$

$$\dot{C} = k_1 R\, A - k_2 C\, A + k_3 R C - k_4 C^2 \tag{3.88}$$

Here, A denotes the concentration of component A, etc. I nondimensionalize the kinetic equations by introducing a time scale $t_0 = \frac{k_4}{k_3 k_2 R}$ and defining

$$a = \frac{k_2}{R k_3} A \qquad\qquad b = \frac{k_4 k_5}{2(R k_3)^2} B \tag{3.89}$$

$$c = \frac{k_4}{R k_3} C \qquad\qquad \tilde{t} = t/t_0 \tag{3.90}$$

resulting in

$$\dot{a} = 2m_1 b - a(c + m_2) \tag{3.91}$$

$$\dot{b} = \frac{c - b}{\tau} \tag{3.92}$$

$$\epsilon \dot{c} = a(m_2 - c) + c(1 - c) \tag{3.93}$$

with the parameters

$$\varepsilon = \frac{k_2}{k_4} \qquad\qquad \tau = \frac{k_2 k_3 R}{k_4 k_5} \qquad\qquad m_2 = \frac{k_1 k_4}{k_2 k_3} \tag{3.94}$$

Of interest is the regime $\varepsilon \ll 1$ and $\tau \gg 1$. With $\varepsilon \ll 1$, one may integrate out Eq. (3.93) and define

$$c(a) = b_\infty(a) \equiv \frac{1}{2}\left[(1 - a) + \sqrt{(1 - a)^2 + 4m_2 a}\right] \tag{3.95}$$

Thus the dynamics become

$$\dot{a} = 2m_1 b - a(b_\infty(a) + m_2) \tag{3.96}$$

$$\dot{b} = \frac{b_\infty(a) - b}{\tau} \tag{3.97}$$

The b-nullcline is given by $b = b_\infty$ and the a-nullcline $\dot{a} = 0$ is given by

$$b = b_{\rm eq}(a) \equiv \frac{a(b_\infty(a) + m_2)}{2m_1} \tag{3.98}$$

Depending on the values of m_1 and m_2, Eqs. (3.96-3.97) can exhibit no-spiking, excitable, and oscillating phases. Our interest is in the regime in which m_1 is sufficiently large to create local excitability, as shown in Fig. 3.13.

For a spatially extended system, Eqs. (3.93-3.92) become

$$\dot{a} = \nabla^2 a + 2m_1 b - a(c + m_2) \tag{3.99}$$

$$\dot{b} = \beta\nabla^2 b + \frac{c - b}{\tau} \tag{3.100}$$

$$\varepsilon\dot{c} = \alpha\nabla^2 c + a(m_2 - c) + c(1 - c) \tag{3.101}$$

In Eqs. (3.99-3.100), I nondimentionalize length using $x \to x/\sqrt{D}$ where $D = D_A t_0$ and D_A is the diffusion constant for species A. In Eq. (3.101) and Eq. (3.100), $\alpha = \varepsilon\frac{D_C}{D_A}$ and $\beta = \frac{D_B}{D_A}$, where D_C and D_B are the diffusion constants for C and B, respectively. Since $\varepsilon \ll 1$, I have $\alpha \ll 1$ and therefore c can be locally integrated out using Eq. (3.95).

In the leftmost chamber, I assume that the catalyst A is rapidly converted into a product and exits the reaction:

$$\text{A} \longrightarrow \text{P} \tag{L1}$$

When the species A is allowed to diffuse across the interface, the governing equations take the form:

$$\dot{a} = \nabla^2 a + \begin{cases} -a & x \in [-\ell, 0] \\ 2m_1 b - a[b_\infty(a) + m_2] & x \in [0, \ell] \end{cases} \tag{3.102}$$

$$\dot{b} = \frac{b_\infty(a) - b}{\tau} \tag{3.103}$$

For Fig. 3.1c, I choose $m_1 = 2$ and $m_2 = 10^{-3}$. In this case, the $x > 0$ reservoir displays excitability (see the phase portrait in Fig. 3.13), and the $x < 0$ reservoir exhibits no spiking. Crucially, however, when the catalyst A is allowed to diffuse, the full interfacial system exhibits oscillations.

3.7 Details on two-dimensional waveguides

3.7.1 Two-dimensional media: interfacial trigger waves

In two dimensions, an interface between two media forms a 1D line. If the interface is excitable, then the 1D line can host a trigger wave, as illustrated by the bioelectric experiments in Fig. 3.1a. In the notation of Eqs. (3.7-3.8), a trigger wave along the interface is described by a profile $A(x, y, t) = A(x, y - c\,t)$ where x runs transverse to the interface, y runs parallel to the interface, and c is the wave speed. In a $\tau \to \infty$ approximation, the sharp front along the interface is described by:

$$D\partial_y^2 A = -c\partial_y A + \frac{\delta \Phi}{\delta A} \tag{3.104}$$

which is a higher dimensional version of the profile equation for standard trigger waves [Di Talia and Vergassola, 2022]. When the interface is excitable, Φ has two minima, the stationary solution $A_0(x)$ and an additional minimum $A_1(x)$. In the simplest approximation, $A_0(x)$

and $A_1(x)$ are the boundary conditions of Eq. (3.104) as $y \to +\infty$ and $-\infty$, respectively. The conditions for trigger-wave propagation can then be understood by a classic rolling ball analogy [Vergassola et al., 2018]: Eq. (3.104) describes a ball of mass D moving with damping c between two maxima [$A_0(x)$ and $A_1(x)$] of a potential $-\Phi$. The front moves in the direction that expands the low potential (larger Φ) region, and the wave speed c corresponds to the (unique) value of dissipation that allows the ball to arrive at rest at the top of the lower peak of $-\Phi$. Notably, an undisturbed system will initially exhibit a uniform profile $A(x, y) = A_0(x)$. Consequently, if $\Phi[A_1] > \Phi[A_0]$, then a sufficiently intense local perturbation will cause the A_1 region to expand, implying that a trigger wave will propagate outward in both direction from the initial perturbation. If $\Phi[A_1] < \Phi[A_0]$, then the initial perturbation will close and the trigger wave will not propagate.

3.7.2 Design of the binary half adder

Here I comment on the design of the binary half adder in Fig. 3.5c-d. Each input channel encodes a Boolean value: *true* corresponds to the presence of a wave train, and *false* corresponds to the absence of a wave train. Within this paradigm, a self-contained logic gate receives input wave trains, subjects them to nonlinear interference, and produces output wave trains. Figure 3.14 shows examples of canonical OR, AND, NOT, and XOR logic gates. In each of these diagrams, a solid line indicates an interface of length $n\lambda$ and a dashed line indicates an interface length $(n + 1/2)\lambda$, where n is an integer, and $\lambda = Tc$, where T is the period of the input pulses and c is the wave velocity along the interface. Each of these logic gates is constructed using only two materials, which implies that each junction must comprise at least four interfaces. The device shown in Fig. 3.5c-d is known as a binary half adder, which takes the sum of two binary numbers. As shown in Fig. 3.15, the binary half adder can be constructed out of XOR and AND gates. In order to embed the logic gates in the 2D plane, an additional trivial gate $\mathrm{CROSS}(x, y) = (x, y)$ must be implemented

that allows two pulses to cross each other without performing a computation. To prevent undesired back scatter at interference junctions, a needle geometry shown in Fig. 3.5a-b is used.

In order for the gates in Fig. 3.14 to be composable, the phase of the output wave train must be independent of the choice of logically equivalent inputs. For example $\mathrm{XOR}(T,F) = T$ and $\mathrm{XOR}(F,T) = T$, so both inputs (T,F) and (F,T) must produce an output wave train with the same phase. However, if the output of the logic gate is the final output for the device, then the phase will not be read so certain logic gates, such as XOR, can be simplified. For example, in the binary half adder the XOR logic gate is simplified to XOR*, as shown in Fig. 3.15.

3.8 Appendix: numerical details and mathematical background

3.8.1 Numerics

Here I provide the details for the numerical simulations presented in § 3.1.

Figure 3.1b. I integrate

$$\dot{p} = \nabla^2 p + \begin{cases} -p & x \in [-\ell, 0] \\ n\, p\, r(p) & x \in (0, \ell] \end{cases} \tag{3.105}$$

$$\dot{n} = \frac{n}{\tau}\left[1 - n - \frac{p}{q}\right] \tag{3.106}$$

with no-flux boundary conditions at $x = \pm\ell$. The parameters used are $\tau = 100$, $q = 0.5$, $\ell = 100$. The function $k(p)$ is given by Eq. (3.36) with $p_* = 0.7$ and $n_* = 3$. An initial

condition

$$p(x,0) = 0.5(\tanh(x/10) + 1.1) \tag{3.107}$$

$$n(x,0) = 0.25(\tanh(-x/10) + 1.1) \tag{3.108}$$

is used and a transient is allowed to pass prior to the time interval shown in Fig. 3.1b. The equations are discretized on a 1D lattice and integrated in Python using `scipy.integrate.solve_ivp`.

Figure 3.1c. I integrate Eqs. (3.102-3.103) with parameters $\ell = 100$, $\tau = 500$, $m_1 = 2.0$ and $m_2 = 0.001$. Our initial conditions are $a(x,0) = b(x,0) = 0.1$. An initial transient is allowed to pass prior to the time interval shown in Fig. 3.1c. The equations are discretized on a 1D lattice and integrated in Python using `scipy.integrate.solve_ivp`.

Figure 3.2e-g. The equations integrated are

$$\dot{p}_i = \epsilon(p_{i-1} + p_{i+1} - 2p_i) + n_i\, p_i\, k(p_i) \tag{3.109}$$

$$\dot{n}_i = \frac{n_i}{\tau}\left(1 - n_i - \frac{p_i}{q}\right) \tag{3.110}$$

for $i = 1, \ldots, N$. Here $p_0 = 0$ represents the desert and setting $p_{N+1} \equiv p_N$ implements a no-flux boundary condition. The parameters used are $\epsilon = 4$, $q = 0.5$, $\tau = 20$. The function $k(p)$ is given by Eq. (3.36) with $p_* = 0.7$ and $n_* = 3$. The initial conditions are given by $p_i = n_i = 0.6$. The equations are integrated in Python using `scipy.integrate.solve_ivp`.

Figure 3.4g-i. I integrate the equations

$$\dot{V} = \nabla^2 V + \begin{cases} f_{\mathrm{K}}(V) & x \in [-\ell, 0] \\ h f_{Na}(V) & x \in (0, \ell] \end{cases} \tag{3.111}$$

$$\dot{h} = \frac{r\Theta(V_* - V) - h}{\tau} \tag{3.112}$$

with

$$f_{\mathrm{K}}(V) = -V \tag{3.113}$$

$$f_{\mathrm{Na}}(V) = \begin{cases} 0 & V < V_a \\ \frac{b(V-V_a)}{V_b - V_a} & V_a \le V < V_b \\ \frac{(1-b)(V-V_b)}{W_{\mathrm{Na}} - V_b} + b & V_b \le V < W_{\mathrm{Na}} \\ \frac{V - V_{\mathrm{Na}}}{W_{\mathrm{Na}} - V_{\mathrm{Na}}} & V \ge W_{\mathrm{Na}} \end{cases} \tag{3.114}$$

In all three kymographs, I use $V_a = -0.1$, $V_b = 0.25$, $W_{\mathrm{Na}} = 0.5$, $b = 0.1$, $V_{\mathrm{Na}} = 1$, $r = 0.1$, $\ell = 100$, and $\tau = 1000$. For panels g, h, and i, I set $V_* = -0.1$, $V_* = 0.2$, $V_* = 0.3$, respectively. For panel g, the initial conditions are given by $V(x, 0) = 0.3$, $h(x, 0) = 0.0$. For panel h, I first initialize the voltage profile to $V(x) = 0.1(\tanh(x/10) + 1.1)$. I then perform a relaxation according to

$$\dot{V} = \nabla^2 V + \begin{cases} f_{\mathrm{K}}(V) & x \in [-\ell, 0] \\ r\Theta(V_* - V) f_{\mathrm{Na}}(V) & x \in [0, \ell] \end{cases} \tag{3.115}$$

$$h = r\Theta(V_* - V) \tag{3.116}$$

to obtain stationary profiles $(V_0(x), h_0(x))$. Finally, I integrate Eqs. (3.111-3.112) using the initial conditions $V(x, 0) = V_0(x) + 1.1$ and $h(x, 0) = h_0(x)$. For panel i, the initial conditions

are given by:

$$V(x,0) = 0.1(\tan(x/10) + 1.1) \tag{3.117}$$

$$h(x,0) = 0.5 \tag{3.118}$$

For all panels, the equations are discretized onto a 1D lattice and integrated in Python using `scipy.integrate.solve_ivp`.

Figure 3.5. I integrate the equations:

$$\dot{V} = \nabla^2 V + s(x,y,t) + \begin{cases} f_{\mathrm{K}}(V) & (x,y) \in \text{Region 1} \\ h f_{\mathrm{Na}}(V) & (x,y) \in \text{Region 2} \end{cases} \tag{3.119}$$

$$\dot{h} = \frac{r\Theta(V_* - V) - h}{\tau} \tag{3.120}$$

where f_{K} and f_{Na} are given by Eqs. (3.113 -3.114) with $V_a = -0.1$, $V_b = 0.25$, $W_{\mathrm{Na}} = 0.5$, $b = 0.1$, $V_{\mathrm{Na}} = 1$, $r = 0.1$, $V_* = 0.15$, and $\tau = 300$. The wave trains are generated by repeated Gaussian pulses

$$s(x,y,t) = \sum_{\alpha} A_\alpha(t) \exp\left\{ \frac{(x - x_\alpha)^2 - (y - y_\alpha)^2}{400} \right\} \tag{3.121}$$

where (x_α, y_α) are the points at which the pulses are initialized. Here, the amplitude is a periodic square wave:

$$A_\alpha(t) = \sum_{n \in \mathbb{Z}} \Theta(1 - t - nT - D_\alpha) - \Theta(t - nT) \tag{3.122}$$

where $T = 2810$ is the period and D_α is a phase shift (only used to produce the interfering wave trains in Fig. 3.5b). The Laplacian is discretized onto a triangular mesh. Initial

conditions are obtained by initializing $V(x, y, 0) = 0.16$ then performing a relaxation

$$\dot{V} = \nabla^2 V + \begin{cases} f_{\mathrm{K}}(V) & (x, y) \in \text{Region 1} \\ r\Theta(V_* - V) f_{\mathrm{Na}}(V) & (x, y) \in \text{Region 2} \end{cases} \tag{3.123}$$

$$h = r\Theta(V_* - V) \tag{3.124}$$

over a time interval $t \in [0, 400]$. The full dynamics, Eqs. (3.119-3.120), were then integrated over a time interval $t \in [0, 40000]$. Integration is performed in Python using the `scipy.integrate.solve_ivp` function.

3.8.2 Explicitly solvable bioelectric interface model

I now present an example of Eqs. (3.5-3.6) for which the stationary solutions and critical points can be computed explicitly. I note that explicit solutions are readily obtained whenever one can solve

$$\nabla^2 V = - f_{\mathrm{K}}(V) \tag{3.125}$$

$$\nabla^2 V = - r f_{\mathrm{Na}}(V) \tag{3.126}$$

analytically for arbitrary initial conditions. One example is to take f_{K} and f_{Na} to be piecewise linear in V, as shown in Fig. 3.16. Namely, I take:

$$f_{\mathrm{K}}(V) = - mV \tag{3.127}$$

$$\begin{aligned} f_{\mathrm{Na}}(V) =& \frac{b(V-V_a)}{V_b - V_a}\Theta_{[V_a,V_b)}(V) + \left(\frac{1-b}{W_{\mathrm{Na}} - V_b}(V - V_b) + b\right)\Theta_{[V_b,W_{\mathrm{Na}})}(V) \\ &+ \frac{V - V_{\mathrm{Na}}}{W_{\mathrm{Na}} - V_{\mathrm{Na}}}\Theta_{[W_{\mathrm{Na}},V_{\mathrm{Na}}]}(V) \end{aligned} \tag{3.128}$$

where for a given interval I, $\Theta_I(V) = 1$ if $V \in I$ and $\Theta_I(V) = 0$ if $V \notin I$. I will use the shorthand $\Theta_1 = \Theta_{[V_a,V_b)}$, $\Theta_2 = \Theta_{[V_b,W_N)}$, and $\Theta_3 = \Theta_{[W_{\mathrm{Na}},V_{\mathrm{Na}})}$. I require that $V_a < 0 < V_b < W_{\mathrm{Na}} < V_{\mathrm{Na}}$.

Given the form of Eq. (3.127), the solution to Eq. (3.125) is given by:

$$V(x) = V(0)e^{\sqrt{m}x} \tag{3.129}$$

where I have enforced that $\partial_x V\big|_{-\infty} = 0$. Hence, the left separatrix is given by $P_{\mathrm{K}}(V) = \sqrt{m}V$. The solution to Eq. (3.126) is slightly more subtle. Since f_{Na} is piecewise linear in V, it will be the more convenient to solve for the inverse $x(V)$. Given the initial conditions

$V(0) = V_I$ and $\partial_x V\big|_0 = P_I$, one obtains

$$x(V; V_I, P_I) = \int_{V_I}^{V} \frac{1}{P(V', V_I, P_I)} \mathrm{d}V' \tag{3.130}$$

where

$$P(V; V_I, P_I) = \sqrt{2r[F_{\mathrm{Na}}(V_I) - F_{\mathrm{Na}}(V)] + P_I^2} \tag{3.131}$$

and F_{Na} is an antiderivative of f_{Na}. Since f_{Na} is piecewise linear, the antiderivative is straightforward to compute:

$$F_{\mathrm{Na}}(V) = \frac{1}{2} \sum_i \Big[A_i (V - B_i)^2 + C_i \Big] \Theta_i(V) \tag{3.132}$$

where

$$A_1 = \frac{b}{V_b - V_a} \qquad B_1 = V_a \qquad C_1 = 0 \tag{3.133}$$

$$A_2 = \frac{1-b}{W_{\mathrm{Na}} - V_b} \qquad B_2 = \frac{bW_{\mathrm{Na}} - V_b}{b-1} \qquad C_2 = \frac{b(V_a - bV_a - V_b + bW_{\mathrm{Na}})}{b-1} \tag{3.134}$$

$$A_3 = \frac{1}{W_{\mathrm{Na}} - V_{\mathrm{Na}}} \qquad B_3 = V_{\mathrm{Na}} \qquad C_3 = V_{\mathrm{Na}} - V_b + b(W_{\mathrm{Na}} - V_a) \tag{3.135}$$

Therefore, one has:

$$P(V; V_I, P_I) = \sum_i \sqrt{D_i - r A_i (V - B_2)^2}\, \Theta_i(V) \tag{3.136}$$

where

$$D_i = r \Big[A_1 (V_I - b_1)^2 + C_1 - C_i \Big] + P_I \tag{3.137}$$

In Eq. (3.137) and onward, I assume for simplicity that $V_I \in [V_a, V_b]$. Next, recall the

following antiderivative

$$\int \frac{1}{\sqrt{D - rA(V-B)^2}} \mathrm{d}V = \frac{1}{\sqrt{rA}} \operatorname{atan}\left[\sqrt{\frac{rA}{D - rA(V-B)^2}}(V-B)\right] \tag{3.138}$$

Thus one obtains the solution

$$x(V; V_I, P_I) = \sum_i X_i(V; V_I, P_I)\Theta_i(V) \tag{3.139}$$

where

$$\begin{aligned} X_1(V; V_I, P_I) =& \frac{1}{\sqrt{rA_1}}\left(\operatorname{atan}\left[\sqrt{\frac{rA_1}{D_1 - rA_1(V-B_1)^2}}(V-B_1)\right]\right. \\ & \left. - \operatorname{atan}\left[\sqrt{\frac{rA_1}{D_1 - rA_1(V_I-B_1)^2}}(V_I-B_1)\right]\right) \end{aligned} \tag{3.140}$$

$$\begin{aligned} X_2(V; V_I, P_I) =& \frac{1}{\sqrt{rA_2}}\left(\operatorname{atan}\left[\sqrt{\frac{rA_2}{D_2 - rA_2(V-B_2)^2}}(V-B_2)\right]\right. \\ & \left. - \operatorname{atan}\left[\sqrt{\frac{rA_2}{D_2 - rA_2(V_b-B_2)^2}}(V_b-B_2)\right]\right) \\ & + X_1(V_b; V_I, P_I) \end{aligned} \tag{3.141}$$

$$\begin{aligned} X_3(V; V_I, P_I) =& \frac{1}{\sqrt{rA_3}}\left(\operatorname{atan}\left[\sqrt{\frac{rA_3}{D_3 - rA_3(V-B_3)^2}}(V-B_3)\right]\right. \\ & \left. - \operatorname{atan}\left[\sqrt{\frac{rA_3}{D_3 - rA_3(W_{\mathrm{Na}}-B_3)^2}}(W_N-B_3)\right]\right) \\ & + X_2(W_{\mathrm{Na}}; V_I, P_I) \end{aligned} \tag{3.142}$$

Since the solution $x(V; V_I, P_I)$ is now known for arbitrary initial conditions, one can explicitly compute the curves highlighted in §3.1. For example, in order to compute $X(V)$

from Eq. (3.73), first note that $V_1(V)$ is given by solving $P(V; V_1, \sqrt{M}V_1) = 0$, yielding

$$V_1(V) = \sum_i \frac{rA_1B_1 + \sqrt{r^2A_1^2B_1^2 - r(m+rA_1)(A_1B_1^2 - A_i(V-B_i)^2 + C_1 - C_i)}}{rA_1 + m}\Theta_i(V) \tag{3.143}$$

In Eq. (3.143), I have assumed that $r < \frac{mV_b^2}{V_{\rm Na}+bW_{\rm Na}-V_b(1+b)}$, so that $V_1 \in [0, V_b]$. Then I obtain $X(V)$ by substituting

$$X(V) = x\big[V; V_1(V), \sqrt{m}V_1(V)\big] \tag{3.144}$$

More explicitly:

$$X(V \in [0, V_b]) = \frac{1}{\sqrt{rA_1}}\left(\frac{\pi}{2} - \text{atan}\left[\sqrt{\frac{rA_1}{D_1 - rA_1(V_1 - B_1)^2}}(V_1 - B_1)\right]\right) \tag{3.145}$$

$$\begin{aligned} X(V \in [V_b, W_{\rm Na}]) =& \frac{1}{\sqrt{rA_2}}\left(\frac{\pi}{2} - \text{atan}\left[\sqrt{\frac{rA_2}{D_2 - rA_2(V_b - B_2)^2}}(V_b - B_2)\right]\right) \\ &+ X_1(V_b; V_1, \sqrt{m}V_1) \end{aligned} \tag{3.146}$$

$$\begin{aligned} X(V \in [W_{\rm Na}, V_{\rm Na}]) =& \frac{1}{\sqrt{rA_3}}\left(\frac{\pi}{2} - \text{atan}\left[\sqrt{\frac{rA_3}{D_3 - rA_3(W_{\rm Na} - B_3)^2}}(W_{\rm Na} - B_3)\right]\right) \\ &+ X_2(W_{\rm Na}; V_1, \sqrt{m}V_1) \end{aligned} \tag{3.147}$$

where the V dependence enters through $D_i[V_1(V)]$ and $V_1(V)$.

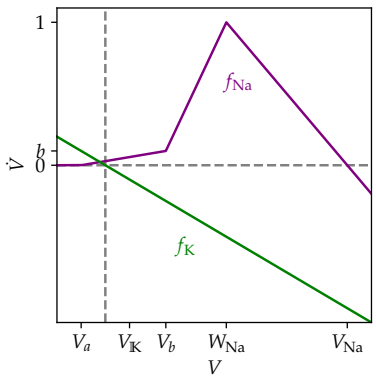

Figure 3.16: **Piecewise linear ion channels.** Adapted from Scheibner et al. [2023].

3.8.3 Preliminaries on the Conley index

Homotopy Conley index

Here I provide supplemental background on the Conley index [Conley and Sciences, 1978, Mischaikow and Mrozek, 2002] and provide derivations of the associated results used in §3.3, 3.5. Let X be a metric space. A flow ϕ on X is a continuous map $\phi : X \times \mathbb{R} \to X$ obeying the following conditions $\phi(x, 0) = x$ and $\phi(x, a+b) = \phi(\phi(x, a), b)$ for all $x \in X$ and $a, b \in \mathbb{R}$. An invariant set $S \subset X$ is one which obeys $\phi(S, \mathbb{R}) = S$. In other words, it is any union of solution curves of the flow. Given a set $N \subset X$, I define $\text{inv}(N) = \{x \in N : \phi(x, \mathbb{R}) \subset N\}$. A compact set N is known as an isolating set if $\text{inv}(N) \cap \partial N = \emptyset$. I say that an isolating set N is an isolating neighborhood of the invariant set S if $S = \text{inv}(N)$. An invariant set S is an isolated invariant set if it permits an isolating neighborhood. A pair of compact sets (N, L) with $L \subset N$ is known as an index pair if they satisfy the three following conditions:

1. $\text{cl}(N \setminus L)$ is an isolating set
2. L is forward invariant in N. That is $N \cap \phi(L, [0, \infty)) \subset L$.
3. L is an exit set for N. That is for all $x \in N$, if $\phi(x, [0, \infty)) \not\subset N$, then there exists $t > 0$ such that $\phi(x, [0, t)) \subset N$ and $\phi(x, t) \in L$.

I say that (N, L) is an index pair for an isolated invariant set S if $S = \text{inv}(N \setminus L)$. One can show that for every isolating set N, there exists an index pair for $\text{inv}(N)$. Given an index pair, I define the homotopy Conley index as follows

$$h(N, L) = \overline{(N/L, [L])} \tag{3.148}$$

Here, the notation $(N/L, [L])$ denotes the pointed topological space formed by the quotient of N and L, i.e. the space formed by identifying L to a single point. Given a pointed topological space (Y, y), the notation $\overline{(Y, y)}$ denotes the equivalence class of all topological spaces that

are homotopically equivalent to Y with fixed point y. If (N, L) and (N', L') are both index pairs for the isolated invariant set S, then one can show that $h(N, L) = h(N', L')$. Hence, given an isolated invariant set S, it is unambiguous to write $h(S)$ and refer to the Conley index as an intrinsic property of the isolated invariant set.

The Conley index obeys two crucial properties typical of topological indices. First, it obeys an addition formula: If S_1 and S_2 are disjoint isolated invariant sets, then

$$h(S_1 \sqcup S_2) = h(S_1) \vee h(S_2) \tag{3.149}$$

where $\sqcup$ is the disjoint union and $\vee$ is the wedge sum, which glues two pointed spaces together by identifying their distinguished points. Second, $h(S)$ has a continuity property. Suppose ϕ_λ has a continuous parameter $\lambda \in \Lambda$. If N_λ is continuous in λ and N_λ is an isolating neighborhood for all $\lambda \in \Lambda$, then $h(\text{inv}(N_\lambda)) = h(\text{inv}(N_{\lambda'}))$ for all $\lambda, \lambda' \in \Lambda$. Hence, one can deform flows and isolating neighborhoods, and so long as the isolated invariant sets do not intersect the boundaries of the proposed isolating neighborhoods, the index is invariant throughout the deformation.

In practice, the following facts are frequently used. For a hyperbolic fixed point p, $h(p) = \overline{\Sigma^d}$, where Σ^d is the pointed d-sphere and d is the unstable dimension of the fixed point. Also, if an isolating neighborhood N does not contain an isolated invariant set, then $\text{inv}(N) = \emptyset$, and $h(\emptyset) = \overline{0}$, where $\overline{0}$ denotes the space with a single point. This yields a seemingly simple but useful existence theorem: if $h(\text{inv}(N)) \neq \overline{0}$, then N must contain an isolated invariant set. This is useful because computing $h(\text{inv}(N))$ only requires information about ϕ on the boundary of N. Hence, one can choose N wisely to simplify computations of $h(\text{inv}(N))$. Finally, I note that for a hyperbolic fixed point p, the unstable dimension d is also known as the Morse index. For this reason, the Conley index may be thought of as generalization of the Morse index that is defined for any isolated invariant set, not just fixed points.

Homological Conley index

Homology theory is a set of algebraic tools for studying homotopy type classes. Given topological spaces $X \subset Y$, their relative homology refers to a sequence

$$H(Y, X) = (H_0(Y, X),\, H_1(Y, X),\, \dots) \tag{3.150}$$

where each H_n is an abelian group. For a pointed space (Y, y), the reduced homology of Y is defined as $H(Y) \equiv H(Y, y)$. There are multiple varieties of homology (i.e. different ways of assigning the sequence of abelian groups to topological spaces) that encode different types of topological information. Alexander-Spanier homology is a standard choice for Conley index theory. (I will simply state the facts that needed without offering a full definition.) All types of homology have the following two properties (among others). First, given two homotopically equivalent pointed topological space Y and Y', $H(Y) \cong H(Y')$, where $\cong$ denotes isomorphism. Hence, one can unambiguously talk about H as being a map from homotopy equivalence classes to graded abelian groups. Next, there is a useful addition property:

$$H(Y \vee Y') \cong H(Y) \oplus H(Y') \tag{3.151}$$

Finally, if $X \subset Y \subset Z$, then

$$\cdots \to H_n(Y, X) \to H_n(Z, X) \to H_n(Z, Y) \to H_{n-1}(Y, X) \to \cdots \tag{3.152}$$

is an exact sequence. By *exact sequence*, I mean that there exists homomorphisms between subsequent groups in the sequence and the image of one homomorphism is equal to the kernel of the next. Exact sequences are a useful construction for the following reason: if Eq. (3.152) contains a subsequence of the form $0 \to A \to B \to 0$, then the exactness property implies

$A \cong B$. For our purposes, the only homology groups explicitly needed are those of spheres:

$$H_n(\Sigma^d) = \begin{cases} 0 & n \neq d \\ \mathbb{Z} & n = d \end{cases} \tag{3.153}$$

and for the single point $H(\overline{0}) = 0$. In the context of Conley index theory, homology theory is used as follows. For any isolated invariant set S, one can always find an index pair (N, L) such that $H(N, L) = H(N/L, [L]) = H(h(S))$. The quantity $H(h(S))$ is known as the homological Conley index.

Morse decompositions

For $x \in X$, define $\alpha(x) = \bigcap_t \mathrm{cl}(\phi(x, (-\infty, -t)))$ and $\omega(x) = \bigcap_t \mathrm{cl}(\phi(x, (t, \infty)))$. Given an isolated invariant set S, a Morse decomposition of S is a finite list $(S_1, S_2, \ldots, S_n)$ of isolated invariant sets with $S_i \subset S$ such that for all $x \in S \setminus \sqcup_i S_i$ there exists $j < k$ such that $\omega(x) \subset S_j$ and $\alpha(x) \subset S_k$. For every Morse decomposition, there exists a sequence of isolating sets $(N_0, N_1, \ldots, N_n)$ such that (N_n, N_0) is an index pair for S and (N_i, N_{i-1}) is an index pair for S_i. Such a sequence is known as a Morse filtration. The notion of a Morse filtration is useful in conjunction with Eq. (3.152). Given a subset (N_{i-1}, N_i, N_{i+1}), one then obtains the exact sequence:

$$\cdots \to H_n(h(S_{i-1})) \to H_n(N_{i+1}, N_{i-1}) \to H_n(h(S_i)) \to H_{n-1}(h(S_{i-1})) \to \cdots \tag{3.154}$$

It turns out that (N_{i+1}, N_{i-1}) is itself an index pair.

Stability lemma

Following Ref. [Conley and Smoller, 1983], the above structure will be used to prove the following lemma. Suppose N is an isolating set with respect to gradient flow ϕ. Suppose

$h(\text{inv}(N)) = \overline{0}$ and N contains exactly two fixed points a and b, and let d_a and d_b denote their unstable dimensions. Then $d_a = d_b \pm 1$ and there exists a heteroclinic orbit from a to b if the $-$ is taken, and from b to a if the $+$ is taken.

To prove this, notice that $h(a) \vee h(b) = \overline{\Sigma^{d_a} \vee \Sigma^{d_b}} \neq \overline{0}$. Hence, there must be additional isolated invariant sets in N. Since gradient flow is being considered, the only possible additional isolated invariant set is a heteroclinic orbit flowing from a to b or from b to a. Without loss of generality, assume the flow runs from a to b. Then (b, a) constitutes a Morse decomposition, so there exists a Morse filtration (N_0, N_1, N). This Morse filtration gives rise to the exact sequence

$$\cdots \to H_n(\Sigma^{d_b}) \to H_n(\overline{0}) \to H_n(\Sigma^{d_a}) \to H_{n-1}(\Sigma^{d_b}) \to \cdots \tag{3.155}$$

But noting that $H_n(\overline{0}) = 0$ and using Eq. (3.153), one obtains the short exact sequence:

$$0 \to \mathbb{Z} \to H_{d_a-1}(\Sigma^{d_b}) \to 0 \tag{3.156}$$

The short exact sequence in Eq. (3.156) implies that $\mathbb{Z} \cong H_{d_a-1}(\Sigma^{d_b})$, which implies through Eq. (3.153) that $d_a = d_b + 1$, as desired.

CHAPTER 4

SPONTANEOUS WRINKLING OF ATOMICALLY THIN FILMS

4.1 Atomically thin films

Atomically thin films, such as graphene and transition-metal dichalcogenides (TMDs), are the thinnest conceivable materials made of atoms. Due to their significant promise for technological applications, such as sensors, actuators, and resonators, there is a growing need to understand their mechanical properties over large length scales with high spatial resolution [Kang et al., 2015, Kim et al., 2020, Yu et al., 2021b]. Achieving this level of understanding and control remains a topic of intense inquiry because atomically thin films are acutely sensitive to a range of both intrinsic and extrinsic extrinsic mechanical forces [Lee et al., 2008, Meyer et al., 2007, Warner et al., 2012, Bao et al., 2009], including thermal fluctuations, structural defects [Bao et al., 2009, Kim et al., 2018], and interactions with their environment [Lee et al., 2013, Han et al., 2020].

The central challenge arises from a simple paradox: to mechanically measure a material, one must first stabilize it. But stabilization itself requires direct interaction that modifies the mechanical state of the material. For instance, the largest freely suspended sheets of a monolayer atomically thin films are on the order of microns [Lee et al., 2008, Lloyd et al., 2016, Kim et al., 2018]. While such suspended configurations are often referred to as free-standing, they are not freestanding in the literal sense of the word: when suspended, a membrane's boundaries remain pinned to a substrate. This pinning subjects the membrane to relatively large and poorly characterized tension [Lee et al., 2008, Liu et al., 2014a] and prevents further motion of the boundaries. As a consequence, little is understood with certainty about the mechanical ground state and mechanical response on larger scales and when confining boundaries are released. This question is increasingly experimentally relevant because monolayer thin films can now be manufactured on the wafer scale using techniques

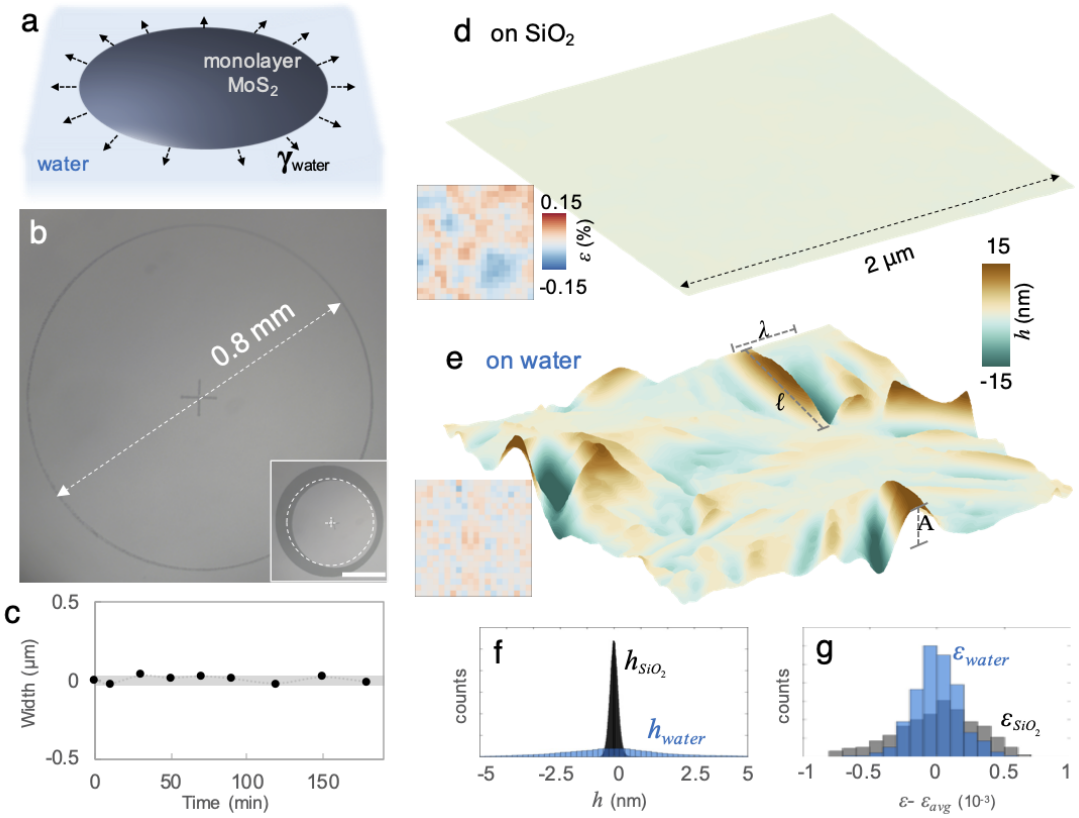

Figure 4.1: **Freestanding atomically thin MoS_2 on water. a.** Schematic describing the mechanical imaging of atomically thin membrane on water. **b.** Optical micrograph of mm-scale floating MoS_2 membrane with ≤ 2 μm gap created by laser patterning. The inset shows a membrane of same dimensions, displaced after 2 hours following patterning of 100 μm gap (the dotted line depicts the initial position). Scale bar=400μm. **c.** Time-dependent change of the gap distance between floating and anchored MoS_2. The standard deviation is shown as gray area. **d-e.** AFM height and the strain maps (inset) of (d) confined and (e) free membranes, respectively. **f-g.** The histogram of (f) height and (g) strain variation between confined and free membranes. Adapted from Yu et al. [2023].

such as metal-organic chemical vapor deposition [Kang et al., 2015]. This chapter, based on Yu et al. [2023], addresses the question: what are the mechanical properties of atomically thin materials when they are free from external perturbations and confinement?

4.1.1 Realizing freestanding atomically thin films on water

To study a freestanding atomically thin film, one must achieve a seemingly impossible objective: freeing and holding large-scale membranes with almost no perturbations to their mechanical states. Figure 4.1a-b shows a recently developed solution to this challenge: place the atomically thin film on water [Yu et al., 2023]. As shown in panel (a), water has two distinct advantages: First, the boundary is not subject to strong van der Waals attractions, but instead the membrane is held in place by uniform, well characterized, and relatively small surface tension of water. Second, the membrane can be directly laminated from a substrate onto water without intermediate fabrication steps, such as exfoliation or stamping via a polymer substrate. The ease of fabrication and the uniformity of water's surface allows for freely floating sheets that are on the mm-scale, over two orders of magnitude larger than μm-scale membranes available in suspended drumhead experiments [Lee et al., 2008, Lloyd et al., 2016, Kim et al., 2018]. Panels (b-c) illustrate a potentially counter intuitive feature of this platform: water is stable. By laser patterning a narrow (1 μm) moat around a freely floating membrane [Yu et al., 2022, Poddar et al., 2022], the membrane is stabilized on hours long timescales. This stabilization is sufficient to enable a full suite of mechanical characterizations on unconfined, wafer-scale atomically thin films.

Placing wafer-scale MoS_2 on water reveals something unexpected: wafer-scale, monolyaer MoS_2 is not flat. Figure 4.1d-e show atomic force microscopy (AFM) measurements of the surface topography of monolayer MoS_2. On the growth substrate (silicon dioxide) (d), the strong van der Waals interactions force the MoS_2 to lie as flat (nanometer smoothness) as the substrate itself. When released from solid confinement, a dramatic change in morphology occurs (e). The film forms wrinkles up to 15 nm in height and 100's of nanometers in length. Repeated measurements reveal that the wrinkles are static and athermal. Raman spectroscopy can be performed to estimate the typical strain on the membrane. While on silicon dioxide, the maximum strains can reach up to $\approx 0.5\%$, while on water the maximal

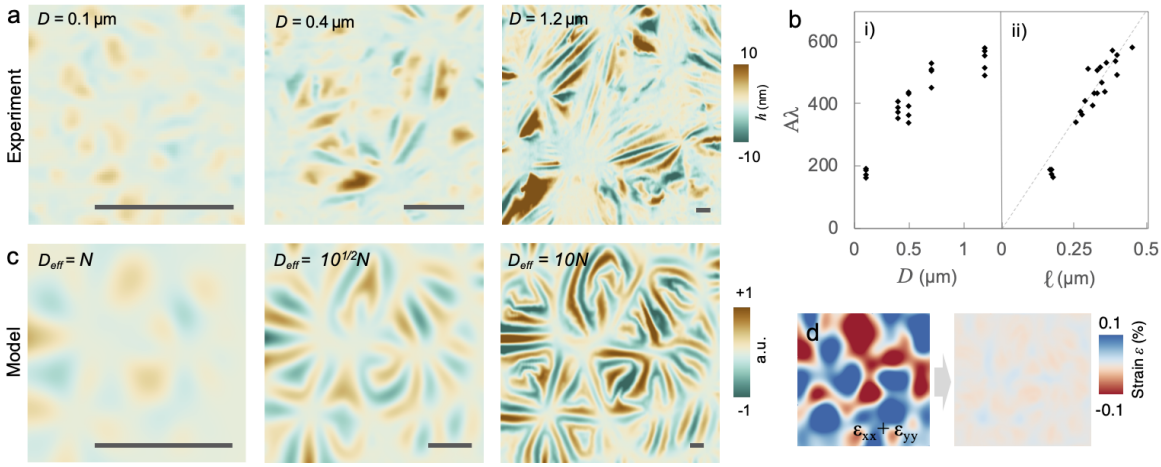

Figure 4.2: **Scaling of wrinklings via continuum elasticity. a.** Experimental measurements of MoS_2 surface topography on the water with increasing domain size D from left to right. Scale bar = 500 nm. **b.** The average wrinkle width λ wavelength and amplitude A plotted as a function of average domain size D and wrinkle length ℓ. The theoretical scaling in Eqs. (4.31-4.33) predicts a linear relationship $A\lambda \propto \ell$. **c.** Numerical relaxation of thin sheets with Gaussian distributed random strain [see Eq. (4.8)]. As the correlation length increases (left to right), the wrinkles become taller in amplitude and more eccentric. **d.** The trace of the strain tensor [Eq. (4.8)] prior to (left) and after (right) relaxation. Adapted from Yu et al. [2023].

strains are on the order of $\approx 0.01\%$, consistent with an estimate of γ/Y, where γ is the surface tension of water and Y is the Young's modulus of MoS_2.

Experiments reveal that the emergent wrinkles are strongly dependent on the intrinsic structure of the MoS_2. As shown in Fig. 4.2a, the experiment in Fig. 4.1 is repeated while the typical polycrystalline domain size D of MoS_2 is varied. With increasing domain size D, a systematic change in the wrinkle morphology is observed. For small domains $D \approx 100$nm, the wrinkles are shallow and relatively round. As the domain size increases, the height A, width λ, and length ℓ of the wrinkles all increase. Moreover, as the domain size increases, the wrinkles become more elongated (ℓ/λ increases). In Fig. 4.2b, $A\lambda$ is plotted as a function of D, revealing a collapse and an increasing relationship.

4.2 Disordered strain model

Here I provide a theoretical analysis that supports three following claims: (i) The wrinkles are not driven by external perturbations, but rather strains intrinsic to the material itself; (ii) The wrinkles are not unique to MoS_2 on water, but are instead expected to be a generic property of polycrystalline thin films when released from external confinement; (iii) The observed changes in morphology with domain size can be deduced using continuum theory without a detailed knowledge of the underlying atomic structure.

To demonstrate the wrinkles are indeed driven by intrinsic strain, and that the details of the atomic structure are unessential for the main morphological changes, I first show that the key morphological observations can be reproduced in a simplified mechanical model. The model, detailed below, has just two ingredients. First, it involves a thin sheet with both a bending B and stretching Y stiffness in which the elastic thickness $t = \sqrt{B/Y}$ is much smaller than any length scale in the plane of the membrane. Second, the sheet is subjected to a disordered initial prestrain. This prestrain is described by an overall magnitude $\Delta\epsilon$ and, crucially, a correlation length ξ. Physically, the correlation length ξ is expected to be a proxy for D, the domain size. No external forces, such as gravity or surface tension of the water, enter the model. (Indeed, both effects can easily be estimated as negligible). Moreover, the model is entirely continuum, taking no detailed facts about the crystalline structure of the membrane or its grain boundaries.

4.2.1 Continuum model

The model will be formulated in terms of a 2D elastic sheet embedded in three dimensional space. In the continuum, one can parameterize a sheet using a coordinate system $s \in \mathbb{R}^2$ and applying an embedding $\vec{r} : \mathbb{R}^2 \to \mathbb{R}^3$. I take the total energy to be:

$$E = E_{\text{stretch}} + E_{\text{bend}} \tag{4.1}$$

The bending energy is given by:

$$E_{\text{bend}} = B \int \text{Tr}\Big(N^2\Big) \sqrt{\det g}\, \mathrm{d}^2 s \tag{4.2}$$

where B is the bending stiffness, while g and N are known as the first and second fundamental forms, respectively. In terms of the embedding $\vec{r}(s)$, the first fundamental form and second fundamental forms can be expressed as:

$$g_{ab} = \partial_a \vec{r} \cdot \partial_b \vec{r} \quad \text{and} \quad N_{ab} = \partial_a \vec{r} \cdot \partial_b \hat{n} \tag{4.3}$$

where

$$\hat{n} = \frac{\vec{n}}{|\vec{n}|} \quad \text{and} \quad \vec{n} = \frac{1}{2} \epsilon_{ab} \partial_a \vec{r} \times \partial_b \vec{r} \tag{4.4}$$

Here, ϵ_{ab} is the Levi-Civita symbol, ∂_a denotes $\frac{\partial}{\partial s^a}$, and repeated indices are summed over. The stretching energy is given by.

$$E_{\text{stretch}} = \frac{1}{8} \int \Big[\lambda_1 \left(\text{Tr}\, \Delta g\right)^2 + \lambda_2 \,\text{Tr}\left(\Delta g\right)^2 \Big] \sqrt{\det g}\, \mathrm{d}^2 s \tag{4.5}$$

where λ_1 and λ_2 are Lamé coefficients. In terms of Lamé coefficients, the Young's modulus Y is given by

$$Y = \frac{4\lambda_2(\lambda_1 + \lambda_2)}{\lambda_1 + 2\lambda_2} \tag{4.6}$$

with torque-free and force-free boundaries. The quantity Δg is the metric deviation $\Delta g = g - g_0$, where g_0 is a target metric.

The key ingredients for the wrinkles are encoded in the target metric g_0. The precise form of the target metric is not crucial, but it should at least have the following qualitative

ingredients: it should involve a disordered strain field that is statistically homogeneous and isotropic; the strain intensity should have a bounded, well defined average; and spatial correlations in the strain field should die off with distance, yielding a well defined correlation length. For instance, here is a concrete construction of one such target metric: For each point s, draw two values $\nu_\parallel(s)$ and $\nu_\perp(s)$ independently from the uniform distribution $[-1, 1]$, and draw an angle $\theta(s)$ from the uniform distribution over $[0, \pi)$. Define the matrix:

$$\eta(s) = \begin{bmatrix} \nu_\parallel \cos^2\theta + \nu_\perp \sin^2\theta & (\nu_\perp - \nu_\parallel)\cos\theta\sin\theta \\ (\nu_\perp - \nu_\parallel)\cos\theta\sin\theta & \nu_\parallel \sin^2\theta + \nu_\perp \cos^2\theta \end{bmatrix} \tag{4.7}$$

which is the matrix with eigenvalues $\nu_\parallel$ and $\nu_\perp$ and eigenvectors $[\cos\theta, \sin\theta]^T$ and $[-\sin\theta, \cos\theta]^T$, respectively. Next, introduce the strain scale $\Delta\epsilon$ and length scale ξ and define

$$g_0(s) = 1 + \frac{\xi\Delta\epsilon}{Z(s)} \int \eta(s') \exp\left[-\frac{d(s,s')^2}{2\xi^2}\right] \mathrm{d}^2 s' \tag{4.8}$$

where $d(s,s') = \sqrt{(s_1 - s_1')^2 + (s_2 - s_2')^2}$ imposes a Euclidean structure on the distinguished coordinate system and $Z(s) = \int \exp\left[-d(s,s')^2/2\xi^2\right] \mathrm{d}s'$ is a normalization constant. (If the sheet has infinite size, then $Z(s) = 2\pi\xi^2$).

I will refer to the elastic stiffness of the sheet as $t = \sqrt{\frac{B}{Y}}$. Our goal is to find embeddings that minimize the total energy E and study these embeddings in the limit that $t \to 0$.

4.2.2 Numerical discretization

To perform a relaxations numerically, a discrete version of the above continuum model is implemented. The thin sheet is represented by a collection of vertices $\mathcal{V}$, each of which is assigned a reference point $\vec{x}_i \in \mathbb{R}^2$ in the flat Cartesian plane, and a target point $\vec{r}_i \in \mathbb{R}^3$ in three dimensions. The reference points $\vec{x}_i$ form a regular triangular lattice of lattice spacing a. The vertices are triangulated to form a set $\mathcal{N}$ of counterclockwise oriented triangular

simplices $\alpha = (\alpha_1, \alpha_2, \alpha_3) \in \mathcal{V}^3$. The total energy is given by:

$$E = E_{\text{stretch}} + E_{\text{bend}} \tag{4.9}$$

The bending energy is given by [Seung and Nelson, 1988]:

$$E_{\text{bend}} = \frac{\kappa}{2} \sum_{\alpha \in \mathcal{N}} \sum_{\beta \in N(\alpha)} \left(1 - \hat{n}_\alpha \cdot \hat{n}_\beta\right) \tag{4.10}$$

where $\hat{n}_\alpha \in \mathbb{R}^3$ is the normal vector to simplex α and $N(\alpha)$ denotes the set of all simplices that share an edge with simplex β. The normals can be computed via the shoelace formula:

$$\hat{n}_\alpha = \frac{\vec{n}_\alpha}{|\vec{n}_\alpha|} \quad \text{with} \quad \vec{n}_\alpha = \frac{1}{2} \sum_{i=1}^{3} \vec{r}_{\alpha_i} \times \vec{r}_{\alpha_{i+1}} \tag{4.11}$$

where the indices on the simplex α are interpreted periodically. In terms of κ, the macroscopic bending stiffness is $B = \sqrt{3}\kappa/2$.

The stretching energy is given by:

$$E_{\text{stretch}} = \frac{1}{8} \sum_{\alpha \in \mathcal{N}} A^\alpha \left[\lambda_1 \left(\operatorname{Tr} \Delta g^\alpha\right)^2 + \lambda_2 \operatorname{Tr}(\Delta g^\alpha)^2\right] \tag{4.12}$$

where A^α is the area of simplex α, which I approximate by its undeformed value $A^\alpha \approx \frac{\sqrt{3}}{2} a^2$. The quantity $\Delta g^\alpha = g^\alpha - g_0^\alpha$ is the metric deviation (i.e., twice the strain tensor). Here, g^α is the discrete metric computed for each simplex, with respect to the coordinate system $\vec{x}_i$ is given by:

$$g^\alpha = X_\alpha^{-T} \cdot M_\alpha \cdot X_\alpha^{-1} \tag{4.13}$$

The matrix X is given by

$$X_\alpha = \begin{bmatrix} \vec{x}_\alpha^{12} & \vec{x}_\alpha^{23} \end{bmatrix} \tag{4.14}$$

where $\vec{x}_\alpha^{12} = \vec{x}_{\alpha_1} - \vec{x}_{\alpha_2}$ and $\vec{x}_\alpha^{23} = \vec{x}_{\alpha_2} - \vec{x}_{\alpha_3}$. The matrix M_α is given by

$$M_\alpha = \begin{bmatrix} \vec{r}_\alpha^{12} \cdot \vec{r}_\alpha^{12} & \vec{r}_\alpha^{23} \cdot \vec{r}_\alpha^{12} \\ \vec{r}_\alpha^{23} \cdot \vec{r}_\alpha^{12} & \vec{r}_\alpha^{23} \cdot \vec{r}_\alpha^{23} \end{bmatrix} \tag{4.15}$$

where $\vec{r}_\alpha^{12} = \vec{r}_{\alpha_1} - \vec{r}_{\alpha_2}$ and $\vec{r}_\alpha^{23} = \vec{r}_{\alpha_2} - \vec{r}_{\alpha_3}$.

The target metric g_0^α is constructed as follows. For each simplex, I draw two values $\nu_\parallel^\alpha$ and $\nu_\perp^\alpha$ from the uniform distribution over $[-1, 1]$, and an angle θ^α from the uniform distribution over $[0, \pi)$. I define the matrix η^α as:

$$\eta^\alpha = \begin{bmatrix} \nu_\parallel^\alpha \cos^2\theta^\alpha + \nu_\perp^\alpha \sin^2\theta^\alpha & (\nu_\perp^\alpha - \nu_\parallel^\alpha)\cos\theta^\alpha \sin\theta^\alpha \\ (\nu_\perp^\alpha - \nu_\parallel^\alpha)\cos\theta^\alpha \sin\theta^\alpha & \nu_\parallel^\alpha \sin^2\theta^\alpha + \nu_\perp^\alpha \cos^2\theta^\alpha \end{bmatrix} \tag{4.16}$$

which is the matrix with eigenvalues $\nu_\parallel^\alpha$ and $\nu_\perp^\alpha$ and orthogonal eigenvectors $[\cos\theta^\alpha, \sin\theta^\alpha]^T$ and $[-\sin\theta^\alpha, \cos\theta^\alpha]^T$, respectively. To construct the target metric, I define a correlation length ξ and a strain magnitude $\Delta\epsilon$ and define

$$g_0^\alpha = 1 + \frac{\xi \Delta\epsilon}{Z_\alpha} \sum_{\beta \in \mathcal{N}} \eta^\beta \exp\left(-\frac{d_{\alpha\beta}^2}{2\xi^2}\right) \tag{4.17}$$

where $d_{\alpha\beta} = \left|\frac{1}{3}\sum_{i=1}^3 (\vec{x}_{\alpha_i} - \vec{x}_{\beta_i})\right|$ is the distance between the centers of simplices α and β, and $Z_\alpha = \sum_{\beta\in\mathcal{N}} \exp\left(-d_{\alpha\beta}^2/2\xi^2\right)$ is a normalization constant. The energy is minimized using the Fast Inertial Relaxation Engine algorithm [Bitzek et al., 2006, Hanakata et al., 2021].

Fig. 4.2 c-e shows the height maps for several values of ξ at constant $\Delta\epsilon$, as well as a

visualization of the typical strain field before and after relaxation. One can observe that the minimal model reproduces the change in morphology observed in experiment, as ξ becomes large, the wrinkles become more elongated and increase in amplitude, width, and length. These shared morphological changes support of the hypothesis that the wrinkles arise to an intrinsic strain driven process that is generic to a disordered strain field.

4.3 Universal scaling relations

Motivated by the strong qualitative agreement between the simulated minimal model and the experiment, below I propose scaling relationships for the morphology of the winkles based on continuum elasticity [Wang et al., 2022, Aharoni et al., 2017, Wu et al., 2013, Vandeparre et al., 2011, Matsumoto et al., 2015, Sharon et al., 2002a, Tobasco, 2021, Komaragiri et al., 2005, Hanakata et al., 2021].

4.3.1 Tension induced wrinkling

The scaling arguments are based on a notion known as tension (or curvature) induced wrinkling [Davidovitch et al., 2011, Tobasco, 2021, Cerda and Mahadevan, 2003, Pocivavsek et al., 2008]. To introduce the concept, I will review the theoretical basis of the scaling in two steps. First, imagine placing a thin sheet of width W and length L on a dense fluid and compressing it by a distance Δ. What is the amplitude and wavelength of the wrinkles that form in the compressed sheet? Since the sheet is being compressed in a quasi-one-dimensional manner, it can relieve nearly all of its compression energy by buckling. The resulting configuration will be determined by a balance between the buoyant energy of the water and the bending energy of the membrane. This is mathememtatized by minimizing the following functional:

$$\mathcal{L} = \frac{LB}{2}\int_0^W \left(\partial_x^2 h\right)^2 \mathrm{d}x + \frac{\rho g L}{2}\int_0^W h^2 \mathrm{d}x + Lp\int_0^W \left[\sqrt{1+(\partial_x h)^2} - 1 + \frac{\Delta}{W}\right]\mathrm{d}x \quad (4.18)$$

where $h(x)$ is the height profile in the buckled direction. The first term in Eq. (4.18) is the bending energy, the second term is the gravitational potential energy from the displaced fluid, and the third term is includes a Lagrange multiplier p that enforces length conservation in the wrinkled direction. Assuming small slopes $\partial_x h$, but not necessarily small amplitudes, the Euler-Lagrange equation become:

$$0 = B\partial_x^4 h + \rho g h + p\partial_x^2 h \tag{4.19}$$

along with

$$\frac{1}{2}\int_0^W (\partial_x h)^2 \mathrm{d}x = \Delta \tag{4.20}$$

Rather than impose rigorous boundary conditions, for our purposes it is sufficient to consider an ansatz $h = A\sin kx$. In this case, the length constraint yields

$$kA = \left(\frac{\Delta}{W}\right)^{1/2} \tag{4.21}$$

Moreover, Eq. (4.19) yields the condition

$$k^2 = \frac{p \pm \sqrt{p^2 - 4B\rho g}}{2B} \tag{4.22}$$

The smallest value of p such that k is real is given by:

$$p = 2\sqrt{B\rho g} \tag{4.23}$$

which implies that

$$k = \left(\frac{\rho g}{B}\right)^{1/4} \tag{4.24}$$

which yields a scaling relationship for k and A in terms of B and ρg.

As a second step, now imagine that the sheet is not on water, but it is under tension T in the y direction. The bending energy is now given by:

$$U_{\text{bend}} = \frac{B}{2}\int_0^W \int_{-L/2}^{L/2} \left(\nabla^2 h\right)^2 \mathrm{d}y\mathrm{d}x \tag{4.25}$$

and the interaction energy with the applied tension is given by:

$$U_{\text{stretch}} = T\int_0^W \left[\int_{-L/2}^{L/2} \sqrt{1+\left(\partial_y h\right)^2}\mathrm{d}y - L\right]\mathrm{d}x \tag{4.26}$$

I assume that the boundaries at $y = \pm L/2$ are pinned vertically, and so I apply the ansatz $h(x,y) = H(x)\cos(\pi y/L)$. In this case, the dominant contribution to the bending energy is:

$$U_{\text{bend}} \approx \frac{LB}{2}\int_0^W \left(\partial_x^2 H\right)^2 \mathrm{d}x \tag{4.27}$$

and the dominant contribution to the stretching energy is:

$$U_{\text{stretch}} \approx \frac{\pi^2 T}{L}\int_0^W H^2 \mathrm{d}x \tag{4.28}$$

Notice that combining Eqs. (4.27-4.28) yields a minimization of the form of Eq. (4.18) with an effective substrate stiffness induced by tension: $\rho g = \pi^2 T/L$. Therefore, the wrinkling under tension obeys the following scaling relations:

$$k \propto L^{-1/2}\left(\frac{T}{B}\right)^{1/4} \tag{4.29}$$

$$kA \propto \left(\frac{\Delta}{W}\right)^{1/2} \tag{4.30}$$

These are the tension induced wrinkling scaling relations.

4.3.2 Implications for disordered strain field

I propose the geometry of the observed wrinkles is governed determined by tension induced wrinkling where the relevant tension is not an external force, but rather internal tension trapped due to grain boundaries. In the spirit of tension field theory [Tobasco, 2021], imagine releasing the membrane in two steps: first allow the atoms to move in-plane, but not in the third dimension. This will reduce the initial stress to some partially relaxed stress field $\sigma_{ij}(\mathbf{x})$. At every point in space the stress tensor $\sigma_{ij}(\mathbf{x})$ can be decomposed into orthogonal principle axes. When one axis is under compression and the other is under tension, the membrane will wrinkle with some characteristic wavelength λ in the direction that relieves compression. One expects that the typical compression will be proportional to $\Delta\epsilon$. So length conservation in the wrinkled direction implies $A/\lambda \propto (\Delta\epsilon)^{1/2}$, as implied by Eq. (4.30).

The wavelength $\lambda = 2\pi/k$ will then be set by the typical tension T and typical length L of the tensile unit, according to Eqs. (4.30). The typical length of the tensile unit is determined before the membrane even relaxes into the third dimension, so it must be set by the length scale ξ. Furthermore, one would expect the typical tension to be proportional to $T \propto Y\Delta\epsilon$, where Y is the Young's modulus. Hence, Eqs. (4.29-4.30) imply

$$A \propto (\Delta\epsilon)^{1/4}\xi^{1/2}t^{1/2} \tag{4.31}$$

$$\lambda \propto (\Delta\epsilon)^{-1/4}\xi^{1/2}t^{1/2} \tag{4.32}$$

$$\ell \propto \xi \tag{4.33}$$

Notice that Eqs. (4.31-4.32) explain the qualitative changes in morphology of the wrinkles: the amplitude A, wavelength λ, and length ℓ all increase with domain size. Moreover, the length of the wrinkles scale as ξ, while the width scales as $\lambda \propto \xi^{1/2}$, implying that the wrinkles become more elongated with domain size. In Fig. 4.2d, a plot $A\lambda$ as a function of ℓ for the measured wrinkles from Fig. 4.2a, revealing a collapse consistent with a linear

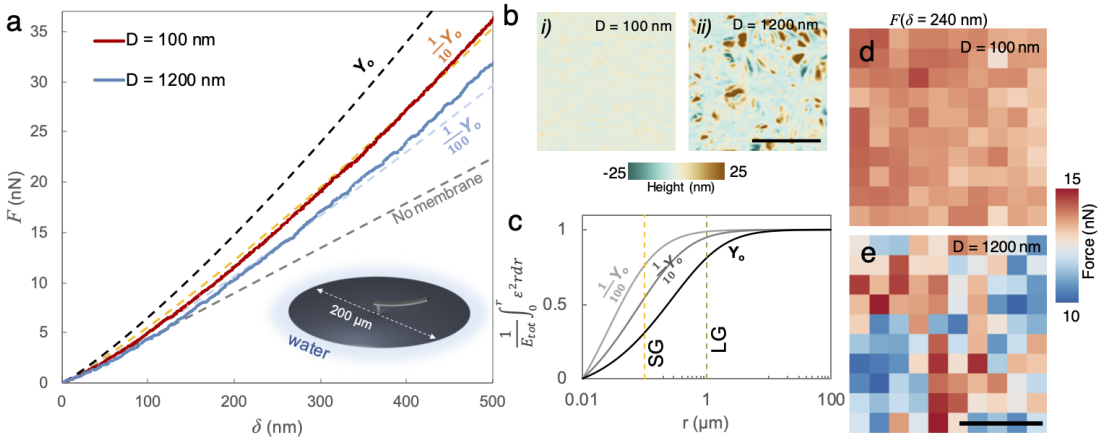

Figure 4.3: **Effective mechanical properties of wrinkled MoS_2. a.** Force-displacement curve for a sheet of MoS_2 by AFM. Red and blue line corresponds large-grain ($D = 1200nm$) and small-grain ($D = 100nm$), respectively. The dotted line shows the theoretical simulation of the floating membrane indentation with different Young's modulus given by Y_0, $Y_0/10$, and $Y_0/100$, where Y_0 is Young's modulus of pristine MoS_2, and Gray dotted line shows without the membrane. Inset shows the schematic of AFM indentation on a floating monolayer MoS_2 membrane. **b.** The surface topography of floating MoS2 with different domain sizes. i) $D = 100nm$, and ii) $D = 1200nm$. Scale bar = $5\mu m$. **c.** Theoretical strain energy profiles of a membrane for a given indentation depth h as a function of radius from the point of indenter $r = 0$ on water with different Modulus. Dotted lines show the size of the typical domains for D = 1200nm(LG), and D = 100 nm(SG). **d-e.** The force response map of $D = 100nm$ (d), and $D = 1200nm$ (e) on the area presented in (b). The force is measured at the indentation depth $\delta = 240nm$. Scale bar = $5\mu m$. Adapted from Yu et al. [2023].

relationship implied by Eqs. (4.31-4.33). Moreover, Eqs. (4.31-4.33) imply that the slope m of the fitted line should be proportional to the elastic thickness t of the membrane, and therefore of a similar order of magnitude. The slope is approximately 1 nm and the thickness of the membrane is approximately 0.3 nm.

4.4 Indentation experiments

In Fig. 4.1, AFM was used as gentle tool to probe the ground state mechanical structure of the freely floating MoS_2. One can also use the AFM as a probe of mechanical response by performing indentation experiments, as shown in Fig. 4.3a. Such an experiment provides a

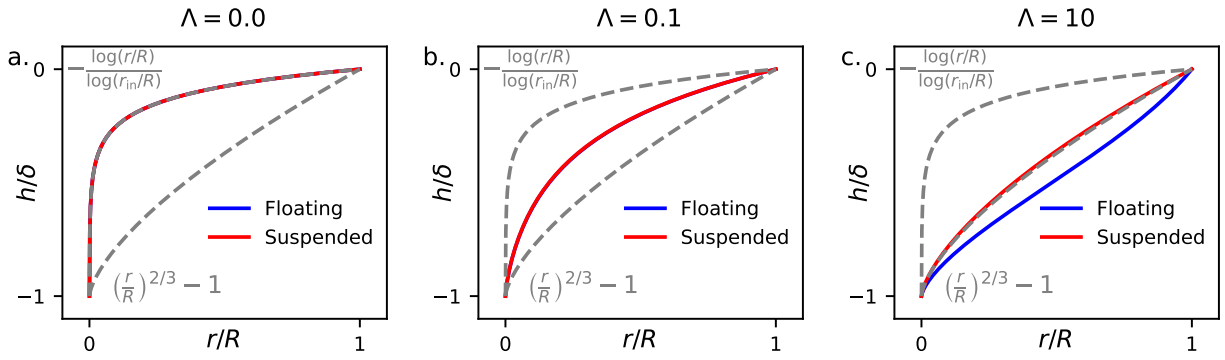

Figure 4.4: **Boundary conditions and indentation regimes.** The spatial profiles $h(r)$ are shown for increasing values of $\Lambda = \frac{Y}{2\gamma}\left(\frac{\delta}{R}\right)^2$. **a.** $\Lambda = 0.0$ corresponds to exposed water with no membrane. **b.** $\Lambda = 0.1$ is the maximum value probed in our experiments. **c.** $\Lambda = 10$ is a regime familiar from nanoindentation of $1\mu m$ drum-heads. The blue curve has an inflection point, indicating that the solution is unstable to an azimuthal buckling instability. The red curves correspond to a pinned boundary condition, as is the case for suspended membrane experiments. The blue curves correspond to constant stress boundary conditions, applicable for floating membranes. The grey dashed lines are asymptotic solutions that can be calculated analytically. Adapted from Yu et al. [2023].

window into how the nontrivial topography of MoS_2 affect its mechanical response.

4.4.1 Föppl-von Kármán theory

Figure 4.3a shows two experimental curves for the force (F) vs displacement (δ) for a 200 μm diameter floating sheet of monolayer MoS_2 with large ($D = 1200$ nm) and small ($D = 100$nm) grains. While it may initially seem that poking is a method of investigation reserved for children, the indentation of shells and membranes is actually a theoretically rich topic [Komaragiri et al., 2005, Box et al., 2017]. Even without considering the role of the wrinkled topography, there are already at least four length scales in the problem: the radius R of the membrane, the thickness t of the membrane, the radius of the indenter r_{tip} and the depth of indentation δ. Moreover, there are competing force scales introduced by the presence of surface tension (e.g. surface tension γ), buoyancy, and elastic forces, which are also potentially influenced by the choice of boundary conditions. The interplay between these scales can give

rise to distinct force-displacement scaling behaviors as well as potential instabilities. As will be shown, the relevant regime for our experiment is actually distinct from that used in 1μm scale drumhead experiments studied previously [Lee et al., 2008], and is not captured by the most common asymptotic expansions [Komaragiri et al., 2005, Box et al., 2017]. Moreover, the following theoretical analysis will also predict when force response to indentation should be homogeneous or heterogeneous over the wrinkled material. When it is homogeneous, order of magnitude estimates of the effective Young's modulus of the wrinkled sheet can be made.

For an asymptotically thin sheets, the mechanics of the out-of-plane deformation are well described by the Föppl-von Kármán equations:

$$B_{\text{eff}}\nabla^4 h + \epsilon_{ij}\epsilon_{kl}\partial_i\partial_k\chi\partial_j\partial_l h + \rho g h = 0 \tag{4.34}$$

$$\nabla^4\chi + \frac{Y_{\text{eff}}}{2}\epsilon_{ij}\epsilon_{kl}\partial_i\partial_k h\partial_j\partial_l h = 0 \tag{4.35}$$

where B_{eff} is the effective bending stiffness, h is the height of the membrane, $\rho g h$ is the force of gravity, χ is the Airy Stress function, Y_{eff} is the effective Young's modulus. The geometry I consider is a circular membrane of radius R on the surface of water subject to a an indentation by a circular indenter of radius r_{tip}. Outside the membrane, there is a narrow channel of exposed water followed by another segment of MoS_2 which I will assume pins the water level to 0.

Anticipating azimuthal symmetry of the indented membrane, one can convert Eqs. (4.34-4.35) to the following set of coupled ordinary differential equations:

$$\frac{B_{\text{eff}}}{r}\frac{\mathrm{d}}{\mathrm{d}r}\left\{r\frac{\mathrm{d}}{\mathrm{d}r}\left[\frac{1}{r}\frac{\mathrm{d}}{\mathrm{d}r}\left(r\frac{\mathrm{d}h}{\mathrm{d}r}\right)\right]\right\} - \frac{1}{r}\frac{\mathrm{d}}{\mathrm{d}r}\left(\frac{\mathrm{d}\chi}{\mathrm{d}r}\frac{\mathrm{d}h}{\mathrm{d}r}\right) + \rho g h = 0 \tag{4.36}$$

$$\frac{\mathrm{d}}{\mathrm{d}r}\left\{r\frac{\mathrm{d}}{\mathrm{d}r}\left[\frac{1}{r}\frac{\mathrm{d}}{\mathrm{d}r}\left(r\frac{\mathrm{d}\chi}{\mathrm{d}r}\right)\right]\right\} + \frac{Y_{\text{eff}}}{2}\frac{\mathrm{d}}{\mathrm{d}r}\left(\frac{\mathrm{d}h}{\mathrm{d}r}\right)^2 = 0 \tag{4.37}$$

Subject to azimuthal symmetry, the airy stress function and the stress tensor are related via:

$$\sigma_{rr} = \frac{1}{r}\frac{\mathrm{d}\chi}{\mathrm{d}r} \quad \text{and} \quad \sigma_{\theta\theta} = \frac{\mathrm{d}^2\chi}{\mathrm{d}r^2} \tag{4.38}$$

The solution to Eqs. (4.36 -4.37) are stable so long as the hoop stress is positive (i.e. $\sigma_{\theta\theta} \geq 0$). If the hoop stress is negative (i.e. $\sigma_{\theta\theta} < 0$), then the radially symmetric solution is unstable and the system undergoes an azimuthal buckling instability to alleviate the azimuthal compression. (As discussed below, we will find that the experimental regime of interest is stable).

To fully specify the problem, one must consider the boundary conditions. The boundary conditions on $h(r)$ include:

$$h(r_{\mathrm{tip}}) = -\delta \tag{4.39}$$

$$\left.\frac{\mathrm{d}h}{\mathrm{d}r}\right|_{r=r_{\mathrm{tip}}} = 0 \tag{4.40}$$

$$h(R) = 0 \tag{4.41}$$

$$\left.\frac{\mathrm{d}}{\mathrm{d}r}\left(r\frac{\mathrm{d}h}{\mathrm{d}r}\right)\right|_{\mathrm{r=R}} = 0 \tag{4.42}$$

where δ is the indentation depth. Condition (4.39) states that the internal indenter has pushed the inner radius down by a distance δ. Condition (4.40) is based on the assumption that the slope of the membrane is flat underneath the indenter and continuous at the edge of the indenter. Condition (4.41) states that the water level is pinned to 0 at the edge of the membrane. Condition (4.42) states that the water does not exert a torque at the edge of the membrane.

The boundary conditions on χ include:

$$\left.\frac{\mathrm{d}\chi}{\mathrm{d}r}\right|_{r=R} = R\gamma \tag{4.43}$$

$$\left(r\frac{\mathrm{d}^2\chi}{\mathrm{d}r^2} - \nu\frac{\mathrm{d}\chi}{\mathrm{d}r}\right)_{r=r_{\mathrm{tip}}} = \gamma(1-\nu) \tag{4.44}$$

$$\frac{\mathrm{d}}{\mathrm{d}r}\left[\frac{1}{r}\frac{\mathrm{d}}{\mathrm{d}r}\left(r\frac{\mathrm{d}\chi}{\mathrm{d}r}\right)\right]_{r=r_{\mathrm{tip}}} = 0 \tag{4.45}$$

$$\chi(R) = 0 \tag{4.46}$$

where γ is the air-water surface tension and ν is the 2D Poisson's ratio of the membrane. Condition (4.43) states that the the outer boundary of the membrane is in mechanical equilibrium with the surface tension of the water. Condition (4.44) states that there is no radial slip at the edge of the indenter. Condition (4.45) is a common assumption that allows for a simplified first integral of Eq. (4.36). Condition (4.46) is a gauge fixing of χ (this condition may be omitted since I need not solve for the field χ, only its derivatives).

Having fully specified the governing equations, Eqs. (4.36-4.37) can be numerically solved without any further mathematical analysis (which will come). If the sheet membrane were not polycrystalline (i.e. it is one undefected crystal), then it would not feature wrinkles. In

this case, the relevant numerical parameters include:

$$\gamma = 7.2 \times 10^{-2} kg/s^2 \tag{4.47}$$

$$B_0 = 1.7 \times 10^{-18}\, kg\, m^2/s^2 \tag{4.48}$$

$$Y_0 = 1.7 \times 10^{2}\, kg/s^2 \tag{4.49}$$

$$\rho g = 10^{4}\, kg/m^2 s^2 \tag{4.50}$$

$$R = 2 \times 10^{-4} m \tag{4.51}$$

$$r_{\text{tip}} \approx 5 \times 10^{-9} m \tag{4.52}$$

$$\nu \approx 0.25 \tag{4.53}$$

where B_0 and Y_0 are the bending stiffness Young's modulus of single crystal MoS_2, ρg sets the buoyancy force of water, and ν is the Poisson's ratio. The maximum indentation depth is $\delta \sim 10^{-5}$m and typical measured forces are on the order of $F \sim 10^{-7}$ kg m/s^2.

Given a solution for h, the reaction force on the indenter can be computed via

$$F = 2\pi B_{\text{eff}} \left\{ r \frac{\mathrm{d}}{\mathrm{d}r} \left[\frac{1}{r} \frac{\mathrm{d}}{\mathrm{d}r} \left(r \frac{\mathrm{d}h}{\mathrm{d}r} \right) \right] \right\}_{r=r_{\text{tip}}} \tag{4.54}$$

Performing this procedure gives rise to the black dashed theoretical curve in Fig. 4.3a. Notice that the measured curves (blue and red) reside below the black line, indicating that the wrinkles have a softening effect. Below I discuss the mathematical structure of the equations that give insight into the dominant mechanism behind the softening.

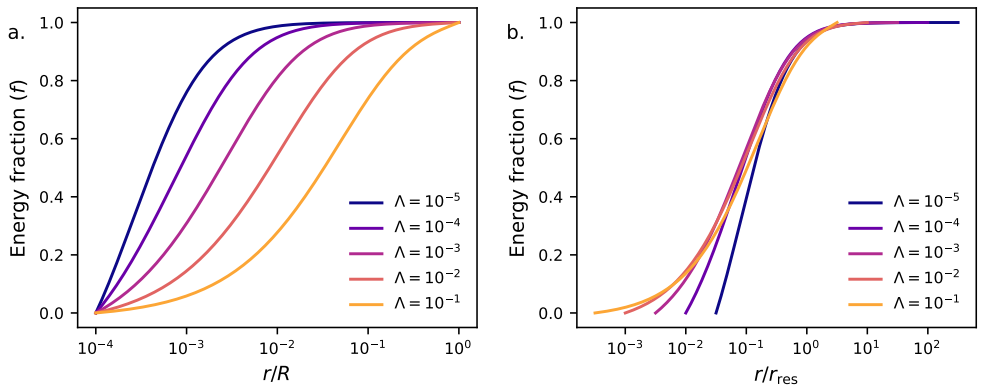

Figure 4.5: **Identification of mechanical resolution a.** The fraction f of deformation energy as a function of $\xi = r/R$ for $\Lambda \ll 1$, see Eq. (4.81). The shoulder in each curve sets a radius, the mechanical resolution, within which the majority of the deformation energy resides. **b.** The location of the shoulder can be collapsed by rescaling r by $r_{\text{res}} = \delta\sqrt{Y/2\gamma}$. Adapted from Yu et al. [2023].

4.4.2 Nondimensionalization

In order to understand the dominant force balance with the indented membrane, one can organize the parameters into a sequence of physically meaningful length scales:

$$t_0 = \sqrt{\frac{B_0}{Y_0}} = 10^{-10} m \qquad \text{Elastic thickness of single-crystal } MoS_2 \tag{4.55}$$

$$r_{\text{tip}} \approx 5 \times 10^{-9} m \qquad \text{AFM tip radius} \tag{4.56}$$

$$\ell_{EC} = \sqrt{\frac{B_0}{\gamma}} \approx 5 \times 10^{-9} m \qquad \text{Elasto-capillary length} \tag{4.57}$$

$$\ell_g = \left(\frac{B_0}{\rho g}\right)^{1/4} = 3.6 \times 10^{-6} m \qquad \text{Elasto-gravitational length} \tag{4.58}$$

$$\delta_{\max} = 10^{-5} m \qquad \text{Maximum depth of indentation} \tag{4.59}$$

$$R = 2 \times 10^{-4} m \qquad \text{Membrane Radius} \tag{4.60}$$

$$\ell_C = \sqrt{\frac{\gamma}{\rho g}} = 2.3 \times 10^{-3} m \qquad \text{Capillary length} \tag{4.61}$$

Additional length scales include the typical domain size, 0.1-1.0μm, and the height of the typical wrinkle 2 -30 nm, the wavelength of a typical wrinkle 0.1-0.5μm, and the typical

length of the wrinkles 0.1-1.0μm.

To understand the general behavior of Eq. (4.36-4.37), I introduce the following nondimensionalization of the variables:

$$\xi = \frac{r}{R} \tag{4.62}$$

$$\tilde{\chi} = \frac{\chi}{\gamma R^2} \tag{4.63}$$

$$h = \frac{h}{\delta} \tag{4.64}$$

in terms of which Eqs. (4.36-4.37) become

$$\frac{\ell_{EC}^2}{R^2}\frac{1}{\xi}\frac{\mathrm{d}}{\mathrm{d}\xi}\left\{\xi\frac{\mathrm{d}}{\mathrm{d}\xi}\left[\frac{1}{\xi}\frac{\mathrm{d}}{\mathrm{d}\xi}\left(\xi\frac{\mathrm{d}\tilde{h}}{\mathrm{d}\xi}\right)\right]\right\} - \frac{1}{\xi}\frac{\mathrm{d}}{\mathrm{d}\xi}\left(\frac{\mathrm{d}\tilde{\chi}}{\mathrm{d}\xi}\frac{\mathrm{d}\tilde{h}}{\mathrm{d}\xi}\right) + \frac{R^2}{\ell_C^2}\tilde{h} = 0 \tag{4.65}$$

$$\frac{\mathrm{d}}{\mathrm{d}\xi}\left\{\xi\frac{\mathrm{d}}{\mathrm{d}\xi}\left[\frac{1}{\xi}\frac{\mathrm{d}}{\mathrm{d}\xi}\left(\xi\frac{\mathrm{d}\tilde{\chi}}{\mathrm{d}\xi}\right)\right]\right\} + \frac{Y}{2\gamma}\left(\frac{\delta}{R}\right)^2\frac{\mathrm{d}}{\mathrm{d}\xi}\left(\frac{\mathrm{d}\tilde{h}}{\mathrm{d}\xi}\right)^2 = 0 \tag{4.66}$$

Equation (4.65) represents force balance in the z-direction. First notice that $(R/\ell_C)^2 \approx 10^{-2}$. Hence, throughout the gravity term only represents a small perturbation to the force balance and can be controllably neglected. Moreover, since $(\ell_{EC}/R)^2 \approx 10^{-10}$, the bending term is almost entirely negligible. It's only function is to form a narrow boundary layer, whose width sets an effective internal radius $r_{\mathrm{in}} \approx r_{AFM} + \ell_{EC}$. Thus, the vertical profile of the indented radius will be determined by the following reduced equations:

$$\frac{\mathrm{d}}{\mathrm{d}\xi}\left(\frac{\mathrm{d}\tilde{\chi}}{\mathrm{d}\xi}\frac{\mathrm{d}\tilde{h}}{\mathrm{d}\xi}\right) = 0 \tag{4.67}$$

$$\xi\frac{\mathrm{d}}{\mathrm{d}\xi}\left[\frac{1}{\xi}\frac{\mathrm{d}}{\mathrm{d}\xi}\left(\xi\frac{\mathrm{d}\tilde{\chi}}{\mathrm{d}\xi}\right)\right] + \Lambda\left(\frac{\mathrm{d}\tilde{h}}{\mathrm{d}\xi}\right)^2 = 0 \tag{4.68}$$

For boundary conditions on Eqs. (4.67-4.68) I will impose on the height field

$$\tilde{h}(\tilde{r}_{\text{in}}) = -1 \tag{4.69}$$

$$\tilde{h}(1) = 0 \tag{4.70}$$

For the interior boundary, I impose a no-slip boundary condition

$$\left(\frac{\mathrm{d}^2\tilde{\chi}}{\mathrm{d}\xi^2} - \frac{\nu}{\xi}\frac{\mathrm{d}\tilde{\chi}}{\mathrm{d}\xi}\right)_{\xi=\tilde{r}_{in}} = 1-\nu \tag{4.71}$$

For the exterior boundary, I will consider two different choices of boundary conditions in order to make comparisons to known membrane results in the literature. If the membrane were suspended from a solid boundary, as in classic drumhead experiments, its outer rim would experience a no-slip boundary condition

$$\left(\frac{\mathrm{d}^2\tilde{\chi}}{\mathrm{d}\xi^2} - \frac{\nu}{\xi}\frac{\mathrm{d}\tilde{\chi}}{\mathrm{d}\xi}\right)_{\xi=1} = 1-\nu \tag{4.72}$$

However, when the membrane is on water, its outer boundary must match the surface tension of water, yielding:

$$\left.\frac{\mathrm{d}\tilde{\chi}}{\mathrm{d}\xi}\right|_{\xi=1} = 1 \tag{4.73}$$

Aside from $\tilde{r}_{\text{in}}$ and ν hidden in the boundary conditions, Eqs. (4.67-4.68) depend only on a single dimensionless parameter

$$\Lambda = \frac{Y}{2\gamma}\left(\frac{\delta}{R}\right)^2 \tag{4.74}$$

This dimensionless parameter summarizes two competitions: the indentation depth relative to the membrane diameter and the elastic stiffness relative to the pre-tension.

In Figure 4.4, I show numerically computed solutions for a range of values of Λ. For intuition, two extreme limits are analytically tractable. The limit $\Lambda = 0$ (panel a) corresponds to an open surface of water with no elasticity (i.e. $Y = 0$). In which case one obtains a logarithmic profile and a constant stress

$$\tilde{h} = -\frac{\log(\xi)}{\log(\tilde{r}_{in})} \tag{4.75}$$

$$\tilde{\chi} = \frac{\xi^2}{2} \tag{4.76}$$

This limit gives rise to a linear force-displacement relationship, which forms the grey dashed line in Fig. 4.3a. The second limiting case is that of $\Lambda \gg 1$. This case has a simple analytical solution when the outer boundary is pinned and $\nu = 1/3$:

$$\tilde{h} \approx \tilde{\xi}^{2/3} - 1 \tag{4.77}$$

$$\tilde{\chi} \approx \frac{2}{3}\Lambda\xi^{4/3} \tag{4.78}$$

where the corrections are subdominant in $\tilde{r}_{in}$ and $1/\Lambda$. This case has been used to analyze μm scale drumhead experiments with solid boundaries. Notice that when $\Lambda \ll 1$, the boundary condition is irrelevant since the indentation depth is much lower than the penetration depth. However, when $\Lambda \gg 1$, the boundary condition is crucial since in proper units, the indentation depth is comparable to the membrane size.

The maximum value of Λ in our experiments is approximately 0.1, which is shown in Fig. 4.4b. This gives us two pieces of information. First, notice that Eq. (4.65) can be re-written as:

$$\frac{\mathrm{d}^2\tilde{h}}{\mathrm{d}\xi^2} = -\frac{\tilde{\sigma}_{\theta\theta}}{\tilde{\sigma}_{rr}}\frac{\mathrm{d}\tilde{h}}{\mathrm{d}\xi} \tag{4.79}$$

Equation (4.79) shows that the hoop stress $\sigma_{\theta\theta}$ only crosses zero if $\tilde{h}$ has an inflection point.

From Fig. 4.4b, one sees that for small Λ, no inflection point is present. This indicates that a buckling instability does not occur. Second, the limit $\Lambda \ll 1$ gives us a way to interpret the force displacement curves in Fig. 4.3a. The limit $\Lambda \ll 1$ should be thought of as a perturbation on the membrane free surface of water. The membrane-free surface of water gives a linear stress-strain relationship and the perturbation $\Lambda \propto Y$ gives an superhookean nonlinear stiffening. This suggests that one way to capture the effects of wrinkles would be to think of the medium as having an effective Young's modulus Y_{eff}. Fig. 4.3a features two additional theoretical curves (red and blue dashed lines) that arise from solving Eqs. (4.36-4.37) with $Y_{\text{eff}} = Y_0/10$ and $Y_0/100$, respectively. Treated as an order of magnitude estimate, such an analysis suggests that the wrinkles likely have a substantial effect on the effective Young's modulus. Moreover, it is crucial to note that response is actually getting weaker for *larger* domains. This is conceptually important from a design point of view because even though large-grain samples are structurally closer to single-crystal MoS_2, they are functionally further in terms of their mechanical response. This is potentially intuitive considering that the wrinkle height A grows with domain size, allowing for an enhanced accordion effect upon indentation.

However, this picture consisting of an effective Young's modulus treats the membrane as a uniform effective medium. This approach is successful for large scale measurements, such as uniaxial compression or stretching experiments. However, a point force load is highly localized and the solution is a superposition of many different wavelengths. In order for the effective medium picture to hold, one would want to ensure that many wrinkles are participating in the deformed region of the indentation. In the next section, I derive criteria under which this is the case.

4.4.3 Mechanical resolution

A point force may at first sound like a highly localized load probe, but like any probe, it comes with a finite spatial resolution. In practice, one can define the resolution of this probe as the radius within which the majority of the deformation under point loading occurs. When this mechanical resolution is much larger than the typical domain or wrinkle size, then poking anywhere on the medium should give the same result. If this mechanical resolution is much smaller than the typical wrinkle dimension, the local pokes will start to depend sensitively on the local geometry.

Since our experiments are in the regime $\Lambda \ll 1$, it is sensible to decompose the stress tensor $\tilde{\sigma} = \sigma/\gamma$ into a prestress and an additional stress $\tilde{\sigma} = 1 + \tilde{\Sigma}$. The energy associated with deformation can be defined as:

$$e(\xi) = \tilde{\Sigma}_{rr}^2 + \tilde{\Sigma}_{\theta\theta}^2 - 2\nu\tilde{\Sigma}_{rr}\tilde{\Sigma}_{\theta\theta} \tag{4.80}$$

Of interest is the fraction of the total deformation energy that is stored within a given radius ξ. This fraction is given by

$$f(\xi) = \frac{1}{N}\int_{\tilde{r}_{\text{in}}}^{\xi} e(\xi')\xi' \mathrm{d}\xi' \tag{4.81}$$

where $N = \int_{\tilde{r}_{in}}^{1} e(\xi')\xi' \mathrm{d}\xi'$ is a normalization constant.

In Fig. 4.5, the function $f(\xi)$ is plotted for several values of Λ. Each curve features an elbow that defines the radius within which roughly 90% of the mechanical energy is stored. The location of this elbow defines the mechanical resolution, and can be deduced using the following argument. For small Λ the location of the elbow r_{res} in dimensionful units should be independent of membrane radius R (since the radius is very large). Moreover, in dimensionless variables, r_{res}/R should depend only on Λ. Putting these two ingredients together yields $r_{\text{res}} \propto \sqrt{\Lambda}R = \delta\sqrt{\frac{Y}{2\gamma}}$. In Fig. 4.5, I rescale the f curves via the radius r_{res}.

The rescaling successfully collapses the elbows of the energy curves, supporting the proposed form of r_{res}. It should be noted that this estimation of the mechanical resolution is expected to be self consistent so long as $r_{\mathrm{in}} \ll r_{\mathrm{res}} \ll R$.

One can put the notion of a mechanical resolution to the test in experiments. Fig. 4.3d-e show spatially resolve indentation experiments for the small (d) and large (e) grain samples of monolayer MoS_2. As shown in panel (c), for the small-grain sample, the typical grain size is about an order of magnitude smaller than the mechanical radius, while for the large grains, the grain size is about a half order of magnitude larger than the mechanical radius. In Fig. 4.3d-e, consistent with theoretical expectations, one sees that the force response is relatively homogeneous for small grains and relatively heterogeneous for large grains. This notion of a mechanical resolution is potentially vital for understanding spatially resolved mechanical measurements via point probes for atomically thin films at their smallest scales.

REFERENCES

A. Adamatzky, B. De Lacy Costello, and T. Asai. *Reaction-Diffusion Computers*. Elsevier Science, 2005. ISBN 9780080461274. URL https://books.google.com/books?id=9naAL-AkHXcC.

Konstantin Agladze, James P. Keener, Stefan C. Müller, and Alexander Panfilov. Rotating spiral waves created by geometry. *Science*, 264(5166):1746–1748, 1994. doi:10.1126/science.264.5166.1746. URL https://www.science.org/doi/abs/10.1126/science.264.5166.1746.

Hillel Aharoni, Desislava V. Todorova, Octavio Albarrán, Lucas Goehring, Randall D. Kamien, and Eleni Katifori. The smectic order of wrinkles. *Nature Communications*, 8(1):15809, 2017. doi:10.1038/ncomms15809. URL https://doi.org/10.1038/ncomms15809.

Sergio Alonso, Francesc Sagués, and Alexander S. Mikhailov. Taming winfree turbulence of scroll waves in excitable media. *Science*, 299(5613):1722–1725, 2003. doi:10.1126/science.1080207. URL https://www.science.org/doi/abs/10.1126/science.1080207.

Roy M. Anderson and Robert M. May. Population biology of infectious diseases: Part i. *Nature*, 280(5721):361–367, 1979. doi:10.1038/280361a0. URL https://doi.org/10.1038/280361a0.

Roy M. Anderson, Helen C. Jackson, Robert M. May, and Anthony M. Smith. Population dynamics of fox rabies in europe. *Nature*, 289(5800):765–771, 1981. doi:10.1038/289765a0. URL https://doi.org/10.1038/289765a0.

C. Atkinson, G. E. H. Reuter, and C. J. Ridler-Rowe. Traveling wave solution for some nonlinear diffusion equations. *SIAM Journal on Mathematical Analysis*, 12(6):880–892, 1981. doi:10.1137/0512074. URL https://doi.org/10.1137/0512074.

J. E. Avron, R. Seiler, and P. G. Zograf. Viscosity of quantum hall fluids. *Physical Review Letters*, 75(4):697–700, Jul 1995. ISSN 1079-7114. doi:10.1103/physrevlett.75.697.

J.M. Ball. *Systems of Nonlinear Partial Differential Equations*. NATO ASI series : Mathematical and physical sciences: Series C. Springer, 1983. ISBN 9789027716293.

Debarghya Banerjee, Anton Souslov, Alexander G. Abanov, and Vincenzo Vitelli. Odd viscosity in chiral active fluids. *Nature Communications*, 8(1):1573, 2017. doi:10.1038/s41467-017-01378-7. URL https://doi.org/10.1038/s41467-017-01378-7.

Wenzhong Bao, Feng Miao, Zhen Chen, Hang Zhang, Wanyoung Jang, Chris Dames, and Chun Ning Lau. Controlled ripple texturing of suspended graphene and ultrathin graphite membranes. *Nature nanotechnology*, 4(9):562–6, 2009. ISSN 1748-3395. doi:10.1038/nnano.2009.191. URL http://www.ncbi.nlm.nih.gov/pubmed/19734927.

Andreas Bauer and Christian Pfleiderer. *Generic Aspects of Skyrmion Lattices in Chiral Magnets*, pages 1–28. Springer International Publishing, Cham, 2016. ISBN 978-3-319-25301-5. doi:10.1007/978-3-319-25301-5_1. URL https://doi.org/10.1007/978-3-319-25301-5_1.

Claudio Benzoni, Bhilahari Jeevanesan, and Sergej Moroz. Rayleigh edge waves in two-dimensional crystals with lorentz forces: From skyrmion crystals to gyroscopic media. *Phys. Rev. B*, 104:024435, Jul 2021. doi:10.1103/PhysRevB.104.024435. URL https://link.aps.org/doi/10.1103/PhysRevB.104.024435.

Donald M. Bers. Cardiac excitation–contraction coupling. *Nature*, 415(6868):198–205, 2002. doi:10.1038/415198a. URL https://doi.org/10.1038/415198a.

Richard Bertram and Jonathan E. Rubin. Multi-timescale systems and fast-slow analysis. *Mathematical Biosciences*, 287:105–121, 2017. ISSN 0025-5564. doi:https://doi.org/10.1016/j.mbs.2016.07.003. URL https://www.sciencedirect.com/science/article/pii/S0025556416300852. 50th Anniversary Issue.

Ephraim S. Bililign, Florencio Balboa Usabiaga, Yehuda A. Ganan, Alexis Poncet, Vishal Soni, Sofia Magkiriadou, Michael J. Shelley, Denis Bartolo, and William T. M. Irvine. Motile dislocations knead odd crystals into whorls. *Nature Physics*, Dec 2021. ISSN 1745-2481. doi:10.1038/s41567-021-01429-3.

Erik Bitzek, Pekka Koskinen, Franz Gähler, Michael Moseler, and Peter Gumbsch. Structural relaxation made simple. *Phys. Rev. Lett.*, 97:170201, Oct 2006. doi:10.1103/PhysRevLett.97.170201. URL https://link.aps.org/doi/10.1103/PhysRevLett.97.170201.

G. Blatter, M. V. Feigel'man, V. B. Geshkenbein, A. I. Larkin, and V. M. Vinokur. Vortices in high-temperature superconductors. *Rev. Mod. Phys.*, 66:1125–1388, Oct 1994. doi:10.1103/RevModPhys.66.1125. URL https://link.aps.org/doi/10.1103/RevModPhys.66.1125.

Melina K. Blees, Arthur W. Barnard, Peter A. Rose, Samantha P. Roberts, Kathryn L. McGill, Pinshane Y. Huang, Alexander R. Ruyack, Joshua W. Kevek, Bryce Kobrin, David A. Muller, and Paul L. McEuen. Graphene kirigami. *Nature*, 524(7564):204–207, 2015. doi:10.1038/nature14588. URL https://doi.org/10.1038/nature14588.

Max Born and Kun Huang. *Dynamical theory of crystal lattices*. Clarendon press, 1954.

J. A. Bourret, R. G. Lincoln, and B. H. Carpenter. Fungal endogenous rhythms expressed by spiral figures. *Science*, 166(3906):763–764, 1969. doi:10.1126/science.166.3906.763. URL https://www.science.org/doi/abs/10.1126/science.166.3906.763.

Mark J. Bowick, Andrej Košmrlj, David R. Nelson, and Rastko Sknepnek. Non-hookean statistical mechanics of clamped graphene ribbons. *Phys. Rev. B*, 95:104109, Mar 2017. doi:10.1103/PhysRevB.95.104109. URL https://link.aps.org/doi/10.1103/PhysRevB.95.104109.

Finn Box, Dominic Vella, Robert W. Style, and Jerome A. Neufeld. Indentation of a floating elastic sheet: Geometry versus applied tension. *Proceedings of the Royal Society A: Mathematical, Physical and Engineering Sciences*, 473(2206), 2017. ISSN 14712946. doi:10.1098/rspa.2017.0335.

Martin Brandenbourger, Colin Scheibner, Jonas Veenstra, Vincenzo Vitelli, and Corentin Coulais. Limit cycles turn active matter into robots, 2022.

Fridtjof Brauns, Jacob Halatek, and Erwin Frey. Phase-space geometry of mass-conserving reaction-diffusion dynamics. *Phys. Rev. X*, 10:041036, Nov 2020. doi:10.1103/PhysRevX.10.041036. URL `https://link.aps.org/doi/10.1103/PhysRevX.10.041036`.

Fridtjof Brauns, Jacob Halatek, and Erwin Frey. Diffusive coupling of two well-mixed compartments elucidates elementary principles of protein-based pattern formation. *Phys. Rev. Res.*, 3:013258, Mar 2021. doi:10.1103/PhysRevResearch.3.013258. URL `https://link.aps.org/doi/10.1103/PhysRevResearch.3.013258`.

Lara Braverman, Colin Scheibner, Bryan VanSaders, and Vincenzo Vitelli. Topological defects in solids with odd elasticity. *Physical Review Letters*, 127(26):268001, Dec 2021. ISSN 1079-7114. doi:10.1103/physrevlett.127.268001.

R. Brearton, L. A. Turnbull, J. A. T. Verezhak, G. Balakrishnan, P. D. Hatton, G. van der Laan, and T. Hesjedal. Deriving the skyrmion hall angle from skyrmion lattice dynamics. *Nature Communications*, 12(1):2723, 2021. doi:10.1038/s41467-021-22857-y. URL `https://doi.org/10.1038/s41467-021-22857-y`.

Jacopo Brivio, Duncan T. L. Alexander, and Andras Kis. Ripples and layers in ultrathin mos2 membranes. *Nano Letters*, 11(12):5148–5153, 12 2011. doi:10.1021/nl2022288. URL `https://doi.org/10.1021/nl2022288`.

M. Brun, I. S. Jones, and A. B. Movchan. Vortex-type elastic structured media and dynamic shielding. *Proceedings of the Royal Society A: Mathematical, Physical and Engineering Sciences*, 468(2146):3027–3046, 2012. doi:10.1098/rspa.2012.0165.

Gil Bub, Alvin Shrier, and Leon Glass. Spiral wave generation in heterogeneous excitable media. *Phys. Rev. Lett.*, 88:058101, Jan 2002a. doi:10.1103/PhysRevLett.88.058101. URL `https://link.aps.org/doi/10.1103/PhysRevLett.88.058101`.

Gil Bub, Alvin Shrier, and Leon Glass. Spiral wave generation in heterogeneous excitable media. *Phys. Rev. Lett.*, 88:058101, Jan 2002b. doi:10.1103/PhysRevLett.88.058101. URL `https://link.aps.org/doi/10.1103/PhysRevLett.88.058101`.

M. A. Budroni and A. De Wit. Localized stationary and traveling reaction-diffusion patterns in a two-layer $a + b \rightarrow$ oscillator system. *Phys. Rev. E*, 93:062207, Jun 2016. doi:10.1103/PhysRevE.93.062207. URL `https://link.aps.org/doi/10.1103/PhysRevE.93.062207`.

M. A. Budroni, L. Lemaigre, D. M. Escala, A. P. Muñuzuri, and A. De Wit. Spatially localized chemical patterns around an a + b →oscillator front. *The Journal of Physical Chemistry A*, 120(6):851–860, 02 2016. doi:10.1021/acs.jpca.5b10802. URL https://doi.org/10.1021/acs.jpca.5b10802.

J. Scott Bunch, Arend M. van der Zande, Scott S. Verbridge, Ian W. Frank, David M. Tanenbaum, Jeevak M. Parpia, Harold G. Craighead, and Paul L. McEuen. Electromechanical Resonators from Graphene Sheets. *Science*, 315(5811):490–493, jan 2007. ISSN 0036-8075. doi:10.1126/science.1136836. URL https://www.science.org/doi/10.1126/science.1136836.

Carlo Carraro and David R. Nelson. Grain-boundary buckling and spin-glass models of disorder in membranes. *Phys. Rev. E*, 48:3082–3090, Oct 1993. doi:10.1103/PhysRevE.48.3082. URL https://link.aps.org/doi/10.1103/PhysRevE.48.3082.

G. Carta, M. Brun, A.B. Movchan, N.V. Movchan, and I.S. Jones. Dispersion properties of vortex-type monatomic lattices. *International Journal of Solids and Structures*, 51(11): 2213 – 2225, 2014. ISSN 0020-7683. doi:https://doi.org/10.1016/j.ijsolstr.2014.02.026. URL http://www.sciencedirect.com/science/article/pii/S0020768314000742.

G. Carta, I. S. Jones, N. V. Movchan, A. B. Movchan, and M. J. Nieves. "deflecting elastic prism"and unidirectional localisation for waves in chiral elastic systems. *Scientific Reports*, 7(1):26, 2017. doi:10.1038/s41598-017-00054-6. URL https://doi.org/10.1038/s41598-017-00054-6.

E. Cerda and L. Mahadevan. Geometry and physics of wrinkling. *Phys. Rev. Lett.*, 90: 074302, Feb 2003. doi:10.1103/PhysRevLett.90.074302. URL https://link.aps.org/doi/10.1103/PhysRevLett.90.074302.

Paul M Chaikin, Tom C Lubensky, and Thomas A Witten. *Principles of condensed matter physics*, volume 10. Cambridge university press Cambridge, 1995.

Jeremy B. Chang and James E. Ferrell Jr. Mitotic trigger waves and the spatial coordination of the xenopus cell cycle. *Nature*, 500(7464):603–607, 2013. doi:10.1038/nature12321. URL https://doi.org/10.1038/nature12321.

Shuai Chen, Junfeng Gao, Bharathi M. Srinivasan, Gang Zhang, Ming Yang, Jianwei Chai, Shijie Wang, Dongzhi Chi, and Yong-Wei Zhang. Revealing the grain boundary formation mechanism and kinetics during polycrystalline mos2 growth. *ACS Applied Materials & Interfaces*, 11(49):46090–46100, 12 2019. doi:10.1021/acsami.9b15654. URL https://doi.org/10.1021/acsami.9b15654.

Yangyang Chen, Xiaopeng Li, Colin Scheibner, Vincenzo Vitelli, and Guoliang Huang. Realization of active metamaterials with odd micropolar elasticity. *Nature Communications*, 12(1), Oct 2021. ISSN 2041-1723. doi:10.1038/s41467-021-26034-z.

H. Cheng, W. J. Lederer, and M. B. Cannell. Calcium sparks: Elementary events underlying excitation-contraction coupling in heart muscle. *Science*, 262(5134):740–744, 1993. doi:10.1126/science.8235594. URL https://www.science.org/doi/abs/10.1126/science.8235594.

K. N. Chueh, C. C. Conley, and J. A. Smoller. Positively invariant regions for systems of nonlinear diffusion equations. *Indiana University Mathematics Journal*, 26(2):373–392, 1977. ISSN 00222518, 19435258. URL http://www.jstor.org/stable/24891350.

C. Conley and J. Smoller. Remarks on the stability of steady-state solutions of reaction-diffusion equations. In Claude Bardos and Daniel Bessis, editors, *Bifurcation Phenomena in Mathematical Physics and Related Topics*, pages 47–56, Dordrecht, 1980. Springer Netherlands. ISBN 978-94-009-9004-3. URL https://link.springer.com/chapter/10.1007/978-94-009-9004-3_2.

C.C. Conley and C.B.M. Sciences. *Isolated Invariant Sets and the Morse Index*. Number no. 38 in Conference Board of the Mathematical Sciences Series No. 38. American Mathematical Society, 1978. ISBN 9780821816882. URL https://books.google.com/books?id=OsmcAwAAQBAJ.

Charles C. Conley. *On traveling wave solutions of nonlinear diffusion equations*, pages 498–510. Springer Berlin Heidelberg, Berlin, Heidelberg, 1975. ISBN 978-3-540-37505-0. doi:10.1007/3-540-07171-7_13. URL https://doi.org/10.1007/3-540-07171-7_13.

Charles C. Conley and Joel A. Smoller. *Algebraic and Topological Invariants for Reaction-Diffusion Equations*, pages 3–24. Springer Netherlands, Dordrecht, 1983. ISBN 978-94-009-7189-9. doi:10.1007/978-94-009-7189-9_1. URL https://doi.org/10.1007/978-94-009-7189-9_1.

Hiram J Conley, Bin Wang, Jed I Ziegler, Richard F Haglund Jr., Sokrates T Pantelides, and Kirill I Bolotin. Bandgap Engineering of Strained Monolayer and Bilayer MoS 2. *Nano Letters*, 13(8):3626–3630, jul 2013. URL http://pubs.acs.org/doi/10.1021/nl4014748papers3://publication/doi/10.1021/nl4014748.

M. C. Cross and P. C. Hohenberg. Pattern formation outside of equilibrium. *Rev. Mod. Phys.*, 65:851–1112, Jul 1993. doi:10.1103/RevModPhys.65.851. URL https://link.aps.org/doi/10.1103/RevModPhys.65.851.

Jorge M. Davidenko, Arcady V. Pertsov, Remy Salomonsz, William Baxter, and José Jalife. Stationary and drifting spiral waves of excitation in isolated cardiac muscle. *Nature*, 355(6358):349–351, 1992. doi:10.1038/355349a0. URL https://doi.org/10.1038/355349a0.

Benny Davidovitch, Robert D. Schroll, Dominic Vella, Mokhtar Adda-Bedia, and Enrique A. Cerda. Prototypical model for tensional wrinkling in thin sheets. *Proceedings of the National Academy of Sciences*, 108(45):18227–18232, 2011. doi:10.1073/pnas.1108553108. URL https://www.pnas.org/doi/abs/10.1073/pnas.1108553108.

S. R. de Groot and P. Mazur. Extension of onsager's theory of reciprocal relations. i. *Phys. Rev.*, 94:218–224, Apr 1954. doi:10.1103/PhysRev.94.218. URL https://link.aps.org/doi/10.1103/PhysRev.94.218.

Steven P. Dear, James A. Simmons, and Jonathan Fritz. A possible neuronal basis for representation of acoustic scenes in auditory cortex of the big brown bat. *Nature*, 364 (6438):620–623, 1993. doi:10.1038/364620a0. URL https://doi.org/10.1038/364620a0.

Julien Dervaux, Pasquale Ciarletta, and Martine Ben Amar. Morphogenesis of thin hyperelastic plates: A constitutive theory of biological growth in the föppl–von kármán limit. *Journal of the Mechanics and Physics of Solids*, 57(3):458–471, 2009. ISSN 0022-5096. doi:https://doi.org/10.1016/j.jmps.2008.11.011. URL https://www.sciencedirect.com/science/article/pii/S0022509608002093.

Stefano Di Talia and Massimo Vergassola. Waves in embryonic development. *Annual Review of Biophysics*, 51(1):327–353, 2022. doi:10.1146/annurev-biophys-111521-102500. URL https://doi.org/10.1146/annurev-biophys-111521-102500. PMID: 35119944.

M. A. Dias, J. A. Hanna, and C. D. Santangelo. Programmed buckling by controlled lateral swelling in a thin elastic sheet. *Phys. Rev. E*, 84:036603, Sep 2011. doi:10.1103/PhysRevE.84.036603. URL https://link.aps.org/doi/10.1103/PhysRevE.84.036603.

B. Drossel and F. Schwabl. Self-organized critical forest-fire model. *Phys. Rev. Lett.*, 69: 1629–1632, Sep 1992. doi:10.1103/PhysRevLett.69.1629. URL https://link.aps.org/doi/10.1103/PhysRevLett.69.1629.

Guillaume Duclos, Raymond Adkins, Debarghya Banerjee, Matthew S. E. Peterson, Minu Varghese, Itamar Kolvin, Arvind Baskaran, Robert A. Pelcovits, Thomas R. Powers, Aparna Baskaran, Federico Toschi, Michael F. Hagan, Sebastian J. Streichan, Vincenzo Vitelli, Daniel A. Beller, and Zvonimir Dogic. Topological structure and dynamics of three-dimensional active nematics. *Science*, 367(6482):1120–1124, 2020. ISSN 0036-8075. doi:10.1126/science.aaz4547. URL https://science.sciencemag.org/content/367/6482/1120.

Brigitta Dúzs, Patrick De Kepper, and István Szalai. Turing patterns and waves in closed two-layer gel reactors. *ACS Omega*, 4(2):3213–3219, 02 2019. doi:10.1021/acsomega.8b02997. URL https://doi.org/10.1021/acsomega.8b02997.

Torsten Eckstein, Estefania Vidal-Henriquez, and Azam Gholami. Experimental observation of boundary-driven oscillations in a reaction–diffusion–advection system. *Soft Matter*, 16: 4243–4255, 2020. doi:10.1039/C9SM02291K. URL http://dx.doi.org/10.1039/C9SM02291K.

A. Fasolino, J. H. Los, and M. I. Katsnelson. Intrinsic ripples in graphene. *Nature Materials*, 6(11):858–861, 2007. doi:10.1038/nmat2011. URL https://doi.org/10.1038/nmat2011.

Flavio Fenton and Alain Karma. Vortex dynamics in three-dimensional continuous myocardium with fiber rotation: Filament instability and fibrillation. *Chaos: An Interdisciplinary Journal of Nonlinear Science*, 8(1):20–47, 1998. doi:10.1063/1.166311. URL https://doi.org/10.1063/1.166311.

Flavio H. Fenton, Elizabeth M. Cherry, Harold M. Hastings, and Steven J. Evans. Multiple mechanisms of spiral wave breakup in a model of cardiac electrical activity. *Chaos: An Interdisciplinary Journal of Nonlinear Science*, 12(3):852–892, 2002. doi:10.1063/1.1504242. URL https://doi.org/10.1063/1.1504242.

Alexander L. Fetter. Rotating trapped bose-einstein condensates. *Rev. Mod. Phys.*, 81:647–691, May 2009. doi:10.1103/RevModPhys.81.647. URL https://link.aps.org/doi/10.1103/RevModPhys.81.647.

Richard J. Field, Endre Koros, and Richard M. Noyes. Oscillations in chemical systems. II. Thorough analysis of temporal oscillation in the bromate-cerium-malonic acid system. *Journal of the American Chemical Society*, 94(25):8649–8664, 12 1972. doi:10.1021/ja00780a001. URL https://doi.org/10.1021/ja00780a001.

R.J. Field and M. Burger. *Oscillations and Traveling Waves in Chemical Systems*. Wiley, 1985. ISBN 9780471893844. URL https://books.google.com/books?id=AsxnQgAACAAJ.

Richard FitzHugh. Impulses and physiological states in theoretical models of nerve membrane. *Biophysical Journal*, 1(6):445–466, 1961. ISSN 0006-3495. doi:https://doi.org/10.1016/S0006-3495(61)86902-6. URL https://www.sciencedirect.com/science/article/pii/S0006349561869026.

Michele Fossati, Colin Scheibner, Michel Fruchart, and Vincenzo Vitelli. Odd elasticity and topological waves in active surfaces, 2022.

Michel Fruchart and Vincenzo Vitelli. Symmetries and dualities in the theory of elasticity. *Physical Review Letters*, 124(24):248001, Jun 2020. ISSN 1079-7114. doi:10.1103/physrevlett.124.248001.

Michel Fruchart, Colin Scheibner, and Vincenzo Vitelli. Odd viscosity and odd elasticity. *Annual Review of Condensed Matter Physics*, 14(1):471–510, 2023. doi:10.1146/annurev-conmatphys-040821-125506. URL https://doi.org/10.1146/annurev-conmatphys-040821-125506.

Yuki Fuseya, Hiroyasu Katsuno, Kamran Behnia, and Aharon Kapitulnik. Nanoscale turing patterns in a bismuth monolayer. *Nature Physics*, 17(9):1031–1036, 2021. doi:10.1038/s41567-021-01288-y. URL https://doi.org/10.1038/s41567-021-01288-y.

Bryan Gin ge Chen, Nitin Upadhyaya, and Vincenzo Vitelli. Nonlinear conduction via solitons in a topological mechanical insulator. *Proceedings of the National Academy of Sciences*, 111(36):13004–13009, 2014. doi:10.1073/pnas.1405969111. URL https://www.pnas.org/doi/abs/10.1073/pnas.1405969111.

John Gemmer, Eran Sharon, Toby Shearman, and Shankar C. Venkataramani. Isometric immersions, energy minimization and self-similar buckling in non-euclidean elastic sheets. *EPL (Europhysics Letters)*, 114(2):24003, apr 2016. doi:10.1209/0295-5075/114/24003. URL https://doi.org/10.1209/0295-5075/114/24003.

Michael Geracie and Dam Thanh Son. Effective field theory for fluids: Hall viscosity from a wess-zumino-witten term. *Journal of High Energy Physics*, 2014(11), Nov 2014. ISSN 1029-8479. doi:10.1007/jhep11(2014)004.

S. Andrew Gifford and Gordon Baym. Dislocation-mediated melting in superfluid vortex lattices. *Phys. Rev. A*, 78:043607, Oct 2008. doi:10.1103/PhysRevA.78.043607. URL https://link.aps.org/doi/10.1103/PhysRevA.78.043607.

Isaac Goldhirsch. Stress, stress asymmetry and couple stress: from discrete particles to continuous fields. *Granular Matter*, 12(3):239–252, mar 2010. doi:10.1007/s10035-010-0181-z.

Richard A. Gray, Arkady M. Pertsov, and José Jalife. Spatial and temporal organization during cardiac fibrillation. *Nature*, 392(6671):75–78, 1998. doi:10.1038/32164. URL https://doi.org/10.1038/32164.

Bastien F. Grosso and E. J. Mele. Bending rules in graphene kirigami. *Phys. Rev. Lett.*, 115:195501, Nov 2015. doi:10.1103/PhysRevLett.115.195501. URL https://link.aps.org/doi/10.1103/PhysRevLett.115.195501.

Bastien F. Grosso and Eugene J. Mele. Graphene gets bent, 2020. ISSN 00319228. URL https://doi.org/10.1063/PT.3.4569.

J. Halatek and E. Frey. Rethinking pattern formation in reaction–diffusion systems. *Nature Physics*, 14(5):507–514, 2018. doi:10.1038/s41567-017-0040-5. URL https://doi.org/10.1038/s41567-017-0040-5.

Edmund Han, Jaehyung Yu, Emil Annevelink, Jangyup Son, Dongyun A. Kang, Kenji Watanabe, Takashi Taniguchi, Elif Ertekin, Pinshane Y. Huang, and Arend M van der Zande. Ultrasoft slip-mediated bending in few-layer graphene. *Nature Materials*, 19 (3):305–309, mar 2020. ISSN 1476-1122. doi:10.1038/s41563-019-0529-7. URL http://www.nature.com/articles/s41563-019-0529-7.

Yimo Han, Kayla Nguyen, Michael Cao, Paul Cueva, Saien Xie, Mark W. Tate, Prafull Purohit, Sol M. Gruner, Jiwoong Park, and David A. Muller. Strain mapping of two-dimensional heterostructures with subpicometer precision. *Nano Letters*, 18(6):3746–3751, 06 2018. doi:10.1021/acs.nanolett.8b00952. URL https://doi.org/10.1021/acs.nanolett.8b00952.

Paul Z. Hanakata, Sourav S. Bhabesh, Mark J. Bowick, David R. Nelson, and David Yllanes. Thermal buckling and symmetry breaking in thin ribbons under compression. *Extreme Mechanics Letters*, 44:101270, 2021. ISSN 2352-4316.

doi:https://doi.org/10.1016/j.eml.2021.101270. URL https://www.sciencedirect.com/science/article/pii/S2352431621000602.

Yufeng Hao, M. S. Bharathi, Lei Wang, Yuanyue Liu, Hua Chen, Shu Nie, Xiaohan Wang, Harry Chou, Cheng Tan, Babak Fallahazad, H. Ramanarayan, Carl W. Magnuson, Emanuel Tutuc, Boris I. Yakobson, Kevin F. McCarty, Yong-Wei Zhang, Philip Kim, James Hone, Luigi Colombo, and Rodney S. Ruoff. The role of surface oxygen in the growth of large single-crystal graphene on copper. *Science*, 342(6159):720–723, 2013. doi:10.1126/science.1243879. URL https://www.science.org/doi/abs/10.1126/science.1243879.

M. Z. Hasan and C. L. Kane. Colloquium: Topological insulators. *Rev. Mod. Phys.*, 82: 3045–3067, Nov 2010. doi:10.1103/RevModPhys.82.3045. URL https://link.aps.org/doi/10.1103/RevModPhys.82.3045.

Soroosh Hassanpour. Dynamics of gyroelastic continua, 2014. URL http://hdl.handle.net/10012/8289.

B. Hasselblatt and A. Katok. *Handbook of Dynamical Systems*. ISSN. Elsevier Science, 2002. ISBN 9780080533445.

S. P. Hastings. On The Existence of Homoclinic and Periodic Orbits for the Fitzhugh-Nagumo Equations. *The Quarterly Journal of Mathematics*, 27(1):123–134, 03 1976. ISSN 0033-5606. doi:10.1093/qmath/27.1.123. URL https://doi.org/10.1093/qmath/27.1.123.

A. Hatcher, Cambridge University Press, and Cornell University. Department of Mathematics. *Algebraic Topology*. Algebraic Topology. Cambridge University Press, 2002. ISBN 9780521795401. URL https://pi.math.cornell.edu/~hatcher/AT/AT.pdf.

Julian Holley, Ishrat Jahan, Ben De Lacy Costello, Larry Bull, and Andrew Adamatzky. Logical and arithmetic circuits in belousov-zhabotinsky encapsulated disks. *Phys. Rev. E*, 84:056110, Nov 2011. doi:10.1103/PhysRevE.84.056110. URL https://link.aps.org/doi/10.1103/PhysRevE.84.056110.

Carlos Hoyos and Dam Thanh Son. Hall viscosity and electromagnetic response. *Physical Review Letters*, 108(6):066805, Feb 2012. ISSN 1079-7114. doi:10.1103/physrevlett.108.066805.

J. Huang, M. Juszkiewicz, W. H. de Jeu, E. Cerda, T. Emrick, N. Menon, and T. P. Russell. Capillary Wrinkling of Floating Thin Polymer Films. *Science*, 317(5838):650–653, aug 2007. ISSN 0036-8075. doi:10.1126/science.1144616. URL https://www.sciencemag.org/lookup/doi/10.1126/science.1144616.

Ping Huang, Thomas Schönenberger, Marco Cantoni, Lukas Heinen, Arnaud Magrez, Achim Rosch, Fabrizio Carbone, and Henrik M. Rønnow. Melting of a skyrmion lattice to a skyrmion liquid via a hexatic phase. *Nature Nanotechnology*, 15(9):761–767, 2020. doi:10.1038/s41565-020-0716-3. URL https://doi.org/10.1038/s41565-020-0716-3.

Pinshane Y. Huang, Carlos S. Ruiz-Vargas, Arend M. van der Zande, William S. Whitney, Mark P. Levendorf, Joshua W. Kevek, Shivank Garg, Jonathan S. Alden, Caleb J. Hustedt, Ye Zhu, Jiwoong Park, Paul L. McEuen, and David A. Muller. Grains and grain boundaries in single-layer graphene atomic patchwork quilts. *Nature*, 469(7330):389–392, jan 2011. ISSN 0028-0836. doi:10.1038/nature09718. URL http://www.nature.com/articles/nature09718.

Sebastian D. Huber. Topological mechanics. *Nature Physics*, 12(7):621–623, 2016. doi:10.1038/nphys3801. URL https://doi.org/10.1038/nphys3801.

H. Hulsman, E.J. Van Waasdijk, A.L.J. Burgmans, H.F.P. Knaap, and J.J.M. Beenakker. Transverse momentum transport in polyatomic gases under the influence of a magnetic field. *Physica*, 50(1):53–76, Nov 1970. ISSN 0031-8914. doi:10.1016/0031-8914(70)90053-4.

J. H. Irving and John G. Kirkwood. The statistical mechanical theory of transport processes. IV. the equations of hydrodynamics. *The Journal of Chemical Physics*, 18(6):817–829, jun 1950. doi:10.1063/1.1747782.

E.M. Izhikevich. *Dynamical Systems in Neuroscience*. Computational neuroscience Dynamical systems in neuroscience. MIT Press, 2007. ISBN 9780262090438. URL https://books.google.com/books?id=kVjM6DFk-twC.

Nityasagar Jena, Dimple, Shounak Dhananjay Behere, and Abir De Sarkar. Strain-induced optimization of nanoelectromechanical energy harvesting and nanopiezotronic response in a mos2 monolayer nanosheet. *The Journal of Physical Chemistry C*, 121(17):9181–9190, 05 2017. doi:10.1021/acs.jpcc.7b01970. URL https://doi.org/10.1021/acs.jpcc.7b01970.

C. L. Kane and T. C. Lubensky. Topological boundary modes in isostatic lattices. *Nature Physics*, 10(1):39–45, 2014. doi:10.1038/nphys2835. URL https://doi.org/10.1038/nphys2835.

Kibum Kang, Saien Xie, Lujie Huang, Yimo Han, Pinshane Y. Huang, Kin Fai Mak, Cheol-Joo Kim, David Muller, and Jiwoong Park. High-mobility three-atom-thick semiconducting films with wafer-scale homogeneity. *Nature*, 520(7549):656–660, 2015. doi:10.1038/nature14417. URL https://doi.org/10.1038/nature14417.

Minseok Kim, Matthias Bertram, Michael Pollmann, Alexander von Oertzen, Alexander S. Mikhailov, Harm Hinrich Rotermund, and Gerhard Ertl. Controlling chemical turbulence by global delayed feedback: Pattern formation in catalytic co oxidation on pt(110). *Science*, 292(5520):1357–1360, 2001. doi:10.1126/science.1059478. URL https://www.science.org/doi/abs/10.1126/science.1059478.

Sunphil Kim, Jaehyung Yu, and Arend M. van der Zande. Nano-electromechanical Drumhead Resonators from Two-Dimensional Material Bimorphs. *Nano Letters*, 18(11):6686–6695, nov 2018. ISSN 15306992. doi:10.1021/acs.nanolett.8b01926. URL https://pubs.acs.org/doi/10.1021/acs.nanolett.8b01926.

Sunphil Kim, Emil Annevelink, Edmund Han, Jaehyung Yu, Pinshane Y. P.Y. Huang, Elif Ertekin, and Arend M. A.M. Van Der Zande. Stochastic Stress Jumps Due to Soliton Dynamics in Two-Dimensional van der Waals Interfaces. *Nano Letters*, 20(2):1201–1207, feb 2020. ISSN 15306992. doi:10.1021/acs.nanolett.9b04619. URL https://pubs.acs.org/doi/10.1021/acs.nanolett.9b04619.

William Kinney. Applying the conley index to fast-slow systems with one slow variable and an attractor. *Rocky Mountain Journal of Mathematics - ROCKY MT J MATH*, 38, 08 2008. doi:10.1216/RMJ-2008-38-4-1177.

Yael Klein, Efi Efrati, and Eran Sharon. Shaping of elastic sheets by prescription of non-euclidean metrics. *Science*, 315(5815):1116–1120, 2007. doi:10.1126/science.1135994. URL https://www.science.org/doi/abs/10.1126/science.1135994.

Steven P. Koenig, Narasimha G. Boddeti, Martin L. Dunn, and J. Scott Bunch. Ultrastrong adhesion of graphene membranes. *Nature Nanotechnology*, 6(9):543–546, 2011. ISSN 1748-3387. doi:10.1038/nnano.2011.123. URL http://www.nature.com/doifinder/10.1038/nnano.2011.123.

Andrej Košmrlj and David R. Nelson. Mechanical properties of warped membranes. *Phys. Rev. E*, 88:012136, Jul 2013. doi:10.1103/PhysRevE.88.012136. URL https://link.aps.org/doi/10.1103/PhysRevE.88.012136.

Andrej Košmrlj and David R. Nelson. Response of thermalized ribbons to pulling and bending. *Phys. Rev. B*, 93:125431, Mar 2016. doi:10.1103/PhysRevB.93.125431. URL https://link.aps.org/doi/10.1103/PhysRevB.93.125431.

S. J. Kole, Gareth P. Alexander, Sriram Ramaswamy, and Ananyo Maitra. Layered chiral active matter: Beyond odd elasticity. *Phys. Rev. Lett.*, 126:248001, Jun 2021. doi:10.1103/PhysRevLett.126.248001. URL https://link.aps.org/doi/10.1103/PhysRevLett.126.248001.

U. Komaragiri, M. R. Begley, and J. G. Simmonds. The Mechanical Response of Freestanding Circular Elastic Films Under Point and Pressure Loads . *Journal of Applied Mechanics*, 72(2):203–212, 03 2005. ISSN 0021-8936. doi:10.1115/1.1827246. URL https://doi.org/10.1115/1.1827246.

Shigeru Kondo and Rihito Asai. A reaction–diffusion wave on the skin of the marine angelfish pomacanthus. *Nature*, 376(6543):765–768, 1995. doi:10.1038/376765a0. URL https://doi.org/10.1038/376765a0.

Shigeru Kondo and Takashi Miura. Reaction-diffusion model as a framework for understanding biological pattern formation. *Science*, 329(5999):1616–1620, 2010. doi:10.1126/science.1179047. URL https://www.science.org/doi/abs/10.1126/science.1179047.

E.L. Koschmieder and S.G. Pallas. Heat transfer through a shallow, horizontal convecting fluid layer. *International Journal of Heat and Mass Transfer*, 17(9):991–1002, Sep 1974. ISSN 0017-9310. doi:10.1016/0017-9310(74)90181-1.

G. Kukucska and J. Koltai. Theoretical Investigation of Strain and Doping on the Raman Spectra of Monolayer MoS2. *Physica Status Solidi (B) Basic Research*, 254(11):1–5, 2017. ISSN 15213951. doi:10.1002/pssb.201700184.

Nitin Kumar, Harsh Soni, Sriram Ramaswamy, and A. K. Sood. Flocking at a distance in active granular matter. *Nature Communications*, 5(1):4688, 2014. doi:10.1038/ncomms5688. URL https://doi.org/10.1038/ncomms5688.

Y. Kuramoto. *Chemical Oscillations, Waves, and Turbulence*. Dover books on chemistry. Dover Publications, 2003. ISBN 9780486428819. URL https://books.google.com/books?id=4ADt7smO5Q8C.

L.D. Landau, E.M. Lifshitz, A.M. Kosevich, J.B. Sykes, L.P. Pitaevskii, and W.H. Reid. *Theory of Elasticity*. Course of theoretical physics. Elsevier Science, 1986. ISBN 9780750626330.

Pierre Le Doussal and Leo Radzihovsky. Flat glassy phases and wrinkling of polymerized membranes with long-range disorder. *Phys. Rev. B*, 48:3548–3551, Aug 1993. doi:10.1103/PhysRevB.48.3548. URL https://link.aps.org/doi/10.1103/PhysRevB.48.3548.

James Lechleiter, Steven Girard, Ernest Peralta, and David Clapham. Spiral calcium wave propagation and annihilation in *Xenopus laevis* oocytes. *Science*, 252(5002):123–126, 1991. doi:10.1126/science.2011747. URL https://www.science.org/doi/abs/10.1126/science.2011747.

Changgu Lee, Xiaoding Wei, Jeffrey W. Kysar, and James Hone. Measurement of the elastic properties and intrinsic strength of monolayer graphene. *Science*, 321(5887):385–388, 2008. doi:10.1126/science.1157996. URL https://www.science.org/doi/abs/10.1126/science.1157996.

Gwan-Hyoung Lee, Ryan C. Cooper, Sung Joo An, Sunwoo Lee, Arend van der Zande, Nicholas Petrone, Alexandra G. Hammerberg, Changgu Lee, Bryan Crawford, Warren Oliver, Jeffrey W. Kysar, and James Hone. High-strength chemical-vapor–deposited graphene and grain boundaries. *Science*, 340(6136):1073–1076, 2013. doi:10.1126/science.1235126. URL https://www.science.org/doi/abs/10.1126/science.1235126.

Myungjae Lee, Jong-Hoon Kang, Fauzia Mujid, Joonki Suh, Ariana Ray, Chibeom Park, David. A. Muller, and Jiwoong Park. Atomically thin, optically isotropic films with 3d nanotopography. *Nano Letters*, 21(17):7291–7297, 09 2021. doi:10.1021/acs.nanolett.1c02478. URL https://doi.org/10.1021/acs.nanolett.1c02478.

O. Lehtinen, S. Kurasch, A. V. Krasheninnikov, and U. Kaiser. Atomic scale study of the life cycle of a dislocation in graphene from birth to annihilation. *Nature Communications*, 4, 2013. ISSN 20411723. doi:10.1038/ncomms3098.

Kai Liu, Qimin Yan, Michelle Chen, Wen Fan, Yinghui Sun, Joonki Suh, Deyi Fu, Sangwook Lee, Jian Zhou, Sefaattin Tongay, Jie Ji, Jeffrey B. Neaton, and Junqiao Wu. Elastic Properties of Chemical-Vapor-Deposited Monolayer MoS 2 , WS 2 , and Their Bilayer Heterostructures. *Nano Letters*, 14(9):5097–5103, 2014a. ISSN 1530-6984. doi:10.1021/nl501793a. URL http://pubs.acs.org/doi/abs/10.1021/nl501793a.

Kai Liu, Qimin Yan, Michelle Chen, Wen Fan, Yinghui Sun, Joonki Suh, Deyi Fu, Sangwook Lee, Jian Zhou, Sefaattin Tongay, Jie Ji, Jeffrey B. Neaton, and Junqiao Wu. Elastic Properties of Chemical-Vapor-Deposited Monolayer MoS 2 , WS 2 , and Their Bilayer Heterostructures. *Nano Letters*, 14(9):5097–5103, 2014b. ISSN 1530-6984. doi:10.1021/nl501793a. URL http://pubs.acs.org/doi/abs/10.1021/nl501793a.

Xiaolong Liu, Zonghui Wei, Itamar Balla, Andrew J. Mannix, Nathan P. Guisinger, Erik Luijten, and Mark C. Hersam. Self-assembly of electronically abrupt borophene/organic lateral heterostructures. *Science Advances*, 3(2):e1602356, 2017. doi:10.1126/sciadv.1602356. URL https://www.science.org/doi/abs/10.1126/sciadv.1602356.

Yuan Liu, Nathan O. Weiss, Xidong Duan, Hung-Chieh Cheng, Yu Huang, and Xiangfeng Duan. Van der waals heterostructures and devices. *Nature Reviews Materials*, 1(9):16042, 2016. doi:10.1038/natrevmats.2016.42. URL https://doi.org/10.1038/natrevmats.2016.42.

Yuanyue Liu and Boris I. Yakobson. Cones, pringles, and grain boundary landscapes in graphene topology. *Nano Letters*, 10(6):2178–2183, 2010. ISSN 15306984. doi:10.1021/nl100988r.

David Lloyd, Xinghui Liu, Jason Woodrow Christopher, Lauren Cantley, Anubhav Wadehra, Brian L. Kim, Bennett B. Goldberg, Anna K. Swan, Joseph Scott Bunch, Jason Woodrow Christopher, Lauren Cantley, Anubhav Wadehra, Brian L. Kim, Bennett B. Goldberg, Anna K. Swan, Joseph Scott Bunch, and Joseph Scott Bunch. Band Gap Engineering with Ultralarge Biaxial Strains in Suspended Monolayer MoS2. *Nano Letters*, 16(9):5836–5841, sep 2016. ISSN 1530-6984. doi:10.1021/acs.nanolett.6b02615. URL http://pubs.acs.org/doi/10.1021/acs.nanolett.6b02615papers3://publication/doi/10.1021/acs.nanolett.6b02615https://pubs.acs.org/doi/10.1021/acs.nanolett.6b02615.

Alex Lobkovsky, Sharon Gentges, Hao Li, David Morse, and T. A. Witten. Scaling properties of stretching ridges in a crumpled elastic sheet. *Science*, 270(5241):1482–1485, 1995. ISSN 00368075, 10959203. URL http://www.jstor.org/stable/2889012.

Martin Loose, Elisabeth Fischer-Friedrich, Jonas Ries, Karsten Kruse, and Petra Schwille. Spatial regulators for bacterial cell division self-organize into surface waves in vitro. *Science*, 320(5877):789–792, 2008. doi:10.1126/science.1154413. URL https://www.science.org/doi/abs/10.1126/science.1154413.

Chun Hung Lui, Li Liu, Kin Fai Mak, George W. Flynn, and Tony F. Heinz. Ultraflat graphene. *Nature*, 462(7271):339–341, 2009. ISSN 0028-0836. doi:10.1038/nature08569. URL http://dx.doi.org/10.1038/nature08569%5Cnhttp://www.nature.com/nature/journal/v462/n7271/suppinfo/nature08569_S1.html.

Stefan Luther, Flavio H. Fenton, Bruce G. Kornreich, Amgad Squires, Philip Bittihn, Daniel Hornung, Markus Zabel, James Flanders, Andrea Gladuli, Luis Campoy, Elizabeth M. Cherry, Gisa Luther, Gerd Hasenfuss, Valentin I. Krinsky, Alain Pumir, Robert F. Gilmour, and Eberhard Bodenschatz. Low-energy control of electrical turbulence in the heart. *Nature*, 475(7355):235–239, 2011. doi:10.1038/nature10216. URL https://doi.org/10.1038/nature10216.

J. F. Lutsko. Generalized expressions for the calculation of elastic constants by computer simulation. *Journal of Applied Physics*, 65(8):2991–2997, apr 1989. doi:10.1063/1.342716.

Zachary F. Mainen and Terrence J. Sejnowski. Influence of dendritic structure on firing pattern in model neocortical neurons. *Nature*, 382(6589):363–366, 1996. doi:10.1038/382363a0. URL https://doi.org/10.1038/382363a0.

Ananyo Maitra and Sriram Ramaswamy. Oriented active solids. *Phys. Rev. Lett.*, 123: 238001, Dec 2019. doi:10.1103/PhysRevLett.123.238001. URL https://link.aps.org/doi/10.1103/PhysRevLett.123.238001.

Ananyo Maitra, Martin Lenz, and Raphael Voituriez. Chiral active hexatics: Giant number fluctuations, waves, and destruction of order. *Phys. Rev. Lett.*, 125:238005, Dec 2020. doi:10.1103/PhysRevLett.125.238005. URL https://link.aps.org/doi/10.1103/PhysRevLett.125.238005.

Kin Fai Mak, Changgu Lee, James Hone, Jie Shan, and Tony F. Heinz. Atomically Thin <math display="inline"> <msub> <mi>MoS</mi> <mn>2</mn> </msub> </math> : A New Direct-Gap Semiconductor. *Physical Review Letters*, 105(September): 136805, 2010. ISSN 0031-9007. doi:10.1103/PhysRevLett.105.136805. URL http://link.aps.org/doi/10.1103/PhysRevLett.105.136805.

Xiaoming Mao and Tom C. Lubensky. Maxwell lattices and topological mechanics. *Annual Review of Condensed Matter Physics*, 9(1):413–433, 2018. doi:10.1146/annurev-conmatphys-033117-054235. URL https://doi.org/10.1146/annurev-conmatphys-033117-054235.

M Marder, E Sharon, S Smith, and B Roman. Theory of edges of leaves. *Europhysics Letters (EPL)*, 62(4):498–504, may 2003. doi:10.1209/epl/i2003-00334-5. URL https://doi.org/10.1209/epl/i2003-00334-5.

Elisabetta A. Matsumoto, Daniel A. Vega, Aldo D. Pezzutti, Nicolás A. García, Paul M. Chaikin, and Richard A. Register. Wrinkles and splay conspire to give positive disclinations

negative curvature. *Proceedings of the National Academy of Sciences*, 112(41):12639–12644, 2015. doi:10.1073/pnas.1514379112. URL https://www.pnas.org/doi/abs/10.1073/pnas.1514379112.

Harold M. McNamara, Stephanie Dodson, Yi-Lin Huang, Evan W. Miller, Björn Sandstede, and Adam E. Cohen. Geometry-dependent arrhythmias in electrically excitable tissues. *Cell Systems*, 7(4):359–370.e6, 2018. ISSN 2405-4712. doi:https://doi.org/10.1016/j.cels.2018.08.013. URL https://www.sciencedirect.com/science/article/pii/S2405471218303600.

Harold M. McNamara, Rajath Salegame, Ziad Al Tanoury, Haitan Xu, Shahinoor Begum, Gloria Ortiz, Olivier Pourquie, and Adam E. Cohen. Bioelectrical domain walls in homogeneous tissues. *Nature Physics*, 16(3):357–364, 2020. doi:10.1038/s41567-019-0765-4. URL https://doi.org/10.1038/s41567-019-0765-4.

Jannik C. Meyer, A. K. Geim, M. I. Katsnelson, K. S. Novoselov, T. J. Booth, and S. Roth. The structure of suspended graphene sheets. *Nature*, 446(7131):60–63, 2007. ISSN 00280836. doi:10.1038/nature05545.

A. Michail, N. Delikoukos, J. Parthenios, C. Galiotis, and K. Papagelis. Optical detection of strain and doping inhomogeneities in single layer MoS2. *Applied Physics Letters*, 108 (17), 2016. ISSN 00036951. doi:10.1063/1.4948357. URL http://dx.doi.org/10.1063/1.4948357.

Jonathan B. Michaux, François B. Robin, William M. McFadden, and Edwin M. Munro. Excitable RhoA dynamics drive pulsed contractions in the early C. elegans embryo. *Journal of Cell Biology*, 217(12):4230–4252, 10 2018. ISSN 0021-9525. doi:10.1083/jcb.201806161. URL https://doi.org/10.1083/jcb.201806161.

Konstantin Mischaikow and Marian Mrozek. Conley index. In B. Fiedler, editor, *Handbook of Dynamical Systems*, volume 2, chapter 9, pages 393–460. Elsevier Science, 2002. URL https://www.elsevier.com/books/handbook-of-dynamical-systems/fiedler/978-0-444-50168-4.

Noah P. Mitchell, Lisa M. Nash, Daniel Hexner, Ari M. Turner, and William T. M. Irvine. Amorphous topological insulators constructed from random point sets. *Nature Physics*, 14(4):380–385, 2018a. doi:10.1038/s41567-017-0024-5. URL https://doi.org/10.1038/s41567-017-0024-5.

Noah P. Mitchell, Lisa M. Nash, and William T. M. Irvine. Tunable band topology in gyroscopic lattices. *Phys. Rev. B*, 98:174301, Nov 2018b. doi:10.1103/PhysRevB.98.174301. URL https://link.aps.org/doi/10.1103/PhysRevB.98.174301.

Noah P. Mitchell, Lisa M. Nash, and William T. M. Irvine. Realization of a topological phase transition in a gyroscopic lattice. *Phys. Rev. B*, 97:100302, Mar 2018c. doi:10.1103/PhysRevB.97.100302. URL https://link.aps.org/doi/10.1103/PhysRevB.97.100302.

Noah P Mitchell, Dillon J Cislo, Suraj Shankar, Yuzheng Lin, Boris I Shraiman, and Sebastian J Streichan. Visceral organ morphogenesis via calcium-patterned muscle constrictions. *eLife*, 11:e77355, may 2022. ISSN 2050-084X. doi:10.7554/eLife.77355. URL https://doi.org/10.7554/eLife.77355.

Sergej Moroz, Carlos Hoyos, Claudio Benzoni, and Dam Thanh Son. Effective field theory of a vortex lattice in a bosonic superfluid. *SciPost Phys.*, 5:39, 2018. doi:10.21468/SciPostPhys.5.4.039.

David C. Morse and T. C. Lubensky. Curvature disorder in tethered membranes: A new flat phase at t=0. *Phys. Rev. A*, 46:1751–1768, Aug 1992. doi:10.1103/PhysRevA.46.1751. URL https://link.aps.org/doi/10.1103/PhysRevA.46.1751.

Bohayra Mortazavi and Gianaurelio Cuniberti. Mechanical properties of polycrystalline boron-nitride nanosheets. *RSC Adv.*, 4:19137–19143, 2014. doi:10.1039/C4RA01103A. URL http://dx.doi.org/10.1039/C4RA01103A.

S. Mühlbauer, B. Binz, F. Jonietz, C. Pfleiderer, A. Rosch, A. Neubauer, R. Georgii, and P. Böni. Skyrmion lattice in a chiral magnet. *Science*, 323(5916):915–919, 2009. doi:10.1126/science.1166767. URL https://www.science.org/doi/abs/10.1126/science.1166767.

James Dickson Murray, E. A. Stanley, and D. L. Brown. On the spatial spread of rabies among foxes. *Proceedings of the Royal Society of London. Series B. Biological Sciences*, 229(1255):111–150, 1986. doi:10.1098/rspb.1986.0078. URL https://royalsocietypublishing.org/doi/abs/10.1098/rspb.1986.0078.

J.D. Murray. *Mathematical Biology: I. An Introduction*. Interdisciplinary Applied Mathematics. Springer New York, 2013. ISBN 9781475777093. URL https://books.google.com/books?id=uuBHvQEACAAJ.

Arvind Murugan and Suriyanarayanan Vaikuntanathan. Topologically protected modes in non-equilibrium stochastic systems. *Nature Communications*, 8(1):13881, 2017. doi:10.1038/ncomms13881. URL https://doi.org/10.1038/ncomms13881.

J. Nagumo, S. Arimoto, and S. Yoshizawa. An active pulse transmission line simulating nerve axon. *Proceedings of the IRE*, 50(10):2061–2070, 1962. doi:10.1109/JRPROC.1962.288235.

Akiko Nakamasu, Go Takahashi, Akio Kanbe, and Shigeru Kondo. Interactions between zebrafish pigment cells responsible for the generation of turing patterns. *Proceedings of the National Academy of Sciences*, 106(21):8429–8434, 2009. doi:10.1073/pnas.0808622106. URL https://www.pnas.org/doi/abs/10.1073/pnas.0808622106.

John Nash. C1 isometric imbeddings. *Annals of Mathematics*, 60(3):383–396, 1954. ISSN 0003486X. URL http://www.jstor.org/stable/1969840.

Lisa M Nash, Dustin Kleckner, Alismari Read, Vincenzo Vitelli, Ari M Turner, and William T M Irvine. Topological mechanics of gyroscopic metamaterials. *Proc. Natl. Acad. Sci. USA*, 112(47):14495–500, nov 2015. ISSN 1091-6490. doi:10.1073/pnas.1507413112. URL http://www.pnas.org/content/112/47/14495.short.

David Nelson and B. Halperin. Dislocation-mediated melting in two dimensions. *Phys. Rev. B*, 19(5):2457–2484, March 1979. ISSN 0163-1829. doi:10.1103/PhysRevB.19.2457.

David R. Nelson. Defects in superfluids, superconductors and membranes, 1995.

David R. Nelson and Leo Radzihovsky. Grain-boundary instabilities and buckling in partially polymerized membranes. *Phys. Rev. A*, 46:7474–7479, Dec 1992. doi:10.1103/PhysRevA.46.7474. URL https://link.aps.org/doi/10.1103/PhysRevA.46.7474.

Nelson, D.R. and Peliti, L. Fluctuations in membranes with crystalline and hexatic order. *J. Phys. France*, 48(7):1085–1092, 1987. doi:10.1051/jphys:019870048070108500. URL https://doi.org/10.1051/jphys:019870048070108500.

Stuart A. Newman and H. L. Frisch. Dynamics of skeletal pattern formation in developing chick limb. *Science*, 205(4407):662–668, 1979. doi:10.1126/science.462174. URL https://www.science.org/doi/abs/10.1126/science.462174.

Dung Xuan Nguyen, Andrey Gromov, and Sergej Moroz. Fracton-elasticity duality of two-dimensional superfluid vortex crystals: defect interactions and quantum melting. *SciPost Phys.*, 9:76, 2020. doi:10.21468/SciPostPhys.9.5.076. URL https://scipost.org/10.21468/SciPostPhys.9.5.076.

Wei-Ming Ni. Diffusion, cross-diffusion, and their spike-layer steady states. *Notices of the American Mathematical Society*, 45:9–18, 1998.

Wei-Ming Ni and Juncheng Wei. On the location and profile of spike-layer solutions to singularly perturbed semilinear dirichlet problems. *Communications on Pure and Applied Mathematics*, 48(7):731–768, 1995. doi:https://doi.org/10.1002/cpa.3160480704. URL https://onlinelibrary.wiley.com/doi/abs/10.1002/cpa.3160480704.

D. Noble. A modification of the hodgkin—huxley equations applicable to purkinje fibre action and pacemaker potentials. *The Journal of Physiology*, 160(2):317–352, 1962. doi:https://doi.org/10.1113/jphysiol.1962.sp006849. URL https://physoc.onlinelibrary.wiley.com/doi/abs/10.1113/jphysiol.1962.sp006849.

Amirali Nojoomi, Junha Jeon, and Kyungsuk Yum. 2D material programming for 3D shaping. *Nature Communications*, 12(1):603, dec 2021. ISSN 2041-1723. doi:10.1038/s41467-021-20934-w. URL http://dx.doi.org/10.1038/s41467-021-20934-whttp://www.nature.com/articles/s41467-021-20934-w.

Javad Noorbakhsh, David J. Schwab, Allyson E. Sgro, Thomas Gregor, and Pankaj Mehta. Modeling oscillations and spiral waves in dictyostelium populations. *Phys. Rev. E*, 91: 062711, Jun 2015. doi:10.1103/PhysRevE.91.062711. URL https://link.aps.org/doi/10.1103/PhysRevE.91.062711.

Hector Ochoa, Se Kwon Kim, Oleg Tchernyshyov, and Yaroslav Tserkovnyak. Gyrotropic elastic response of skyrmion crystals to current-induced tensions. *Phys. Rev. B*, 96:020410, Jul 2017. doi:10.1103/PhysRevB.96.020410. URL https://link.aps.org/doi/10.1103/PhysRevB.96.020410.

Lars Onsager. Reciprocal relations in irreversible processes. i. *Phys. Rev.*, 37:405–426, Feb 1931. doi:10.1103/PhysRev.37.405. URL https://link.aps.org/doi/10.1103/PhysRev.37.405.

Hillel Ori, Eve Marder, and Shimon Marom. Cellular function given parametric variation in the Hodgkin and Huxley model of excitability. *Proceedings of the National Academy of Sciences*, 115(35):E8211–E8218, 2018. doi:10.1073/pnas.1808552115. URL https://www.pnas.org/doi/abs/10.1073/pnas.1808552115.

Hillel Ori, Marc Duque, Rebecca Frank Hayward, Colin Scheibner, He Tian, Gloria Ortiz, Vincenzo Vitelli, and Adam E. Cohen. Observation of topological action potentials in engineered tissues. *Nature Physics*, 19(2):290–296, 2023. doi:10.1038/s41567-022-01853-z. URL https://doi.org/10.1038/s41567-022-01853-z.

Anshuman S. Pal, Luka Pocivavsek, and Thomas A. Witten. Faceted wrinkling by contracting a curved boundary, 2022.

Joseph D. Paulsen, Evan Hohlfeld, Hunter King, Jiangshui Huang, Zhanlong Qiu, Thomas P. Russell, Narayanan Menon, Dominic Vella, and Benny Davidovitch. Curvature-induced stiffness and the spatial variation of wavelength in wrinkled sheets. *Proceedings of the National Academy of Sciences*, 113(5):1144–1149, 2016. doi:10.1073/pnas.1521520113. URL https://www.pnas.org/doi/abs/10.1073/pnas.1521520113.

Jian Payandeh, Todd Scheuer, Ning Zheng, and William A. Catterall. The crystal structure of a voltage-gated sodium channel. *Nature*, 475(7356):353–358, 2011. doi:10.1038/nature10238. URL https://doi.org/10.1038/nature10238.

Merlin Pelz and Michael J. Ward. The emergence of spatial patterns for compartmental reaction kinetics coupled by two bulk diffusing species with comparable diffusivities, 2023. URL https://arxiv.org/abs/2301.05986.

Alexander P. Petroff, Xiao-Lun Wu, and Albert Libchaber. Fast-moving bacteria self-organize into active two-dimensional crystals of rotating cells. *Physical Review Letters*, 114(15):158102, Apr 2015. ISSN 1079-7114. doi:10.1103/physrevlett.114.158102.

Luka Pocivavsek, Robert Dellsy, Andrew Kern, Sebastián Johnson, Binhua Lin, Ka Yee C. Lee, and Enrique Cerda. Stress and fold localization in thin elastic membranes. *Science*,

320(5878):912–916, 2008. doi:10.1126/science.1154069. URL https://www.science.org/doi/abs/10.1126/science.1154069.

Preeti K. Poddar, Yu Zhong, Andrew J. Mannix, Fauzia Mujid, Jaehyung Yu, Ce Liang, Jong-Hoon Kang, Myungjae Lee, Saien Xie, and Jiwoong Park. Resist-Free Lithography for Monolayer Transition Metal Dichalcogenides. *Nano Letters*, 22(2):726–732, 2022. ISSN 1530-6984. doi:10.1021/acs.nanolett.1c04081.

ALEXANDER POGROMSKY, TORKEL GLAD, and HENK NIJMEIJER. On diffusion driven oscillations in coupled dynamical systems. *International Journal of Bifurcation and Chaos*, 09(04):629–644, 1999. doi:10.1142/S0218127499000444. URL https://doi.org/10.1142/S0218127499000444.

Alexis Poncet and Denis Bartolo. When soft crystals defy newton's third law: Nonreciprocal mechanics and dislocation motility. *Phys. Rev. Lett.*, 128:048002, Jan 2022. doi:10.1103/PhysRevLett.128.048002. URL https://link.aps.org/doi/10.1103/PhysRevLett.128.048002.

Gyula Rabai, Kenneth Kustin, and Irving R. Epstein. A systematically designed ph oscillator: the hydrogen peroxide-sulfite-ferrocyanide reaction in a continuous-flow stirred tank reactor. *Journal of the American Chemical Society*, 111(11):3870–3874, 05 1989. doi:10.1021/ja00193a018. URL https://doi.org/10.1021/ja00193a018.

Leo Radzihovsky and David R. Nelson. Statistical mechanics of randomly polymerized membranes. *Phys. Rev. A*, 44:3525–3542, Sep 1991. doi:10.1103/PhysRevA.44.3525. URL https://link.aps.org/doi/10.1103/PhysRevA.44.3525.

Jeffrey Rauch and Joel Smoller. Qualitative theory of the Fitzhugh-Nagumo equations. *Advances in Mathematics*, 27(1):12–44, 1978. ISSN 0001-8708. doi:https://doi.org/10.1016/0001-8708(78)90075-0. URL https://www.sciencedirect.com/science/article/pii/0001870878900750.

C. Rice, R. J. Young, R. Zan, U. Bangert, D. Wolverson, T. Georgiou, R. Jalil, and K. S. Novoselov. Raman-scattering measurements and first-principles calculations of strain-induced phonon shifts in monolayer MoS <math display="inline"> <msub> <mrow/> <mn>2</mn> </msub> </math>. *Physical Review B*, 87(8):081307, 2013. ISSN 1098-0121. doi:10.1103/PhysRevB.87.081307. URL https://link.aps.org/doi/10.1103/PhysRevB.87.081307.

F. Rieke, D. Warland, R. De Ruyter van Steveninck, and W. Bialek. *Spikes: Exploring the Neural Code*. Bradford book. MIT Press, 1997. ISBN 9780262181747. URL https://books.google.com/books?id=0xmDcOLZGu0C.

Pejman Rohani, David J. D. Earn, and Bryan T. Grenfell. Opposite patterns of synchrony in sympatric disease metapopulations. *Science*, 286(5441):968–971, 1999. doi:10.1126/science.286.5441.968. URL https://www.science.org/doi/abs/10.1126/science.286.5441.968.

H. H. Rotermund, W. Engel, M. Kordesch, and G. Ertl. Imaging of spatio-temporal pattern evolution during carbon monoxide oxidation on platinum. *Nature*, 343(6256):355–357, 1990. doi:10.1038/343355a0. URL https://doi.org/10.1038/343355a0.

Ylann Rouzaire and Demian Levis. Defect superdiffusion and unbinding in a 2d xy model of self-driven rotors. *Phys. Rev. Lett.*, 127:088004, Aug 2021. doi:10.1103/PhysRevLett.127.088004. URL https://link.aps.org/doi/10.1103/PhysRevLett.127.088004.

Miguel Ruiz-García and Eleni Katifori. Emergent dynamics in excitable flow systems. *Phys. Rev. E*, 103:062301, Jun 2021. doi:10.1103/PhysRevE.103.062301. URL https://link.aps.org/doi/10.1103/PhysRevE.103.062301.

Carlos S. Ruiz-Vargas, Houlong L. Zhuang, Pinshane Y. Huang, Arend M. Van Der Zande, Shivank Garg, Paul L. McEuen, David A. Muller, Richard G. Hennig, and Jiwoong Park. Softened elastic response and unzipping in chemical vapor deposition graphene membranes. *Nano Letters*, 11(6):2259–2263, 2011. ISSN 15306984. doi:10.1021/nl200429f.

Colin Scheibner, William T. M. Irvine, and Vincenzo Vitelli. Non-hermitian band topology and skin modes in active elastic media. *Phys. Rev. Lett.*, 125:118001, Sep 2020a. doi:10.1103/PhysRevLett.125.118001. URL https://link.aps.org/doi/10.1103/PhysRevLett.125.118001.

Colin Scheibner, Anton Souslov, Debarghya Banerjee, Piotr Surówka, William T. M. Irvine, and Vincenzo Vitelli. Odd elasticity. *Nature Physics*, 16(4):475–480, Mar 2020b. ISSN 1745-2481. doi:10.1038/s41567-020-0795-y.

Colin Scheibner, Hillel Ori, Adam E. Cohen, and Vincenzo Vitelli. Spiking at the edge, 2023.

Maria Elena Schonbek. Boundary value problems for the fitzhugh-nagumo equations. *Journal of Differential Equations*, 30(1):119–147, 1978. ISSN 0022-0396. doi:https://doi.org/10.1016/0022-0396(78)90027-X. URL https://www.sciencedirect.com/science/article/pii/002203967890027X.

Sergey N. Semenov, Lewis J. Kraft, Alar Ainla, Mengxia Zhao, Mostafa Baghbanzadeh, Victoria E. Campbell, Kyungtae Kang, Jerome M. Fox, and George M. Whitesides. Autocatalytic, bistable, oscillatory networks of biologically relevant organic reactions. *Nature*, 537(7622):656–660, 2016. doi:10.1038/nature19776. URL https://doi.org/10.1038/nature19776.

H. S. Seung and David R. Nelson. Defects in flexible membranes with crystalline order. *Phys. Rev. A*, 38:1005–1018, Jul 1988. doi:10.1103/PhysRevA.38.1005. URL https://link.aps.org/doi/10.1103/PhysRevA.38.1005.

Daniel P. Shams, Xingbo Yang, Pankaj Mehta, and David J. Schwab. Spatial gradient sensing and chemotaxis via excitability in *Dictyostelium discoideum*. *Phys. Rev. E*, 101:062410, Jun 2020. doi:10.1103/PhysRevE.101.062410. URL https://link.aps.org/doi/10.1103/PhysRevE.101.062410.

Suraj Shankar, Anton Souslov, Mark J. Bowick, M. Cristina Marchetti, and Vincenzo Vitelli. Topological active matter. *Nature Reviews Physics*, 4(6):380–398, 2022. doi:10.1038/s42254-022-00445-3. URL https://doi.org/10.1038/s42254-022-00445-3.

Eran Sharon, Benoît Roman, Michael Marder, Gyu-Seung Shin, and Harry L. Swinney. Buckling cascades in free sheets. *Nature*, 419(6907):579–579, 2002a. doi:10.1038/419579a. URL https://doi.org/10.1038/419579a.

Eran Sharon, Benoît Roman, Michael Marder, Gyu-Seung Shin, and Harry L. Swinney. Buckling cascades in free sheets. *Nature*, 419(6907):579–579, 2002b. doi:10.1038/419579a. URL https://doi.org/10.1038/419579a.

Jonathan A. Sherratt. Periodic travelling wave selection by dirichlet boundary conditions in oscillatory reaction-diffusion systems. *SIAM Journal on Applied Mathematics*, 63(5): 1520–1538, 2003. doi:10.1137/S0036139902392483. URL https://doi.org/10.1137/S0036139902392483.

S. Smale. *A Mathematical Model of Two Cells Via Turing's Equation*, pages 354–367. Springer New York, New York, NY, 1976. ISBN 978-1-4612-6374-6. doi:10.1007/978-1-4612-6374-6_24. URL https://doi.org/10.1007/978-1-4612-6374-6_24.

Vishal Soni, Ephraim S. Bililign, Sofia Magkiriadou, Stefano Sacanna, Denis Bartolo, Michael J. Shelley, and William T. M. Irvine. The odd free surface flows of a colloidal chiral fluid. *Nature Physics*, 15(11):1188–1194, Sep 2019. ISSN 1745-2481. doi:10.1038/s41567-019-0603-8.

E. B. Sonin. Vortex oscillations and hydrodynamics of rotating superfluids. *Rev. Mod. Phys.*, 59:87–155, Jan 1987. doi:10.1103/RevModPhys.59.87. URL https://link.aps.org/doi/10.1103/RevModPhys.59.87.

Michael F. Staddon, Edwin M. Munro, and Shiladitya Banerjee. Pulsatile contractions and pattern formation in excitable actomyosin cortex. *PLOS Computational Biology*, 18(3): 1–21, 03 2022. doi:10.1371/journal.pcbi.1009981. URL https://doi.org/10.1371/journal.pcbi.1009981.

Oliver Steinbock, Petteri Kettunen, and Kenneth Showalter. Anisotropy and spiral organizing centers in patterned excitable media. *Science*, 269(5232):1857–1860, 1995a. doi:10.1126/science.269.5232.1857. URL https://www.science.org/doi/abs/10.1126/science.269.5232.1857.

Oliver Steinbock, Ágota Tóth, and Kenneth Showalter. Navigating complex labyrinths: Optimal paths from chemical waves. *Science*, 267(5199):868–871, 1995b. doi:10.1126/science.267.5199.868. URL https://www.science.org/doi/abs/10.1126/science.267.5199.868.

M.D. Stern. Theory of excitation-contraction coupling in cardiac muscle. *Biophysical Journal*, 63(2):497–517, 1992. ISSN 0006-3495. doi:https://doi.org/10.1016/S0006-3495(92)81615-6. URL https://www.sciencedirect.com/science/article/pii/S0006349592816156.

Norbert Stoop, Romain Lagrange, Denis Terwagne, Pedro M. Reis, and Jörn Dunkel. Curvature-induced symmetry breaking determines elastic surface patterns. *Nature Materials*, 14(3):337–342, 2015. doi:10.1038/nmat4202. URL https://doi.org/10.1038/nmat4202.

Tzer Han Tan, Jinghui Liu, Pearson W. Miller, Melis Tekant, Jörn Dunkel, and Nikta Fakhri. Topological turbulence in the membrane of a living cell. *Nature Physics*, 16(6):657–662, 2020. doi:10.1038/s41567-020-0841-9. URL https://doi.org/10.1038/s41567-020-0841-9.

Tzer Han Tan, Alexander Mietke, Junang Li, Yuchao Chen, Hugh Higinbotham, Peter J. Foster, Shreyas Gokhale, Jörn Dunkel, and Nikta Fakhri. Odd dynamics of living chiral crystals. *Nature*, 607(7918):287–293, Jul 2022. ISSN 1476-4687. doi:10.1038/s41586-022-04889-6.

K. H. W. J. ten Tusscher, D. Noble, P. J. Noble, and A. V. Panfilov. A model for human ventricular tissue. *American Journal of Physiology-Heart and Circulatory Physiology*, 286 (4):H1573–H1589, 2004a. doi:10.1152/ajpheart.00794.2003. URL https://doi.org/10.1152/ajpheart.00794.2003. PMID: 14656705.

K. H. W. J. ten Tusscher, D. Noble, P. J. Noble, and A. V. Panfilov. A model for human ventricular tissue. *American Journal of Physiology-Heart and Circulatory Physiology*, 286 (4):H1573–H1589, 2004b. doi:10.1152/ajpheart.00794.2003. URL https://doi.org/10.1152/ajpheart.00794.2003.

Andrea Testa, Mirco Dindo, Aleksander A. Rebane, Babak Nasouri, Robert W. Style, Ramin Golestanian, Eric R. Dufresne, and Paola Laurino. Sustained enzymatic activity and flow in crowded protein droplets. *Nature Communications*, 12(1):6293, 2021. doi:10.1038/s41467-021-26532-0. URL https://doi.org/10.1038/s41467-021-26532-0.

1878-1972 Timoshenko, Stephen. *Strength of materials ...* D. Van Nostrand Company, inc., New York,, array edition, 1940.

V. K. Tkachenko. Elasticity of vortex lattices. *JETP*, 29:945, Nov 1969. URL http://www.jetp.ac.ru/cgi-bin/e/index/e/29/5/p945?a=list.

VK Tkachenko. Stability of vortex lattices. *Sov. Phys. JETP*, 23(6):1049–1056, 1966a.

VK Tkachenko. On vortex lattices. *Sov. Phys. JETP*, 22(6):1282–1286, 1966b.

Ian Tobasco. Curvature-driven wrinkling of thin elastic shells. *Archive for Rational Mechanics and Analysis*, 239(3):1211–1325, 2021. doi:10.1007/s00205-020-01566-8. URL https://doi.org/10.1007/s00205-020-01566-8.

Ian Tobasco, Yousra Timounay, Desislava Todorova, Graham C. Leggat, Joseph D. Paulsen, and Eleni Katifori. Exact solutions for the wrinkle patterns of confined elastic shells. *Nature Physics*, 2022. doi:10.1038/s41567-022-01672-2. URL https://doi.org/10.1038/s41567-022-01672-2.

Nathan Tompkins, Ning Li, Camille Girabawe, Michael Heymann, G. Bard Ermentrout, Irving R. Epstein, and Seth Fraden. Testing turing's theory of morphogenesis in chemical cells. *Proceedings of the National Academy of Sciences*, 111(12):4397–4402, 2014. doi:10.1073/pnas.1322005111. URL https://www.pnas.org/doi/abs/10.1073/pnas.1322005111.

Ágota Tóth and Kenneth Showalter. Logic gates in excitable media. *The Journal of Chemical Physics*, 103(6):2058–2066, 1995. doi:10.1063/1.469732. URL https://doi.org/10.1063/1.469732.

Oleh Tovkach, Junbo Chen, Monica M. Ripp, Teng Zhang, Joseph D. Paulsen, and Benny Davidovitch. Mesoscale structure of wrinkle patterns and defect-proliferated liquid crystalline phases. *Proceedings of the National Academy of Sciences*, 117(8):3938–3943, 2020. doi:10.1073/pnas.1916221117. URL https://www.pnas.org/doi/abs/10.1073/pnas.1916221117.

C. Truesdell and R. Toupin. The classical field theories. *Encyclopedia of Physics / Handbuch der Physik*, page 226–858, 1960. ISSN 2197-4195. doi:10.1007/978-3-642-45943-6_2.

Clifford Ambrose Truesdell. The meaning of betti's reciprocal theorem. *Journal of Research of the National Bureau of Standards Section B Mathematics and Mathematical Physics*, page 85, 1963.

Alan Mathison Turing. The chemical basis of morphogenesis. *Philosophical Transactions of the Royal Society of London. Series B, Biological Sciences*, 237(641):37–72, 1952. doi:10.1098/rstb.1952.0012. URL https://royalsocietypublishing.org/doi/abs/10.1098/rstb.1952.0012.

John J. Tyson. *The Belousov-Zhabotinskii reaction.* Lecture notes in biomathematics. Springer-Verlag, Berlin; New York, 1976.

John J. Tyson. Scaling and reducing the Field-Koros-Noyes mechanism of the Belousov-Zhabotinskii reaction. *The Journal of Physical Chemistry*, 86(15):3006–3012, 07 1982. doi:10.1021/j100212a039. URL https://doi.org/10.1021/j100212a039.

Arend M van der Zande, Pinshane Y Huang, Daniel a Chenet, Timothy C Berkelbach, YuMeng You, Gwan-Hyoung Lee, Tony F Heinz, David R Reichman, David a Muller, and James C Hone. Grains and grain boundaries in highly crystalline monolayer molybdenum

disulphide. *Nature materials*, 12(6):554–61, 2013. ISSN 1476-1122. doi:10.1038/nmat3633. URL http://www.ncbi.nlm.nih.gov/pubmed/23644523.

Hugues Vandeparre, Miguel Piñeirua, Fabian Brau, Benoit Roman, José Bico, Cyprien Gay, Wenzhong Bao, Chun Ning Lau, Pedro M. Reis, and Pascal Damman. Wrinkling hierarchy in constrained thin sheets from suspended graphene to curtains. *Phys. Rev. Lett.*, 106: 224301, Jun 2011. doi:10.1103/PhysRevLett.106.224301. URL https://link.aps.org/doi/10.1103/PhysRevLett.106.224301.

Bryan VanSaders and Sharon C. Glotzer. Sculpting crystals one burgers vector at a time: Toward colloidal lattice robot swarms. *Proceedings of the National Academy of Sciences*, 118(3), 2021. ISSN 0027-8424. doi:10.1073/pnas.2017377118. URL https://www.pnas.org/content/118/3/e2017377118.

Dominic Vella and Benny Davidovitch. Regimes of wrinkling in an indented floating elastic sheet. *Physical Review E*, 98(1):1–20, 2018. ISSN 24700053. doi:10.1103/PhysRevE.98.013003.

Massimo Vergassola, Victoria E. Deneke, and Stefano Di Talia. Mitotic waves in the early embryogenesis of *Drosophila*: Bistability traded for speed. *Proceedings of the National Academy of Sciences*, 115(10):E2165–E2174, 2018. doi:10.1073/pnas.1714873115. URL https://www.pnas.org/doi/abs/10.1073/pnas.1714873115.

Estefania Vidal-Henriquez, Vladimir Zykov, Eberhard Bodenschatz, and Azam Gholami. Convective instability and boundary driven oscillations in a reaction-diffusion-advection model. *Chaos: An Interdisciplinary Journal of Nonlinear Science*, 27(10):103110, 2017. doi:10.1063/1.4986153. URL https://doi.org/10.1063/1.4986153.

Michael Vinson, Sergey Mironov, Scott Mulvey, and Arkady Pertsov. Control of spatial orientation and lifetime of scroll rings in excitable media. *Nature*, 386(6624):477–480, 1997. doi:10.1038/386477a0. URL https://doi.org/10.1038/386477a0.

Pai Wang, Ling Lu, and Katia Bertoldi. Topological Phononic Crystals with One-Way Elastic Edge Waves. *Physical review letters*, 115(10):104302, sep 2015. ISSN 1079-7114. doi:10.1103/PhysRevLett.115.104302.

Qiming Wang and Xuanhe Zhao. A three-dimensional phase diagram of growth-induced surface instabilities. *Scientific Reports*, 5(1):8887, 2015. ISSN 2045-2322. doi:10.1038/srep08887. URL http://www.nature.com/articles/srep08887.

Ting Wang, Yifan Yang, and Fan Xu. Mechanics of tension-induced film wrinkling and restabilization: a review. *Proceedings of the Royal Society A: Mathematical, Physical and Engineering Sciences*, 478(2263):20220149, 2022. doi:10.1098/rspa.2022.0149. URL https://royalsocietypublishing.org/doi/abs/10.1098/rspa.2022.0149.

Jamie H. Warner, Elena Roxana Margine, Masaki Mukai, Alexander W. Robertson, Feliciano Giustino, and Angus I. Kirkland. Dislocation-driven deformations in graphene. *Science*, 337(6091):209–212, 2012. ISSN 10959203. doi:10.1126/science.1217529.

Jamie H. Warner, Ye Fan, Alex W. Robertson, Kuang He, Euijoon Yoon, and Gun Do Lee. Rippling graphene at the nanoscale through dislocation addition. *Nano Letters*, 13(10): 4937–4944, 10 2013. doi:10.1021/nl402902q. URL https://doi.org/10.1021/nl402902q.

Yujie Wei, Jiangtao Wu, Hanqing Yin, Xinghua Shi, Ronggui Yang, and Mildred Dresselhaus. The nature of strength enhancement and weakening by pentagon–heptagon defects in graphene. *Nature Materials*, 11(9):759–763, 2012. doi:10.1038/nmat3370. URL https://doi.org/10.1038/nmat3370.

Manon C. Wigbers, Fridtjof Brauns, Tobias Hermann, and Erwin Frey. Pattern localization to a domain edge. *Phys. Rev. E*, 101:022414, Feb 2020. doi:10.1103/PhysRevE.101.022414. URL https://link.aps.org/doi/10.1103/PhysRevE.101.022414.

Manon C. Wigbers, Tzer Han Tan, Fridtjof Brauns, Jinghui Liu, S. Zachary Swartz, Erwin Frey, and Nikta Fakhri. A hierarchy of protein patterns robustly decodes cell shape information. *Nature Physics*, 17(5):578–584, 2021. doi:10.1038/s41567-021-01164-9. URL https://doi.org/10.1038/s41567-021-01164-9.

A. T. Winfree. Electrical turbulence in three-dimensional heart muscle. *Science*, 266(5187): 1003–1006, 1994a. doi:10.1126/science.7973648. URL https://www.science.org/doi/abs/10.1126/science.7973648.

A. T. Winfree. Persistent tangled vortex rings in generic excitable media. *Nature*, 371(6494): 233–236, 1994b. doi:10.1038/371233a0. URL https://doi.org/10.1038/371233a0.

Francis X. Witkowski, L. Joshua Leon, Patricia A. Penkoske, Wayne R. Giles, Mark L. Spano, William L. Ditto, and Arthur T. Winfree. Spatiotemporal evolution of ventricular fibrillation. *Nature*, 392(6671):78–82, 1998. doi:10.1038/32170. URL https://doi.org/10.1038/32170.

T. A. Witten. Stress focusing in elastic sheets. *Rev. Mod. Phys.*, 79:643–675, Apr 2007. doi:10.1103/RevModPhys.79.643. URL https://link.aps.org/doi/10.1103/RevModPhys.79.643.

Jianyang Wu, Pinqiang Cao, Zhisen Zhang, Fulong Ning, Song-sheng Zheng, Jianying He, and Zhiliang Zhang. Grain-size-controlled mechanical properties of polycrystalline monolayer mos2. *Nano Letters*, 18(2):1543–1552, 02 2018. doi:10.1021/acs.nanolett.7b05433. URL https://doi.org/10.1021/acs.nanolett.7b05433.

Zi Liang Wu, Michael Moshe, Jesse Greener, Heloise Therien-Aubin, Zhihong Nie, Eran Sharon, and Eugenia Kumacheva. Three-dimensional shape transformations of hydrogel sheets induced by small-scale modulation of internal stresses. *Nature Communications*, 4 (1):1586, 2013. doi:10.1038/ncomms2549. URL https://doi.org/10.1038/ncomms2549.

Saien Xie, Lijie Tu, Yimo Han, Lujie Huang, Kibum Kang, Ka Un Lao, Robert A Distasio Jr, and Jiwoong Park. Coherent, atomically thin transition-metal dichalcogenide superlattices with engineered strain. *Science*, 359(March):1131–1136, 2018. ISSN 0036-8075. doi:10.1126/science.aao5360.

Chunfu Xu, Peilong Lu, Tamer M. Gamal El-Din, Xue Y. Pei, Matthew C. Johnson, Atsuko Uyeda, Matthew J. Bick, Qi Xu, Daohua Jiang, Hua Bai, Gabriella Reggiano, Yang Hsia, T. J. Brunette, Jiayi Dou, Dan Ma, Eric M. Lynch, Scott E. Boyken, Po-Ssu Huang, Lance Stewart, Frank DiMaio, Justin M. Kollman, Ben F. Luisi, Tomoaki Matsuura, William A. Catterall, and David Baker. Computational design of transmembrane pores. *Nature*, 585 (7823):129–134, 2020. doi:10.1038/s41586-020-2646-5. URL `https://doi.org/10.1038/s41586-020-2646-5`.

Kenneth K. Yamamoto, Toby L. Shearman, Erik J. Struckmeyer, John A. Gemmer, and Shankar C. Venkataramani. Nature's forms are frilly, flexible, and functional. *The European Physical Journal E*, 44(7):95, 2021. doi:10.1140/epje/s10189-021-00099-6. URL `https://doi.org/10.1140/epje/s10189-021-00099-6`.

J. Yan, S. C. Bae, and S. Granick. Rotating crystals of magnetic Janus colloids. *Soft Matter*, 11(1):147–153, 2015. ISSN 1744-683X. doi:10.1039/C4SM01962H. URL `http://xlink.rsc.org/?DOI=C4SM01962H`.

Oleg V. Yazyev and Steven G. Louie. Topological defects in graphene: Dislocations and grain boundaries. *Physical Review B - Condensed Matter and Materials Physics*, 81(19): 1–7, 2010. ISSN 10980121. doi:10.1103/PhysRevB.81.195420.

Ryo Yoshida. Self-oscillating gels driven by the belousov–zhabotinsky reaction as novel smart materials. *Advanced Materials*, 22(31):3463–3483, 2010. doi:https://doi.org/10.1002/adma.200904075. URL `https://onlinelibrary.wiley.com/doi/abs/10.1002/adma.200904075`.

Ryo Yoshida and Takeshi Ueki. Evolution of self-oscillating polymer gels as autonomous polymer systems. *NPG Asia Materials*, 6(6):e107–e107, 2014. doi:10.1038/am.2014.32. URL `https://doi.org/10.1038/am.2014.32`.

Jaehyung Yu, Sunphil Kim, Elif Ertekin, and Arend M. van der Zande. Material-Dependent Evolution of Mechanical Folding Instabilities in Two-Dimensional Atomic Membranes. *ACS Applied Materials & Interfaces*, 12(9):10801–10808, mar 2020. ISSN 1944-8244. doi:10.1021/acsami.9b20909. URL `https://pubs.acs.org/doi/10.1021/acsami.9b20909`.

Jaehyung Yu, Edmund Han, M. Abir Hossain, Kenji Watanabe, Takashi Taniguchi, Elif Ertekin, Arend M. van der Zande, and Pinshane Y. Huang. Designing the Bending Stiffness of 2D Material Heterostructures. *Advanced Materials*, 33(9):1–8, 2021a. ISSN 15214095. doi:10.1002/adma.202007269.

Jaehyung Yu, M. Abir Hossain, Sun Phil Kim, Paolo F. Ferrari, Siyuan Huang, Yue Zhang, Hyunchul Kim, Dina A. Michel, and Arend M. van der Zande. Mechanically sensing and tailoring electronic properties in two-dimensional atomic membranes. *Current Opinion in Solid State and Materials Science*, 25(2):100900, 2021b. ISSN 13590286. doi:10.1016/j.cossms.2021.100900. URL https://doi.org/10.1016/j.cossms.2021.100900.

Jaehyung Yu, Ce Liang, Myungjae Lee, Soumik Das, Andrew Ye, Fauzia Mujid, Preeti K Poddar, Baorui Cheng, Nicholas L Abbott, and Jiwoong Park. Two-Dimensional Mechanics of Atomically Thin Solids on Water. *Nano Letters*, sep 2022. ISSN 1530-6984. doi:10.1021/acs.nanolett.2c02499. URL https://pubs.acs.org/doi/10.1021/acs.nanolett.2c02499.

Jaehyung Yu, Colin Scheibner, Vincenzo Vitelli, Thomas A. Witten, and Jiwoong Park. Mechanics of atomically thin films on water. *in prep.*, 2023.

X. Z. Yu, Y. Onose, N. Kanazawa, J. H. Park, J. H. Han, Y. Matsui, N. Nagaosa, and Y. Tokura. Real-space observation of a two-dimensional skyrmion crystal. *Nature*, 465 (7300):901–904, 2010. doi:10.1038/nature09124. URL https://doi.org/10.1038/nature09124.

Zhihao Yu, Yiming Pan, Yuting Shen, Zilu Wang, Zhun-Yong Ong, Tao Xu, Run Xin, Lijia Pan, Baigeng Wang, Litao Sun, Jinlan Wang, Gang Zhang, Yong Wei Zhang, Yi Shi, and Xinran Wang. Towards intrinsic charge transport in monolayer molybdenum disulfide by defect and interface engineering. *Nature Communications*, 5(1):5290, 2014. doi:10.1038/ncomms6290. URL https://doi.org/10.1038/ncomms6290.

Yuchen Zhao, Xiaoming Zhou, and Guoliang Huang. Non-reciprocal rayleigh waves in elastic gyroscopic medium. *Journal of the Mechanics and Physics of Solids*, 143:104065, 2020. ISSN 0022-5096. doi:https://doi.org/10.1016/j.jmps.2020.104065. URL http://www.sciencedirect.com/science/article/pii/S0022509620302994.

Wu Zhou, Xiaolong Zou, Sina Najmaei, Zheng Liu, Yumeng Shi, Jing Kong, Jun Lou, Pulickel M. Ajayan, Boris I. Yakobson, and Juan-Carlos Idrobo. Intrinsic structural defects in monolayer molybdenum disulfide. *Nano Letters*, 13(6):2615–2622, 06 2013. doi:10.1021/nl4007479. URL https://doi.org/10.1021/nl4007479.

L.M. Zubov. *Nonlinear Theory of Dislocations and Disclinations in Elastic Bodies*. Lecture Notes in Physics Monographs. Springer Berlin Heidelberg, 2008. ISBN 9783540684305.